A satellite image showing a coastal region. On the left, a complex network of rivers and streams flows through a brownish, hilly landscape. The rivers are a mix of dark blue and light blue, indicating varying depths and sediment loads. On the right, a large, light-colored body of water, likely an ocean or a large bay, is visible. The water has a textured appearance with small blue specks and ripples, suggesting phytoplankton activity. The overall scene is a mix of land and water, with the rivers acting as a bridge between the two.

Development of new
remote sensing retrievals for
snow/ice characteristics and
phytoplankton properties

Therese Keck

Development of new remote sensing retrievals for snow/ice characteristics and phytoplankton properties




DISSERTATION

zur Erlangung des akademischen Grades
eines Doktors der Naturwissenschaften
am Fachbereich für Geowissenschaften
der Freien Universität Berlin.

vorgelegt von

Therese Keck

Berlin, April 2018

 2018 Therese Keck

Cover MODIS/Aqua true-colour image (bands 1, 4, and 3)
from western Greenland for 4th August 2017
provided by NASA Worldview
URL <https://worldview.earthdata.nasa.gov>

Development of new remote sensing retrievals for snow/ice characteristics and phytoplankton properties

Entwicklung neuer Fernerkundungsalgorithmen zur
Schnee-/Eis-Charakterisierung und für
Phytoplankton-Eigenschaften

Therese Keck

Erstgutachter: Prof. Dr. Jürgen Fischer
Freie Universität Berlin

Zweitgutachter: Prof. Dr. Luis Guanter
Geoforschungszentrum Potsdam

Tag der Disputation: 06. Juli 2018

Selbstständigkeitserklärung

Hiermit erkläre ich an Eides statt, dass ich die vorliegende Arbeit selbstständig und ohne fremde Hilfe angefertigt, keine anderen als die angegebenen Quellen und Hilfsmittel benutzt und die den benutzen Quellen wörtlich oder inhaltlich entnommenen Stellen als solche kenntlich gemacht habe. Diese Arbeit hat in gleicher oder ähnlicher Form noch keiner Prüfungsbehörde vorgelegen.

Berlin, den 25. April 2018

Therese Keck

Abstract

This dissertation introduces two new remote sensing retrieval methods for snow and ice characteristics and phytoplankton properties. A synergistic usage might be a promising advanced application to investigate ice algae in high latitudes. The retrievals exploit the discrimination power of emissivity and phytoplankton absorption, scattering, and fluorescence due to specific dependency of the properties on object and wavelength.

The cryospheric algorithm sorts three surface emissivities, which are converted from remotely sensed thermal infra-red (TIR) brightness temperatures from Advanced Along-Track Spectro-Radiometer (AATSR) 11 μm and 12 μm bands in nadir and forward view, in a classification scheme. The scheme is based on measurements of Hori et al. (2006) and discriminates between *fine*, *medium*, *coarse* grained snow and *suncrust* and *ice*. Depending on the physical surface temperature *wet* areas are detected. *Invalid* pixels mostly occur at topographically complex areas and due to collocation of the two views. Scenes in Antarctica and Greenland exhibit classified pixels between 60% to 90%.

Phytoplankton is characterized with Total Algae Peak Integration Retrieval (TAPIR) linking the local reflectance maximum in the chlorophyll-a fluorescence domain from 650 nm to 730 nm with the local chlorophyll-a absorption maximum at 670 nm *a670*. Radiative transfer simulations show high sensitivity on chlorophyll-a absorption, phytoplankton scattering and chlorophyll-a fluorescence, which are combined in *a670* in TAPIR. The peak's shape, magnitude and spectral location is mainly influenced from those properties which are considered by a spectral peak integration in the retrieval. TAPIR functions are retrieved for several hyper-spectral instruments such as Environmental Mapping and Analysis Program (EnMAP) and can be applied to multi-spectral sensors, e.g. Ocean and Land Colour Imager (OLCI), with a fitting function.

An application of both algorithms to Lake Erie at the Canadian/American border reveals good performance of TAPIR for high algae concentrations but insufficient results for low phytoplankton amount. A qualitative comparison between classification of snow and ice with meteorological quantities show good agreement. Therefore, the cryospheric algorithm qualifies for detection of snow types and TAPIR for medium to high chlorophyll-a concentration with promising potential to retrieve phytoplankton species and fluorescence.

Kurzfassung

Diese Dissertation führt zwei neue Methoden zur fernerkundlichen Ableitung einer Schnee/Eis-Charakterisierung und von Phytoplankton-Eigenschaften ein. Eine synergetische Anwendung könnte eine vielversprechende weitergehende Anwendung zur Erforschung von Eis-Algen in höheren Breiten sein. Die Ableitungen schöpfen das Abgrenzungsvermögen von Emissivität und Phytoplankton-Absorption, -Streuung und -Fluoreszenz durch die spezifische Abhängigkeit von Objekt und Wellenlänge dieser Eigenschaften aus.

Der Kryosphären-Algorithmus sortiert drei Boden-Emissivitäten, welche aus fernerkundeten thermalen infra-roten (TIR) Helligkeitstemperaturen in Nadir- und Vorwärts-Blickrichtung in den 11 µm und 12 µm-Bändern von Advanced Along-Track Spectro-Radiometer (AATSR) berechnet wurden, in ein Klassifizierungsschema ein. Das Schema basiert auf Messungen von Hori et al. (2006) und unterscheidet zwischen fein, mittel und grob gekörnten Schnee sowie suncrust (Harsch) und Eis. Topographisch komplexe Regionen oder die Kollokation der beiden Beobachtungsrichtungen können zu ungünstigen Pixeln führen. Szenen in der Antarktis und auf Grönland weisen zwischen 60 % und 90 % klassifizierte Pixel auf.

Phytoplankton wird mit dem Total Algae Peak Integration Retrieval (TAPIR) charakterisiert, welches das lokale Reflektanzmaximum im Bereich der Chlorophyll-a-Fluoreszenz von 650 nm bis 730 nm mit der Chlorophyll-a-Absorption bei 670 nm a_{670} in Zusammenhang bringt. Strahlungstransport-Simulationen zeigen eine hohe Sensitivität auf Chlorophyll-a-Absorption, Phytoplankton-Streuung und Chlorophyll-a-Fluoreszenz, welche in TAPIR mit a_{670} zusammengefasst sind. Die Form, die Größe und die spektrale Position des Reflektanzmaximums wird hauptsächlich durch jene Eigenschaften beeinflusst, was in der Methode durch eine spektrale Integration des Maximums berücksichtigt wird. Für hyperspektrale Instrumente wie das Environmental Mapping and Analysis Program (EnMAP) werden TAPIR-Funktionen erstellt und die Ableitung kann auch auf multispektrale Sensoren, z.B. den Ocean and Land Colour Imager (OLCI), mit einer Annäherungsfunktion angewendet werden.

Die Anwendung beider Algorithmen auf den Eriesee an der kanadisch-amerikanischen Grenze zeigt eine gute Durchführbarkeit von TAPIR für hohe Algenkonzentrationen aber unzureichende Ergebnisse für geringe Phytoplanktonmengen. Ein qualitativer Vergleich der Schnee- und Eisklassifizierung mit meteorologischen Größen zeigt eine gute Übereinstimmung. Deshalb qualifiziert sich der Kryosphärenalgorithmus für die Erkennung von Schneearten und TAPIR für mittlere bis hohe Chlorophyll-a-Konzentrationen mit einem vielversprechenden Potenzial Phytoplanktonspezies und Fluoreszenz abzuleiten.

Contents

Abstract	vii
<i>Kurzfassung</i>	ix
Contents	xi
1 Introduction	1
1 Using remote sensing for earth observation	2
1.1 On the applicability of remote sensing	2
1.2 Principle of space-borne remote sensing measurements	3
1.3 On the significance of remote sensing	5
1.4 Algae on ice – an observation	12
2 Thesis scope and outline	16
2 Fundamentals	19
1 Radiative transfer	20
1.1 Radiative transfer theory	20
1.2 Radiative transfer modelling	21
1.3 Retrieving parameters	22
2 Radiation in the atmosphere and in waters	23
2.1 Solar and terrestrial radiation	23
2.2 Radiometric quantities	25
2.3 Optically active constituents in the water	29
2.4 Remote sensing observations in VIS and TIR	39

3	Remotely retrieved cryospheric properties	45
1	Introduction	46
1.1	On the determination of snow and ice	46
1.2	Scope and content of the study	47
2	Instruments and data	48
2.1	AATSR	48
2.2	MERIS	48
2.3	Scene selection	49
2.4	Scene preparation	51
3	Methodology	53
3.1	Physical background and remote sensing	53
3.2	Forward model	54
3.3	Optimization	56
3.4	Emissivity	56
3.5	Characterization method	63
4	Characterization of snow and ice scenes	66
4.1	Exemplary case study	66
4.2	Characterization of all scenes	69
5	Discussion	72
6	Conclusions	75
4	Remotely retrieved phytoplankton properties	77
1	Introduction	78
1.1	On the determination of remotely sensed phytoplankton	78
1.2	On the phytoplankton peak in the fluorescence domain	81
1.3	On the relation of the peak and chl-a absorption at 670 nm	83
1.4	Scope and content of the study	84
2	Radiative transfer simulation with MOMO	86
2.1	MOMO simulation	86
2.2	Sensitivity	88
2.3	Initial validation efforts	96
3	Methodology	100
3.1	Total Algae Peak	100
3.2	TAPIR functions	100
4	Algorithm sensitivity and uncertainty	102
4.1	Sensitivity analysis	102
4.2	Uncertainty assessment	106

4.3	Supplemental <i>TAPIR</i> functions	108
5	Initial algorithm validation efforts	112
6	Discussion	115
7	Conclusions	118
5	Application	121
1	Observing Lake Erie	122
2	Case studies	124
2.1	Algae bloom	124
2.2	Lake ice	127
3	Discussion and conclusions	132
6	Conclusions	135
	Bibliography	139
	List of tables	155
	List of figures	158
	List of acronyms	159
	List of symbols	163
	Curriculum Vitae	165
	<i>Danksagung</i>	167

Abstract

Remote sensing enables us to obtain data on global scale in high spatio-temporal resolution. In the frame of climate change, the cryosphere is directly linked to global warming and observing waters supports the understanding of their condition and the carbon cycle, which includes carbon dioxide that is one of the major radiative forcers. An observation at Greenland shows algae growing on the ice sheet in small melt ponds or liquid water layers. The thesis's scope is the introduction of i) the investigation of the condition of snow and ice covered surfaces and ii) the determination of phytoplankton properties. A combination of both retrievals might be beneficial for future research on ice algae.

Sections 1.1 and 1.2 and parts of section 1.3.3 are based on my contribution in Mascarenhas and Keck (2018, subm., chapter 2). Section 1.3.2 is partly adopted from Keck et al. (2017).

1 Using remote sensing for earth observation

1.1 On the applicability of remote sensing

Remote sensing is a technique of measuring properties of an object without having physical contact. Animals and humans use remote sensing every day exploring the environment with their eyes. Human eyes are sensible to the solar electro-magnetic spectrum from 400 nm to 700 nm ranging from violet to red (visible spectrum (VIS)). Observing clear “blue” water, most of the red and green part of solar light is absorbed and blue radiation is back-scattered to the eyes. Water appears greenish or brownish if it contains constituents, e.g. algae or dissolved or particular matter. Snow and ice appear white due to a relatively high back-scattering in the entire VIS but would be observed very darkly in spectra with longer wavelengths in the thermal infra-red (TIR) due to high absorptive properties.

Generally, one of the most common questions in satellite remote sensing is “Why do we spend so much effort in converting electro-magnetic signals sensed with expensive and complex instruments which are far away in space”? Indeed, *in situ* and field measurements directly offer properties of observed matter (e.g. algae content, temperature, snow depth). Similar results from remote sensing require planning and operation of expensive sensors and their platforms and sophisticated algorithms to retrieve physical “products” (e.g. chlorophyll-a concentration, water vapour content, temperature, or snow grain size) from the satellite sensor signals. Nevertheless, the advantages are a relatively high and continuous spatial and temporal coverage of the entire globe.

For example, at Lake Erie at the border of Canada and the United States, large algae blooms appear every summer that can vary quickly in spatial and temporal dimension (Rowe et al., 2016). Harmful algae blooms (HABs) strongly influence the environment and their degradation products are toxic to animals and humans. Satellite remote sensing enables us to investigate such events without being at the location or taking *in situ* samples. Analysing satellite sensor images, information about spatial extent, location, and chlorophyll concentration can be retrieved alongside other parameters. These data are useful for the development of climatologies and warnings. Even hardly reachable areas such as polar regions are accessible via remote sensing (Bokhorst et al., 2016). For example, Hori et al. (2007) present snow coverage for the Northern Hemisphere in 2003 (fig. 1.1), which cannot be produced with interpolation between rare field measurements particularly in high latitudes.

Additionally, it is possible to detect a pattern’s temporal and spatial variability because

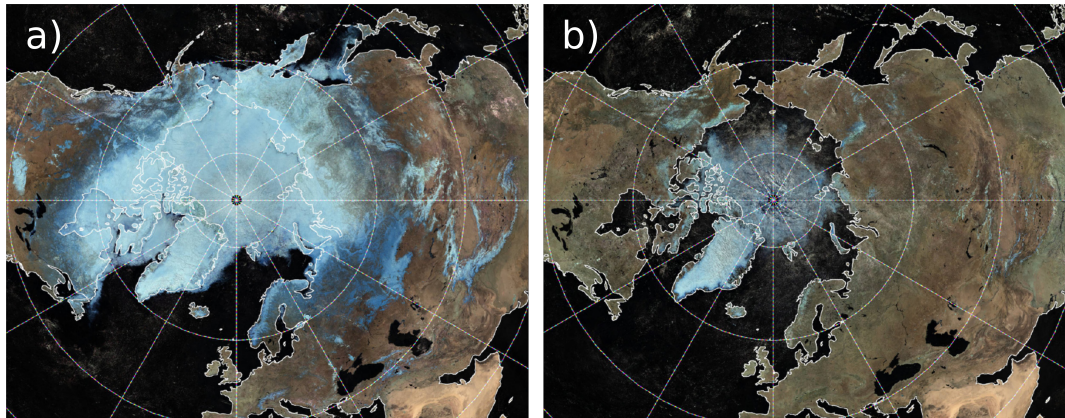


Figure 1.1: False-colour RGB composite images from Global Imager (GLI) on-board Advanced Earth Observing Satellite 2 (ADEOS-2) show 16-day average snow coverage of the northern hemisphere from 7-22 April 2003 and 14-19 September 2003 (Hori et al., 2007).

satellites revisit the same geographic area every few days (e.g. polar-orbiting satellites Terra and Aqua have a revisiting time of 1-2 days) or scan the area every few minutes to hours (e.g. geostationary Meteosat Second Generation 10 (MSG-10) (EUMETSAT, 2017)). We are able to observe the atmosphere, earth's surface, and waters with space-borne remote sensing since more than 50 years on a daily to weekly base in a reasonable spatial resolution ranging from a few meters to several kilometres covering the entire Earth.

However, there is also remote sensing on earth conducted in the field (e.g. on ships or at Aerosol Robotic Network (AERONET) stations) or in the air with instruments mounted on planes. This thesis focuses on space-borne remote sensing and radiative transfer modelling at top of the atmosphere (TOA).

1.2 Principle of space-borne remote sensing measurements

Sensors that measuring signals from Earth's atmosphere, waters and land surfaces are mounted on satellite platforms. Each satellite circulates in a specific orbit around the earth loaded with power supplies, navigation tools, and support systems for the instruments. Generally, the most common satellite orbits are geostationary or polar-orbiting which leads to differences in spatio-temporal resolutions. Geostationary satellites continuously monitor specified geographical locations above the earth's surface in a height of approximately 36 000 km (e.g. EUMETSAT, 2017). Therefore, they cannot cover the entire globe but television and communication satellites usually operate in this orbit due

to the stable position. For example, Geostationary Ocean Color Imager (GOCI) on-board Communication Ocean and Meteorological Satellite 1 (COMS-1) captures images over Korean waters eight times a day (Ryu et al., 2012) or Spinning Enhanced Visible and Infrared Imager (SEVIRI) mounted on MSG-10 scans Europe and the North Atlantic Ocean every 15 min (EUMETSAT, 2017).

Polar-orbiting satellites circle around the globe in approximately 100 min at a height of about 700 km to 800 km (ESA, 2006, Xiong et al., 2013). Their sensors are capable to cover the entire surface of the earth. The time to receive a full coverage depends on the sensor's swath (the scanning line or area on the ground) and can last from 2 to several days. The sensor Moderate Resolution Imaging Spectrometer (MODIS) on-board platforms Aqua and Terra has a revisiting time of less than 3 days due to its large swath of 2330 km (Xiong et al., 2013). Polar-orbiting satellites are usually sun-synchronous: They cross the equator at the same local time (LT). Aqua passes the equator from South to North (ascending node) at 1:30 p.m. LT and Terra has an equator-crossing time of 10:30 a.m. LT in a descending node (Xiong et al., 2013).

There are two main measurement techniques for passive sensors. MODIS on-board Aqua and Terra is a whiskbroom scanner which oscillates across the satellite flight direction. Subsequently, it scans a part of the swath area from one side to the other and backwards while the satellite continues moving (Xiong et al., 2013). A sensor with a pushbroom measuring technique scans along the entire swath width at once and the scanning line is pushed forward with the satellite flight direction and movement. Medium Resolution Imaging Spectrometer (MERIS) on-board Environmental Satellite (ENVISAT) or its successor Ocean and Land Colour Imager (OLCI) on-board Sentinel-3 (S3) are prominent examples (ESA, 2006, 2017).

Most instruments for earth observation have a near-nadir viewing geometry with a measurement sensor directly looking downwards (e.g. MERIS in chapter 3 section 2.2). An off-nadir measurement with a viewing zenith angle greater than 0° from the normal axis between satellite and surface increases the path between the location of the upwelling radiation and the sensor. The signal either increases by diffuse scattering in the atmosphere or attenuates due to more opportunities for absorption and scattering by molecules and particles. This measurement principle provides advanced geometry dependent analysis (e.g. in chapter 3 sections 2.1 and 3 using Advanced Along-Track Spectral Radiometer (AATSR)).

Sensors in space usually possess multiple measuring bands or channels to detect a certain spectral interval of light and its intensity. Mainly, a channel is defined by its central wavelength and the band width described by an individual response function. The response function defines how much of an infinitesimal wavelength interval contributes

to the finally measured signal at this band. For instance, MODIS band 1 ranges from 620 nm to 670 nm detecting photons within this wavelength interval (Xiong et al., 2013). The spectral distribution of sensor channels due to features of the atmosphere and the water are discussed in chapter 2 section 2.4.

However, an enhancement of the spectral abilities reduces the spatial and temporal resolution due to a cost function of scientific gain, technical opportunities, and, of course, financial costs (Hestir et al., 2015). For example, launching in 2020, Hyperspectral Imager (HSI) on-board satellite Environmental Mapping and Analysis Program (EnMAP) will exhibit about 90 narrow channels every 6.5 nm within the visible and near infrared spectrum from 420 nm to 1000 nm (and additional bands in the short-wave infra-red (SWIR)). It provides a high spatial resolution with 30 m per pixel but the swath width is only 30 km increasing the revisiting time to more than 30 days^{1a}. A high spectral resolution of measurement bands supports science and observation of features which exhibit a narrow spectral extension or shift spectrally (e.g. observing the phytoplankton peak in chapter 4). Additionally, the satellite and the sensor must be able to communicate with the ground-based operating centre and also transfer the measured data. Therefore, technical possibilities and scientific objectives constrain the design of a space-borne sensor.

1.3 On the significance of remote sensing

Space-borne remote sensing provides data about meteorological, geo-chemical, and biological quantities in a rather high temporal and spatial resolution depending on sensor and variable (Thies and Bendix, 2011, Hestir et al., 2015). These measurements are already standard input for climate models (e.g. Seiz et al., 2011, Yang et al., 2013, Hawcroft et al., 2017, Santer et al., 2017), reanalysis datasets (cf. Dee et al., 2016) and weather prediction models (e.g. Kumar et al., 2014, Li et al., 2015). They are also used to validate climate and weather model output (e.g. Bani Shahabadi et al., 2016, Enriquez-Alonso et al., 2016). Global Climate Observation System (GCOS) defined 50 essential climate variables (ECVs) including parameters for ocean colour, glaciers, sea and lake states, snow cover, albedo, and photosynthetic active radiation (PAR) which are relevant for climate. Analyses and predictions are significantly based on the retrieval of those ECVs from satellite observations (Yang et al., 2013). Even in a rather “raw” format, satellite observations are used for daily weather forecast and presentation. For example, multiple maps per day of SEVIRI on-board Meteosat Second Generation (MSG) (Schmetz et al., 2002) support the daily weather report illustrating the shift of air

^{1a}EnMAP Hyperspectral Imager, Sensor, <http://www.enmap.org/?q=sensor>, accessed 2018-02-01

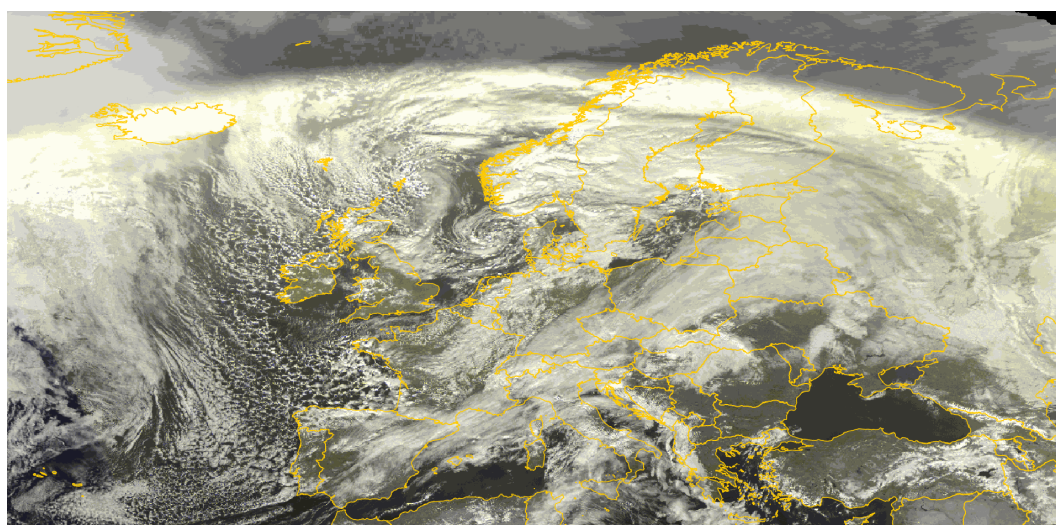


Figure 1.2: *Meteosat-10 RGB image of Europe for the 21st of February 2018 provided by the satellite image viewer from the German national weather service (Deutscher Wetterdienst (DWD) at https://www.dwd.de/DE/leistungen/satellit_betrachter/sat-viewer/sat-viewer_node.html). The image is updated every three hours and the series mainly shows the location of clouds which supports the estimation of the variation of air masses.*

masses, clouds, and temperatures. Figure 1.2 shows a current MSG-10 Red-Green-Blue (RGB) image which supports an overview of the actual state of atmospheric conditions at the North Atlantic Ocean and Europe.

In the eighties, using Total Ozone Mapping Spectrometer (TOMS) on-board Nimbus-7, verification and medial presentation of the “Ozone Hole”, actually being a negative anomaly to the average, led to extensive governmental regulations^{1b} banning the usage of anthropogenic Chlorofluorocarbons (CFCs). CFCs were widely used because they are non-toxic to humans and environment but are involved in depletion of atmospheric ozone which absorbs a major part of solar ultra-violet (UV). Without ozone, UV light reaches the surface harming humans, animals, and environment and heats the surface supporting global warming. This example shows the impact of radiation on global warming and climate change. Therefore, in order to reduce anthropogenic global warming, it is necessary to assess sensitivity and uncertainty of radiative forcing of terrestrial components in the frame of the Earth’s energy budget.

^{1b}The Montreal Protocol On Substances That Deplete The Ozone Layer, URL <http://ozone.unep.org/en/treaties-and-decisions/montreal-protocol-substances-deplete-ozone-layer>, accessed 2018-02-01

1.3.1 Energy budget and radiative forcing

The climate and the atmospheric circulations are mainly driven by solar irradiance heating the ground and the air masses. In general, the solar shortwave radiation (cf. chapter 2 section 2.1) is partly absorbed and partly reflected by atmospheric components or the surface (fig. 1.3). The Earth and the atmosphere emit radiation in the long-wave spectral range (cf. chapter 2 section 2.1) which contributes to warming. Due to the natural greenhouse effect, incoming and outgoing radiation are balanced and the Earth's surface has an average temperature of approximately 14 °C. The temperature would average to -19 °C without globally averaged albedo of 0.3 (Treut et al., 2007, p. 97). Perturbing the equilibrium by changing the proportions of the components in the atmosphere (e.g. additional carbon dioxide (CO₂)) or reducing highly reflective areas (e.g. ice sheets), the coupled earth-atmosphere systems heats up.

The anthropogenic greenhouse effect already led to global average warming of 0.8 K since the end of the 19th century (e.g. Jones and Kennedy, 2017). The warming trend increases and the global average temperature will be risen by approximately 2 K in 2100 compared to the pre-industrial time (e.g. Zickfeld et al., 2017). Butterbach-Bahl and Wolf (2017) stated that *"It has become evident that only reducing greenhouse gas emissions from the industrial, transport and energy sectors will not achieve the 1.5 °C target by 2100"*. The major radiative drivers are greenhouse gases (fig. 1.4) absorbing long-wave radiation. Clouds and surfaces covered with snow and ice have a high short-wave albedo (Petty, 2006, p. 102) and are thus negative radiative forcers. For instance, an increase of the global CO₂ or a reduction of the ice sheets support the global warming (IPCC, 2013). Ingesting CO₂ from the atmosphere, the ocean acidifies and ocean circulations transport the CO₂ to deeper layers where it can be stored for thousands of years (Rhein et al., 2013). Additionally, vegetation on land and algae (phytoplankton) in waters decarbonate the atmosphere by the process of photosynthesis. Unfortunately, the 5th Assessment Report of the Intergovernmental Panel on Climate Change (IPCC) from 2013 (IPCC, 2013), which is often cited and base of many policy agreements, hardly mentions phytoplankton as carbon sink. However, it is necessary to understand the physiology and spatio-temporal behaviour of phytoplankton (Hestir et al., 2015) and its role to the global changes in climate. This thesis contributes studies about the cryosphere in chapter 3 and phytoplankton in coastal and inland waters in chapter 4 which are both motivated in the following.

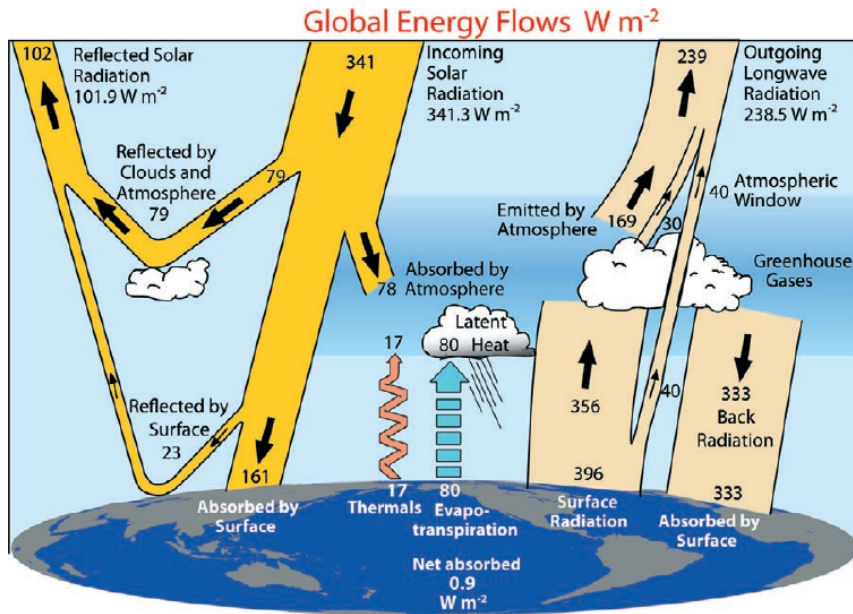


Figure 1.3: Earth's radiative energy budget (picture adopted from Trenberth et al. (2009)). Increasing the amount of absorbers for long-wave radiation (e.g. greenhouse gases) leads to warming of the atmosphere.

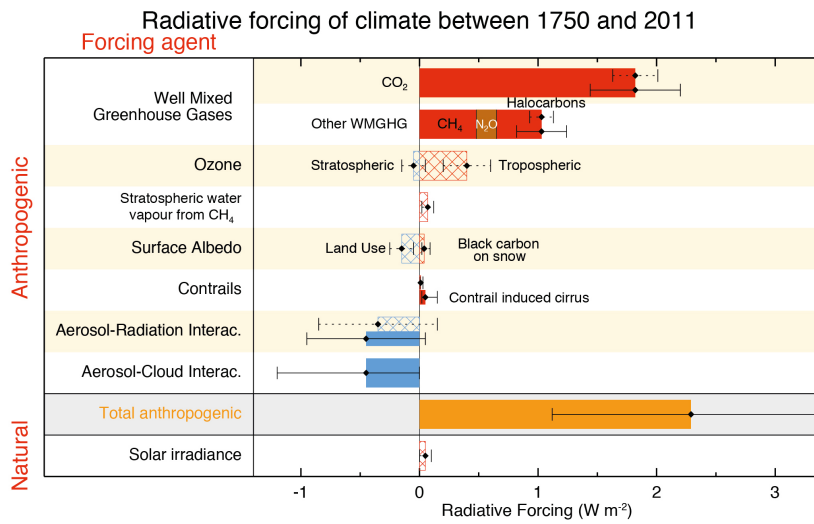


Figure 1.4: Radiative forcing (picture adopted from Myhre et al. (2013)). CO₂ plays a major role in absorbing long-wave radiation and heating the atmosphere and the surface albedo decreases when snow and ice surfaces are impured. Both increasing CO₂ and lower surface albedo support global warming.

1.3.2 Observing the cryosphere

The cryosphere, comprising snow, river and lake ice, sea ice, glaciers, ice shelves and ice sheets, and frozen ground, plays a major role in the Earth's climate system through its impact on the surface energy budget, the water cycle, primary productivity, surface gas exchange and sea level. The cryosphere is thus a fundamental control on the physical, biological and social environment over a large part of the Earth's surface. Given that all of its components are inherently sensitive to temperature change over a wide range of time scales, the cryosphere is a natural integrator of climate variability and provides some of the most visible signatures of climate change.

— Vaughan et al. (2013) in the 5th IPCC report (2013)

According to Vaughan et al. (2013, p. 320), total ice loss of both ice sheets, Antarctica and Greenland, for 1991-2011 amounts in average 4260 Gt (11.6 mm increase of the global sea level). Reduced ice sheets cause lower surface albedo and increasing solar ground absorption supports melting processes. The continuous increasing loss of ice mass demands the understanding of the process' origins and consequences for environment and humankind.

In order to improve global climate models, the analysis of past melt events and the prediction of future melting is a current research topic. For instance, Bennartz et al. (2013) and Neff et al. (2014) investigated a prominent melting in 2012 on the Greenland ice sheet caused by clouds. Beginning and duration of melt events and the magnitude of ice loss are important issues to understand and model the cryosphere. The potential of rapid ice sheet variations within a few weeks and their impact on global climate require sufficient spatial and temporal observation and analysis. For example, Wang et al. (2018) present the number of days of snow coverage retrieved from a fusion of remote sensing instruments MODIS, Advanced Microwave Scanning Radiometer - Earth Observing System (AMSR-E), Landsat Thematic Mapper (TM), and Indian Micro-Satellite (IMS) in fig. 1.5a. Hori et al. (2007) analysed a range of cryospheric parameters including coverage, snow depth, snow grain size, and others, with GLI on-board ADEOS-2. In fig. 1.5b, they show the day of the melt-onset. Both studies provide insight into the high variability and current condition of the cryosphere which is necessary for modelling and investigating climate.

In order to determine the feedback of climate change and cryosphere on each other, the state of snow, which may include age, consistency, impurities, depth, and spatial and temporal extent, has to be analysed. Knowledge about the actual state of snow and meteorological-climatological quantities may support the prediction of sea level rise, melting of glaciers and ice sheets, and also avalanches for which can be warned and

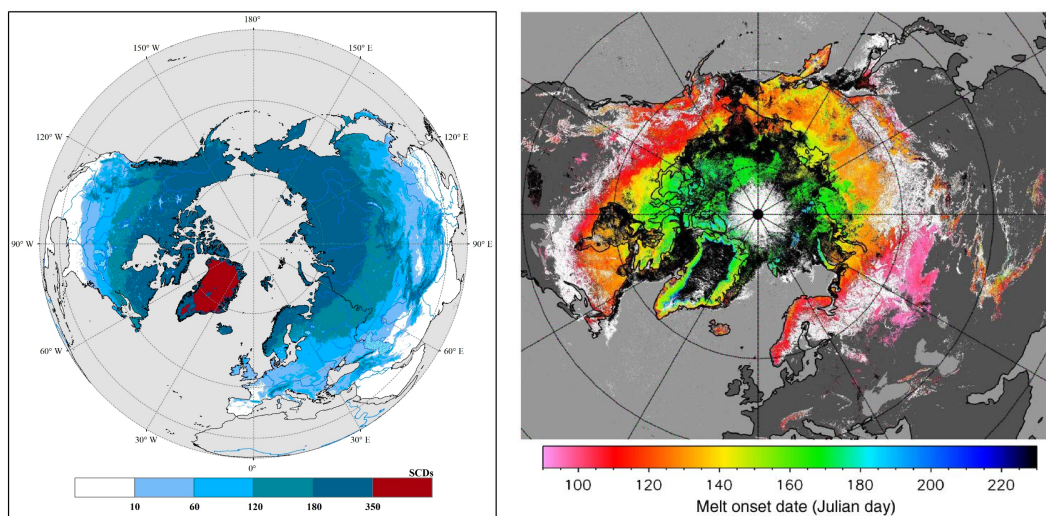


Figure 1.5: Days of snow coverage for the northern hemisphere from 2000 to 2015 (left picture from Wang et al. (2018)). On the right, Hori et al. (2007) show the day of melt onset in 2003.

prepared (Bokhorst et al., 2016). Therefore, in chapter 3, I introduce a remote sensing retrieval that characterizes actual state properties of snow and ice.

1.3.3 Observing oceanic, coastal and fresh waters

Both anthropogenic climate change and anthropogenic ocean acidification are caused by increasing carbon dioxide (CO_2) concentrations in the atmosphere. Rising levels of CO_2 , along with other greenhouse gases, indirectly alter the climate system by trapping heat as it is reflected back from the Earth's surface. Anthropogenic ocean acidification is a direct consequence of rising CO_2 concentrations as seawater currently absorbs about 30% of the anthropogenic CO_2 from the atmosphere.

— Rhein et al. (2013) in the 5th IPCC report (2013)

According to fig. 1.4, CO_2 is one of the major radiative forcing agents for global warming. In order to find methods for CO_2 depletion, the carbon discharge and consumption mechanisms of the total Earth system, including biosphere, hydrosphere, and atmosphere, has to be analysed (cf. fig. 1.6). The “slow carbon cycle” describes the interaction between carbon-containing rocks and sediments with oceans, rivers, and the atmosphere due to volcanic eruption and erosion. Related to relatively short time spans, the “rapid carbon cycle” includes carbon consuming lifeforms such as phytoplankton which discharge carbon to the environment during decomposition (Ciais et al., 2013).

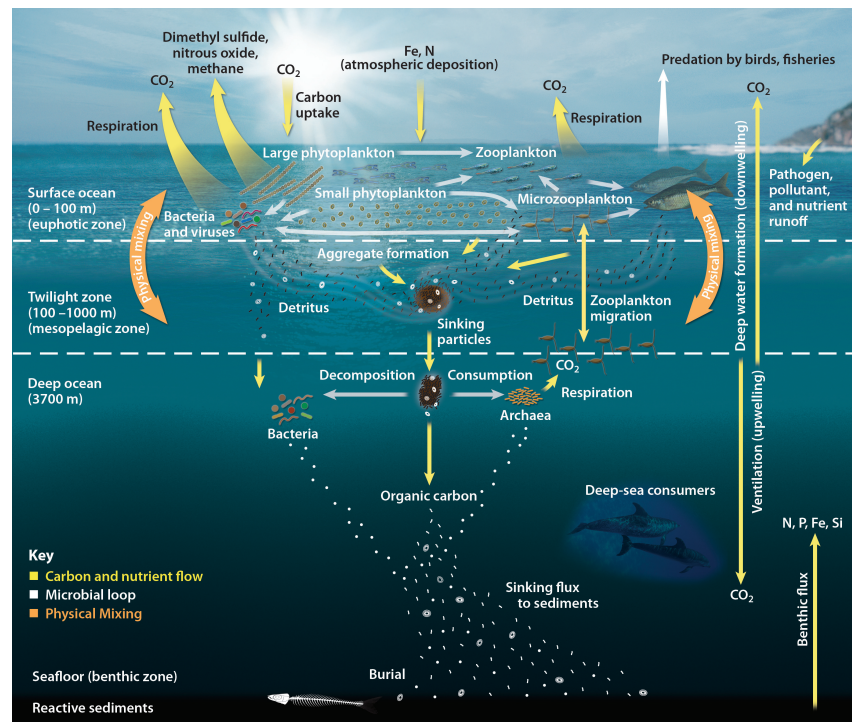


Figure 1.6: Scheme of the carbon cycle in the marine ecosystem in which phytoplankton plays a significant and central role (picture adopted from U.S. DOE (2008, p. 81))

In return for oxygen, vegetation requires carbon, water, and light for photosynthesis producing photo-chemical energy (Krause and Weis, 1991). Therefore, land plants and phytoplankton are sinks for CO_2 (e.g. Merico et al., 2006, Moreira and Pires, 2016, León et al., 2018) but there are still large uncertainties related to the interactions between the marine carbon cycle and phytoplankton (Carr et al., 2006, Tagliabue et al., 2011). During the process of photosynthesis, algae produce oxygen which once established an atmosphere with 21 % oxygen fraction favouring current life forms. Today, 50 % of the global oxygen production originates from algae (Chapman, 2013). Consuming carbon, phototrophical organisms are responsible for primary production describing the growth of biomass. Measuring primary production, the portion of depleted carbon can be estimated (e.g. Carr et al., 2006). Field (1998) reported that 46.8 % of total net primary production is performed in marine ecosystems. A change in phytoplankton population does not only impact the carbon cycle but also the food chain. Many fishes and aquatic mammals consume algae and tracking phytoplankton supports fisheries, the transportation industry

and tourism industry identifying regions of high fish content (Moreira and Pires, 2016) which they can either systematically avoid or locate. Additionally, some phytoplankton species produce large algae blooms which may be toxic and referred to as HABs (e.g. Heisler et al., 2008). In order to warn against the toxicity, governmental institutes are interested in identifying and tracking HABs using remote sensing (Schaeffer et al., 2015).

The imagery from space provides observation of the capacity of freshwater reservoirs. For example, the people in Cape Town, South Africa, currently suffer from severe drought and fresh water supply is strongly restricted since the beginning of 2018 due to a decrease of the largest reservoir, the Theewaterskloof Dam, to around 13 % of its average capacity^{1c}. Remote sensing supports the observation of waters with respect to evaporation, quality, consumption, condition and constituents. Therefore, multiple scientific algorithms can be applied to retrieve physical quantities such as temperature and salinity or water constituents such as algae. Further water constituents such as coloured dissolved organic matter (*cdom*) modify the received optical signal (chapter 2 section 2.3), which complicates phytoplankton retrievals in coastal or inland waters, for instance. In chapter 4, I introduce a technique to obtain optical phytoplankton properties as a proxy for phytoplankton concentration in optically complex waters.

1.4 Algae on ice – an observation

1.4.1 The “dark bands” at western Greenland

During an expedition on the Greenland ice sheet in 1970, Adolf E. Nordenskiöld wondered about small holes (around millimetres to tens of centimetres in diameter (Cook et al., 2016)) in the snow filled with water and contaminated with a “grey powder”. The grey powder also colours the ambient snow cover greyish and accumulates to little granules to which he refers to as cryoconites (Yallop et al., 2012). After Nordenskiöld’s return, Sven Berggren analysed the “powder” and found mainly algae which is referred to as ice algae. Nordenskiöld (1872) noticed that the light absorption had been increased at sites with greyish snow and noted that the darkening may be the “*most dangerous enemy to the mass of ice*”. Indeed, the surface albedo of snow and ice play a role in the process of melting (Box et al., 2012). “Dark bands” have been observed with satellite remote sensing (e.g. Tedesco et al., 2011) illustrated in fig. 1.7. They occur in summer when the insolation increases surface temperatures and the snow and ice start to melt.

For a long time, the colour has been solely related to dust impurities but recently the darkening is linked to the presence of algae (e.g. Takeuchi et al., 2003). Neverthe-

^{1c}A. Voiland, 2018-01-30, <https://earthobservatory.nasa.gov/IOTD/view.php?id=91649>, accessed 2018-02-09

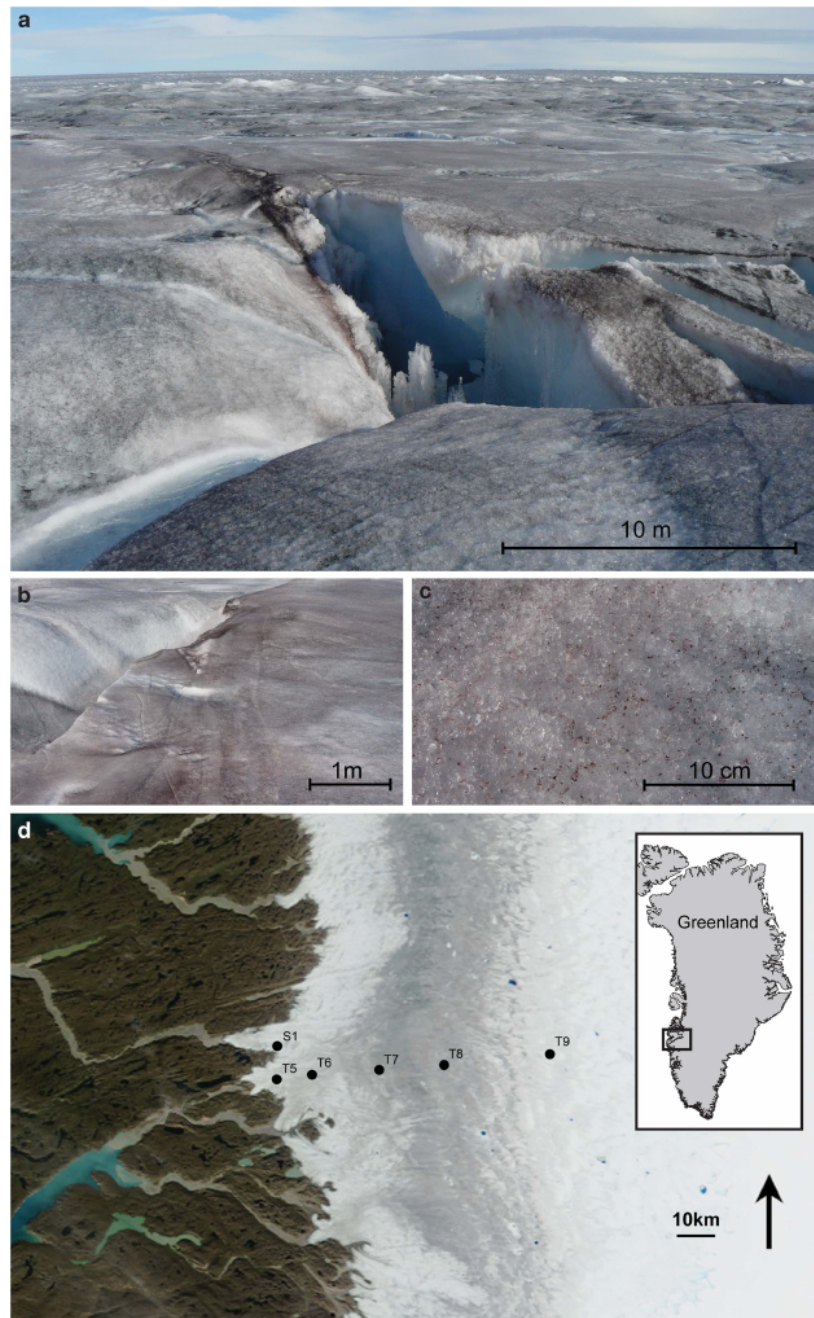


Figure 1.7: Images a) – c) are photographs of ice algae of the western Greenland ice sheet from 2010-08-05 at point T7 of panel d) which is a MODIS/Terra RGB image from 2010-08-17 (picture adopted from Yallop et al. (2012))

less, Yallop et al. (2012) claim that “*the role played by the photosynthetic organisms [...] on the [Greenland ice sheet] has largely been ignored since the early pioneering work*”. Recently, the interest in the “dark bands” increased and the algae on the western Greenland ice sheet are investigated (e.g. Uetake et al., 2010, Lutz et al., 2016, Anesio et al., 2017, Williamson et al., 2018). The impact of algae on surface albedo is topic of latest research (e.g. Box et al., 2012, Benning et al., 2014, Lutz et al., 2016, Stibal et al., 2017, Tedstone et al., 2017). In the frame of global warming, the ice sheets and their albedo are linked to the global energy budget driven by solar irradiance. In order to investigate the Greenland ice sheet and point to its importance, the project Dark Snow (<https://www.darksnow.org>) provides and distributes analyses to the public and supports expeditions and research projects.

1.4.2 On the knowledge of ice algae and ice albedo

According to Yallop et al. (2012) and Williamson et al. (2018), dark snow and ice regions can appear due to snow and ice algae occurring during summer melting periods. The algae grow within the upper few centimetres of a snow pack inside a liquid layer. There is less knowledge about ice algae than snow algae with respect to distribution, taxonomy, biochemical structure, growth rate, carbon fixation, nutrient consumption, and others (Anesio et al., 2017). Anesio et al. (2017) reported that both organic and inorganic impurities “*provide nutrients for the growth of snow (mainly dominated by Chlamydomonadales) and ice algae (mainly dominated by Zygnematales) and heterotrophic bacteria*”. In spite of the differentiation of algae habitats in snow or ice in literature, I will refer to both as ice algae for abbreviation reasons.

At the beginning of the melting season, it is assumed that phytoplankton migrates to the surface for blooming. This behaviour has not been scientifically published yet due to lacking knowledge of the process (cf. Anesio et al., 2017). Stibal et al. (2017) reported a mean doubling of the algae population in western Greenland of around 5 days if no precipitation disturbs the growth. In western Greenland, *in situ* samples of ice algae are only found in melting zones and the chlorophyll-a concentration ranged from $(1.43 \pm 0.51) \text{ mg m}^{-3}$ to $(21.08 \pm 0.95) \text{ mg m}^{-3}$ in 2016 (Stibal et al., 2017, Williamson et al., 2018). Due to their large abundance, ice algae are strong carbon fixers and are transported in the ocean during melt water run-offs.

The bio-reduction of ice albedo (“darkening”) is assumed to be driven by high packaging of ice algae and their specific pigment absorption properties (Yallop et al., 2012). Analysing albedo of the Greenland ice sheet with MODIS measurements from 2000 to 2012, Box et al. (2012) reported an average reduction of 0.056 ± 0.007 for the entire sheet

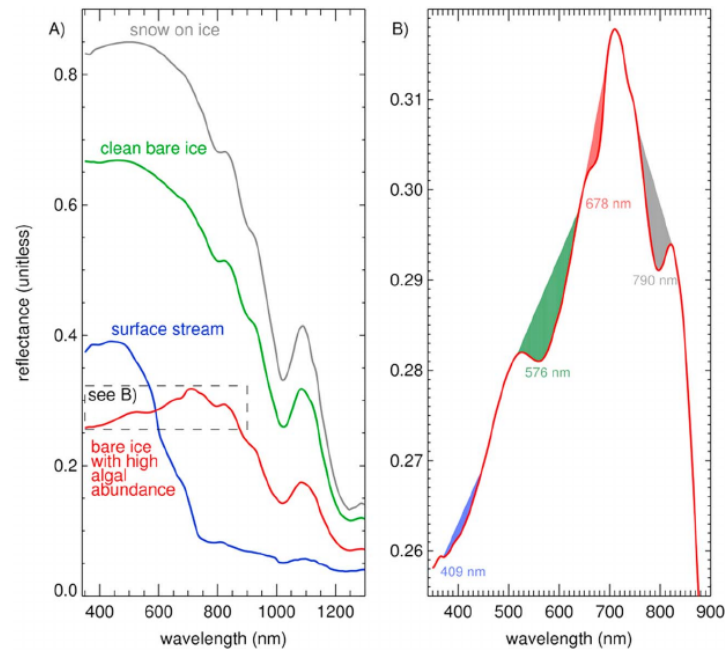


Figure 1.8: Example reflectance of snow, bare ice, and algae growing on ice measured at western Greenland from June to August 2014 (picture adopted from Stibal et al. (2017)).

and 0.091 ± 0.021 for ablation areas in the months June to August. Snow accumulation increases the albedo but due to the overall albedo reduction the surface temperatures have generally increased in average and may lead to increased melting processes (Box et al., 2012).

Melting processes, in turn, produce habitats for ice algae which additionally decrease albedo. Stibal et al. (2017) state that the albedo reduction due to algae is larger than for impurities and retrieve a net albedo reduction of 0.038 ± 0.0035 in western Greenland in 2014. Figure 1.8 shows example *in situ* reflectance measurements over snow, bare ice, and ice algae growing on ice. The second panel exhibits specific absorption features of chlorophyll-a in the blue VIS and near 678 nm. In the frame of global warming and climate change, the large impact of algae on snow and ice albedo leads to the imperative of continuous research on this topic. In particular, since remote sensing techniques and algorithms continuously improve and measurements can be provided in even hardly reachable areas such as the polar region, outreaching investigations are possible.

2 Thesis scope and outline

This thesis addresses both cryospheric and phytoplankton properties retrieved by remote sensing techniques exploiting radiometric properties which are specifically dependent on the observed matter, spectrum, and viewing geometry.

Chapter 1 already motivated the advantages of remote sensing and the role of sensors in space for global scientific applications with respect to climate change and global warming. Algae on ice and snow have a particular influence on the albedo of ice sheets and are assumed to contribute to melting processes. Both algae and albedo, play a significant role in climate change with respect to decarbonisation and global warming.

A characterization method of the snow and ice covered surface might support the determination of required environmental conditions for ice algae. The characterization relates the retrieved radiometric surface conditions in the TIR to the wetness and the snow grain size. Avoiding optical influence such as *cdom*, the reflectance of the red visible spectrum is linked to phytoplankton absorption which is a proxy for phytoplankton content. Both retrievals are based on properties which are specific for the observed object (snow/ice or phytoplankton chlorophyll-a), the wavelength interval (TIR or VIS), and the viewing geometry (nadir/off-nadir or isotropic): TIR emissivity and VIS chlorophyll-a extinction and fluorescence.

Chapter 2 gives an overview of fundamental radiometric quantities and concepts in preparation for the retrievals. Section 1 provides a brief insight into the radiative transfer theory and modelling. Section 2 shortly introduces the radiation in the atmosphere and in waters and commonly used optical quantities. VIS and TIR are selected due to favourable radiometric conditions of the atmosphere and the observed objects.

Chapter 3 presents a retrieval for cryospheric characterization. Section 1 introduces the research in cryospheric remote sensing and the knowledge on the actual state of the ice and snow cover. Section 2 presents the measurement data from AATSR and MERIS and the scene selection and preparation. The deviation of the characterization of snow and ice is based on remotely sensed emissivity retrieved from brightness temperature in the TIR from two viewing angles (section 3). In section 4, the retrieval is applied to 26 AATSR scenes in northern mid-latitudes, Greenland, and Antarctica. The discussion and conclusions follow in sections 5 and 6.

Chapter 4 introduces the Total Algae Peak Integration Retrieval (*TAPIR*) using the phytoplankton reflectance peak in the fluorescence domain from 650 nm to 730 nm and chlorophyll-a absorption at 670 nm. Section 1 introduces phytoplankton property retrievals from space. Section 2 gives an overview of Matrix Operator Model (MOM) simulations along with a model sensitivity study. Additionally, a first validation effort for to the modelled peak and the implemented process of fluorescence is conducted. The proposed technique is motivated and described in section 3. Total Algae Peak Integration Retrieval (*TAPIR*) performance due to sensitivity and uncertainty is presented in section 4 followed by an initial validation assessment with measured *in situ* data in the North Sea and Indonesian waters in section 5. The retrieval is discussed in section 6 and conclusions are given in section 7.

Chapter 5 presents the application of both retrievals to S3 scenes of Lake Erie at the American and Canadian Border, which is known for extreme HABs in summer and a frozen surface in winter which is introduced in section 1. Therefore, scenes from a large bloom in September 2017 and a partly frozen lake in February 2018 are chosen and analysed in section 2. The findings are discussed in section 3.

Chapter 6 recapitulates the thesis with a concluding summary and a brief outlook.

The dissertation includes parts from my contributions in Keck (2014), Keck et al. (2017), Keck et al. (2018), and Mascarenhas and Keck (2018). The affected sections or subsections are indicated at the beginning of each chapter.

“Adopted” parts are included with only minor changes due to syntactic adaption or careful updating. Sections that are “based on” publications underwent major changes. They only follow the main concept or particular paragraphs have been added to the original text.

Abstract

This chapter introduces physical quantities, relations, and concepts which are relevant to the studies of the thesis. Atmospheric radiation and spectral features in the visible spectrum (VIS) and thermal infra-red (TIR) are described. Section 1 gives a brief overview of the radiative transfer theory and modelling. Section 2 characterizes optical properties and quantities of atmospheric components and aquatic constituents. The quantities TIR emissivity, VIS phytoplankton inherent optical properties (IOPs), and chlorophyll-a fluorescence near 683 nm are emphasized due to their particular dependence on solely the viewing geometry, spectrum, and matter.

Sections 2.1 and 2.2 are partly based on Keck (2014, Master's thesis, chapter 2). Sections 2.3.5 and 2.4 are partly based on my contribution in Mascarenhas and Keck (2018, subm., chapter 2).

1 Radiative transfer

1.1 Radiative transfer theory

1.1.1 The radiative transfer equation RTE

In order to analyse the radiometric signals measured at top of the atmosphere (TOA) from satellite sensors it is required to understand the interaction of light with the atmosphere. Radiance or radiant intensity L is the strength of a radiation field and is dependent on both solid angle and wavelength (Petty, 2006) in units $[\text{W m}^{-2} \text{nm}^{-1} \text{sr}^{-1}]$ or $[\text{W m}^{-2} \mu\text{m}^{-1} \text{sr}^{-1}]$. Crossing a semitransparent medium such as atmosphere and water, the intensity of the directional radiation L changes due to the interaction of particles and molecules by absorption, scattering, and emission of photons. Thus, the deviation of radiation along a certain path $\vec{s}(s; \theta, \phi)$ due to extinction, emission and scattering is as follows:

$$(2.1) \quad dL = -cL ds + \varepsilon B(T) ds + dL_{\text{scat}}$$

The first two terms extinguish radiation along the path, where c is the extinction coefficient as sum of the scattering and absorption coefficients, a and b , and B is the black body radiation (cf. section 2.2.2). The last term describes light that is scattered into the direction of the incident light beam with a phase function P constraining the scattering direction Ψ in all solid angles Ω .

$$(2.2) \quad dL_{\text{scat}}(\Omega) = \frac{b}{4\pi} \int_{\Omega} P(\Psi, \Omega) L(\Omega) d\Omega$$

Assuming a plan-parallel layered atmosphere in a spherical coordinate system, the equation can be rewritten using $ds = 1/\mu dz$ as vertical coordinate and the single scattering albedo $\omega_0 = b/c$.

$$(2.3) \quad \frac{\mu}{c} \frac{dL(\Omega)}{dz} = -L(\Omega) + (1 - \omega_0)B + \frac{b}{4\pi} \int_{\Omega} P(\Psi, \Omega) L(\Omega) d\Omega ds$$

The solid angle Ω combines $\mu = \cos \theta$ with θ as zenith angle and ϕ as azimuth angle. According to Chandrasekhar (1960), Petty (2006), and others, the general form of the

radiative transfer equation (RTE) with the source term J is as follows:

$$(2.4) \quad -\frac{\mu}{c(\lambda, z)} \frac{dL(\lambda, z, \mu, \phi)}{dz} = L(\lambda, z, \mu, \phi) - J(\lambda, z, \mu, \phi)$$

1.1.2 Fluorescence

According to Gordon (1979), phytoplankton absorbs radiative energy from visible spectrum (VIS) which excites chlorophyll molecules that emit photons near 685 nm during the process of fluorescence (see 2.3.2.3). Therefore, a mathematical source function J_F for the process requires a description of the excitation A and a function G for the spectral distribution of the emission. The ratio between absorbed and emitted photons is the fluorescence efficiency factor η which scales the excitation:

$$(2.5) \quad A(z, \theta) = \int_{\Lambda_E} \lambda a(\lambda, z) H(\lambda, z, \theta) d\lambda$$

$$(2.6) \quad H(\lambda, z, \theta) = \int_0^{2\pi} \int_0^\pi L(\lambda, z, \theta, \phi) d\phi d\theta$$

$$(2.7) \quad G(\lambda, \lambda_F, \sigma_F) = \frac{1}{\sqrt{2\pi\sigma_F^2}} \exp\left\{-\frac{(\lambda-\lambda_F)^2}{2\sigma_F^2}\right\}$$

Assuming isotropy (factor 4π), the function G distributes emitted fluorescence radiation with a Gaussian function around λ_F with a standard deviation σ_F . The wavelength λ_F and the spectral width σ_F are set to 683 nm and 10.6 nm for calculations. The excitation A is the integral over available radiation (the scalar irradiance H) and *chl-a* absorption in the interval from $\Lambda_E = [395, 685]$ nm. Using A and G , the process of fluorescence in the fluorescence domain from 650 nm to 730 nm is expressed with the source function J_F :

$$(2.8) \quad J_F(\lambda, z, \theta) = \frac{1}{c(\lambda, z)} \frac{\eta(z)}{\lambda_F} \frac{1}{4\pi} * G(\lambda, \lambda_F, \sigma_F) * A(a, z, \theta)$$

The source function is dependent on vertical depth, wavelength within the fluorescence domain and sun zenith angle.

1.2 Radiative transfer modelling

The general RTE provides no analytical solution except for specific cases. However, numerical solutions approximate the RTE and can become very complex which may

consume much time and computational capacity. For instance, Plass and Kattawar (1969) used a Monte Carlo method to estimate the probability of photon interactions and Chandrasekhar (1960) proposed the discretization of the integrated RTE with the Discrete Ordinate Radiative Transfer Model (DISORT). There is a range of radiative transfer models (RTMs) available and the models Radiative Transfer for TIROS Operational Vertical Sounder (RTTOV) and Matrix Operator Model (MOM0) are shortly introduced in chapter 3 section 3.2 and chapter 4 section 2, respectively. In general, a RTM approximates the RTE for constrained variables and parameterizations (e.g. for a determined wavelength interval where specific assumptions are applicable to simplify the computation). They simulate the transmission of radiation through several atmospheric layers optionally considering clouds, aerosols, gas compositions, and the surface. The output of the models is usually a radiometric quantity such as radiance at TOA and bottom of the atmosphere (BOA).

1.3 Retrieving parameters

Knowing the input parameters of a RTM, the simulation results are used to retrieve geophysical, meteorological, or biological quantities from remote sensing measurements. Thus, algorithms invert and optimize the comparison of simulation and measurement which finally leads to the required quantity. The inversion is based on the concept that the retrieved radiative signal carries information about atmosphere, surface, and waters after the transit. Therefore, a forward model F is created, $\vec{y} = F(\vec{x})$, where \vec{y} is the measurement vector defined by the simulations and \vec{x} is the state vector containing the input parameters. Inverting F to $\vec{x} = F^{-1}(\vec{y})$ enables us to retrieve properties from satellite measurements (cf. chapter 3 section 3.2). The optimization can become rather complex. In chapter 3 section 3.3 a relatively simple optimization method, Newton's Iteration, is applied.

2 Radiation in the atmosphere and in waters

2.1 Solar and terrestrial radiation

Remote sensing techniques investigate physical variables, for instance water vapour content, aerosols, amount of water constituents, indirectly by measuring radiometric quantities without physical contact. Thus, Earth observation is based on the understanding of the interaction of the radiation with the atmosphere, water bodies, and the land surface. Each atmospheric component (e.g. aerosols), each water constituent (e.g. phytoplankton), the soil condition (e.g. a snow covered surface or desert), and the “air” and the water themselves possess specific object dependent spectral signatures caused by their optical properties and scaled with their amount. Every physical body emits radiation depending on its physical temperature. The incident solar spectrum almost follows Planck’s Law (see section 2.2.2) for a sun temperature of about 6000 K approximately ranging from 200 nm to 4000 nm with a maximum in the green visible spectrum near 550 nm illustrated in fig. 2.1a. Assuming an average temperature of 15 °C (288 K), the Earth emits radiation in longer wavelengths from 3 μm to 70 μm . The solar or short-wave radiation covers the spectral regimes of ultra-violet (UV), VIS, and near infra-red (NIR) and the terrestrial or long-wave radiation mainly embraces NIR and thermal infra-red (TIR). Figure 2.1a shows an overlap of both solar and terrestrial radiation regimes near 3.5 μm . However, analysing spectral features in the VIS, the signals are not interfered from terrestrial radiation. Vice versa, signals in the TIR are not affected from solar radiation.

Earth-observing space-borne sensors measure radiation that transit the atmosphere. In some spectral intervals, the upwelling radiation reaches the TOA nearly unaffected. For instance, in the TIR regime from 8 μm to 14 μm and in the VIS, the atmosphere is nearly transparent for radiation (fig. 2.1b). In the UV and most parts of the TIR beyond 14 μm , the radiation is nearly completely extinguished and cannot reach any TOA sensors. The atmosphere extinguishes the radiation mainly due to strong absorption of water vapour (top panel in fig. 2.1c and section 2.4.1). Further gaseous absorbers are ozone and oxygen which highly absorb in the UV and partly in the VIS or carbon dioxide (CO_2) and NO_x which absorb in TIR.

The thesis focuses on two spectral regimes: A spectral TIR region around 11 μm to 12 μm (see section 2.4.4 and chapter 3), which is mainly influenced from water vapour absorption, and the VIS (see section 2.4.3 and chapter 4), which is partly interfered from Rayleigh scattering, water vapour, ozone, and oxygen absorption. Analysing the

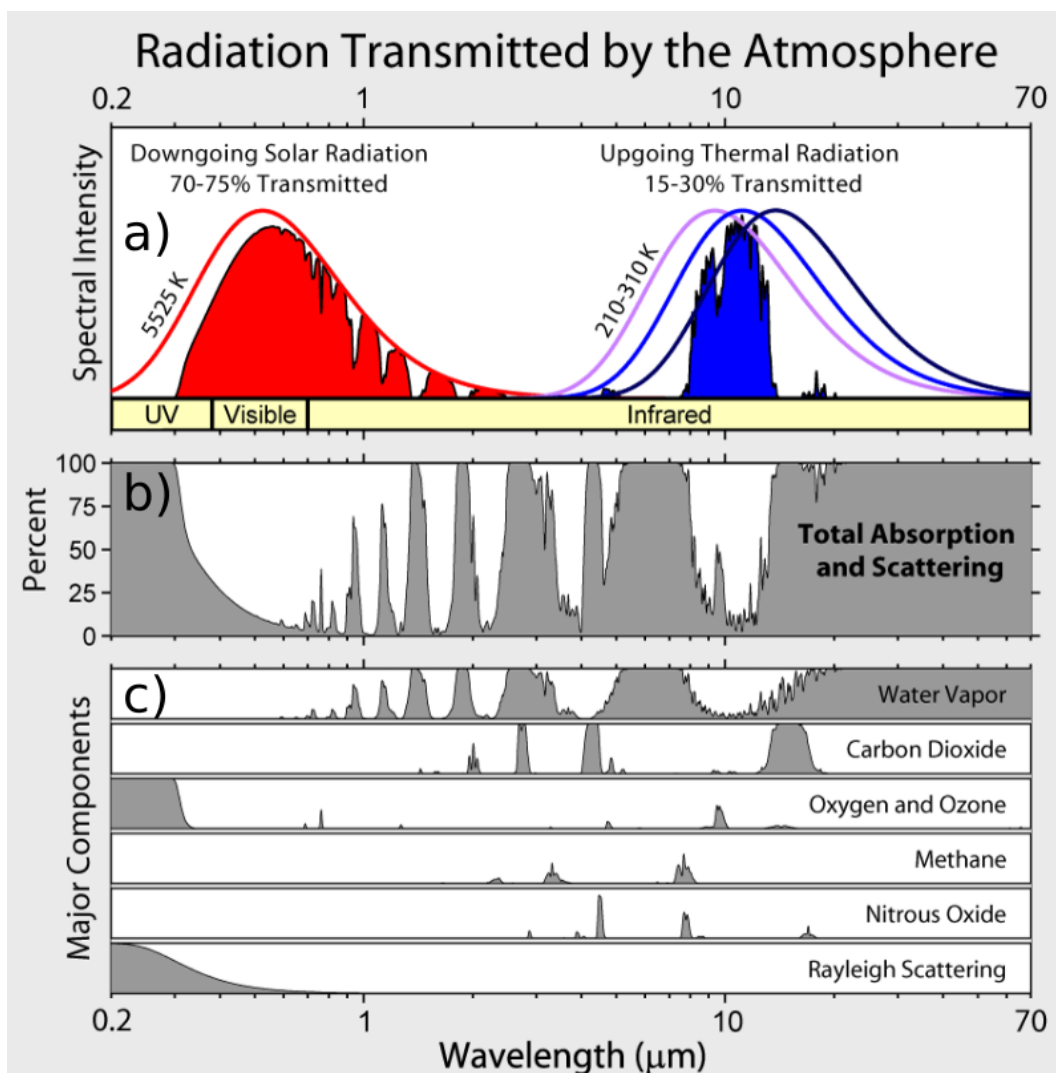


Figure 2.1: The panels^{2.1} show a) Normalized blackbody intensity for solar and terrestrial radiation, b) total light extinction due to atmospheric components, and c) spectral extinction of the major contributing atmospheric components.

^{2.1} R.A. Rohde (2007), Radiation Transmitted by the Atmosphere, https://commons.wikimedia.org/wiki/File:Atmospheric_Transmission.png, CC BY-SA 3.0, modified, accessed 2018-01-24

TIR part, the TOA signals originate from the observed matter, which is snow and ice brightness temperature and emissivity in chapter 3. The investigation of the VIS combines both the solar backscattering influenced from atmosphere and water condition and object dependent emission, which is chlorophyll-a fluorescence and scattering in the red visible part in chapter 4.

2.2 Radiometric quantities

2.2.1 Reflectance and irradiance

Integrating the hemispherical radiance field L , the quantity irradiance E in $[W m^{-2} nm^{-1}]$ is retrieved.

$$(2.9) \quad E(\lambda) = \int L(\lambda, \Omega) \cdot \Omega d\Omega \stackrel{\text{isotrop.}}{=} \pi L(\lambda)$$

In remote sensing terms and in this thesis, the reflectance R is the ratio between upwelling radiance L_u and downwelling irradiance E_d . Using reflectance for analyses, measurements at different locations and dates are comparable due to decoupling from actual intensity of in- and out-going light.

$$(2.10) \quad R(\lambda, \theta) = \frac{L_u(\lambda, \theta, \phi)}{E_d(\lambda, \theta)}$$

However, R is still dependent on sun zenith angle θ and may be disturbed from reflection on the surface. Analysing upwelling radiation from waters directly above the surface, the remote sensing reflectance R_{RS} is applied. It reduces upwelling radiance L_u by diffuse solar radiation L_r reflected on the surface to retrieve water-leaving radiance L_w :

$$(2.11) \quad R_{RS}(\lambda, \theta) = \frac{L_u(\lambda, \theta, \phi) - \rho * L_r(\lambda, \theta, \phi)}{E_d(\lambda, \theta)}$$

The factor ρ is the fraction of direct reflection of diffuse light according to Fresnel equations and is often used with a value around 0.028 although it is dependent on windspeed (and induced waves), viewing angle, wavelength, and sky condition (Mobley, 1999).

2.2.2 Brightness temperature

A black body is the theoretical concept of an object which perfectly absorbs incident radiation and totally emits absorbed energy within a spectral interval depending on

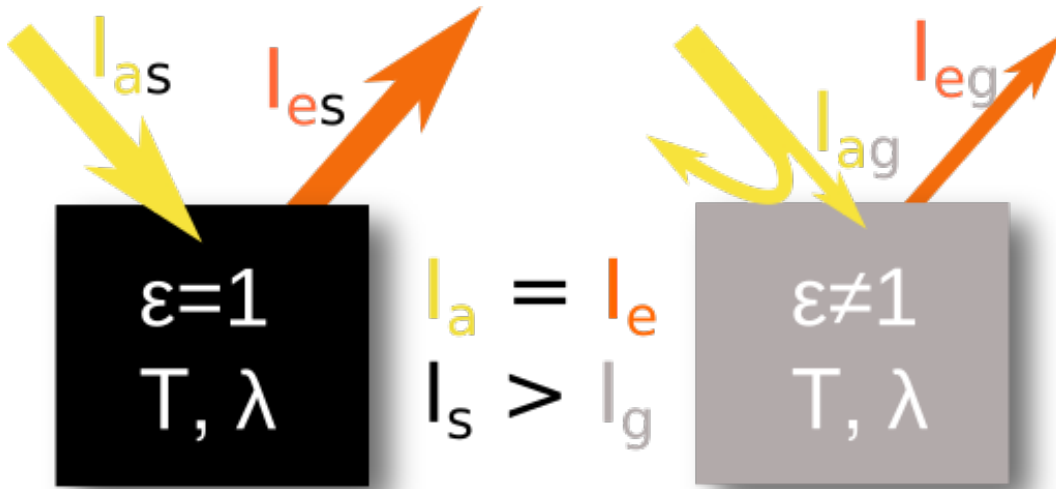


Figure 2.2: Concept of a blackbody and a natural body (greybody), respectively (picture adopted from Keck (2014)).

Table 2.1: Constants for Planck's Law according to Petty (2006).

property	symbol	quantity	unit
speed of light	c_s	$2.998 \cdot 10^8$	m s^{-1}
Planck constant	h	$6.626 \cdot 10^{-34}$	J s
Boltzmann constant	k_B	$1.381 \cdot 10^{-23}$	J K^{-1}

the object's temperature T (fig. 2.2). Considering the Second Thermodynamic Law, Kirchhoff's Law describes the equality of absorptivity and emissivity of a blackbody in a thermal equilibrium dependent on wavelength and solid angle with $a(\lambda, \Omega) = \varepsilon(\lambda, \Omega)$. Planck's Law in eq. (2.12) expresses the spectral distribution and intensity of emitted radiation illustrated in fig. 2.3. The constants c_s , h , and k_B are listed in table 2.1.

$$(2.12) \quad B(\lambda, T) = \frac{2hc_s^2}{\lambda^5 \cdot \left(\exp \left\{ \frac{hc_s}{k_B \lambda \cdot T} \right\} - 1 \right)} = \varepsilon^{-1} L(\lambda)$$

Assuming emissivity of 1, the physical temperature of a blackbody equals the brightness temperature. A natural body emits radiation incompletely (greybody, fig. 2.2). The spectral intensity $L(\lambda)$ is expressed with Planck's Law $B(\lambda)$ reduced by the emission rate ε in eq. (2.12). Therefore, the temperature of a greybody is higher than the brightness temperature. BT is retrieved by inverting Planck's Law in eq. (2.13). It is dependent

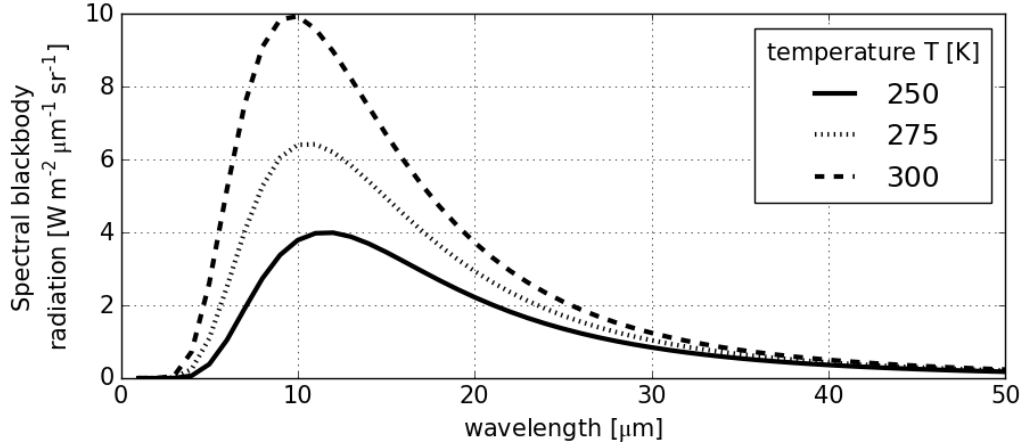


Figure 2.3: Planck's Law for terrestrial temperatures.

on wavelength, emissivity, and physical temperature and varies with polarization and incident angle (Bohren and Clothiaux, 2006).

$$(2.13) \quad BT(\lambda, T) = B^{-1}(\lambda, T; \varepsilon) = \frac{hc_s}{k_B \lambda} \cdot \frac{1}{\ln \left[1 + \frac{1}{\varepsilon} \cdot \left(\exp \left\{ \frac{hc_s}{k_B \lambda \cdot T} \right\} - 1 \right) \right]}$$

Absorbed energy is emitted in a specific infinitesimal wavelength interval dependent on thermodynamic temperature of the object. Therefore, the temperature can be obtained by measuring emitted intensity L if wavelength and emissivity are known. Vice versa, knowing the temperature, emissivity can be calculated.

2.2.3 Emissivity

The emission rate or emissivity ε is monochromatically defined as ratio between blackbody radiation and actual (greybody) radiation. The rate ranges from 0 to 1.

$$(2.14) \quad \varepsilon(\lambda) \equiv \frac{L(\lambda)}{B(\lambda, T)}$$

Figure 2.4a shows the relation of brightness temperature and emissivity for various wavelengths at the temperature $T = 300$ K. The brightness temperature approximately increases linearly for long wavelengths (e.g. 100 μm).

For snow and ice covered surfaces, a minimum emissivity of 0.6 can be assumed

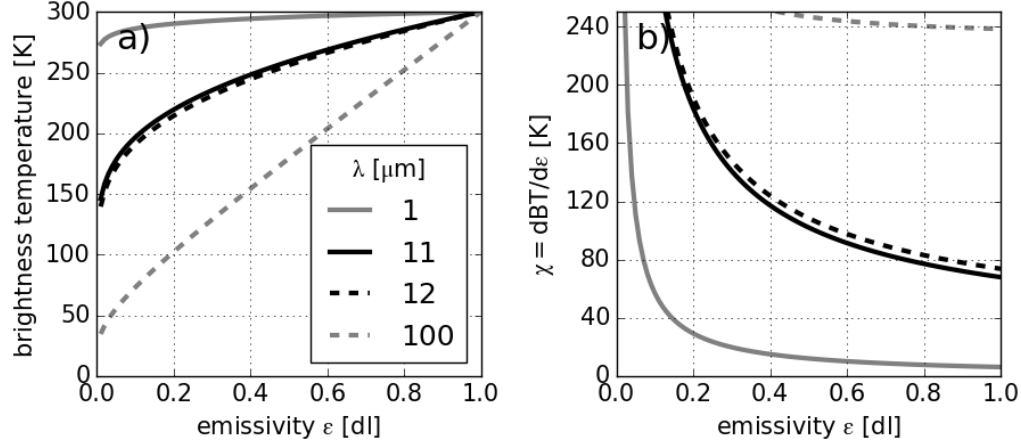


Figure 2.4: Relation of brightness temperatures of several wavelengths with emissivity for a physical temperature of 300 K (panel a). The relation is linear for 11 μm and 12 μm and emissivities >0.7 (panel b).

for $>10 \mu\text{m}$. For emissivities greater than 0.7, the slope can still be assumed to be linear (fig. 2.4b) for wavelengths 11 μm and 12 μm , which are used in the study in chapter 3. The variation of brightness temperature and the variation of emissivity are directly proportional. The deviation of brightness temperature with respect to emissivity can be obtained analytically with eq. (2.15).

$$\begin{aligned}
 \chi(\lambda, T) &= \frac{dBT(\lambda, T)}{d\epsilon} \\
 (2.15) \quad &= \frac{hc_s}{k_B \lambda} \frac{\exp\left\{\frac{hc_s}{k_B \lambda \cdot T}\right\} - 1}{\ln\left[1 + \frac{1}{\epsilon} \cdot \left(\exp\left\{\frac{hc_s}{k_B \lambda \cdot T}\right\} - 1\right)\right]^2 \epsilon \left(\epsilon + \exp\left\{\frac{hc_s}{k_B \lambda \cdot T}\right\} - 1\right)}
 \end{aligned}$$

A brightness temperature variation of 1 K results in an average emissivity variation of approximately 0.013 K^{-1} for T from 250 K to 280 K and the wavelengths 11 μm and 12 μm . Analogously, an emissivity variation of 0.01 for emissivities >0.7 results in an approximate average temperature variation of $(0.52 \pm 0.09) \text{ K}$ for 11 μm and 12 μm .

2.3 Optically active constituents in the water

2.3.1 The colour of waters

In ocean remote sensing the term “Ocean Colour” has been established due to different colours of waters constrained by their constituents in the visible spectrum (fig. 2.5). However, observing not only oceans but also lakes, rivers, and coastal waters I prefer the term “water colour”.

Natural water bodies are a composition of water with constituents. Waters can contain organic or inorganic matter in a dissolved or particulate condition. Each constituent exhibits matter and wavelength dependent properties which are known as inherent optical properties (IOPs). IOPs of water and all water optically active constituents (OACs) constrain the upwelling radiation.

In this thesis, IOPs of phytoplankton (section 2.3.2), coloured dissolved organic matter (*cdom*) (section 2.3.3), water (section 2.4.1), and some supplemental constituents (section 2.3.4) are considered. Figure 2.6 displays IOPs of phytoplankton, *cdom*, and water which sum up to the total extinction

$$(2.16) \quad c_{tot} = a_{tot} + b_{tot} = a_w + b_w + a_{cdom} + a_{ph} + b_{ph}$$

where a and b are absorption and scattering, respectively. *Cdom* scattering is negligible and is not considered.

2.3.2 Phytoplankton

In remote sensing, the terms phytoplankton, algae, and phyla are often equally used and describe drifting microscopic organisms performing photosynthesis in the water.

2.3.2.1 Photosynthesis and chlorophyll-a Photosynthesis is performed in sub-cellular chloroplasts which are filled with the pigment chlorophyll absorbing light in the VIS. In short, a fraction of absorbed light energy supports the chemical conversion of carbon dioxide and water to carbohydrates and oxygen. The oxygen is released and phytoplankton uses “sugar” as photochemical energy source for biochemical activities (Krause and Weis, 1991). Unused absorbed photons are partly released as heat dissipation or during the process of fluorescence in longer wavelengths which is described in 2.3.2.3 (fig. 2.8a). Primarily, phytoplankton chloroplasts contain the pigment chlorophyll-a which colours algae green. In the presence of alternative pigments (e.g. chlorophyll-b or carotenoids) the colour can become more brownish or reddish due to individual spectral absorptive properties.

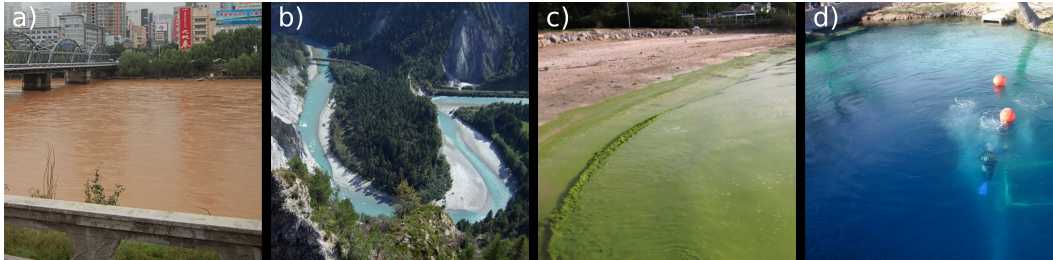


Figure 2.5: Colours of natural waters induced by water optically active constituents (OACs). a)^{2.5a} The Yellow River in Zhongshan (Lanzhou, China) appears brown due to high c_{dom} absorption. b)^{2.5b} The sediments in the Rhine River at the Ruinaulta gorge (Grisons, Switzerland) brightens the water due to high backscattering. c)^{2.5c} In Lake Erie (Canada/USA), an algae bloom colours the water green. d)^{2.5d} Clear water appears blue (Blue Hole lake of Santa Rosa, Mexico).

^{2.5a} von Dobschütz, S. (2009), <https://commons.wikimedia.org/wiki/File:Zhongshan-Br%C3%BCcke-01.JPG>, CC BY-SA 3.0, clipped, accessed 2018-01-30

^{2.5b} Biovit (2007), <https://commons.wikimedia.org/wiki/File:Rhine.jpg>, CC BY-SA 3.0, clipped, accessed 2018-01-30

^{2.5c} NOAA GLERL (2009), https://www.flickr.com/photos/noaa_glerl/4076018686/in/photostream/, CC BY-SA 2.0, clipped, accessed 2018-01-30

^{2.5d} Autopilot (2000), https://commons.wikimedia.org/wiki/File:Blue_Hole_-_New_Mexico.jpg, CC BY-SA 3.0, clipped, accessed 2018-01-30

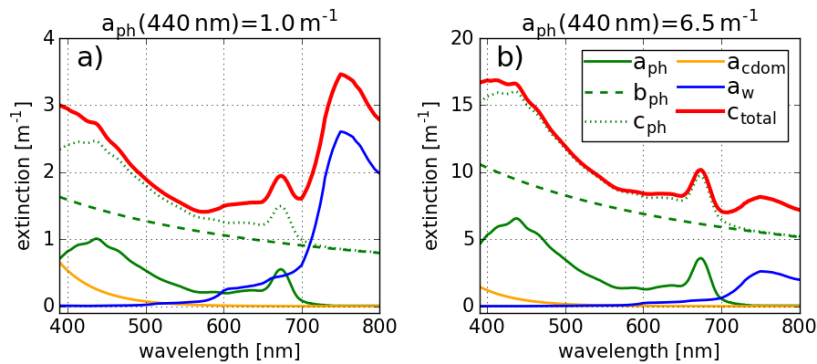


Figure 2.6: Spectral IOPs for water and water constituents. Water scattering is very low and negligible in VIS. Cdom is assumed to be a pure absorber. The higher chlorophyll-a concentration and chlorophyll-a absorption, respectively, the less important is the influence of water absorption in the total extinction coefficients c_{total} in the red VIS and short NIR.

Mostly, phytoplankton remote sensing retrievals use chlorophyll-a concentration as proxy for phytoplankton amount because chlorophyll-a is the optical relevant part of the phytoplankton cell. However, chlorophyll-a concentration is previously retrieved with empirical bio-optical models (BOMs) (see section 2.3.5) which are either based on reflectance ratios (e.g. Ocean Colour quartic algorithm (*OC4*)) or chlorophyll-a absorption at a specific wavelength (e.g. Bricaud et al., 1998) and often do not consider the influence of phytoplankton cell walls which may increase scattering.

Additionally, there is an overlap in the terms of *TSM*, *chl-a*, total *chl-a* (*Tchl-a*), and actual phytoplankton amount measured *in situ*. Investigating phytoplankton, one has to be careful about the actual measured quantity. *TSM* usually combines total particulate matter larger than a certain particle size mainly including also non-phytoplankton content. The difference between *Tchl-a* and *chl-a* mostly occurs due to different *in situ* measuring methods using chemical bleaching or spectroscopy which may include additional pigments (e.g. phaeopigments).

2.3.2.2 Phytoplankton extinction Phytoplankton extinction c_{ph} is the sum of chlorophyll-a absorption a_{ph} and phytoplankton scattering b_{ph} (fig. 2.6). Scattering occurs due to the phytoplankton pigments and cell walls and decreases spectrally with longer wavelengths (dashed green lines in (fig. 2.6)). Light is mainly scattered forward in the direction of the incident beam and only a small fraction with a backscattering to total scattering ratio of $b_{ph,b}/b_{ph}(650\text{ nm}) = 0.0138 \pm 0.0083$ (Loisel et al., 2007) is scattered in the upwelling direction.

A phase function describes scattering of light in the ambient field. Based on measurements of Petzold (1972), a phase function is found which is often used to describe scattering of phytoplankton. Using a backscattering ratio, Petzold's phase function can be expressed with the Fournier-Forand equation (Fournier and Forand, 1994, Fournier and Jonasz, 1999) in eq. (2.17) which is shown in fig. 2.7.

$$(2.17) \quad FF(\psi) = \frac{1}{4\pi(1-\delta)^2\delta^\nu} \left[\nu(1-\delta) - (1-\delta^\nu) \right. \\ \left. + [\delta(1-\delta^\nu) - \nu(1-\delta)] \sin^{-2} \left(\frac{\psi}{2} \right) \right] \\ + \frac{1-\delta_{180}^\nu}{16\pi(\delta_{180}-1)\delta_{180}^\nu} (3\cos^2\psi - 1) \\ \text{with } \nu = \frac{3-\mu}{2} \quad \text{and } \delta = \frac{4}{3(n-1)^2} \sin^2 \left(\frac{\psi}{2} \right)$$

Mobley et al. (2002) proposed a method generating *FF* solely based on backscattering

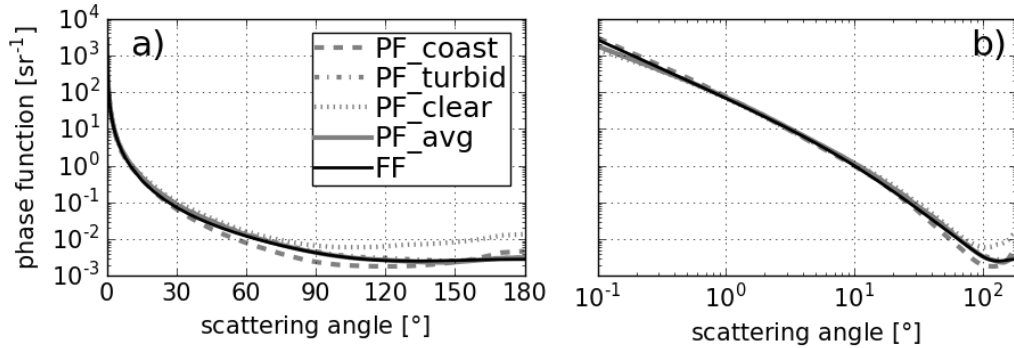


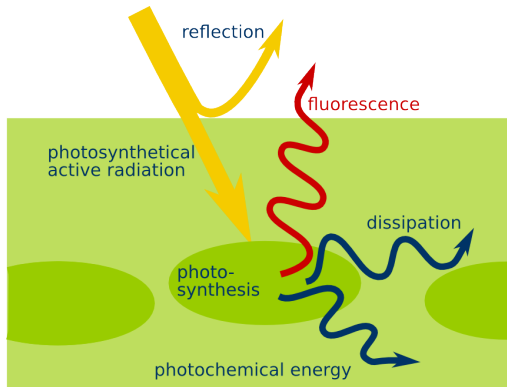
Figure 2.7: Phytoplankton phase function FF analytically retrieved with the equation from Fournier and Jonasz (1999) in eq. (2.17) for a backscattering ratio of 0.01983 and phase functions calculated from measured volume scattering functions from Petzold (1972). Panel b) shows phase functions from a) for scattering angles on a logarithmic scale.

ratio. The backscattering ratio of the averaged Petzold's phase function is given with 0.01986. Aas (1996) reported a refractive index for algae from 1.146 to 1.167 dependent on phytoplankton species and water volume fraction within cells. Therefore, in eq. (2.17), coefficients of refractive index n and Junge slope μ are used with 1.150 for phytoplankton and 3.42304 for particle distribution, respectively. Figure 2.7 shows the phase function for phytoplankton with a ratio of 0.01986.

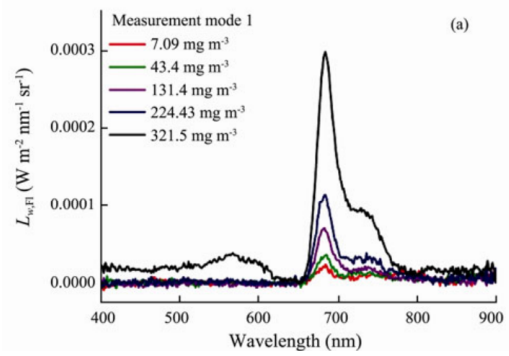
Phytoplankton absorbs light mainly in chlorophyll-a pigments and exhibits two local maxima in the VIS near 440 nm and 670 nm (solid green lines in fig. 2.6). The location and spectral width and strength of the maxima is dependent on phytoplankton amount and health, ratio of chlorophyll-a to other pigments, environmental conditions, and, for analyses, measurement technique. Due to relative low absorptive properties in the green visible range, light is reflected and most plants and algae appear green (fig. 2.8d).

In land remote sensing, vegetation is often quantified with the "red edge", a strong increase in reflectance due to absent phytoplankton absorption beyond 700 nm compared to VIS. However, water absorption rapidly increases at 700 nm inhibiting phytoplankton observations with "red edge" retrievals.

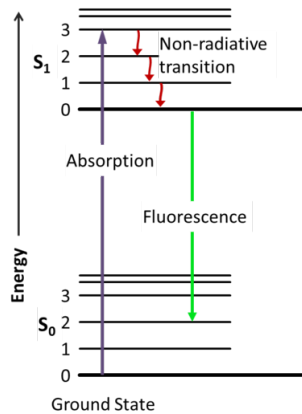
2.3.2.3 Chlorophyll-a fluorescence The energy carried by a photon exaggerates a chlorophyll-a molecule, which has absorbed light, and its orbital electrons are raised from ground state (S_0) to a higher energy level (S_1) (fig. 2.8c). The energized electron



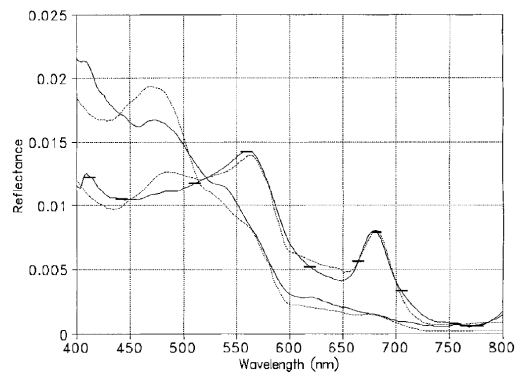
(a) The fate of absorbed photons: Photosynthesis, dissipation, and fluorescence.



(b) Wang et al. (2017) retrieved the pure fluorescence signal peaking near 683 nm with polarization techniques.^{2.8b}



(c) Energy level transition during the process of fluorescence.^{2.8c}



(d) Gower et al. (1999) simulated and measured reflectance with an apparent fluorescence peak near 683 nm due to high chl-a and low reflectance in the red VIS due to water absorption.^{2.8d}

Figure 2.8: The process and effects of fluorescence

^{2.8b} Wang et al. (2017), p. 1006

^{2.8c} Jacobkhd (2012), https://commons.wikimedia.org/wiki/File:Jablonski_Diagram_of_Fluorescence_Only.png, accessed 2018-02-11

^{2.8d} Gower et al. (1999), p. 1783

remains only a short time in the higher electronic state due to an unfavourable energy equilibrium. The electron decays to ground state and releases excess energy by emission of a photon (Krause and Weis, 1991). The process of emitting the photon is called fluorescence. Chlorophyll-a absorbs mainly in the blue and yellow-red part of the VIS and fluorescence appears near 683 nm in the red (Pedrós et al., 2008). The photon emitted during the fluorescence process carries lower energy than the absorbed light and therefore appears “redder” (Stokes Shift) because the exaggerated electron only relaxes to the second vibrational state of the ground state (S_0V_2) retaining some energy (fig. 2.8c).

The strength of fluorescence varies with i) amount of chlorophyll-a (fig. 2.8b), ii) efficiency or quantum yield, and iii) available light. The efficiency factor, which is the ratio between absorbed photons to emitted photons, varies from 0.3% to 1.0% for phytoplankton (Fischer and Kronfeld, 1990, Gilerson et al., 2007). Combining *chl-a* amount, available light, and fluorescence efficiency, the excitation for the fluorescence process can be calculated. Gordon (1979) describes the excitation as an integral of absorbed energy by phytoplankton over the visible spectrum ranging from 390 nm to 685 nm with scalar irradiance and *chl-a* absorption. The excitation is weighted with the efficiency and distributed with a Gaussian function centred at $\lambda_F = 683$ nm with a standard deviation of $\sigma_F = 10.6$ nm. The fluorescence source function $J_F(A)$ is given section 1.1.2 in eq. (2.8).

Measuring water-leaving reflectance, emitted radiation due to fluorescence appears as positive anomaly near 683 nm (figs. 2.8b and 2.8d). However, increasing concentration, chlorophyll-a absorption also increases and emitted fluorescence is partly reabsorbed. The effective peak appears to be shifted towards longer wavelengths. Mostly, fluorescence is quantified with the Fluorescence Line Height (*FLH*) technique (Fischer and Kronfeld, 1990, Gilerson et al., 2007, Gower, 2016), a three-wavelength method obtaining the reflectance difference between fluorescence signal near 685 nm and a baseline usually constrained by reflectance near 660 nm and 710 nm (Neville and Gower, 1977, Fischer and Kronfeld, 1990). However, the effective phytoplankton peak can shift towards longer wavelengths particularly for high *chl-a* and the technique may underestimate phytoplankton properties. In 1977, Neville and Gower discussed the peak’s origin near 685 nm and assumed “[...] that fluorescence is the mechanism that is producing the observed peak. From an operational point of view it matters little which process [fluorescence or scattering] is dominant, since the resulting peak from each will be proportional to the chlorophyll concentration.” In subsequent literature, authors mostly refer solely to the peak as (effective) fluorescence peak. In chapter 4 section 1.2, the interaction of phytoplankton scattering, absorption, and chlorophyll-a fluorescence is discussed.

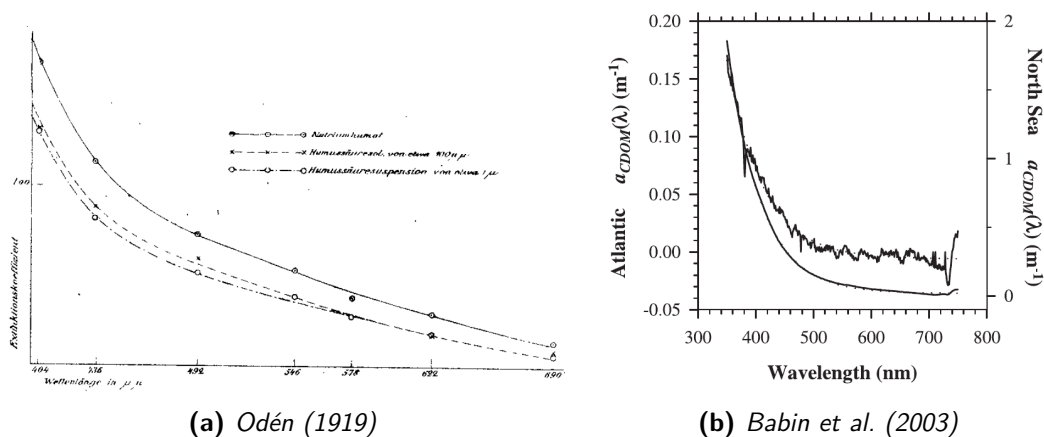


Figure 2.9: The spectral absorption of *cdom* exponentially decays with longer wavelengths. Mathematically, the strength of the decay depends on the slope factor described in section 2.3.5.

2.3.3 Coloured dissolved organic matter

Coloured dissolved organic matter (*cdom*) is a humin acid that is completely dissolved in water colouring it yellowish to brownish. Therefore, *cdom* is previously called yellow substance or *gelbstoff* in literature (Jerlov, 1953, Otto, 1967, Bricaud et al., 1981, Fischer and Kronfeld, 1990). It has firstly been investigated spectrally from Odén (1919) who analysed dissolved *Ackererde* (field soil) and reported an exponential decrease of absorption coefficient in the VIS (fig. 2.9). Otto (1967) summarized remote sensing results from Kalle (1937, 1949, 1961) investigating *cdom* in waters spectrally. *Cdom* is assumed to be a pure absorber and highly minimizes the penetration depth of light in the blue visible range. The spectral decay of absorption can be expressed by exponential functions (see section 2.3.5) *Cdom* can limit the growth of phytoplankton due to light availability. However, it is also a supply for nutrients in the aquatic food web and has a fluorescent component in the UV to blue VIS (Fellman et al., 2010).

2.3.4 Supplemental quantities and constituents

Alongside phytoplankton and *cdom*, supplemental quantities influence the ambient light field within and above waters but play a minor role in this thesis. Temperature, wind, and salinity control the physical condition of water bodies. Organic and inorganic particles occur due to biological degradation products (e.g. detritus), erosion, deposition of atmospheric particles washed out by precipitation, and river run-offs.

2.3.4.1 Temperature, wind, and salinity The angle between incident or water-leaving radiation with the water surface changes with refractive index influenced by temperature and salinity. Wind-induced waves constrain surface roughness which plays a role in the orientation of the planar water surface. A tilted surface allows different incident angles than a plan-parallel surface which is an important factor for the ambient light field constrained by incident and viewing geometry. Additionally, upwelling or wind-induced water bubbles and wind-induced white caps highly reflect visible light appearing white and hardly contain information about the water body constitution.

Surface roughness firstly has been investigated by Cox and Munk (1954, 1956), who provide equations describing average slopes of waves and roughness with respect to windspeed and refractive index. Liu et al. (2013) analysed the influence of different windspeeds on IOPs retrieved from reflectance measurements. Although, there is a variation, this thesis does not investigate the sensitivity to windspeed.

2.3.4.2 Inorganic particles Inorganic particles, e.g. mineral sediments, can brighten water-leaving radiation. Binding et al. (2005) show an increase in the entire visible BOA reflectance with increasing sediment load. For sediment concentrations from 10 g m^{-3} to 15 g m^{-3} the reflectance near 550 nm increases by up to 13%. Meland et al. (2010) retrieved phase functions for mineral dust aerosols (quartz) in the VIS which can compared to sediments in water. Phase functions range from 10^{-1} sr^{-1} in backscattering direction to $0.5 \cdot 10^{-1} \text{ sr}^{-1}$ in forward scattering direction. Compared to the phytoplankton phase function obtained from Petzold (1972) in fig. 2.7, the phase function appears with a rather similar slope with a large forward scattering peak and a lower backscattering but the range spans three magnitudes instead of six magnitudes. The scattering behaviour changes with particle size, shape, and density (Binding et al., 2005).

Additionally, in shallow waters, the ground, which is usually sand or rocks, may gleam through the water and influences measured remote sensing signals. Conducting transfer simulations in this thesis, the ground is assumed to be “black” and, therefore, does not influence radiation although this effect mainly occurs to coastal and inland waters.

2.3.4.3 Organic particles Dead vegetation particles and degradation products, detritus or tripton, colours the water brownish. In combination with phytoplankton, they are often referred to as *TSM* (cf. section 2.3.2) which may also incorporate inorganic particles due to filtering measurement methods. The spectral absorption decreases exponentially and the spectral decay than for *cdom*. Additionally, organic particles can originate from land erosion and agriculture products may washed in rivers, lakes, and coastal waters.

2.3.5 Bio-optical models

A bio-optical model (BOM) links optical measurements and biological parameters with a mathematical expression. Mostly, relations are empirically found by correlating an IOP or reflectance measurement with a simultaneously measured biogeochemical variable. Exemplary, several chlorophyll-a concentration algorithms are based on bio-optical models (BOMs). BG is the relation between a “green” and “blue” measurement band in the VIS providing a qualitative estimate of the relative presence of phytoplankton in case-1 waters (Morel and Prieur, 1977). According to O'Reilly et al. (2000), Ocean Colour quartic algorithm for MERIS ($OC4E$) is an empirical relation between the maximum reflectance blue-green ratio and chlorophyll-a measurements.

$$(2.18) \quad BG(OC4E) = \max \left\{ \frac{R([443, 490, 510] \text{ nm})}{R(560 \text{ nm})} \right\}$$

$$(2.19) \quad \log_{10} chl-a(OC4E) = 0.3255 - 2.7677 * (\log_{10} BG) + 2.4409 * (\log_{10} BG)^2 - 1.1288 * (\log_{10} BG)^3 - 0.4990 * (\log_{10} BG)^4$$

There is a wide range of “OC” algorithms depending on used instrument and degree of the polynomial. BOMs also can describe the spectral slope of IOPs:

$$(2.20) \quad cdom(\lambda) = cdom(\lambda_0) \exp \{-S(\lambda - \lambda_0)\}$$

$$(2.21) \quad a_{ph}(\lambda) = A(\lambda) * chl-a^{1-B(\lambda)}$$

Equations (2.20) and (2.21) are commonly used models to describe $cdom$ and phytoplankton absorption (e.g. Gilerson et al., 2008, Brewin et al., 2011, McKee et al., 2014). Usually, slope factor S ranges from 0.005 nm^{-1} to 0.031 nm^{-1} (e.g. Bricaud et al., 2012, Brewin et al., 2015, Chen et al., 2017) and is highly dependent on the reference λ_0 which is set to an available blue wavelength around 440 nm.

Bricaud et al. (1995, 1998) found eq. (2.21) empirically with spectral dependent coefficients A [$\text{m}^3 \text{ mg}^{-1}$] and B [dl] in open oceans. Therefore, the model is mainly valid for case-1 waters and based on knowledge of $chl-a$, which has to be estimated or measured beforehand, to retrieve the spectral shape of $a_{ph}(\lambda)$. Figure 2.10 demonstrates correlations of *in situ* measurement data from $chl-a$ and absorption coefficient at 440 nm (a_{440}) which are highly dependent on the collection site. Therefore, it may be valuable to retrieve optical properties such as absorption coefficients from optical remote sensing measurements at first and afterwards apply a regional dependent bio-optical model. In chapter 4, I introduce an approach to retrieve absorption solely from optical reflectance measurements. A BOM for $chl-a$ can be applied afterwards.

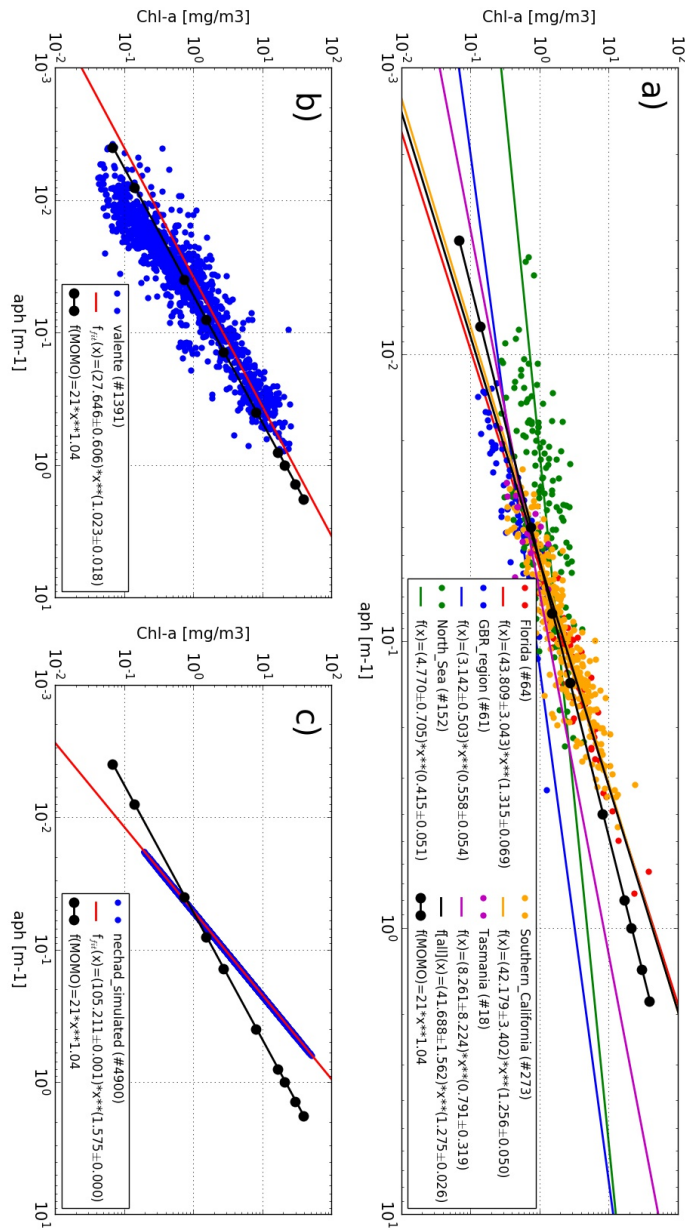


Figure 2.10: Bio-optical models for phytoplankton for various oceanic regions from various data sets merged by Nechad et al. (2015) in a) and Valente et al. (2016) in b). Panel c) shows HydroLight simulation input conducted by Nechad et al. (2015).

Alongside relations between optical properties and biogeochemical constituents and the spectral expression of IOPs, BOMs can also relate different IOPs to each other. For instance, degradation products of phytoplankton exhibit optical properties similar to $cdom$ and the amount increases with increasing $chl-a$ (e.g. Bricaud et al., 2012, Dall’Olmo et al., 2017). Thus, there is a natural correlation of both absorption coefficients. Based on data of the North Sea merged from Nechad et al. (2015), a case-1 BOM relating $cdom$ and phytoplankton $a440$ yields for 440 nm

$$(2.22) \quad cdom(440 \text{ nm}, a440) = 0.24 * a440^{0.43} = g(a440).$$

In chapter 4, eqs. (2.20) and (2.22) are used with with shape factor $S = 0.02 \text{ nm}^{-1}$.

2.4 Remote sensing observations in VIS and TIR

In previous sections, properties of optically active constituents and radiometric quantities has been outlined. The properties of observed matter and atmosphere mainly constrain the spectral “window” of observation with space-borne remote sensing. Major limiting factors are strongly absorbing atmospheric water vapour (section 2.4.1) and natural and technical restrictions and obstacles (section 2.4.2). Therefore, exploiting spectral features of water, atmosphere, and object of interest, the visible spectrum is the domain for phytoplankton observations (section 2.4.3) and the thermal-infrared spectrum is used for cryospheric characterizations (section 2.4.4).

2.4.1 Water and atmospheric water vapour

Water vapour plays an important role in weather, climate, and atmospheric circulation. Figure 2.1b shows strong radiation extinctions in NIR and TIR which mainly occurs due to atmospheric water vapour (top panel in fig. 2.1c and fig. 2.11). There are two big “windows” with weaker water vapour absorption: The VIS and the TIR from approximately $8 \mu\text{m}$ to $14 \mu\text{m}$ (fig. 2.11). However, measurements are still sensitive to water vapour and signals usually have to be corrected for at least water vapour. The application of water vapour products (e.g. Lindstrot et al., 2014) supports the “cleaning” of TOA signals for further retrievals. Water vapour absorption coefficients are rather well known and the challenge is to obtain the actual amount of water vapour per pixel.

In contrast to the atmosphere, where the total water vapour amount of a unit column rarely exceeds a few centimetres, the water column of lakes and oceans range from metres to kilometres. Water colour algorithms use measurements in the VIS because the upwelling signal at longer wavelengths (NIR/TIR) becomes very small due to water

absorption. Figure 2.6 illustrate increasing water absorption beyond 600 nm and strong increase beyond 700 nm (Pope and Fry, 1997). The observed water depth is limited by penetration depth which is constrained by at least water absorption. The depth reduces with additional absorbing constituents (e.g. *cdom*). For example, in clear waters, blue light reaches approximately 70 m but red light penetrates only a few meters (Gordon and McCluney, 1975). This limits water colour algorithms to the VIS.

2.4.2 Obstacles

Both solar and terrestrial radiation can be measured with remote sensing techniques. Passive remote sensing instruments measure electrical counts within the VIS at certain measurement channels. After downlinking measured data, counts are usually converted to physical quantities radiance L or reflectance R (cf. section 2.2), that are used for scientific analyses. However, in the TIR, direct physical quantities such as brightness temperature (cf. section 2.2) are obtained. The measurements change with spectrum, viewing geometry, intensity and polarization's degree. However, the influence of polarization is not incorporated in the studies of this thesis and model and measurement data are assumed to be unpolarized.

Dependent on the scientific mission of the satellite, the sensor band are specified by spectral distribution (central wavelength and number of bands) and spectral width. For example, Medium Resolution Imaging Spectrometer (MERIS) and Ocean and Land Colour Imager (OLCI) are multi-spectral sensors in the VIS designed for water observation and obtaining the "fluorescence peak". Nevertheless, the fluorescence band has been shifted from 685 nm to 681.25 nm due to oxygen absorption (O2B, cf. section 2.4.3). Due to the shift, the actual peak of phytoplankton is difficult to estimate because the closest bands are located near 673 nm and 708 nm (cf. chapter 4 section 4.3).

Among others, major natural obstacles in remote sensing of surfaces and water bodies are clouds, sunglint, and interfering atmosphere. For example, in the microwave regime, clouds are transparent and sensors can measure underlying surface (e.g. Wentz, 2000). Usually, microwave instruments are used for detection of sea surface temperature, surface height, and snow water equivalent and grain size retrievals (e.g. Gentemann et al., 2010, Foster et al., 2005, Buckingham et al., 2014, Brucker et al., 2010). For optical measurements, certain algorithms ("cloud masks") exclude pixels with expected cloud coverage (e.g. Istomina et al., 2010, Vermote et al., 2014, Hollstein et al., 2015, Marks et al., 2016, Stengel et al., 2017). Sunglint occurs at smooth and highly reflective surfaces if solar light is directly reflected into the sensor. The bright reflection can oversaturate a sensor's measurement capability and also contains very low or no information

about the observed object which can be avoided by changing viewing geometry.

Finally measured TOA radiation had to transit the atmosphere, which changes the upwelling signal due to optical properties of aerosols, clouds, and atmospheric gases (e.g. water vapour). The influence of the atmosphere on the TOA-signal can be estimated by modelling and supplemental measurements. Using estimations, the signal can be corrected for atmospheric contribution ("Atmospheric Correction"). Inaccurate estimations can cause large uncertainties due to insufficiently described atmospheric conditions of a high variability of the components composition (e.g. water vapour content), clouds and aerosols.

2.4.3 Observing phytoplankton in the VIS

In the visible spectrum (VIS), the atmosphere exhibits three major agents for extinction:

- atmospheric water vapour absorption
- atmospheric ozone and oxygen absorption
- Rayleigh scattering

Absorption bands of water vapour start around 600 nm and become rather continuous beyond 750 nm (fig. 2.11) which requires a proper water vapour correction for water remote sensing using the red VIS.

Atmospheric oxygen has two absorption bands in the VIS near 688 nm (O2B-band) and near 765 nm (O2A-band) (fig. 2.11). The O2B band has influence on chlorophyll-a fluorescence near 683 nm whereas the O2A-band is located beyond 750 nm where water is already strongly absorbing. Thus, the design of multi-spectral optical instruments avoids measurement bands near 688 nm and, for instance, the MERIS band intended for fluorescence retrievals was adjusted to 681.25 nm. Ozone accumulates in approximately 50 km height and absorbs almost the entire UV. From around 500 nm to 700 nm, ozone exhibits an absorption continuum bi-peaking near 575 nm and 603 nm (Chappuis bands).

Rayleigh scattering describes scattering at particles which are small compared to incident wavelengths. In the VIS, particles have to be smaller than 1 nm, which applies for air molecules, to perform Rayleigh scattering. The scattering mainly influences water observation in the blue VIS (cf. fig. 2.1c).

Figure 2.11 shows that observing terrestrial waters with radiometric measurements is prohibited outside the VIS due to strong absorption of water vapour and other gases in the UV, NIR, and TIR. Commonly, phytoplankton is investigated in the blue and green VIS due to strong absorption of chlorophyll-a near 440 nm and high reflectance near 550 nm (fig. 2.6) using, for instance, blue-green ratios. However, using the range from

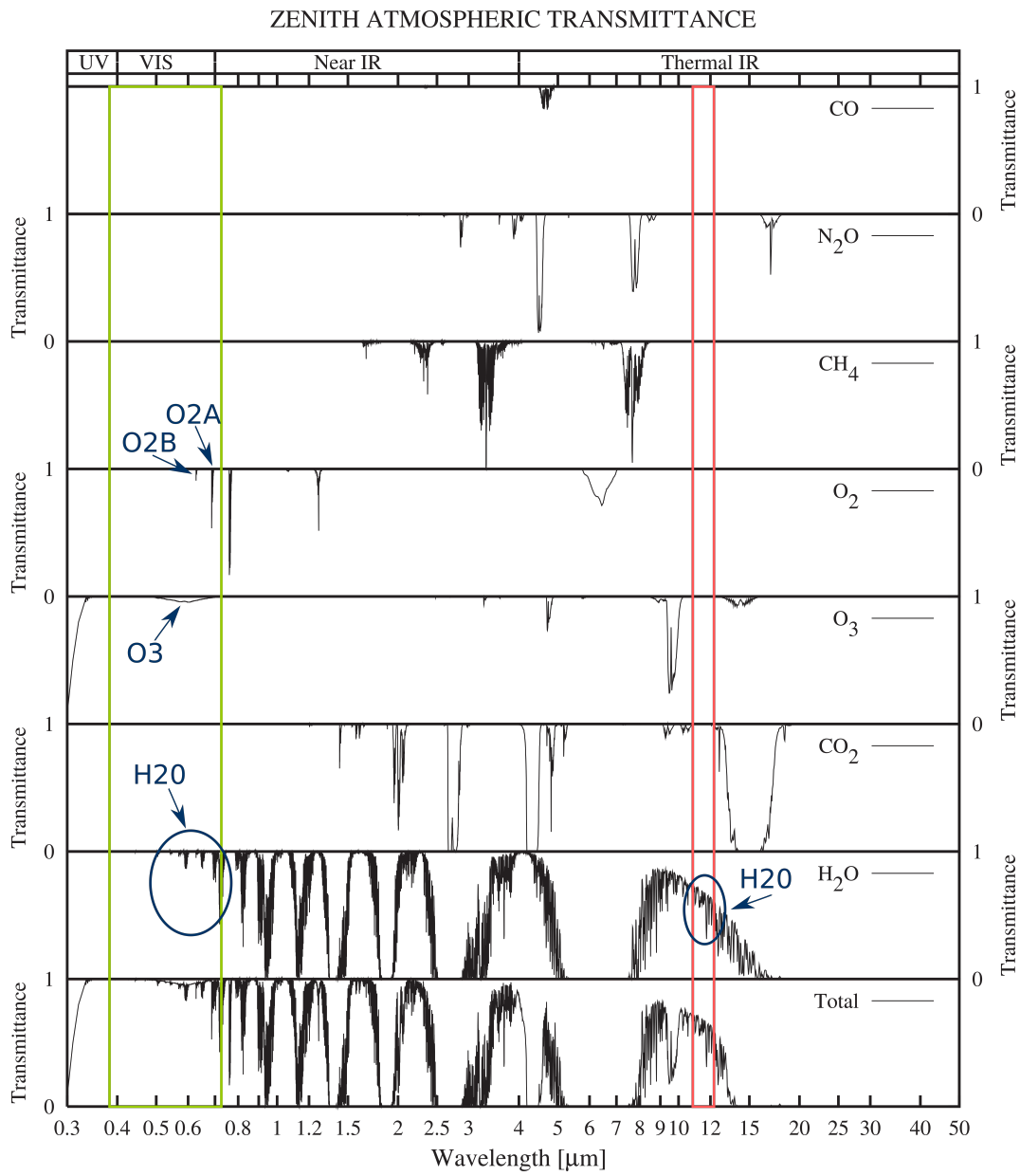


Figure 2.11: Atmospheric transmission of the atmosphere (bottom panel) and major atmospheric absorbers (picture from Petty (2006), modified). Coloured boxes indicate spectra for the cryospheric study in chapter 3 (red) and the phytoplankton study in chapter 4 (green).

670 nm to 740 nm for phytoplankton observation, the strong impact of *cdom* absorption in the blue VIS is avoided (cf. fig. 2.6).

Additionally, for increasing *chl-a*, the influence of water absorption in the red becomes weaker comparing fig. 2.6a and fig. 2.6b. Therefore, the red VIS domain provides sufficient properties obtaining phytoplankton in optically complex waters such as coasts or lakes for medium to high *chl-a*. On top, chlorophyll-a fluorescence near 683 nm can be exploited which is specific for only phytoplankton and vegetation.

2.4.4 Observing snow and ice in the TIR

Snow and ice appear “black” in the thermal infra-red (TIR) due to high absorption and “white” in the VIS due to high albedo (Stroeve et al., 1997). If radiation is only reflected at the surface it usually contains little or no information about matter and therefore it is unfavourable to observe snow in the VIS. In the TIR, radiation solely originates from terrestrial and atmospheric objects because solar radiation is negligible small (see fig. 2.1a). In contrast to the entire TIR and NIR, fig. 2.11 shows that from 10.5 μm to 12.5 μm only water vapour absorbs radiation. Other greenhouse gases such as CO₂ or methane do not interfere in this spectral interval. Thus, measured TOA signals solely originate from observed snow and ice cover and are influenced by atmospheric water vapour which has to be considered. Measuring the “temperature” of emitted radiation, emissivity can be calculated. The exploitation of emissivity favours the solitude observation of snow and ice due to the dependency on the object and wavelength.

Remotely retrieved cryospheric properties

Abstract

This study provides a method determining characteristics of snow and ice by converting top of atmosphere brightness temperature to surface emissivity which depends on wavelength and observation angle with respect to snow and ice properties. Advanced Along-Track Spectral Radiometer (AATSR) on-board Environmental Satellite (ENVISAT) features dual-view thermal infra-red measured brightness temperature. Using bands $11\ \mu\text{m}$ and $12\ \mu\text{m}$ in nadir and forward (55°) view and a total column water vapour (*TCWV*) product from Medium Resolution Imaging Spectrometer (MERIS), four measurements per pixel are obtained. Three surface emissivities $\varepsilon(\lambda, \theta)$ per pixel are retrieved from simulated surface temperatures related to $11\ \mu\text{m}$ /nadir view values. Using angular and spectral field measurements of snow grain size and emissivity above snow and ice from Hori et al. (2006, 2007), emissivity “classes” are defined: *fine*, *medium*, *coarse*, *sun crust*, and *ice*. Remaining pixels are either *indistinct* between classes, *unclassified*, or *invalid*. Temperatures above the freezing point label pixels as *wet*. The portion of classification in Greenland, Antarctica, and the sea ice of the Hudson Bay is high for 26 AATSR scene in 2007 and 2008. Steep and heterogeneous topography may cause *invalid* and *unclassified* pixels in Eurasia. Close to coasts, snow temperatures are generally higher and a large number of *wet* pixels is retrieved.

The chapter is adopted from Keck et al. (2017).

1 Introduction

1.1 On the determination of snow and ice

Since space-borne remote sensing is available, the cryosphere community focused on analysing snow grain size and reflectivity (Wiscombe and Warren, 1980, Aoki et al., 2007) and snow mass equivalent sensed with micro-wave sensors (Chang et al., 1982, Foster et al., 2005, Clifford, 2010). Using reflectance from Advanced Very High Resolution Radiometer (AVHRR) on-board Television Infrared Observation Satellite Next-generation (TIROS-N), Dozier et al. (1981) showed an opportunity to retrieve snow grain size in the near infra-red (NIR) spectral range. Dozier and Warren (1982) related spectral and angular dependent emissivity to thermal infra-red (TIR) brightness temperature of snow covered surfaces. A alternative viewing angle can cause a brightness temperature difference of up to 3 K from 8 μm to 14 μm . However, emissivity variations were insensitive to snow grain size.

Dozier and Marks (1987) developed a snow classification using Landsat Thematic Mapper (TM) reflectance relations. They distinguished between clean new snow, older snow, and vegetation-snow mixtures relying on snow grain size and single scattering. However, they never verified their results with *in situ* measurements. Based on Mie theory and Discrete Ordinate Radiative Transfer Model (DISORT) (Stamnes et al., 1988), new snow grain size algorithms were developed. Nolin and Dozier (1993) found good agreement with ground measurements for Airborne Visible/Infrared Imaging Spectrometer (AVIRIS) nadir NIR observations. Fily (1997) used Landsat NIR reflectance spectra and gained diverging results for TM4 (good agreement to ground measurements) and TM5/7 (too large remotely sensed snow grain size). Applying Multiple Endmember Snow-Covered Area and Grain size (MEMSCAG) to AVIRIS data and using snow grain size microscopic measurements (ranging from 10 μm to 1100 μm) from Mammoth Mountain, USA, in 1994, 1996, and 1998, Painter et al. (2003) found an Root Mean Square Error (RMSE) of 48 μm for the modelled snow grain size. Using Mosaic over Antarctica (MOA), Scambos et al. (2007) combined 260 Moderate Resolution Imaging Spectrometer (MODIS) scenes in 2003 and 2004 to obtain temporally averaged snow grain sizes applying a normalized radiance ratio of bands 1 and 2. They retrieved fine snow (grain size between 100 μm and 400 μm) in inner Antarctica and coarser snow grains (from 400 μm up to more than 1000 μm) at coasts where they expected melting zones. Aoki et al. (2007) obtained snow parameters by MODIS and Global Imager (GLI) aboard Advanced Earth Observing Satellite 2 (ADEOS-2) using NIR reflectance for snow

grain size and TIR brightness temperatures for snow temperature validated with emissivity and snow grain size field measurements in Eastern Hokkaido, Japan, and Barrow, Alaska, USA (also see Hori et al. (2006)). They found snow grain sizes within 10 μm to 1000 μm . Lyapustin et al. (2009) used visible spectrum (VIS)/NIR/short-wave infra-red (SWIR) MODIS normalized radiance band ratios in Greenland in 2004 to investigate snow grain sizes up to 50 μm to 1000 μm on land and up to 2000 μm at coasts. Their retrieval results qualitatively agreed well with measurements from Aoki et al. (2007).

Conducting laboratory measurements, Salisbury et al. (1994) investigated a discrepancy of angular and spectral emissivity for ice and various snow types depending on snow grain size. Hori et al. (2006) measured *in situ* angular and spectral snow emissivity with a TIR spectrometer and the snow grain size by microscope. The measurement sites are located in Eastern Hokkaido, Japan, in 2002 and 2004, and Barrow, Alaska, USA, in 2003. The spectral emissivity slope peaks at 10.85 μm with 0.99 for almost all investigated observation angles and snow grain sizes. In the interval from 8 μm to 14 μm , significant emissivity differences appear for longer wavelengths: emissivity decreases with increasing snow grain size and observation angle. Subsequently, Aoki et al. (2007), Hori et al. (2007), and Stamnes et al. (2007) showed several retrievals and results of remotely sensed snow parameters (snow grain size, snow temperature, a possible vertical structure of the upper snow layer) using the visible and the near infrared spectral range of the sensors GLI aboard ADEOS-2 and MODIS aboard Terra. Hori et al. (2007) compared snow grain size and snow surface temperature to determine the start of the melting period in the northern hemisphere, which is erroneous for non-flat and thin snow covers. Hori et al. (2013) developed a snow emissivity model based on a black-body component and a fraction of the apparent specular emissivity. Unfortunately, the model was not able to fully reproduce the field measurements of Hori et al. (2006) although the spectral emissivity shape resembles the measurements. However, the emissivity model can be applied to snow and ice classification (Hori et al., 2013).

1.2 Scope and content of the study

A novel model for snow and ice characteristics is provided using multi-view emissivities within 8 μm to 14 μm . The technique is generic and can be applied to any multi-view sensor with TIR channels. In this study, the dual-view TIR channels of AATSR are exploited. Section 2 describes instruments and used data sets. In section 3, the ground emissivity from brightness temperature measurements are deduced and the retrieval of snow and ice properties is explained. The results are presented and discussed in sections 4 and 5 followed by the conclusion in section 6.

2 Instruments and data

The platform Environmental Satellite (ENVISAT) operated from 1 March 2002 until 12 April 2012 800 km above ground in a sun-synchronous polar orbit with an equator crossing time of 10:00 a.m. local time in a descending node (ESA, 2006, 2007). This study includes data from instruments Advanced Along-Track Spectral Radiometer (AATSR) described in section 2.1 and Medium Resolution Imaging Spectrometer (MERIS) (section 2.2) avoiding time lapses due to the same host platform. In section 2.3 selected AATSR scenes are introduced which are prepared to ensure only to use snow or ice covered pixels (section 2.4).

2.1 AATSR

AATSR features a dual-view (nadir view in an angle between 0° to 21° and forward view at 55°), seven channels in the visible and thermal spectral range and a swath width of about 500 km (ESA, 2007). The spatial resolution is 1 km in nadir view and 2 km in forward view. AATSR measures the top of atmosphere brightness temperature directly due to a calibration on an intern black-body plate (ESA, 2007). Four measured brightness temperatures $BT_{\text{meas}}^{\text{TOA}}(\lambda, \vartheta)$ are obtained per pixel using both viewing angles ϑ and two TIR channels λ with central wavelengths at $10.85 \mu\text{m}$ (hereinafter simplified to $11 \mu\text{m}$) and $12 \mu\text{m}$.

2.2 MERIS

MERIS provides five push-broom imaging spectrometers in 15 programmable channels in a spectral range between 390 nm and 1040 nm with a spatial resolution of 300 m (full resolution) or 1 km (reduced) along a swath width of 1150 km. Usually, a combination of AATSR's $11 \mu\text{m}$ and $12 \mu\text{m}$ measurements can be applied to atmospheric correction. In order to use the TIR channel information content, a proper radiative transfer requires the input of water vapour measurements. Lindstrot et al. (2012, 2014) developed a *TCWV* product from MERIS using band 15 at 900 nm where water vapour is strongly absorbing. The product is provided in a 0.05° spatial resolution over land from 2003 to 2008 and can be accessed via www.globvapour.info. Lindstrot et al. (2012) state a high accuracy and precision of the MERIS *TCWV* retrieval compared to ground measurements. Lindstrot et al. (2014) validated the product with GUAN radiosonde data and report a weak wet bias of 0.74 mm and a standard deviation of 4.4 mm.

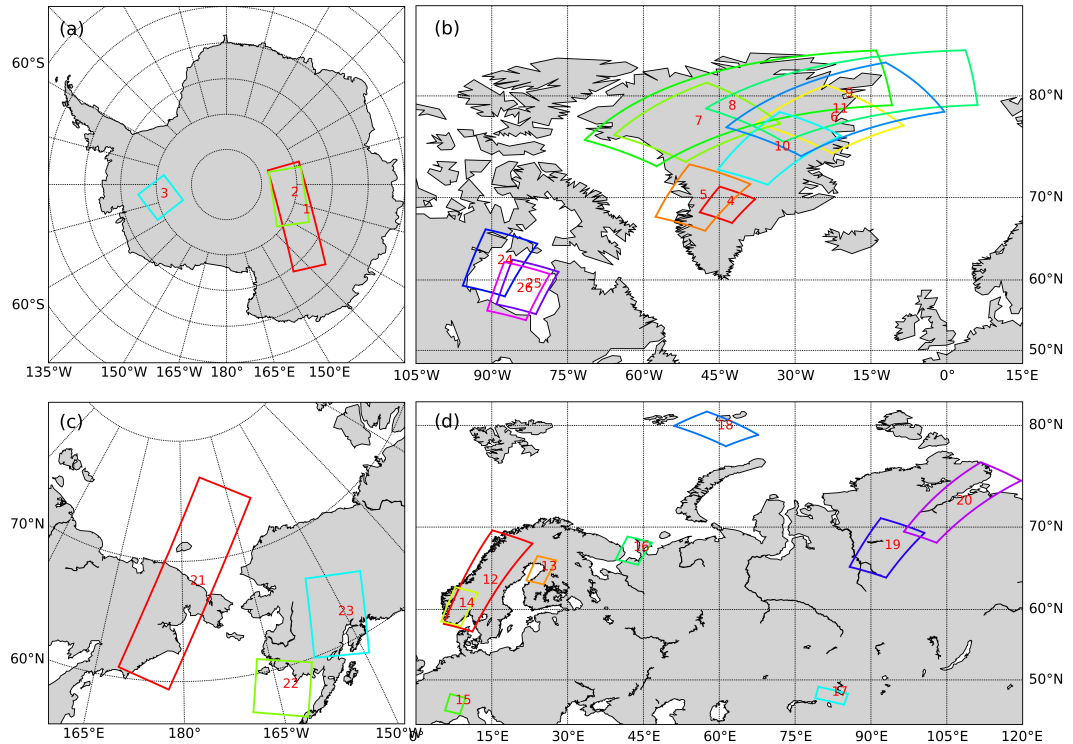


Figure 3.1: Location of 26 selected AATSR scenes in (a) Antarctica (1-3), Greenland (4-11) and Hudson-Bay (24-26), (c) Chukotka/East-Siberia (21) and Alaska (22-23), and (d) Eurasia (12-20). For detailed scene information see table 3.1.

2.3 Scene selection

The AATSR scenes are almost cloud-free and most of the pixels are snow/ice covered. Most of the scenes are located in Greenland because scenes in Eurasia and North America are often overcast. Additionally, during winter time, proper scenes in higher latitudes are limited due to the low sun zenith angle. In fig. 3.1 and table 3.1, 26 AATSR scenes in 2007 and 2008 are introduced. There are 11 scenes above the ice sheets of Antarctica (scene 1-3) and Greenland (4-11). Scenes 12-26 are located in Europe (12-16), Asia (17-21) and North America (22-26). Scenes 16, 18, 22, and 24-26 contain sea ice.

Table 3.1: Overview of the selected AATSR scenes with numbers referring to fig. 3.1. The column available pixels lists the portion of pixels which are clear-sky and snow/ice-covered due to the masks described in section 2.4. The last two columns contain spatial median averaged surface temperatures obtained from RTTOV and MERIS total column water vapour.

#	region	date	# pixel	$\overline{T_s}$ [K]	\overline{TCWV} [mm]
1	East-Central-Antarctica-1	2008-01-01	371 953	239.76	0.09
2	East-Central-Antarctica-2	2008-01-05	175 250	238.30	0.16
3	West-Central-Antarctica	2008-01-05	68 604	250.73	0.72
4	South-Greenland	2007-07-15	30 604	269.79	1.89
5	West-Coast-Greenland	2008-07-05	80 095	272.41	3.92
6	North-East-Coast-Greenland	2007-07-28	95 801	272.36	5.31
7	North-West-Greenland	2007-07-12	106 672	269.41	3.49
8	North-Greenland	2008-07-05	267 660	271.90	3.79
9	North-Coast-Greenland	2007-06-18	266 177	272.89	5.90
10	Central-Greenland	2007-04-11	83 804	233.42	0.05
11	North-East-Greenland	2008-07-05	209 782	273.46	5.32
12	Scandinavia	2007-03-21	136 019	268.80	3.03
13	Baltic-Sea	2007-03-23	32 277	271.90	4.63
14	South-Scandinavia	2007-03-21	66 921	268.84	2.13
15	Alps	2007-03-12	16 586	271.42	1.81
16	White-Sea	2007-03-25	23 006	271.70	6.95
17	Lake-Zaysan	2008-01-02	41 410	253.11	0.97
18	Barents-Sea	2007-07-01	27 217	273.08	6.89
19	Central-Siberia	2007-03-21	147 405	256.90	1.33
20	Khatanga-Gulf	2007-03-12	166 692	242.16	1.58
21	Chukotka	2007-03-09	424 259	246.84	0.89
22	Bristol-Bay	2007-03-12	128 290	265.22	2.16
23	South-Alaska	2007-02-19	155 405	251.26	0.69
24	West-Hudson-Bay	2007-03-18	232 197	247.72	0.50
25	Central-Hudson-Bay-1	2007-03-19	210 050	248.38	0.60
26	Central-Hudson-Bay-2	2007-03-22	203 614	253.96	0.99

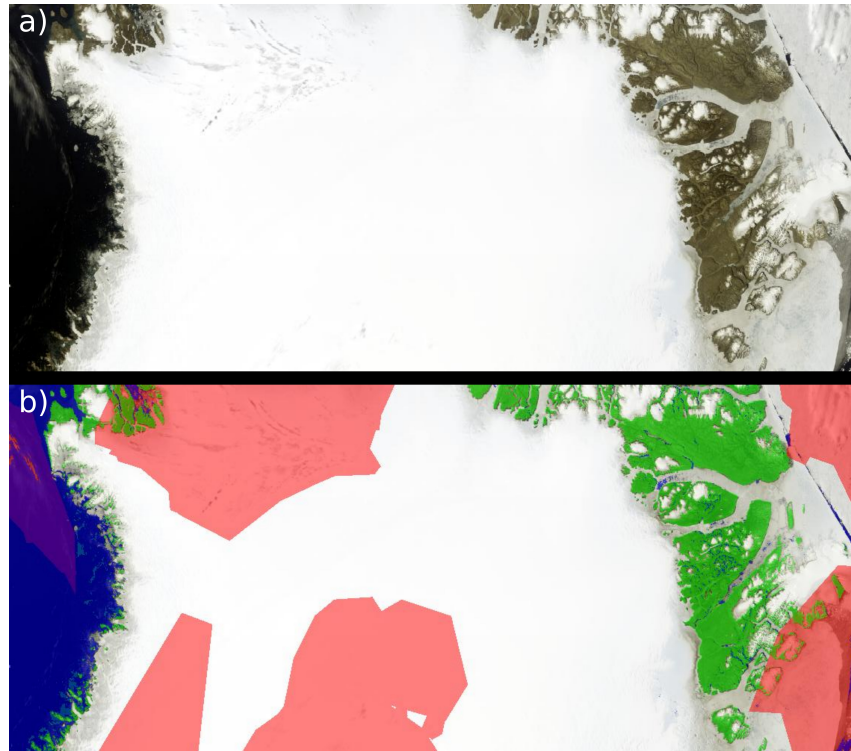


Figure 3.2: RGB view of North-Greenland (scene 8) in panel a) and with masks for clouds (red), water (blue) and bare land (green) in panel b) produced with the software Sentinel Application Platform (SNAP).

2.4 Scene preparation

A proper discrimination of clouds and snow covered surfaces is complex. Therefore, the software SNAP (free download via <http://step.esa.int/main/toolboxes/snap/>) is used to identify cloudy structures. Each scene excludes clouds with individually prepared cloud mask combining the MERIS Red-Green-Blue (RGB) view, an AATSR brightness temperature ratio and the Normalised Difference Cloud Index (NDCI). Using the Red-Green-Blue (RGB) view, clouds are identified by structure and shadows. Cirrus clouds are detected applying the nadir view ratio $(BT(11\ \mu\text{m}) - BT(12\ \mu\text{m})) / BT(11\ \mu\text{m})$ which is based on a higher absorption coefficient of ice for $12\ \mu\text{m}$ than for $11\ \mu\text{m}$ (Chylek et al., 2006). Pepe et al. (2005) introduce the NDCI as a ratio of the AATSR bands 5 and 6 at $3.7\ \mu\text{m}$ and $11\ \mu\text{m}$ considering a reflectance drop at $3.7\ \mu\text{m}$ above snow and ice and a remaining high reflectance above clouds. Ratios greater than 0.026 classify a cloud. Their cloud detection accuracy is about 96 % even for topographic complex areas.

Additionally, a water mask for lakes, open water at coasts and rivers is applied using the AATSR reflectance at 868 nm lower than 0.1 considering water bodies absorb most of the solar signal beyond 750 nm. Analogously, the AATSR reflectance at 550 nm exhibits lower reflectivity for land and vegetation than for snow. The land mask excludes pixels that have a 550 nm reflectance lower than 0.3. For instance, case 8 is situated in North-Greenland and its RGB image shows mostly snow and ice covered areas in fig. 3.2a. However, areas with clouds, water and bare land are apparent which are excluded from following computations with the above-described masks. The masks are coloured in red, blue, and green for clouds, water, and bare land in fig. 3.2b.

3 Methodology

3.1 Physical background and remote sensing

In this study, emissivity is used to characterize snow and ice covered surfaces. Emissivity is the relating factor between theoretical black-body radiance and measured radiance at a given temperature (cf. chapter 2 section 2.2.3). Emissivity directly links to brightness temperature and depends on the object's material, the observation angle, and the considered wavelength. These properties particularly justify the usage of emissivity to describe and classify an object. In section 3.4, emissivity is computed by a relation of retrieved surface temperatures. Space-borne land surface temperature products require pre-determined emissivity spectra and land cover types (e.g. MODIS *LST*: Snyder et al. (1998), Wan and Zhang (1999), Hori et al. (2006)). Thus, a given surface temperature product is not used. According to Hori et al. (2006), the interval from 8 μm to 14 μm provides "a fundamental surface property for determining snow surface temperature from space". Within the AATSR channels 11 μm and 12 μm , emissivity exhibits particular features (Hori et al., 2006, 2013): In nadir view, emissivity is 0.99 at 10.85 μm for almost all snow grain sizes and ice (see fig. 3.3); hereafter denoted as $\varepsilon^* = \varepsilon(\lambda = 11 \mu\text{m}, \vartheta = 0^\circ)$. Furthermore, emissivity decreases with increasing grain size for 12 μm .

The 11 μm and 12 μm channel information is usually used for atmospheric water vapour estimation. Using MERIS *TCWV* and vertical water vapour profiles (see section 3.2), the channels' information content is enabled in both forward and nadir viewing angle for the emissivity calculation. Influence of solar radiation and potential snow impurities are negligible for AATSR TIR measurements (Aoki et al., 2007). Wavelengths in the thermal infrared spectrum exhibit a small penetration depth (Tanikawa et al., 2002) that avoid distracting signals observing the snow surface.

Four top of the atmosphere (TOA) brightness temperatures for both viewing angles and the bands 11 μm and 12 μm per pixel are the initial data base. The model Radiative Transfer for TIROS Operational Vertical Sounder (RTTOV) which accounts for atmospheric water vapour (see sections 3.2 and 3.3) retrieves appropriate surface temperatures per brightness temperature. Subsequently, the physical relationship between temperature and emissivity (see section 3.4) is exploited to obtain the surface emissivities per pixel, wavelength and observation angle. The classification methodology is demonstrated in section 3.5.

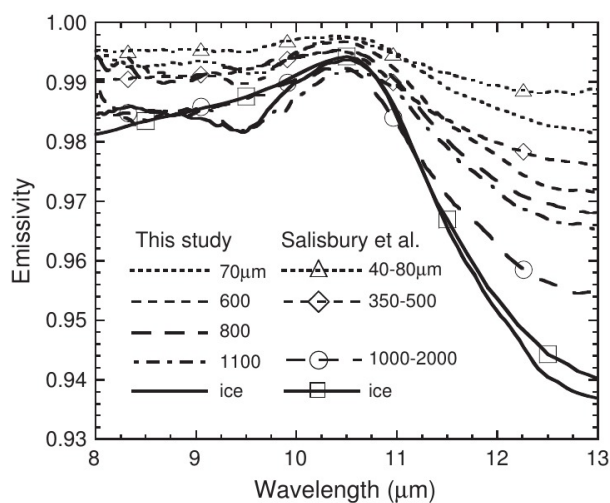


Figure 3.3: Measured nadir emissivity above snow with various grain sizes conducted by Hori et al. (2006). Emissivity changes with increasing snow grain size and increasing wavelength. Independent from snow grain size, the emissivity is approximately 0.99 for almost all measurements at 10.85 μm.

3.2 Forward model

Radiometric TOA measurements contain information of the surface and the atmosphere. Forward modelling simulates TOA measurements for given parameters (e.g. surface temperature and water vapour) which can be accessed for particular TOA measurements by an inversion. Thus, a forward model $y = F(x)$ may express the TOA brightness temperature. The measurement vector is defined as $y = BT_{sim}^{TOA}$ with x as state vector containing surface and atmospheric information and F describes the physical model.

The radiative transport model RTTOV (Eyre, 1991) is notable for fast and accurate simulation of the TOA brightness temperature and radiance for a range of space-borne TIR and micro-wave radiometers. In this study, RTTOV version 11 runs in a clear-sky mode, with default aerosol mixtures and a fixed ground emissivity of 0.99 (for more information see Hocking et al. (2013)). RTTOV requires vertical atmospheric profiles of pressure, temperature and water vapour.

McClatchey et al. (1972) combined aerosol and transmission models with ground and radiosonde measurements and created vertical atmosphere models for several latitudes and seasons (*mid-latitude summer/winter, arctic summer/winter, and US standard*) which contain a set of vertical distributions of pressure, temperature and atmospheric gases (e.g. water vapour, ozone, CO_x, NO_x). The standard profiles are modified for

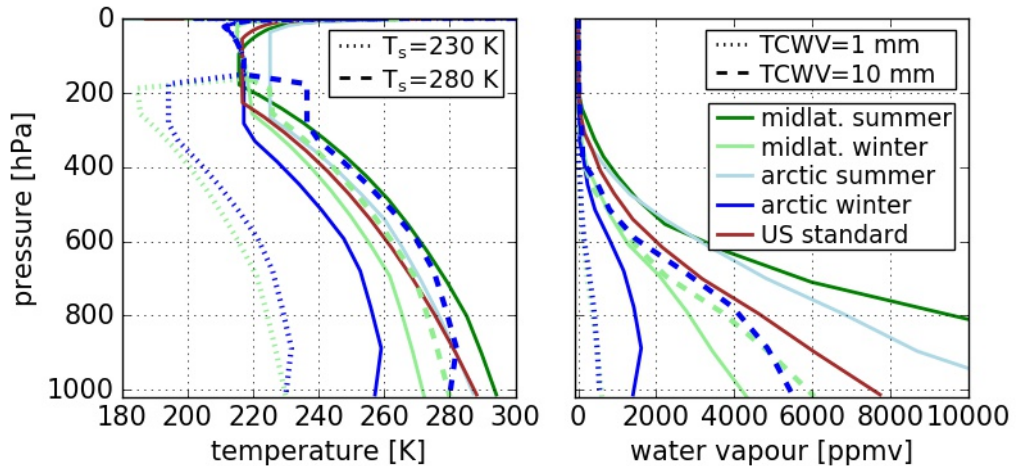


Figure 3.4: Vertical profiles of temperature and water vapour for five standard regions and seasons after McClatchey et al. (1972) indicated by coloured solid lines. Table 3.2 lists surface temperature and total water vapour column of these standard atmospheres. Dashed lines indicate modified profiles for arctic winter (blue) and mid-latitude winter (light green) for a given surface temperature (left) and a given total water vapour content (right).

certain surface temperatures and total water vapour columns to obtain a set of vertical atmospheric profiles (see fig. 3.4). Depending on the state vector x (surface temperature T_s , total water vapour column $TCWV$, viewing zenith angle ϑ , AATSR channel λ and vertical profile model atm) a 5D look-up table (LUT) of BT_{sim}^{TOA} for a fixed ground emissivity of $\varepsilon = 0.99$ is generated.

$$(3.1) \quad BT_{sim}^{TOA} = F(T_s, TCWV, \vartheta, \lambda, atm; \varepsilon)$$

Comparing the median MERIS $TCWV$ per scene (see table 3.1) and the $TCWV$ of the standard models (see table 3.2) deciding upon one of the standard atmospheric models atm . Using MERIS $TCWV$ the usage of the AATSR TIR channels for atmospheric correction is avoided and their information is available for the emissivity retrieval. Most scenes are close to the profile *subarctic winter* except scenes 16 and 18. These scenes have a median $TCWV$ of around 7 mm and are classified as *mid-latitudes in winter*.

Successively, the dimensions of the LUT are reduced by interpolation for the known variables $TCWV$, ϑ , and λ . Eventually, the only depending variable is the surface temperature T_s which is retrieved in the next step by optimization.

Table 3.2: Surface temperatures and total column water vapour of the vertical standard profiles after McClatchey et al. (1972) are listed (see solid lines in fig. 3.4). The calculation of TCWV considers atmospheric normal conditions ($T=273.15$ K, $p=1013$ hPa) and the air layer thickness per level.

region	T_s [K]	TCWV [mm]
mid-latitude (summer)	295.2	29.80
mid-latitude (winter)	272.2	8.10
subarctic (summer)	287.2	21.22
subarctic (winter)	257.2	4.11
US-standard	288.2	15.47

3.3 Optimization

The surface temperature is obtained optimizing $BT_{\text{sim}}^{\text{TOA}}(T_s, \text{TCWV}, \vartheta, \lambda, \text{atm}) = F(T_s)$ with Newton's Iteration. The first guess of the surface temperature is assumed with $T_{s,n} = BT_{\text{meas}}^{\text{TOA}} + 2$ K.

$$(3.2) \quad G(T_{s,n}) = G[BT(T_{s,n})] = BT_{\text{meas}}^{\text{TOA}} - F(T_{s,n})$$

$$(3.3) \quad g(T_{s,n}) = \frac{dG(T_{s,n})}{dT_s} = -\frac{F(T_2) - F(T_1)}{T_2 - T_1}$$

$$(3.4) \quad T_{s,n+1} = T_{s,n} - \frac{G(T_{s,n})}{g(T_{s,n})}$$

$T_{s,n+1}$ is accepted if $|G(T_{s,n})| < 0.1$ K and $|G/g| \leq 0.01$ else $T_{s,n+1}$ is set to $T_{s,n}$ and further iterations occur. The number of iterations is limited to ten. T_1 and T_2 are the nearest neighbours of $T_{s,n}$ in the LUT. The methodology of sections 3.2 and 3.3 is conducted for all four measured brightness temperatures per pixel receiving corresponding surface temperatures for 11 μm /nadir, 11 μm /forward, 12 μm /nadir, and 12 μm /forward (hereafter abbreviated 11n, 11f, 12n, and 12f) which are based on an emissivity of 0.99.

In general, the retrieved surface temperatures in the 11 μm channel are higher than for 12 μm and forward view temperatures are lower than in nadir view listed in the statistics in table 3.3. The median difference between 11n and 12f temperatures can exceed 1 K in certain scenes.

3.4 Emissivity

The following three assumptions are the base of the emissivity computations:

$$(3.5) \quad \varepsilon^* =: \varepsilon(\lambda^* = 11 \mu\text{m}, \vartheta^* = 0^\circ) = 0.99$$

$$(3.6) \quad \chi =: \frac{dB T(\lambda^*, \vartheta^*)}{d\varepsilon} = f(\lambda^*, T_s^*, \varepsilon^*)$$

$$(3.7) \quad \frac{\Delta T_s}{\Delta \varepsilon} = \frac{T_s^* - T_s(\lambda, \vartheta)}{\Delta \varepsilon(\lambda, \vartheta)}$$

The superscript ‘*’ indicates variables with setting $\lambda = 11 \mu\text{m}$ in nadir view (11n). Hori et al. (2006, 2007, 2013) found an emissivity of 0.99 for this setting for almost all snow grain sizes shown in fig. 3.3. Therefore, the radiative transfer model runs with a reference emissivity of 0.99. Equation (3.5) sets the 11n emissivity to $\varepsilon(11n) = 0.99$ for all scenes and pixels. Referring to the first assumption with $\varepsilon^* = 0.99$, the analytical derivative χ is computed with eq. (3.6) (see details in eq. (2.15)) for 11n per pixel assuming the retrieved $T_s(11n) = T_s^*$ matches the physical surface temperature. Furthermore, the difference between two retrieved surface temperatures of one pixel corresponds to the emissivity difference (eq. (3.7)). Combining χ from eq. (3.6) with $\Delta T_s/\Delta \varepsilon$ from eq. (3.7) assuming $\varepsilon^* = 0.99$, three emissivities with corresponding surface temperatures in relation to the 11n surface temperature T_s^* are calculated:

$$(3.8) \quad \Delta \varepsilon(\lambda, \vartheta) = \frac{T_s^* - T_s(\lambda, \vartheta)}{\chi}$$

$$(3.9) \quad \varepsilon(\lambda, \vartheta) = \varepsilon^* - \Delta \varepsilon(\lambda, \vartheta)$$

Hence, 11f, 12n, and 12f emissivities per pixel with eq. (3.9) are obtained. In general, an increasing viewing angle and an increasing wavelength within $11 \mu\text{m}$ to $14 \mu\text{m}$ cause lower emissivities (see table 3.3). A temperature difference of 1 K results in an averaged emissivity variation of 0.020 within the temperature interval from 230 K to 280 K.

Table 3.3: The table lists statistics for the 12n, 12f, and 11f temperature/emissivity residuals relying on the 11n values. Increasing viewing angle and increasing wavelength cause lower temperatures and emissivities, respectively.

#	setting	$T_s(11, 0) - T_s(\lambda, \vartheta)$ [K]			$\varepsilon(11, 0) - \varepsilon(\lambda, \vartheta)$ [dl]		
		median	mean	std	median	mean	std
1	f11	0.0269	0.1076	0.8507	0.0006	0.0023	0.0192
	n12	0.5472	0.5760	0.7231	0.0124	0.0130	0.0163
	f12	0.7956	0.8471	0.8800	0.0181	0.0190	0.0197
2	f11	0.0389	0.1231	0.7959	0.0009	0.0027	0.0182
	n12	0.6424	0.6122	0.7544	0.0148	0.0140	0.0172
	f12	0.9782	0.9793	0.8710	0.0225	0.0224	0.0197

Table 3.3: *continued*

#	setting	$T_s(11, 0) - T_s(\lambda, \vartheta)$ [K]			$\varepsilon(11, 0) - \varepsilon(\lambda, \vartheta)$ [dl]		
		median	mean	std	median	mean	std
3	f11	0.2054	0.2160	0.5806	0.0043	0.0045	0.0121
	n12	0.6691	0.6569	0.3319	0.0139	0.0136	0.0069
	f12	1.0693	1.0368	0.7061	0.0222	0.0215	0.0147
4	f11	0.5182	0.9959	2.2376	0.0093	0.0179	0.0404
	n12	0.8172	0.7646	0.4206	0.0147	0.0138	0.0076
	f12	1.6763	2.1206	2.3056	0.0301	0.0382	0.0416
5	f11	0.5483	0.6873	2.7137	0.0097	0.0119	0.0495
	n12	0.8383	0.7729	1.6373	0.0149	0.0136	0.0298
	f12	1.6673	1.7674	2.8060	0.0296	0.0310	0.0511
6	f11	0.1614	0.2396	1.8891	0.0029	0.0041	0.0334
	n12	0.6252	0.5444	1.3055	0.0112	0.0097	0.0233
	f12	0.9709	0.9011	1.9972	0.0174	0.0161	0.0354
7	f11	0.3835	0.3251	0.4305	0.0069	0.0058	0.0078
	n12	0.6454	0.5874	0.5165	0.0116	0.0106	0.0093
	f12	1.2851	1.3347	0.4794	0.0230	0.0240	0.0086
8	f11	0.3843	0.3289	0.6992	0.0069	0.0058	0.0122
	n12	0.8082	0.6679	0.6647	0.0144	0.0119	0.0117
	f12	1.4867	1.3099	0.9453	0.0265	0.0233	0.0167
9	f11	0.2924	0.2774	0.8096	0.0052	0.0049	0.0141
	n12	0.6297	0.6195	0.7321	0.0112	0.0111	0.0129
	f12	1.1094	1.1164	0.9372	0.0197	0.0200	0.0166
10	f11	0.1107	0.1153	0.3250	0.0026	0.0028	0.0077
	n12	0.3168	0.3115	0.3693	0.0076	0.0074	0.0086
	f12	0.5847	0.5948	0.3256	0.0140	0.0142	0.0077
11	f11	0.0387	-0.0287	0.8751	0.0007	-0.0005	0.0152
	n12	0.3892	0.1652	0.8832	0.0069	0.0030	0.0155
	f12	0.6620	0.2446	1.4561	0.0117	0.0045	0.0255
12	f11	-0.2246	-0.0970	2.0718	-0.0041	-0.0019	0.0379
	n12	0.3549	0.2618	1.0960	0.0065	0.0047	0.0204
	f12	0.2391	0.4303	2.0967	0.0043	0.0077	0.0383

Table 3.3: *continued*

#	setting	$T_s(11, 0) - T_s(\lambda, \vartheta)$ [K]			$\varepsilon(11, 0) - \varepsilon(\lambda, \vartheta)$ [dl]		
		median	mean	std	median	mean	std
13	f11	0.0228	-0.2482	1.2657	0.0004	-0.0044	0.0226
	n12	0.2142	0.0722	1.0394	0.0038	0.0012	0.0186
	f12	0.2869	0.0971	1.3312	0.0051	0.0017	0.0237
14	f11	0.2811	0.2514	3.0690	0.0051	0.0041	0.0556
	n12	0.4459	0.3841	1.8669	0.0082	0.0068	0.0336
	f12	0.8828	0.8816	3.1048	0.0160	0.0156	0.0561
15	f11	0.7945	0.7980	5.6796	0.0142	0.0125	0.1012
	n12	0.4038	0.3170	4.9973	0.0072	0.0042	0.0892
	f12	1.0441	1.0519	5.6971	0.0185	0.0171	0.1014
16	f11	0.3609	0.3781	0.8104	0.0064	0.0067	0.0144
	n12	0.3577	0.3197	0.4617	0.0064	0.0057	0.0082
	f12	0.7938	0.8751	0.8444	0.0141	0.0155	0.0150
17	f11	0.3953	0.5169	2.4054	0.0081	0.0099	0.0481
	n12	0.1596	0.2624	1.1906	0.0032	0.0051	0.0234
	f12	0.5632	0.7171	2.4279	0.0115	0.0138	0.0486
18	f11	0.2041	0.2202	0.4155	0.0036	0.0039	0.0072
	n12	0.2888	0.2317	0.3638	0.0051	0.0041	0.0064
	f12	0.4207	0.4356	0.5632	0.0074	0.0076	0.0098
19	f11	0.0580	0.1999	2.1010	0.0011	0.0037	0.0421
	n12	0.3334	0.3461	0.9487	0.0066	0.0068	0.0189
	f12	0.4722	0.5806	2.1228	0.0093	0.0112	0.0425
20	f11	0.0149	0.0613	1.5737	0.0003	0.0011	0.0336
	n12	0.1304	0.2097	0.8441	0.0029	0.0045	0.0179
	f12	0.1120	0.1106	1.6351	0.0025	0.0021	0.0350
21	f11	0.3028	0.6136	2.3556	0.0065	0.0122	0.0480
	n12	0.4291	0.5389	1.1286	0.0092	0.0111	0.0228
	f12	0.8127	1.1731	2.3451	0.0175	0.0239	0.0474
22	f11	0.6824	0.6722	1.3687	0.0128	0.0125	0.0255
	n12	0.9679	0.9194	0.5475	0.0180	0.0171	0.0103
	f12	1.9890	2.0037	1.3831	0.0372	0.0373	0.0255

Table 3.3: *continued*

#	setting	$T_s(11, 0) - T_s(\lambda, \vartheta)$ [K]			$\varepsilon(11, 0) - \varepsilon(\lambda, \vartheta)$ [dl]		
		median	mean	std	median	mean	std
23	f11	-0.0298	0.3495	3.1780	-0.0006	0.0061	0.0646
	n12	0.2343	0.2781	1.3207	0.0049	0.0056	0.0269
	f12	0.2280	0.6030	3.1952	0.0047	0.0113	0.0649
24	f11	0.4539	0.5265	1.3767	0.0098	0.0111	0.0289
	n12	0.5665	0.5656	1.0821	0.0121	0.0121	0.0231
	f12	1.2047	1.1772	1.4793	0.0259	0.0250	0.0313
25	f11	0.4338	0.4861	0.5488	0.0092	0.0102	0.0114
	n12	0.5641	0.5744	0.2357	0.0119	0.0122	0.0049
	f12	1.1615	1.1948	0.5442	0.0246	0.0253	0.0113
26	f11	0.4200	0.4620	0.7427	0.0085	0.0093	0.0147
	n12	0.5974	0.6020	0.3132	0.0121	0.0122	0.0062
	f12	1.1928	1.2020	0.7658	0.0242	0.0243	0.0151

Table 3.4: *The table demonstrates the evaluation of the portion of valid, invalid, classified and indistinct pixels in relation to available pixels for the scenes. Applying an emissivity uncertainty of 0.005 and a distance weighting method enhances the classification with more valid and classified pixels.*

#	uncert. [dl]	dist. -	valid [%]	invalid [%]	class. [%]	indist. [%]
1	0.000	no	78.092	21.908	14.237	0.000
	0.005	no	87.747	12.253	46.957	28.024
	0.005	yes	87.747	12.253	67.373	7.608
2	0.000	no	74.078	25.922	22.277	0.041
	0.005	no	82.886	17.114	37.272	30.185
	0.005	yes	82.886	17.114	58.075	9.383
3	0.000	no	82.830	17.170	10.730	0.080
	0.005	no	90.369	9.631	40.356	26.898
	0.005	yes	90.369	9.631	59.619	7.635
4	0.000	no	81.761	18.239	7.352	0.029
	0.005	no	85.162	14.838	42.390	19.638
	0.005	yes	85.162	14.838	53.601	8.427

Table 3.4: *continued*

#	uncert. [dl]	dist. –	valid [%]	invalid [%]	class. [%]	indist. [%]
5	0.000	no	82.823	13.720	2.071	0.012
	0.005	no	84.575	11.968	50.951	8.741
	0.005	yes	84.575	11.968	55.392	4.300
6	0.000	no	58.511	34.624	9.867	0.032
	0.005	no	67.144	25.990	28.943	18.559
	0.005	yes	67.144	25.990	42.313	5.190
7	0.000	no	88.827	11.028	3.982	0.112
	0.005	no	91.678	8.177	42.358	19.917
	0.005	yes	91.678	8.177	52.892	9.383
8	0.000	no	84.218	9.682	9.705	0.001
	0.005	no	87.467	6.434	46.942	28.163
	0.005	yes	87.467	6.434	62.036	13.069
9	0.000	no	86.413	8.566	7.222	0.024
	0.005	no	88.364	6.616	42.425	22.476
	0.005	yes	88.364	6.616	56.405	8.496
10	0.000	no	93.621	6.379	0.195	0.000
	0.005	no	96.987	3.013	55.505	9.698
	0.005	yes	96.987	3.013	62.036	3.166
11	0.000	no	53.488	13.460	7.291	0.001
	0.005	no	56.035	10.913	26.958	22.399
	0.005	yes	56.035	10.913	42.246	7.111
12	0.000	no	31.913	62.191	0.237	0.001
	0.005	no	40.787	53.318	12.947	1.175
	0.005	yes	40.787	53.318	13.850	0.272
13	0.000	no	41.488	44.081	0.226	0.012
	0.005	no	49.949	35.620	9.530	0.871
	0.005	yes	49.949	35.620	10.057	0.344
14	0.000	no	24.566	57.199	0.350	0.000
	0.005	no	30.552	51.213	7.939	1.466
	0.005	yes	30.552	51.213	9.090	0.315

Table 3.4: *continued*

#	uncert. [dl]	dist. –	valid [%]	invalid [%]	class. [%]	indist. [%]
15	0.000	no	1.670	67.171	0.060	0.000
	0.005	no	2.484	66.357	0.434	0.078
	0.005	yes	2.484	66.357	0.500	0.012
16	0.000	no	80.605	19.169	0.191	0.000
	0.005	no	87.321	12.453	19.686	2.060
	0.005	yes	87.321	12.453	21.390	0.356
17	0.000	no	30.954	69.046	0.053	0.000
	0.005	no	45.576	54.424	5.477	0.401
	0.005	yes	45.576	54.424	5.786	0.092
18	0.000	no	56.895	41.129	0.154	0.000
	0.005	no	80.802	17.221	24.591	1.958
	0.005	yes	80.802	17.221	26.256	0.294
19	0.000	no	36.359	63.641	0.128	0.000
	0.005	no	45.830	54.170	12.357	1.034
	0.005	yes	45.830	54.170	13.190	0.201
20	0.000	no	32.996	67.004	0.032	0.000
	0.005	no	48.103	51.897	8.263	0.194
	0.005	yes	48.103	51.897	8.418	0.039
21	0.000	no	54.796	45.204	0.967	0.007
	0.005	no	62.614	37.386	21.203	4.106
	0.005	yes	62.614	37.386	24.441	0.867
22	0.000	no	75.276	24.724	10.508	0.142
	0.005	no	80.881	19.119	24.377	16.326
	0.005	yes	80.881	19.119	35.511	5.192
23	0.000	no	23.497	76.498	0.149	0.005
	0.005	no	30.755	69.240	5.798	0.501
	0.005	yes	30.755	69.240	6.184	0.115
24	0.000	no	83.759	16.241	3.438	0.000
	0.005	no	87.568	12.432	32.135	12.967
	0.005	yes	87.568	12.432	41.485	3.617

Table 3.4: *continued*

#	uncert. [dl]	dist. –	valid [%]	invalid [%]	class. [%]	indist. [%]
25	0.000	no	94.529	5.471	1.099	0.000
	0.005	no	96.607	3.393	38.219	12.921
	0.005	yes	96.607	3.393	48.135	3.004
26	0.000	no	91.475	8.525	2.075	0.000
	0.005	no	94.283	5.717	40.389	12.565
	0.005	yes	94.283	5.717	49.758	3.196

3.5 Characterization method

The characterization for snow and ice covered areas is based on remotely sensed emissivity. It incorporates spectral and angular dependent emissivity analyses and snow types classified by grain size which are evolved from Hori et al. (2006), Aoki et al. (2007), Hori et al. (2007), Stamnes et al. (2007), and Hori et al. (2013). Hori et al. (2006) measured the snow grain size during field studies in Japan and examined five “classes”: *fine*, *medium*, and *coarse grained snow*, *sun crust*, and *ice*. Separately, they measured the angular spectral emissivity of each classified snow or ice sample within 8 μm to 14 μm using thermal infrared spectrometers. Figure 3.5 illustrates the emissivity ranges per class (blue and green bars) separated for the three emissivities $\varepsilon(12n)$, $\varepsilon(12f)$, and $\varepsilon(11f)$.

The method of Hori et al. (2006) results in overlaps and some gaps between classes' emissivity ranges denoted with uppercase letters and Greek symbols in fig. 3.5. For instance, the 12n-emissivity prohibits a pixel's classification within $\varepsilon(12n) = (0.945, 0.960)$ (gap “C”) because Hori et al. (2006) did not define a class for this interval. Analogously, the overlap “ η ” of *sun crust*, *coarse*, and *medium* within $\varepsilon(12n) = [0.970, 0.975]$ may lead to an ambiguous decision. Hence, depending on the three emissivities, a pixel is either

1. *valid* and
 - a) classified (*fine*, *medium*, *coarse*, *sun crust*, *ice*), or
 - b) *indistinct*, or
 - c) *unclassified*

or
2. *invalid*

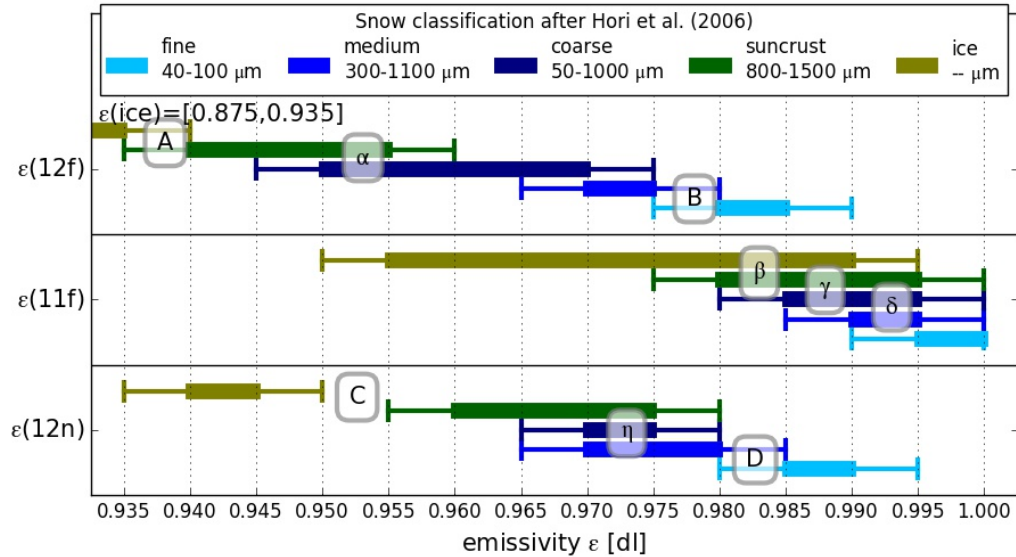


Figure 3.5: The classification scheme illustrates the emissivity ranges of the pre-defined classes fine, medium, coarse, suncrust and ice (blue and green bars) per emissivity $\varepsilon(12f)$, $\varepsilon(11f)$, $\varepsilon(12n)$ after Hori et al. (2006). Additionally, uppercase letters and Greek symbols label the gaps between these ranges and overlaps, respectively. Class wet is not shown because it is only dependent on surface temperature. The thin bars show the emissivity ranges after applying the emissivity uncertainty factor of 0.005.

In the following descriptions, all pixels and percentage values are related to the prepared scenes with pixels that are only snow or ice covered.

1) A pixel is potentially classifiable (*valid*) if each of its three emissivities sits within the corresponding lower *ice* boundary and the upper *fine* boundary, respectively. Therefore, a pixel's validity is determined by $[0.875, 0.955, 0.940] < [\varepsilon(12f), \varepsilon(11f), \varepsilon(12n)] \leq [0.985, 1.000, 0.990]$, which fig. 3.5 displays as thick bars. In order to cover measurement and approximation uncertainties, an emissivity uncertainty of ± 0.005 is applied to the classes' boundaries (thin bars in fig. 3.5). Hence, the pixel's validity ranges from $[0.870, 0.950, 0.935] < [\varepsilon(12f), \varepsilon(11f), \varepsilon(12n)] \leq [0.990, 1.000, 0.995]$. Additionally, surface temperature $T_s(11n)$ equals snow temperature requiring to be lower than 274 K.

1a) A *valid* pixel is definitely classified if the three emissivities belong to the same class which corresponds to the same colour code of the bars in fig. 3.5. Applying the uncertainty factor of 0.005 highly enhances the number of classified pixels listed in table 3.4.

1b) A *valid* pixel becomes *indistinct* if at least one of its emissivities belongs to more than one class (see Greek letters in fig. 3.5). The effect of the classes overlaps increases by applying the uncertainty to the boundaries (see table 3.4). Therefore, a two-step re-classification is performed:

- i) re-location: If a pixel changes from classified to *indistinct* after applying the uncertainty the pixel is re-located to its previous class.
- ii) distance weighting: The most proper class for all three emissivities is estimated with a distance weighting with eq. (3.10).

$$(3.10) \quad \varepsilon = w_1 \cdot \varepsilon_1 + w_2 \cdot \varepsilon_2 \quad \text{with } w_1 + w_2 = 1$$

$$(3.11) \quad w_i = \frac{|\varepsilon - \varepsilon_j|}{|\varepsilon_1 - \varepsilon_2|} \quad \text{for } i, j = 1, 2 \text{ and } i \neq j$$

The pixel's emissivity ε is described with the weighted upper and lower emissivity boundaries ε_1 and ε_2 of the two nearest classes. The lower weighting factors w decides upon the proper class. A pixel remains *indistinct* if the weighting factors are within $w_{i,j} = [0.45, 0.55]$

1c) A *valid* pixel remains *unclassified* if the emissivities belong to different classes or at least one does not fit in any class' emissivity range due to the gaps shown in fig. 3.5.

2) A pixel is *invalid* if at least one of the three emissivities is out of the classification ranges described in (1) or its snow temperature $T_s(11n)$ is above 274 K which is labelled with *wet*.

4 Characterization of snow and ice scenes

4.1 Exemplary case study

In case 8 (North-Greenland), 87.5% of available snow or ice pixels are *valid* (table 3.4). The term “available pixels” refers to the prepared scenes after excluding clouds, water, and bare land with the masks described in section 2.4. Figure 3.6a illustrates the relation listed in items (1a) - (1c) in section 3.5. *Valid* pixels (brown dotted) are either classified (brown checked), *indistinct* (yellow) or *unclassified* (red). Classified pixels split up in one of the five classes evolved from Hori et al. (2006) displayed in blueish and greenish colours. In scene 8, 62.0% of the available pixels are classified and mainly classes *coarse* and *suncrust* (dark blue and dark green in fig. 3.6a) are retrieved. About 13.1% of the pixels are *indistinct* and 12.4% remain *unclassified*. Referring to table 3.4, the application of the uncertainty factor enhances the number of *valid* and classified pixels from 84.2% to 87.5% and 9.7% to 46.9%, respectively. Conducting the re-classification described in item (1b), the number of classified pixels again increases from 46.9% to the final amount of 62.0%.

Pixels are flagged *invalid* if one or more of the three pixel emissivities exceed the minimum or maximum boundaries of *ice* and *fine*. Figure 3.6b shows them in purple, grey, and white bars depending on the number of emissivities per pixel that do not fit the classification scheme. Fortunately, in scene 8, only 6.4% of all available pixels are *invalid* due to the emissivities which fig. 3.6b shows as black checked bar. Pixels are also *invalid* if the snow temperature $T_s(11n)$ is greater than 274 K. Figure 3.6b displays the portion of *wet* pixels, which is 6.1% for scene 8, in orange. *Wet* pixels may incorporate either *valid* or *invalid* emissivity values. The total amount of *invalid* pixels is the sum of *wet* pixels and the *invalid* pixels due to emissivity (shown as black dotted bar). In scene 8, 12.5% of the available pixels are *invalid*.

Figure 3.7 represents the spatial distribution of the available pixels of scene 8 in North Greenland with mainly retrieved classes *coarse*, *suncrust*, and *medium*. The most *indistinct* pixels are found at the transition from *suncrust* to *medium* grained snow corresponding to the overlaps of the emissivity ranges of *suncrust* and *medium* displayed in fig. 3.5. *Wet* pixels are located close to the coasts where higher temperatures than in the central region are expected and also obtained. *Unclassified* and *invalid* pixels mostly sit at complex topographic areas. For instance, a line of *unclassified* pixels lies at the steep western coast of Greenland.

In order to analyse the reasons for invalidity, *invalid* pixels are sorted due to

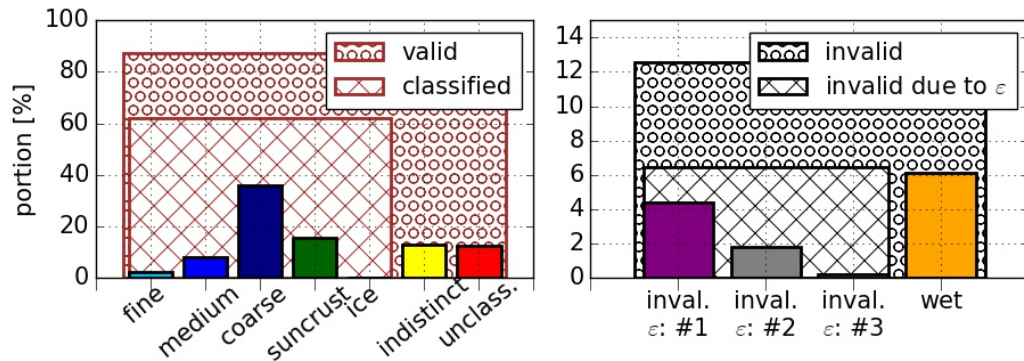


Figure 3.6: The figure shows nested portions of valid pixels (brown dotted) in the left panel and invalid pixels (black dotted) in the right panel, respectively, for case 8 (North-Greenland). Valid pixels are either indistinct (yellow), unclassified (red) or classified (brown checked) after the classes evolved from Hori et al. (2006) (blueish and greenish colours). Pixels become invalid either due to high temperatures (wet pixels: orange) or the emissivities are out of range (black checked). These emissivities are separated due to the number of the pixel's emissivities that account for invalidity (purple, grey, and white bars).

- i) the accountable invalid emissivities per pixel, and
- ii) the actual emissivity value that induces invalidity.

i) Corresponding to fig. 3.6b, the background bar colour in fig. 3.8 indicates the accountable emissivities which are out of range. Pinkish and greyish bars show invalidity due to one and two emissivities per pixel, respectively. The black bars show the portion of pixels with all three emissivities appear to be out of the classification scheme and contribute to invalidity. For instance, the last two grey bars labelled with “f12 & f11” show the number of pixels that are invalid due to both forward view emissivities. The first pink bar accounts for the number of pixels that are *invalid* because $\varepsilon(n12)$ exceeds the permitted emissivity boundaries.

ii) A bar's pattern indicates the reason for the emissivity's invalidity: Either the emissivity sits below the permitted lower *ice* boundary (orange pattern) or above the upper *fine* boundary. Figure 3.8 displays emissivities between the higher *fine* boundary and 1 with a red pattern. The emissivity $\varepsilon(11f)$ cannot have a red pattern because the upper *fine* boundary is 1.0 (see fig. 3.5). The emissivity is non-physical (blue pattern) for values exceeding 1. For instance, the last two grey bars mainly show invalidity due to emissivities larger than 1 due to computational and uncertainty issues. Some f12 values are still physical but larger than the allowed upper *fine* boundary (left light grey bar).

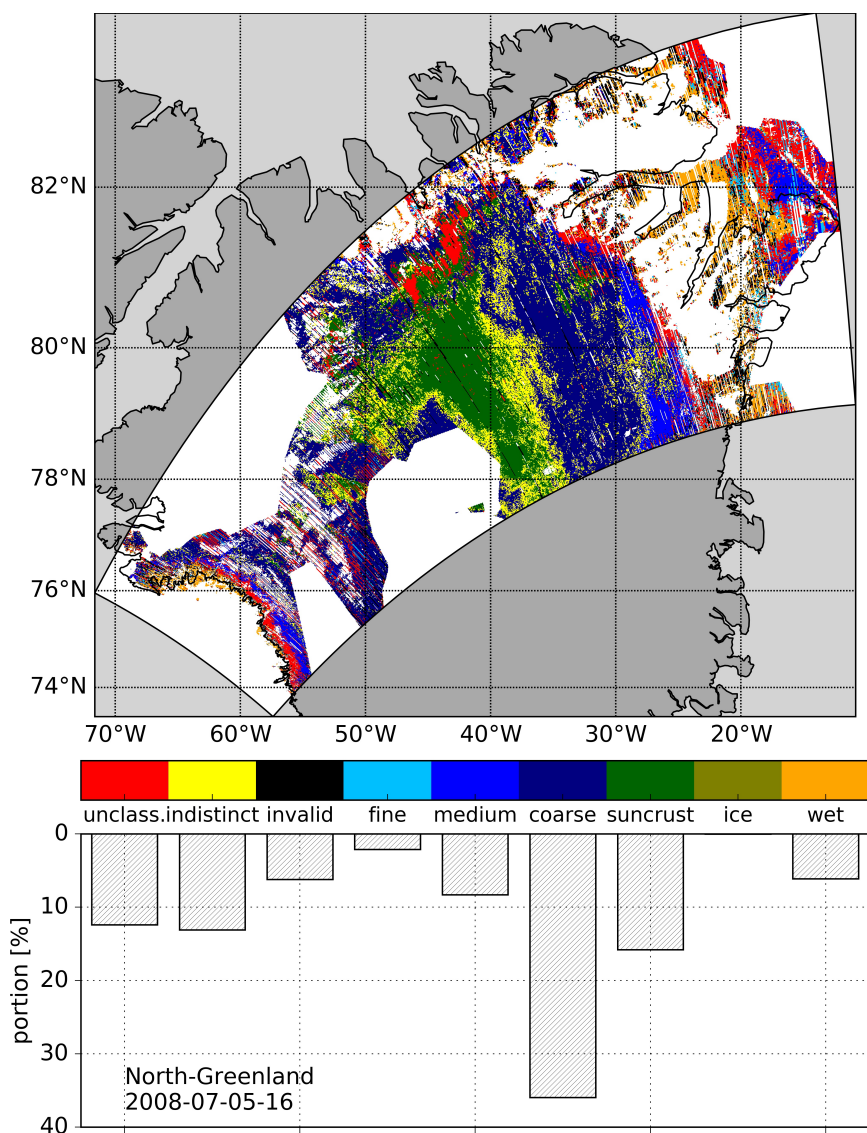


Figure 3.7: Valid and invalid pixels are shown for scene 8 (North-Greenland). Missing values occur due to nadir/forward view co-registration, and masked clouds, water, and bare land corresponding to fig. 3.2. The bottom panel illustrates the portion of occurrence of each class (blueish and greenish colours), indistinct (yellow), unclassified (red), and wet pixels (orange) corresponding to fig. 3.6. Black pixels account for invalidity caused by emissivities out of range (see black checked bar in fig. 3.6b). The colours of the top panel correspond to the label colours of the histogram.

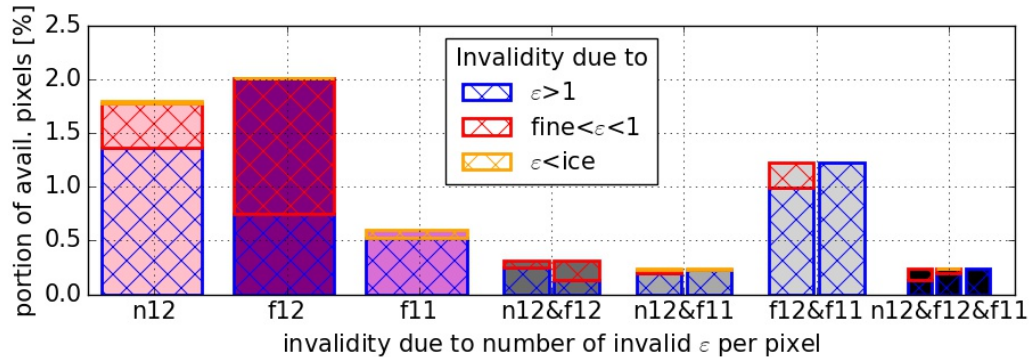


Figure 3.8: The split bars illustrate details of invalid pixels corresponding to the right panel of fig. 3.6. On the one hand, the invalidity due to the responsible emissivity is shown (background colour). On the other hand, the pattern of the bars indicate the reason for invalidity: The emissivity value is below the lower ice boundary (orange) or the upper fine boundary. The latter one splits in bigger than fine and below an emissivity of 1.0 (red) and a nonphysical emissivity greater than 1.0 (blue). The emissivity boundaries for ice and fine differ for f11, f12, and n12 (see fig. 3.5).

In general, in scene 8, very little pixels exhibit too low values. Mostly, high emissivities cause invalidity and a big portion is nonphysical due to values greater than 1. The 12 μm emissivities (rose and purple bars) contribute the most to the total amount of *invalid* pixels. Additionally, fig. 3.6b demonstrates that mainly a single emissivity (purple bar) accounts for invalidity.

4.2 Characterization of all scenes

Figure 3.9 shows the portion of classified (blue and green bars), remaining potentially classifiable (*unclassified* in red and *indistinct* in yellow), *invalid* (black) and *wet* (orange) pixels for all scenes.

Greenland scenes 4-11 mainly exhibit classes *coarse*, *medium* and *suncrust*. More than the half of the *valid* pixels can be classified referring to table 3.4. According to Lyapustin et al. (2009) who retrieved snow grain sizes up to 1000 μm in Greenland and the corresponding snow grain sizes of the classes *medium* and *coarse* (300 μm to 1000 μm), the retrieved classes are reasonable. On contrary to Eurasian and Antarctic scenes, some *suncrust* and a few *wet* pixels occur due to temperatures close to the freezing point causing an alternating melting and freezing of the top-layer snow. In fig. 3.7, Greenland's *suncrust* is located at the centre of the ice sheet and *wet* pixels lie

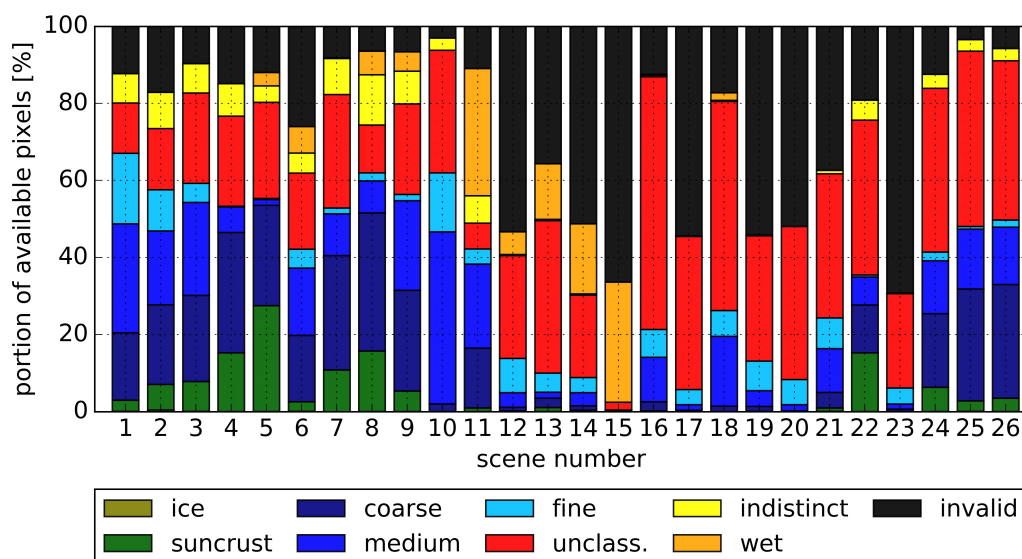


Figure 3.9: Portions of classified (blueish and greenish), unclassified and indistinct (red and yellow), wet (orange), and invalid (black) pixels for all selected AATSR scenes.

close to coasts. Remaining Greenland scenes display similar situations (not shown).

The Eurasian scenes 12-21 show less *valid* pixels (from 30% to 87% except for the Alps with 2.5%) and the number of classified pixels ranges from 5.5% to 26.3% due to a large number of *wet* and *invalid* pixels. On the one hand, the European scenes 12-15 show an increased number of *wet* pixels due to average temperatures around the freezing point (table 3.1) and the location close to coasts. On the other hand, in contrast to Greenland's centre, the complex heterogeneous topography of Scandinavia and the Alps could increase the number of *invalid* and *unclassified* pixels. For instance, in scene 14 (South-Scandinavia, not shown), many *invalid* pixels occur in tight valleys and *unclassified* pixels appear on top of mountains which can be caused by a non-flat surface. This effect appears also for scene 8 in fig. 3.7 close to the coast where the topography is steep and heterogeneous.

The Asian cases 16-21 have 46% to 87% *valid* pixels with a classification of less than 26%. Mainly *fine* and *medium* appear. A large amount of *unclassified* pixels may occur due to an unexpected reflectivity of sea ice (e.g. the White Sea or also partly the Hudson Bay scenes) and frozen rivers (e.g. Kathanga Gulf) which are supposed to be classified as *ice* or *suncrust*.

The American scenes 22-26 exhibit large areas of sea ice except for case 23 in Alaska which is mountainous. Approximately 40% of all pixels are classified and the same amount remains *unclassified*. The classification ranges from *medium* to *suncrust* and less than 19% are *invalid*. The little number of *invalid* pixels may correspond to the flat topography due to sea ice.

In Antarctica (scenes 1-3) around 80% pixels are *valid* and approximately 60% of all pixels have classes *fine*, *medium*, *coarse* or *suncrust*. Scambos et al. (2007) found snow grain sizes within 100 μm to 150 μm in Eastern Antarctica (-80°N, 120°E) and 100 μm to 400 μm at East Antarctic Plateau that matches the snow classes of the Antarctic scenes 1-3. Although the average surface temperature is below 250 K, *suncrust* and in scene 2 *ice* occur. A textured surface is observed in RGB images where the classes *suncrust* and *ice* appear.

Close to coasts or transitions from a cloudy to a clear sky, *wet* pixels (orange) may denote melting processes or clouds that could not yet be identified by our cloud masking method. However, no case exhibits *ice* (except scene 2 in Antarctica) and no Asian scene show even *suncrust*. Complementary, scene 8 in North-Greenland shows a line of *unclassified* pixels at the western coast in fig. 3.7 which could be ice or *suncrust* compared to fig. 3.2. Possibly, the emissivity ranges for *ice* (see fig. 3.5) from Hori et al. (2006) do not apply to the selected cases.

5 Discussion

In the following, four explanations are proposed for the occurrence of *invalid* and *unclassified* pixels:

- i) numerical inaccuracy
- ii) technical issues
- iii) discrepancy within retrieved surface temperatures
- iv) insensitivity of $\varepsilon(11f)$ for snow classification

i) In the retrieval, a 0.25 K inaccuracy in the brightness temperature induces an emissivity difference up to 0.005 (eq. (3.8) and table 3.3) which can lead to a shift in classes or non-classification (see fig. 3.5). We use weighted means and Newton's Iteration to interpolate simulated brightness temperatures related to measurements for the emissivity retrieval. However, a computed surface temperature is accepted if the simulated brightness temperature and the measured brightness temperature differ less than 0.1 K according to the AATSR accuracy (Cardaci, 2013). Matricardi (2009) validated RTTOV with the Infrared Atmospheric Sounding Interferometer (IASI) and retrieved an accuracy of approximately ± 0.4 K for $12\ \mu\text{m}$ and $11\ \mu\text{m}$. The spectral response functions of AATSR have a bandwidth of $1.5\ \mu\text{m}$ for channel $11\ \mu\text{m}$ and $2\ \mu\text{m}$ for $12\ \mu\text{m}$. In this spectral range emissivity of snow, ice or water varies up to 10^{-3} (Wan and Zhang, 1999).

Therefore, we introduce an uncertainty factor in the emissivity classification scheme accounting for the uncertainties of the emissivity retrieval, the AATSR brightness temperature measurements, the RTTOV simulation, and the emissivity variation within the AATSR bands, respectively. Assuming an emissivity uncertainty of 0.005 ($\Delta T_s \approx 0.25$ K) highly increases the number of classified pixels of most scenes (see table 3.4). Applying a greater emissivity uncertainty (e.g. accounting for the AATSR uncertainty obtained by Matricardi (2009)), the classification retrieval results in a large number of *indistinct* pixels due to increased emissivity classification ranges leading to wider overlaps of the classes (fig. 3.5). In order to avoid emissivity classification range overlaps, a more continuous snow class emissivity database is required.

The lower limits of RTTOV are 0.1 mm *TCWV* and a surface temperature of 230 K. Therefore, low temperatures and low total column water vapour contents (e.g. in Antarctica) border these limits and can contribute to an increased uncertainty of the emissivity computations. Hence, this inaccuracy may appear as *invalid* and *unclassified* pixels in the Antarctic scenes.

ii) The sensitivity of the classification method to observation angles is also a technical obstacle because a plane ground surface is assumed. However, Antarctica and Greenland have an elevated topography (Greenland: up to 4000 m (IPCC, 2013)) and steep coasts. The Eurasian scenes are affected from mountains and valleys which may cause shadowing effects. Additionally, a proper co-registration of AATSR forward and nadir view is difficult at slopes. Cloud masking of AATSR above snow is still poor and erroneous (Istomina et al., 2010). Therefore, we use a hand made cloud mask. Nevertheless, *invalid* and *unclassified* pixels may occur due to still uncapped clouds and the almost neglected topography.

iii) The retrieved emissivities in the AATSR settings are inconsistent within the proposed characterization method. An increased difference between a surface temperature and the 11n surface temperature increases the retrieved emissivity (see eq. (3.8)). For example, in order to retrieve class *fine* for 12n (emissivity range 0.985–0.990), its surface temperature demands an increase of up to 3 K compared to $T_s(11n)$. Retrieving class *fine* for 11f, $T_s(11f)$ need to decrease 2 K to 4 K.

Krüger et al. (2011) and Lindstrot et al. (2012) stated the estimated surface temperature effectively depends on the vertical temperature profile. Usually, temperature profiles over cold surfaces show a near ground inversion which is not included in profiles of McClatchey et al. (1972) (see fig. 3.4). Therefore, retrieved RTTOV surface temperatures could be increased artificially. On this account, emissivity values generally may erroneously increase due to a missed lower surface temperature of an expected profile with an inversion. Therefore, fig. 3.8 might show invalidity caused by emissivities that are too large.

Additionally, the smaller the snow grain size, the more homogeneous is the brightness temperature of a unit surface (Hori et al., 2013). Possibly, it is more difficult to classify coarser snow by remote sensing because the signal from one pixel composed from rather heterogeneous sub-pixels averages to a mismatching estimated emissivity. However, the orientation of snow crystals, mixtures of various snow grain sizes in the top snow pack and the variation of a snow surface during a day by cementation, alternate freezing and melting complicates a characterization.

iv) The insensitivity of the forward 11 μm emissivity is most likely responsible for complicating classification results. Considering available emissivity ranges for classes *fine* to *coarse* including the uncertainty factor in fig. 3.5, the 11f emissivity merely has access to a span of 0.020 for three classes whereas the emissivities of 12n and 12f can use ranges of 0.030 and 0.045 widths, respectively. Hence, 11f shows more overlaps than 12n and 12f. As exposed earlier, already small changes in emissivity and surface temperature lead to class shifts.

The insensitivity of $\varepsilon(11f)$ agrees with findings of Hori et al. (2006, 2013). There are *unclassified* pixels because the f11 emissivity values are lower than expected for the corresponding f12 and n12 emissivities. Hence, 11 μm measurements seem to be solely proper for identification of snow. On the other hand, channel 12 μm measurements are useful for snow type classification. Apart from *invalid* and *unclassified* pixels, it is possible to detect different snow classes evolved from measurements by Hori et al. (2006). For all scenes, the classification results are reasonable with smooth transitions (e.g. from *medium* to *coarse* at the Eastern part of scene 1) and *wet* areas only occur close to coasts. However, they are not validated with field snow grain size measurements.

6 Conclusions

The method characterizes snow and ice based on TIR multi-view emissivities. Considering the discrimination power of emissivity (dependency on wavelength, observation angle, and matter), the brightness temperature measurements are used for the 11 μm and 12 μm AATSR channels in nadir and forward view. RTTOV serves as forward model and the use of MERIS *TCWV* enables us to estimate the surface temperature in these bands. Three emissivities are retrieved per pixel ($\varepsilon(11f)$, $\varepsilon(12n)$, $\varepsilon(12f)$) based on a relation of estimated surface temperatures and an assumed emissivity of $\varepsilon(11n) = 0.990$ for all snow grain sizes. The pixel emissivities are sorted in a classification scheme based on classes evolved from field measurements from Hori et al. (2006). Their classes are mainly based on snow grain sizes but also inherit information about age and environmental conditions which cause snow property changes.

26 AATSR scenes in Greenland, Eurasia, North America, and Antarctica are investigated. The number of potentially classifiable *valid* pixels is high for Greenland (56%-97%), above sea ice of the Hudson-Bay and South-Alaska (80%-97%), and Antarctica (85%-90%) and lower for Eurasia (31%-87%) due to temperatures above the freezing point and a complex topographic structure. Greenland and in North America mainly exhibit *medium* and *coarse* snow and Antarctica shows classes *coarse* to *fine*. Eurasian scenes have a small classification portion containing mainly *fine* and *medium* snow. In European scenes, many *wet* pixels occur.

The results are consistent with findings of Scambos et al. (2007) and Lyapustin et al. (2009) (see section 1). However, spectral and angular field emissivity measurements for snow classes in discrete non-overlapping snow grain size intervals may increase the number of classified pixels and decrease the amount of *unclassified* and *indistinct* pixels. Advanced handling of the dual-view co-registration and elevation slopes might support an improved classification.

Generally, the proposed technique is generic. If a sensor provides a 11 μm channel for the reference emissivity of 0.99 the method can be applied to more TIR channels within 8 μm to 14 μm . Using an hyper-spectral sensor, it might be possible only using several nadir channels to avoid co-registration.

In order to improve and proceed snow classifications as introduced in this study, AATSR and MERIS successors Sea and Land Spectral Radiometer (SLSTR) and Ocean and Land Colour Imager (OLCI) on-board the Sentinel-3 series are very promising (cf. chapter 5).

Remotely retrieved phytoplankton properties

Abstract

Total Algae Peak Integration Retrieval (*TAPIR*) relates the chlorophyll-a absorption coefficient at 670 nm (a_{670}) to the reflectance peak in the fluorescence domain from 650 nm to 730 nm. An overview about phytoplankton retrievals and the relation between the reflectance peak's shape, location and magnitude and phytoplankton properties is presented. The algorithm development is based on Matrix Operator Model (MOM0) simulations which reveal the reflectance peak sensitivity on fluorescence and chlorophyll-a absorption mainly influencing the peak's shape and location and phytoplankton scattering mainly affecting the magnitude. Depending on fluorescence efficiency and phytoplankton amount, the fluorescence portion of the total reflectance peak ranges within 3 % to 18 %. The optical phytoplankton properties can be related to a_{670} . The two-step retrieval provides both hyper-spectral quantification of phytoplankton fluorescence, scattering, and absorption and estimation of a_{670} from reflectance signals: Integrating the peak, Total Algae Peak (*TAP*) accounts for variance in the peak's magnitude, shape, and central peak wavelength and linking *TAP* with a_{670} , *TAPIR* functions are developed from which phytoplankton properties can be retrieved by reflectance measurements. *TAPIR* is sensitive on phytoplankton properties and aerosol optical thickness. Water constituents such as *cdom* play a minor role. An uncertainty assessment reveals uncertainties of about 30 % to 35 % for *TAPIR* a_{670} greater than 0.5 m^{-1} . In optically complex waters, first validation efforts promise applicability of *TAPIR* for medium to high chlorophyll-a concentration estimations in the presence of additional water constituents.

Sections 1.1, 1.2, 2.1, 2.3.1, 3, 4.1, 4.2 and 5 to 7 are based on Keck et al. (2018).

1 Introduction

1.1 On the determination of remotely sensed phytoplankton

The space-borne observation of natural waters is mainly limited by three factors: Firstly, strong water absorption restricts passive remote sensing to the visible spectrum (VIS) mostly preventing application of available measurement bands in the near infra-red (NIR) or beyond (see chapter 1 section 2.4).

Secondly, the top of the atmosphere (TOA) measurement is the sum of water-leaving radiation and contribution of atmospheric constituents. Hence, TOA measurement contain both atmospheric information (e.g. aerosols) and information about the water body. Unfortunately, the atmospheric part of the TOA signal is rather large. Retrievals for water constituents either require a proper atmospheric correction or evade the atmospheric influence with sophisticated relations.

Thirdly, apart from atmospheric influence, retrieving a particular water constituent can become ambiguous due to various possible optically active constituent (OAC) compositions for a specific TOA signal. inherent optical properties (IOPs) of water OACs define the resulting water-leaving radiation. In optically complex waters (e.g. at coasts or lakes), Reinart et al. (2004) and Zheng et al. (2015) exemplarily reported superposition of the effects of IOPs of a wide range of OACs (e.g. phytoplankton, coloured dissolved organic matter (*cdom*), inorganic particles).

Bio-optical models (BOMs) relate IOPs to biogeochemical variables (e.g. Morel, 2001, Bricaud et al., 1998, Loisel et al., 2001, Doerffer and Schiller, 2007, Le et al., 2009a, Nechad et al., 2015, Valente et al., 2016). For instance, Bricaud et al. (1995) empirically found spectral coefficients for the relation between spectral chlorophyll absorption and chlorophyll-*a* concentration which is a proxy for phytoplankton amount. Blue-green ratios and polynomial Ocean Colour algorithms (e.g. Ocean Colour quartic algorithm (*OC4*), Ocean Colour quartic algorithm for MERIS (*OC4E*); cf. chapter 2 section 2.3.5) for a wide range of space sensors (Gordon et al., 1988, Morel, 1988, O'Reilly et al., 2000) retrieve *chl-a* in case-1 waters which contain mainly phytoplankton (Morel and Prieur, 1977). In optically complex waters (case-2) with constituents uncorrelated to phytoplankton, Huot et al. (2007) and Gower (2016) recently demonstrated the complicating impact of mainly *cdom* on *chl-a* retrievals due to high *cdom* absorption at the required bands for the blue-green ratio.

Jerlov (1953) and Doerffer and Fischer (1994) investigated the spectral absorption from *cdom* in the visible spectrum from *in situ* measurements and satellite retrievals,

respectively. *Cdom* absorption exponentially decreases from 400 nm to 800 nm (Odén, 1919) and becomes rather small in the interval from 630 nm to 730 nm which may be beneficial for phytoplankton properties algorithms. Additionally, the phytoplankton pigment chlorophyll-a exhibits the optical feature of the process of fluorescence that releases radiation near 683 nm (Gordon, 1979, Fischer and Kronfeld, 1990, Schalles, 2006, Zhou et al., 2008). The amount of *chl-a* and the photosynthetic activity scale the amount of emitted fluorescence (Pedrós et al., 2008).

Physically, fluorescence is the process of light emission transforming energy of a released electron of a relaxed chlorophyll-a molecule which was excited by solar radiation (cf. chapter 2 section 2.3.2). Although, the phenomenon can occur for both living and deceased phytoplankton cells, this study focuses on animated cells. Besides photosynthesis and heat dissipation, fluorescence is one of the major competitive fates of absorbed VIS light (Maxwell and Johnson, 2000). Therefore, fluorescence does not only indicate chlorophyll-a but also “living activity” of phytoplankton although Xing et al. (2007) report less than 5 % of total absorbed light used for the fluorescence process. In spite of a rather small fluorescence efficiency, which is the ratio between the number of emitted fluorescent absorbed photons available for the fluorescence process, of 0.1 % to 1.0 % (Gordon, 1979, Fischer and Kronfeld, 1990, Maritorena et al., 2000, Gilerson et al., 2007, Zhou et al., 2008), space-borne sensors are able to observe emitted fluorescence in reflectance spectra (e.g. Neville and Gower, 1977, Behrenfeld et al., 2009, Hu and Feng, 2016).

In the last four decades, sun-induced fluorescence in waters was investigated theoretically (e.g. Gordon, 1979, Fischer and Kronfeld, 1990) and *in situ* (Roesler and Perry, 1995, Claustre et al., 1999, Zarco-Tejada et al., 2001). Using multi-spectral space-borne measurements, for instance, from Moderate Resolution Imaging Spectrometer (MODIS) on-board Aqua and Terra and Medium Resolution Imaging Spectrometer (MERIS) on-board Environmental Satellite (ENVISAT), fluorescence can be obtained with Fluorescence Line Heights (*FLHs*) (Letelier, 1996, Gower et al., 1999, Meroni et al., 2009, Palmer et al., 2015). Ocean and Land Colour Imager (OLCI) onboard Sentinel-3 (S3) launched in February 2016 also provides bands for *FLH* algorithms. *FLH* estimates the reflectance peak magnitude by the difference of measurements at a peak wavelength (e.g. 681.25 nm for OLCI) and a baseline retrieved from two additional bands (Neville and Gower, 1977, Fischer and Kronfeld, 1990, Gower et al., 1999). For high phytoplankton amount, the reflectance peak shifts towards longer wavelengths and Schalles (2006) and Gilerson et al. (2007), exemplary, reported a redshift from 680 nm to 705 nm for 0 mg m^{-3} to 30 mg m^{-3} chlorophyll-a concentration. Accounting for the redshift, baseline algorithms such as Maximum Chlorophyll Index (*MCI*) and Maximum Peak

Height (*MPH*), which use alternative measurement bands to *FLH*, are introduced (Gower et al., 2005, Matthews et al., 2012). For example, the *MPH* algorithm uses available multi-spectral measurement bands in the red VIS and NIR domain from 660 nm to 880 nm and, exemplarily for MERIS, selects the reference or signal band individually at 681 nm, 709 nm and 753 nm depending on the maximum reflectance (Matthews et al., 2012, Matthews and Odermatt, 2015). A reflectance minimum near 681 nm occurs for extreme algae concentrations such as harmful algae blooms (HABs) resulting in negative *FLH*. Wynne et al. (2008) and Stumpf et al. (2012) used negative *FLH*, which equals positive Cyanobacterial Index (*CI*), to detect cyanobacteria blooms in the Great Lakes, United States and Canada. However, multi-spectral imagers such as MODIS, MERIS, and OLCI may not represent the actual phytoplankton peak near 690 nm due to the spectral resolution with a few bands in the red VIS and NIR and the relatively large measurement bands. Blondeau-Patissier et al. (2014) reviewed *chl-a* retrievals and summarized that *FLH* works in coastal waters with concentrations up to 20 mg m^{-3} but that a linear baseline leads to underestimations for higher concentrations due to water absorption and *chl-a* distortion. Depending on the observed water body, the comparison between *in situ chl-a* and chlorophyll-a concentration derived from *FLH*, *MCI*, and *MPH* still shows high variations (Matthews and Odermatt, 2015).

Hyper-spectral simulations promise improved estimations of fluorescence and phytoplankton properties with hyper-spectral sensors (Gilerson et al., 2007, Blondeau-Patissier et al., 2014). Besides Hyperspectral Imager for the Coastal Ocean (HICO) mounted on International Space Station (ISS) and Compact High Resolution Imaging Spectrometer (CHRIS) on-board satellite Project for On-Board Autonomy 1 (PROBA-1), Earth Observing satellite 1 (EO-1) carried hyper-spectral sensor Hyperion with 220 bands in the VIS and NIR from November 2000 to January 2017. Recently, Sentinel-5 Precursor (S5p) carrying Tropospheric Monitoring Instrument (TROPOMI) was launched in October 2017. Hyper-spectral Precursor and Application Mission (PRISMA), Environmental Mapping and Analysis Program (EnMAP), Hyperspectral Infrared Imager (HyspIRI), and Plankton, Aerosol, Cloud, ocean Ecosystem (PACE) launching in 2018, 2019, 2022, and 2022, respectively, are promising future space missions for application of advanced fluorescence and phytoplankton algorithms. For instance, Hyperspectral Imager (HSI) on-board EnMAP provides 65 bands with a full width at half-maximum (FWHM) from 6 nm to 9 nm within the range from 420 nm to 800 nm (Guanter et al., 2015).

1.2 On the phytoplankton peak in the fluorescence domain

In the chlorophyll-a fluorescence domain from 650 nm to 750 nm, the reflectance of clear water decreases towards longer wavelengths (cf. fig. 2.8d) due to water absorption. The phytoplankton pigment chlorophyll-a absorbs light within the total visible spectrum with two local absorption maxima near 440 nm and 670 nm and phytoplankton scattering spectrally decreases with longer wavelengths in the VIS but is still apparent in the fluorescence domain. Total absorption from water and chlorophyll-a exhibits a local minimum near 690 nm (cf. fig. 2.6). Therefore, waters containing phytoplankton reveal a reflectance peak near 690 nm (see fig. 4.1a).

Figure 4.1 shows details of bottom of the atmosphere (BOA) reflectance in the fluorescence domain produced from radiative transfer simulations which are introduced in section 2. The concentration of phytoplankton and chlorophyll-a absorption are related and the figure expresses an increase in phytoplankton amount with chlorophyll-a absorption at 440 nm. The relation between the quantities is highly individual and depends mainly on phytoplankton species and environmental conditions. Analogously, the magnitude of phytoplankton scattering depends on the amount of phytoplankton. For increasing chlorophyll-a, simulated reflectance increases within the fluorescence interval (fig. 4.1a) due to increased phytoplankton scattering and an increased available energy for the process of fluorescence. The black solid and grey dashed lines represent the reflectance with and without considering the process of fluorescence, respectively. The major fraction of the phytoplankton peak originates from phytoplankton scattering and a smaller portion (the difference between the solid and dashed lines) is contributed from the process of fluorescence emitting photons near 683 nm (Pedrós et al., 2008, cf. chapter 2 section 2.3.2.3).

The local reflectance maximum $R(\lambda_p)$ at the maximum peak wavelength λ_p shifts towards longer wavelengths for a higher amount of phytoplankton (fig. 4.1b). Particularly for low to medium chlorophyll-a absorption, the fluorescence plays a role in the location of the maximum peak comparing the solid black and grey dashed line in panel b). Neglecting the emission from the process of fluorescence, the peak magnitude is underestimated and the maximum peak location is overestimated.

Figure 4.1c reveals the relative shape of the effective reflectance peak for increasing phytoplankton amount. The peak's magnitude enlarges due to increased phytoplankton scattering and fluorescence but its slope narrows due to

- i) phytoplankton absorption near 670 nm, and
 - ii) water absorption.
- i) The local chlorophyll-a absorption exhibits a local maximum near 670 nm which is

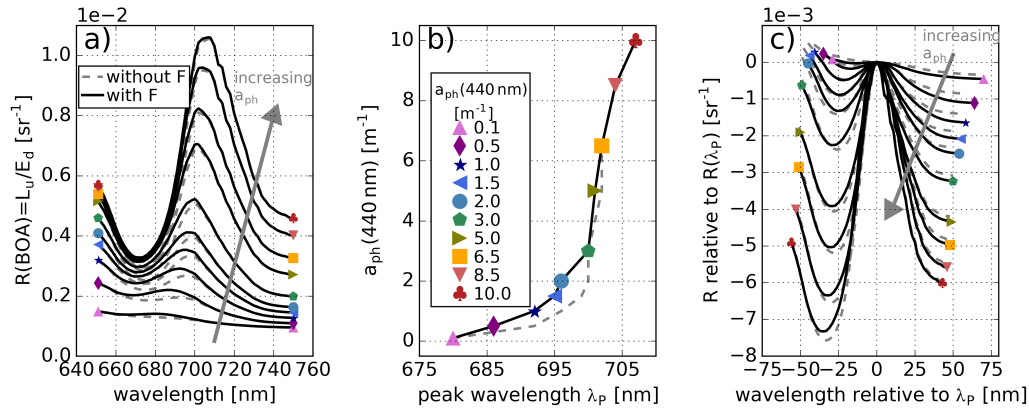


Figure 4.1: The figure shows details of simulated BOA reflectance, introduced in section 2, with and without considering fluorescence (black solid and grey dashed lines, respectively) for different chl-a absorption coefficients (indicated with coloured symbols) within the fluorescence domain from 650 nm to 730 nm. a) Effective phytoplankton peak, b) shift of maximum reflectance $R(\lambda_P)$ towards longer wavelengths (redshift), and c) shape and amplitude of the phytoplankton peak relative to peak wavelength λ_P and local maximum $R(\lambda_P)$. Symbols in panels a), b) and c) correspond to the legend in panel b) and line colours (grey and black) correspond to the legend in panel a).

responsible for re-absorption of phytoplankton scattering and emitted fluorescence. The absorption maximum spectrally expands for increased phytoplankton amount. Therefore, the maximum of the effective reflectance peak appears to be shifted towards longer wavelengths and the slope of the peak's left edge raises.

ii) The peak becomes spectrally broader for higher amount of phytoplankton induced by higher phytoplankton scattering and increased fluorescence emission. Hence, the reflectance peak reaches in the interval beyond 700 nm where water absorption rapidly increases (cf. fig. 2.6). Water partly re-absorbs phytoplankton scattering and fluorescence and the the peak's right edge becomes steeper (Ahn and Shanmugam, 2007).

Hence, those two independent mechanisms non-uniformly influence the peak resulting in different peak shapes illustrated in fig. 4.1c. For an increasing phytoplankton amount constraining fluorescence, scattering, and absorption, the peak exhibits

- i) an increased magnitude,
- ii) a shift towards longer wavelengths,
- iii) an increased spectral width, and
- iv) a narrowed slope.

Due to highly variable peak characteristics, baseline retrievals may underestimate actual phytoplankton properties. *CI* and *MPH* exploit the redshift and relate the reflectance difference between baseline and signal band to cyanobacteria. However, the baseline is different for each reflectance spectrum which may lead to uncertainties and NIR bands are also affected from adjacency effects (e.g. scattering sediments) influencing the baseline slope (Gower et al., 1999). Often, the peak in the fluorescence domain is solely attributed to fluorescence (e.g. Fischer and Kronfeld, 1990, Gower et al., 1999, Gilerson et al., 2007, Blondeau-Patissier et al., 2014) which might be likely for low phytoplankton concentrations with low phytoplankton scattering (Gilerson et al., 2007). Reviewing several baseline algorithms, Blondeau-Patissier et al. (2014, sec. 3.3.5) noted that *FLH* cannot be used for high phytoplankton amounts. The penetration depth of water in the red visible and near infra-red spectrum is limited to a few meters due to water absorption (Gordon and McCluney, 1975). Therefore, all retrievals based on reflectance in the fluorescence domain are limited to the upper water layer. The effect of slightly lowered phytoplankton on the reflectance peak has to be investigated and early initial attempts are conducted in section 2.2.3. However, in order to capture the peak's variability induced by phytoplankton properties, the reflectance peak is spectrally integrated in this study (see section 3).

1.3 On the relation of the peak and chl-a absorption at 670 nm

The reflectance peak in the fluorescence domain is controlled from phytoplankton scattering and chlorophyll-a fluorescence, which both influence magnitude, and chlorophyll-a and water absorption, which both are responsible for radiation depletion. Thus, the peak contains information about phytoplankton absorption, scattering, and fluorescence which are additionally dependent on each other. The properties are directly related to the amount of phytoplankton (Gilerson et al., 2007) and the relation may vary with phytoplankton species and their condition (health, productivity) and environmental conditions such as light availability and nutrient supply. Besides environmental and physiological conditions, chlorophyll-a fluorescence is directly related to chlorophyll-a absorption (see chapter 2 sections 1.1.2 and 2.3.2) because a fraction of absorbed photons are used in the process of fluorescence. The scattering and backscattering coefficient are also dependent on phytoplankton amount and algae condition. Therefore, phytoplankton scattering can be set in relation to chlorophyll-a absorption dependent on chlorophyll-a concentration: The more phytoplankton the more absorption and scattering. Phytoplankton scattering spectrally decays (see chapter 2 section 2.3.2) and single scattering albedo links chlorophyll-a absorption and phytoplankton scattering. Depending on the state

of algae, absorption and scattering change proportionally for a changing phytoplankton amount.

Chlorophyll-a exhibits two local absorption maxima near 440 nm and 670 nm, respectively. As outlined in previous sections, the latter one plays an important role in depletion of the phytoplankton reflectance peak and the redshift and, therefore, is directly linked to shape, size, and location of the peak. Assuming a dependency of the absorption magnitude near 670 nm and the size of the phytoplankton peak, which is mainly produced by phytoplankton scattering, chlorophyll-a absorption at 670 nm and scattering in the fluorescence domain can be linked. Referring to Porcar-Castell et al. (2014), red photons absorbed near 670 nm are mainly involved in the process of fluorescence. Therefore, in the fluorescence domain, the magnitude of fluorescence and phytoplankton scattering are related to chlorophyll-a absorption at 670 nm a_{670} which additionally has a direct impact on the reflectance peak by re-absorption. Thus, both reflectance peak and a_{670} contain information about phytoplankton absorption, scattering, fluorescence, and amount and may be set in relation. Additionally, there is a dependence on vertical phytoplankton location which plays a minor role in the thesis but exhibits a dominant impact on the magnitude of the peak (cf. section 2.2.3).

1.4 Scope and content of the study

This chapter investigates the reflectance peak in the fluorescence domain from 650 nm to 730 nm and a phytoplankton properties retrieval is introduced considering the high variability of the peak. The Total Algae Peak Integration Retrieval (*TAPIR*) accounts for the spectral shape, size, and location of the peak which are effects of phytoplankton properties chlorophyll-a absorption, phytoplankton scattering, and fluorescence. The parameter a_{670} plays a major role for the reflectance peak appearance and is related not solely to absorption but also contains information about phytoplankton scattering and fluorescence. Therefore, *TAPIR* links a_{670} and the spectral peak integral to retrieve phytoplankton properties from remotely sensed radiometric measurements.

The retrieval development is based on simulations with the radiative transfer model (RTM) MDMO which is introduced in section 2.1. The sensitivity on implemented fluorescence, phytoplankton parameterization, layer thickness and signal depth are investigated in section 2.2. A first initial effort comparing MDMO simulations with hyper-spectral *in situ* measurements are conducted in section 2.3. Section 3 describes the peak integration routine and the method of linking a_{670} with the peak area. In section 4, the algorithm's sensitivity on several parameters such as $cdom$ or aot are analysed and an uncertainty propagation for *TAPIR* retrieved a_{670} is presented. *TAPIR* functions and

a670 uncertainties for TROPOMI, EnMAP, and HICO are shown. *TAPIR* can be applied on multi-spectral instruments such as OLCI with a polynomial fitting function. A BOM is applied on *a670* to retrieve *chl-a* and a first initial validation effort is conducted with *in situ* measurements (section 5). The study is discussed in section 6 and followed by conclusions and outlook in section 7.

TAPIR exploits the presumably available hyper-spectral TOA measurements and estimates the phytoplankton amount. The application of *TAPIR* for TOA or surface measurements supports a direct estimation of *chl-a* with an individual bio-optical model adjusted for regional conditions. The comparison of highly resolved simulations and theoretical EnMAP measurements shows a sufficient reproduction of the peak near 683 nm.

2 Radiative transfer simulation with MOMO

2.1 MOMO simulation

The Matrix Operator Model MOMO is an advanced radiative transfer code for multiple applications in coupled atmosphere-water-systems (Fischer and Grassl, 1984, Fell and Fischer, 2001, Hollstein and Fischer, 2012). It includes an individual selection of number and thickness of layers, viewing and sun geometry, atmospheric conditions, and state of the water body parameterized by IOPs from water constituents.

In this study, simulations include a water body with 200 layers, each 10 cm thick, and 8 atmospheric layers up to 50 km of diverse geometrical thickness. The simulations are cloud-free and are based on standard atmospheres from McClatchey et al. (1972) including temperature, pressure, water vapour profiles. Aerosols are controlled with aerosol optical thickness aot and located in about 2 km height. Water is assumed to be homogeneous with an equal distribution of constituents (phytoplankton and $cdom$) in each layer. The chlorophyll-a extinction coefficient and the corresponding single scattering albedo control the amount and spectral signature of phytoplankton. A normalized chlorophyll-a absorption spectrum is scaled at 440 nm to retrieve the absorption spectrum $a_{ph}(\lambda)$ for different phytoplankton amounts (fig. 4.2a). The single scattering albedo ω_0 at 440 nm is set to 0.68 (J. Fischer, pers. communication, 2017) to calculate spectral phytoplankton scattering $b_{ph}(\lambda)$ with

$$(4.1) \quad b_{ph}(\lambda) = a440 \frac{\omega_0}{1 - \omega_0} \frac{\lambda}{440 \text{ nm}}.$$

Therefore, an increase in $a440$ increases $a_{ph}(\lambda)$ and $b_{ph}(\lambda)$ proportionally. A varied ω_0 (fig. 4.2b) only changes phytoplankton extinction due to changed b_{ph} and unaffected a_{ph} . Phytoplankton scattering is constrained by a phase function measured from Petzold (1972) which can be mathematically expressed with the Fournier-Forand function in eq. (2.17) (chapter 2 section 2.3.2) and exhibits a backscattering ratio of 0.01986. MOMO models emitted phytoplankton fluorescence near 683 nm with an excitation based on photosynthetically active radiation (PAR) from 395 nm to 685 nm, fluorescence efficiency and phytoplankton absorption as outlined in chapter 2 section 1.1.2.

Table 4.1 summarizes parameters used in simulations from 390 nm to 790 nm (λ) for various phytoplankton concentrations. Chlorophyll-a absorption at 440 nm $a440$ ranges from 0.1 m^{-1} to 10.0 m^{-1} referring to high $a440$ measurements in China (Le et al., 2009b) and laboratory measurements (Mitchell, 1990). There are three normalized

Table 4.1: Overview of parameters varied in MOMO simulations. Bold values refer to the reference simulation.

parameter	range	unit
a_{440}	0.1, 0.5, 1.0, 1.5, 2.0, 3.0, 5.0, 6.5, 8.5 and 10.0	m^{-1}
$a_{ph}(\lambda)$	Doerffer , NechadMIN, NechadMAX (fig. 4.2a)	m^{-1}
aot	0.0, 0.2 , and 0.4	—
b	0.0 , 1.0, 5.0, and 10.0	m^{-1}
$cdom$	$g(a_{440})$, 0.0, 1.5, and 3.0	m^{-1}
η	0.003 , 0.01, and 0.03	—
λ	390 to 790 (with $\Delta\lambda=1$ nm)	nm
ω_0	0.68 , 0.75, and 0.82 (fig. 4.2b)	—
s	0, and 35	PSU
atm	arct. winter, mid.-lat. summer , and tropical	—
θ	0, 25, 50 , and 68	$^\circ$
T	4.5 , and 25	$^\circ\text{C}$

absorption spectra a_{ph} with low, medium, and high absorption maxima and three variations of single scattering albedo ω_0 based on particle IOPs measurements from Babin et al. (2003) (see fig. 4.2). The spectra NechadMIN and NechadMax are averaged from normalized HydroLight absorption spectra (Nechad et al., 2015) for a_{670} ranges from 0.2 m^{-1} to 0.3 m^{-1} and 0.7 m^{-1} to 0.8 m^{-1} , respectively. They vary in magnitude and width of the local absorption maximum at 670 nm and spectral shape (e.g in the blue visible range in fig. 4.2a). Additionally, the fluorescence efficiency η is varied from 0.003 (Fischer and Kronfeld, 1990) to 0.01 and 0.03 (Gilerson et al., 2007). The $cdom$ absorption coefficient at 440 nm is coupled with a_{440} based on a collection of *in situ* measurements from Nechad et al. (2015) (see section 2.3.1).

$$(2.22) \quad cdom(a_{440}, 440 \text{ nm}) = 0.24 * a_{440}^{0.43} = g(a_{440})$$

Spectral $cdom$ absorption decreases exponentially towards longer wavelengths with a slope factor of 0.02 nm^{-1} (see chapter 2 section 2.3.5). However, a set of simulations include independent $cdom$ absorption coefficients at 440 nm with 0.0 m^{-1} , 1.5 m^{-1} and 3.0 m^{-1} . Additionally, simulations exhibit variations of white water scatterer b with backscattering ratio of 0.001, salinity s , and surface temperature T . In the atmosphere, the selection of the standard atmosphere atm and aerosol optical thickness aot are varied. The sun zenith angle θ ranges within 0° and 89° and four angles between 0° and 68° are used for investigation.

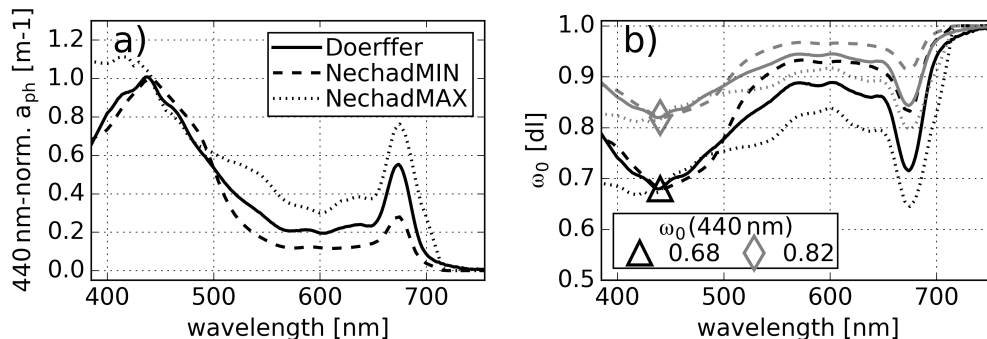


Figure 4.2: Variation of a) phytoplankton absorption spectrum (normalized to $a_{ph}(440 \text{ nm})$) and b) corresponding single scattering albedo for $\omega_0(440 \text{ nm})=0.68$ (reference) and 0.82 (grey). Black solid lines illustrate reference spectra and dashed lines variations collected from HydroLight simulations by Nechad et al. (2015).

Each simulation considers the above-mentioned parameters for the VIS/NIR and chlorophyll-a absorption scaling factors a_{440} from table 4.1. Compared to a “reference” simulation with “reference” parameter values (bold in table 4.1), each simulation solely varies one of the parameters and other parameters remain to the “reference” set-up. The nadir reflectance $R = L_u/E_d$ is calculated from simulated upwelling radiance L_u and downwelling irradiance E_d .

2.2 Sensitivity

In the following, MOMO sensitivity is analysed due to the implementation of the process of fluorescence (section 2.2.1), variation of phytoplankton IOPs (section 2.2.2), influence of water layer thickness, and dependency on depth and signal depth of phytoplankton (section 2.2.3). Water-leaving reflectance (BOA) with reference parameters from table 4.1 is used avoiding a second interaction with the atmosphere. In this section, the term fluorescence F refers to the difference between two MOMO simulations with (peak; black solid lines in fig. 4.3a) and without (pure; grey dashed lines) implemented fluorescence (fig. 4.3d):

$$(4.2) \quad F(\lambda) := \Delta R(\lambda) = R(\lambda, \text{peak}) - R(\lambda, \text{pure})$$

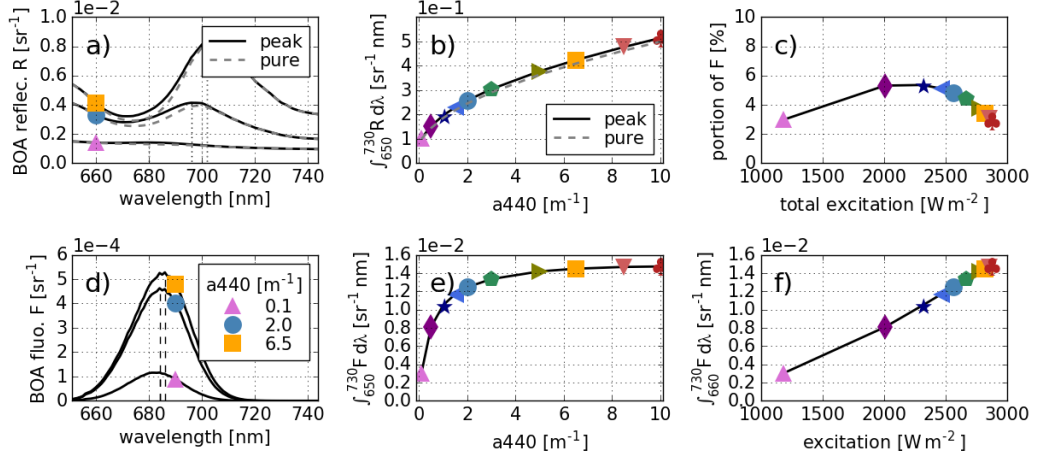


Figure 4.3: The rows refer to reflectance R and fluorescence F above water (BOA) for different phytoplankton amounts. The first column shows spectra for a_{440} of 0.1 m^{-1} , 2.0 m^{-1} and 6.5 m^{-1} . The second column presents the integral from 650 nm to 730 nm of the reflectance peak in b) and fluorescence in e) for all simulated a_{440} . Panel c) shows the fraction of fluorescence integrals from e) and reflectance integrals from b) dependent on total excitation in the water body. Panel f) illustrates the linear relationship between excitation and fluorescence integral.

2.2.1 Fluorescence

The spectral fluorescence peaks near 683 nm (fig. 4.3d), which is expected for fluorescence (Pepe et al., 2005), and is about 1 magnitude lower than reflectance near 683 nm in fig. 4.3a. In order to compare simulations with and without implemented fluorescence, reflectance and fluorescence retrieved with eq. (4.2) are integrated from 650 nm to 730 nm :

$$(4.3) \quad RA = \int_{650 \text{ nm}}^{730 \text{ nm}} R(\lambda) d\lambda$$

$$(4.4) \quad FA = \int_{650 \text{ nm}}^{730 \text{ nm}} F(\lambda) d\lambda$$

Fluorescence contributes to the total phytoplankton peak: The comparison of RAs from simulations with (peak) and without (pure) fluorescence reveal that the spectrum is slightly raised (figs. 4.3a and 4.3b). Total amount of fluorescence FA extracted from reflectance with eq. (4.2) increases with increasing a_{440} (fig. 4.3e). Fluorescence contributes between 3% to 6% to the effective reflectance peak ranges (fig. 4.3c) comparing

the integrals RA and FA from reflectance (panel b)) and fluorescence (panel e)) in the interval from 650 nm to 730 nm. However, the fraction decreases with increasing total excitation because absorption of chlorophyll-a near 670 nm increases and the effective reflectance peak approaches the domain of high water absorption. Gilerson et al. (2007) found fractions of lower than 3% for simulations with high non-algae particles and fractions from 5% to 30% for chlorophyll-a concentrations up to 100 mg m^{-3} and an assumed efficiency factor of 0.01. Using an efficiency factor of 0.01 in MOMO, the portion of fluorescence in the reflectance peak is between 10% to 18%. The higher the total excitation of a homogeneous water body the higher is the resulting emission of fluorescence above the surface (fig. 4.3f). The relation is linear: The more excitation is available the more fluorescence is emitted (fig. 4.3f). However, the relation between fluorescence and phytoplankton amount is non-linear (fig. 4.3e).

In order to investigate the influence of chlorophyll-a absorption and phytoplankton scattering on fluorescence, three experimental simulations with fluorescence were conducted:

- i) $\omega_0 = NaN$: clear water (no phytoplankton absorption or scattering),
- ii) $\omega_0 = 0$: only chlorophyll-a absorption, and
- iii) $\omega_0 = 1$: only phytoplankton scattering.

The calculation of spectral b_{ph} and a_{ph} refers to section 2.1 with a defined single scattering albedo at 440 nm of 0.68. The above-mentioned ω_0 indicate whether the experimental simulations permit either phytoplankton scattering ($\omega_0 = 1$) or absorption ($\omega_0 = 0$) or neither of these ($\omega_0 = NaN$). The excitation is calculated with considered absorption coefficients although the experiments $\omega_0 = NaN$ and $\omega_0 = 1$ prohibit chlorophyll-a absorption. Omitting either absorption, scattering, or both, the effects on the reflectance and the fluorescence are highly different and are shown in fig. 4.4 exemplarily for two phytoplankton amounts (a_{440} : 2.0 m^{-1} and 6.5 m^{-1}). Experimental simulations are shown with dashed lines and reference simulations with reference parameterization (table 4.1) are indicated with solid lines.

i) Assuming clear water ($\omega_0 = NaN$), the fluorescence implementation produces large peaks at 683 nm without redshift due to missing re-absorption of phytoplankton near 670 nm (figs. 4.4a and 4.4d). The reflectance is generally lower in the fluorescence domain due to missing phytoplankton scattering. Fluorescence is directly proportional to the scaling absorption factor a_{440} used in excitation calculation and 10 times larger than the reference fluorescence signal (fig. 4.4d).

ii) Waters that contain only absorbing phytoplankton ($\omega_0 = 0$) have a similar reflectance spectrum from 650 nm to 740 nm to clear waters (figs. 4.4a and 4.4b) but

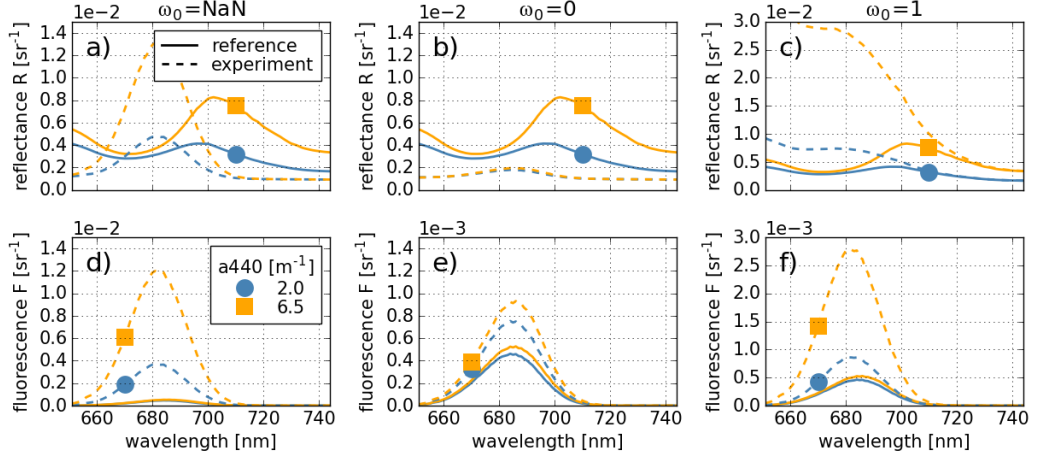


Figure 4.4: Experimental MOMO simulations for the analysis of the implemented process of fluorescence. The rows show BOA reflectance and the fluorescence signal after eq. (4.2), respectively, for a_{440} of 2.0 m^{-1} and 6.5 m^{-1} (blue and orange). The columns show the response of fluorescence for clear water ($\omega_0 = \text{NaN}$), only-absorbing phytoplankton ($\omega_0 = 0$), and only-scattering phytoplankton ($\omega_0 = 1$) compared to the reference simulation (solid lines).

the fluorescence peak is smaller due to chlorophyll-a absorption which is strong near 670 nm and not negligible up to 700 nm. The fluorescence signal reduces by a magnitude from 10^{-3} sr^{-1} to 10^{-4} sr^{-1} and the difference between low and high a_{440} becomes smaller (figs. 4.4d and 4.4e). The fluorescence peaks are slightly shifted towards longer wavelengths for higher a_{440} and the signal from experimental only-absorbing phytoplankton (dashed) is slightly larger than the signal from reference MOMO simulation (fig. 4.4e).

iii) In contrast to clear water and waters with only-absorbing algae, simulations with pure-scattering phytoplankton ($\omega_0 = 1$) raise the reflectance spectrum significantly (fig. 4.4c). The experimental reflectance spectra exhibit no significant phytoplankton peak. However, the fluorescence signal is doubled for high chlorophyll-a (dashed orange). It is in a similar magnitude for lower phytoplankton amount (blue dashed) compared to fluorescence signals from waters with only-absorbing algae (figs. 4.4e and 4.4f). The fluorescence signals of only-scattering phytoplankton exhibit no redshift (fig. 4.4f)

In conclusion, the fluorescence portion of total reflectance is proportional to excitation constrained by total extinction of each water layer. According to literature and simulations, fluorescence is emitted near 683 nm and ranges in magnitudes of 10^{-4} sr

to 10^{-3} sr. The total reflectance peak mainly originates from phytoplankton scattering whereas phytoplankton absorption constrains the redshift. Both phytoplankton IOPs contribute to a reduction of the fluorescence due to re-absorption and scattering in directions other than backwards. Nevertheless, fluorescence increases the effective phytoplankton reflectance peak and contributes up to 6 %.

2.2.2 Phytoplankton IOPs

In this section, the influence of assumed

- i) fluorescence efficiency η ,
- ii) normalized chlorophyll-a absorption spectra a_{ph} , and
- iii) relative phytoplankton scattering strength constrained by ω_0 (eq. (4.1))

are investigated for two phytoplankton amounts (a_{440} : 2.0 m^{-1} and 6.5 m^{-1} indicated with solid and dashed lines in fig. 4.5). The rows show reflectance R , fluorescence F according to eq. (4.2), and the redshift as maximum peak wavelength λ_F for various phytoplankton amounts a_{440} . Red lines refer to the reference MOMO set-up from table 4.1, and grey and black lines to simulations with varied efficiency η (first column), absorption spectrum a_{ph} (second column), and single scattering albedo ω_0 at 440 nm or relative strength of phytoplankton scattering, respectively, (third column).

i) Increasing the efficiency factor from 0.003 to 0.01 and 0.03, the reflectance increases in the fluorescence domain (fig. 4.5a) and the fluorescence portion increases by that factor (fig. 4.5d). The maximum of the effective reflectance phytoplankton peak shifts towards shorter wavelengths (fig. 4.5g) which may be referred to as “blueshift” analogously to the redshift.

ii) Changing the normalized absorption spectrum (cf. fig. 4.2a), the reflectance spectra highly vary spectrally (fig. 4.5b) due to stronger (grey) or weaker (black) normalized absorption spectra. Stronger absorption spectra cause lower reflectance but slightly higher fluorescence (fig. 4.5e) due to larger amount of absorbed photons for equal conditions in light availability and water. The absorption band near 670 nm is significantly broader for “NechadMAX” (grey) than for “Doerffer” and “NechadMIN” (cf. fig. 4.2a) which results in lower reflectance (fig. 4.5b) and increased redshift (fig. 4.5h). A reciprocal mechanism can be observed for weaker normalized absorption spectra (second column in fig. 4.5).

iii) Changing the ratio between chlorophyll-a absorption and phytoplankton scattering, the spectral absorption coefficients do not change but scattering coefficients increase or decrease, respectively. An increase in the scattering portion magnifies the reflectance

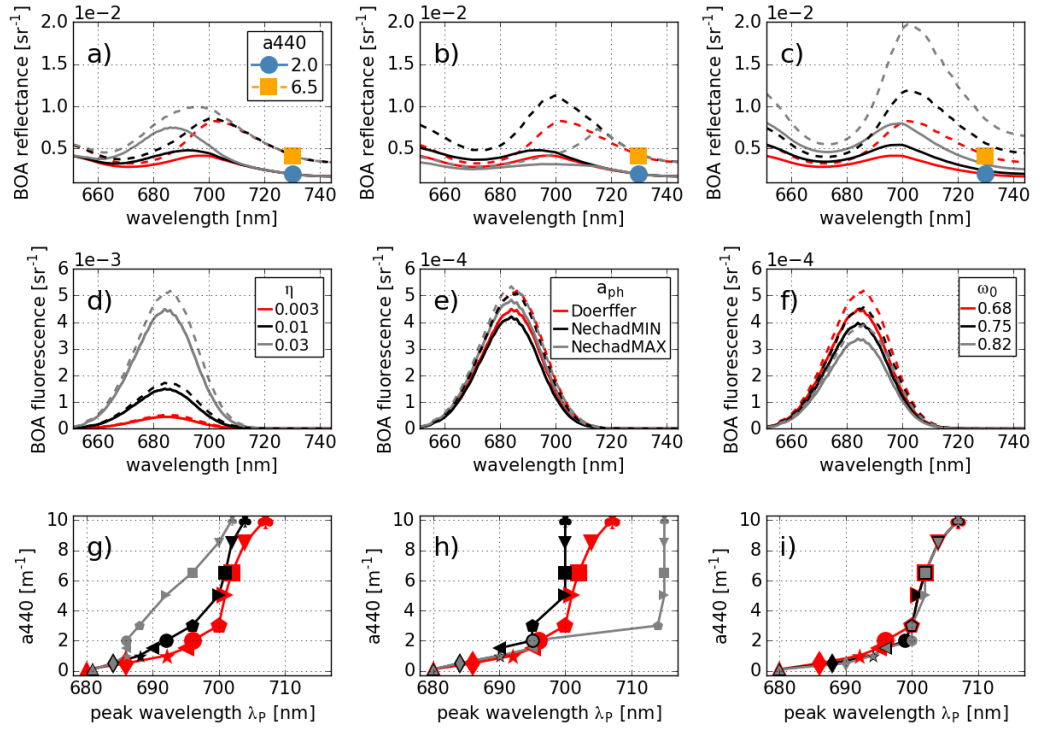


Figure 4.5: Variation of phytoplankton IOPs in MOMO for two phytoplankton amounts (a_{440} : 2.0 m^{-1} and 6.5 m^{-1} with solid lines/blue bullet and dashed lines/orange square). The line colours correspond to the legends in the second row per column. The rows show BOA reflectance R , fluorescence F , and the redshift, respectively, above water. The columns show variations of η , a_{ph} , and ω_0 (grey and black lines). Red lines refer to reference simulation using bold parameter values from table 4.1.

spectrum (fig. 4.5c) but hardly spectrally shift features (fig. 4.5i). The fluorescence portion decreases for increasing ω_0 due to less available photons that can be absorbed (fig. 4.5f).

Thus, the phytoplankton reflectance peak is constrained by phytoplankton amount controlling chlorophyll-a concentration and absorption, phytoplankton scattering, and the fluorescence. Phytoplankton scattering and chlorophyll-a fluorescence contribute to the peak's magnitude whereas chlorophyll-a absorption reduces reflectance and is important for the fluorescence portion. The redshift mainly occurs due to increased chlorophyll-a absorption- Increased fluorescence due to an increased efficiency factor antagonizes by a "blue shift". Phytoplankton scattering mainly controls the effective size of

the peak. Therefore, the effective peak conglomerates a bunch of information combining chlorophyll-a absorption, phytoplankton scattering, and fluorescence efficiency. They are dependent on phytoplankton species, health, and concentration.

2.2.3 Depth dependency and water layer thickness

In this section layer dependent characteristics for an homogeneous water body are analysed:

- i) decay of excitation and fluorescence with depth,
- ii) geometric layer thickness, and
- iii) signal response of phytoplankton in deeper layers covered with clear water.

i) Figure 4.6 displays correspondence between water depth, chlorophyll-a excitation, and fluorescence expressed with FA (eq. (4.4)) from simulations with implemented fluorescence (peak simulations). Fluorescence and excitation decrease with depths as expected (figs. 4.6a and 4.6b) due to less available light in deeper layers. They both decrease exponentially according to Beer's Law of light extinction. However, both excitation and fluorescence decrease faster with depth for higher a_{440} . Below a few decimetres (approx. 50 cm), excitation for high a_{440} is a magnitude lower than for low a_{440} (fig. 4.6a) due to high total absorption of chlorophyll-a and water. Similar conditions can be found for FA in fig. 4.6b, which hardly may be detectable below 3 m (fig. 4.6b) according to the maximum light penetration depth of 3 m for clear water in the red visible spectrum (Gordon and McCluney, 1975). Apart from phytoplankton amount, similar excitation constrain similar fluorescence portions (fig. 4.6c). The difference between FA s of a_{440} of 2.0 m (blue) and 6.5 m (orange) in fig. 4.6c occurs due to slightly higher excitation induced by higher a_{440} in the excitation calculation (chapter 2 section 1.1.2).

ii) Due to maximum water penetration depth of a few meters in the red visible spectrum, high sensitivity of excitation on layer position and MOMO computations starting at the centre of each layer, simulations for fluorescence must include vertically high resolved water layers at least in the upper 5 m. Using thicker layers, e.g. a layer thickness of 1 m, leads to an underestimation of reflectance and fluorescence constrained by an underestimated excitation due to strong absorption per layer reducing available light. Figure 4.7 shows a relative error of about 2% for the VIS comparing reflectance simulations above water with geometrically thick (1 m) and thin (0.1 m) layers. In the fluorescence domain the error approaches more than 15% and cannot be neglected.

iii) In order to analyse the signal from deep layered phytoplankton, a homogeneous water body containing phytoplankton and $cdom$ is assumed as outlined in section 2.1.

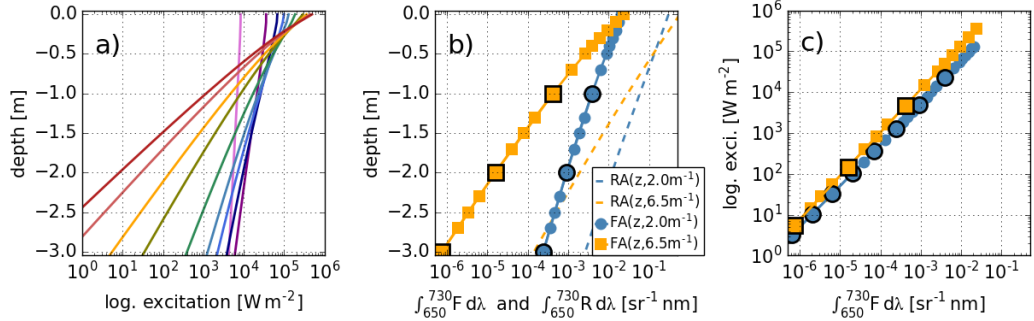


Figure 4.6: Excitation and FA from eq. (4.4) dependent on depth in a) and b), respectively, and dependent on each other in c) for the upper 3 m. Panel a) represents the excitation decay with depth for all modelled phytoplankton concentrations a_{440} (cf. table 4.1 and fig. 4.1b). Panels b) and c) show the decay of FA with depth and excitation for 2.0 m^{-1} and 6.5 m^{-1} (blue and orange) exemplarily. Black outlined symbols indicate the depth in intervals of 1 m.

Then, phytoplankton is lowered to deeper layers preserving the original phytoplankton extinction coefficient which results in a homogeneous water body with phytoplankton and $cdom$ covered with clear water. The start of the phytoplankton concentration is simulated at 0.0 m, 0.5 m, 1.0 m, 2.0 m, 3.0 m and 4.0 m depth (fig. 4.8) and simulations beginning at 0 m (yellow) equal original reference simulation (black) referring to table 4.1 without clear water cover layer. Figure 4.8 shows water-leaving reflectance (directly above water surface) which strongly decreases if phytoplankton is not located at top of the water body. For a_{440} of 1.0 m^{-1} and 2.0 m^{-1} , reflectance near 683 nm approximately halves (figs. 4.8a and 4.8b) and for 6.5 m^{-1} reflectance reduces to a third (fig. 4.8c) when the same amount of phytoplankton in the water body is covered by 1 m clear water. The effect is also observed for fluorescence: The higher the phytoplankton amount the stronger reduces the reflectance peak for deeper layered phytoplankton (figs. 4.8d to 4.8f). The fluorescence is hardly detectable for phytoplankton located lower than 2 m and the phytoplankton peak is also nearly unapparent.

On the one hand, fig. 4.9a shows that a maximum peak reflectance is not found for phytoplankton located lower than 2 m (no purple and blue lines apparent). On the other hand, lowering phytoplankton to deeper layers causes a blueshift of several nanometres which additionally complicates the discrimination with respect to phytoplankton amount or depth. The contribution of fluorescence to the phytoplankton peak also strongly decreases and is stronger for higher phytoplankton amount (fig. 4.9b). The blueshift might be attributed to water absorption and the fluorescence fraction reduction due to both

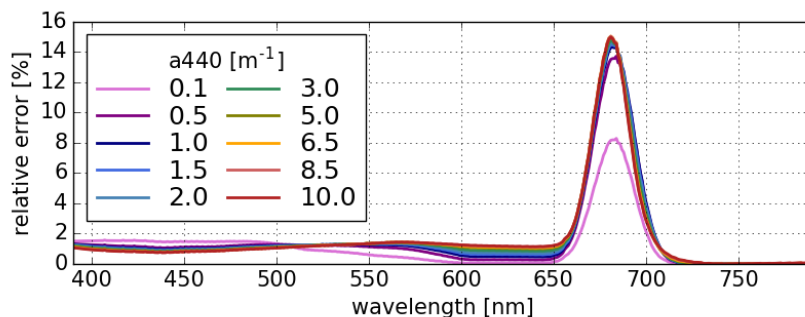


Figure 4.7: Relative error using 1 m-layers in reflectance simulations instead of geometrically thinner layers of 0.1 m. The effect mainly impacts the fluorescence domain and is about 15% for optically medium to thick waters.

water and chlorophyll-a absorption. Both processes highly reduce the water-leaving signal in the fluorescence domain which cannot be increased by phytoplankton scattering because it might be too deep in the water. Comparing reflectance areas RA (eq. (4.3)) from reference simulations without clear water cover and simulations with lowered phytoplankton by 1 m, RA reduces by 35% to 58% for considered phytoplankton amounts of 1.0 m^{-1} to 6.5 m^{-1} (salmon line in fig. 4.9c). Again, reflectance spectra corresponding to higher chlorophyll-a concentration are more depleted which might be attributed to the phytoplankton absorption. Therefore, using the fluorescence domain from 630 nm to 750 nm phytoplankton observations using the phytoplankton peak might only be possible if phytoplankton is located in the upper two meters. According to fig. 4.6b, which presents the depth dependency of FA and RA for homogeneous distributed phytoplankton in the entire water body, the reflectance peak for higher chlorophyll-a amount ($a_{440}=6.5\text{ m}^{-1}$; dashed orange line) is lower than for lower chlorophyll-a concentrations (blue dashed line) below a depth of approximately 60 cm. In conclusion, the detection of phytoplankton might only be possible if algae is apparent in the upper 2 m according to fig. 4.9 and a proper discrimination of phytoplankton amount only in the upper 1 m according to fig. 4.6b.

2.3 Initial validation efforts

The modelled phytoplankton peak varies in shape, magnitude and spectral location. Phytoplankton and additional water constituents have nonlinear influence on total reflectance which makes it difficult to compare simulation and measurements due to unknown constituents measurements or various possible constituents' parameterization.

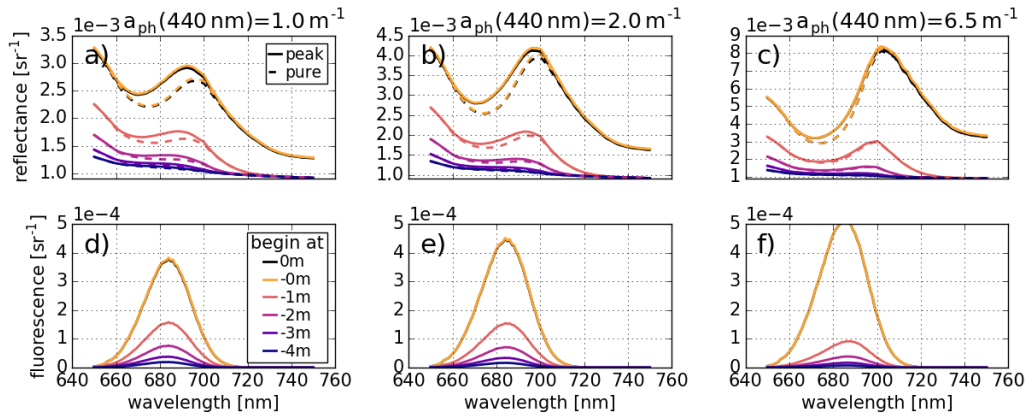


Figure 4.8: Reduction of reflectance (first row) and fluorescence (second row) for phytoplankton located below 0 m to 4 m depth (colours) and covered with clear water for three phytoplankton amounts (columns; a_{440} : 1.0 m^{-1} , 2.0 m^{-1} and 6.5 m^{-1}). Black lines refer to reference simulation of a homogeneous water body after section 2.1. In the top row, solid lines refer to simulations with fluorescence (peak) and dashed lines show reflectance without fluorescence (pure).

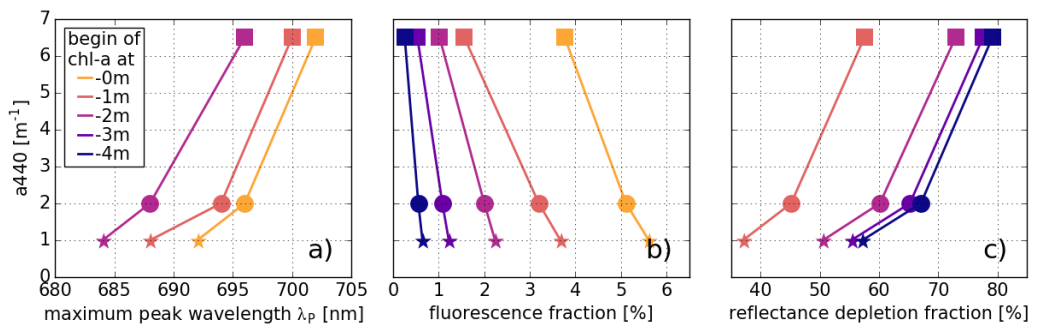


Figure 4.9: Panel a) shows the maximum peak wavelength (redshift) for phytoplankton covered by clear water and phytoplankton located deeper than 2 m do not exhibit a reflectance peak. The fraction of fluorescence reduces with lower located phytoplankton (panel b) and hardly contributes to the peak if algae are located lower than 2 m. The reflectance peak reduces strongly if a clear water layer above phytoplankton exceeds 1 m shown in panel c).

2.3.1 Measurement dataset

For first validation efforts in this section and in section 5, datasets collected by Nechad et al. (2015) are used. The entire data set from Nechad et al. (2015) contains a wide range of measurement sites but many only provide multi-spectral measurements not covering the fluorescence domain. Additionally, some sites provide either biogeochemical quantities or reflectance or they are measured at different dates. Therefore, hyper-spectral and chlorophyll-a concentration measurements from the North Sea (NoS) and Indonesian Waters (InW) are used. Besides various IOPs and apparent optical properties (AOPs), each set contains spectral phytoplankton absorption coefficients $a_{ph}(\lambda)$ and reflectance. In the following, the BOA phytoplankton peak in the range from 650 nm to 730 nm is qualitatively compared to *in situ* hyper-spectral reflectance in NoS and InW.

2.3.2 Qualitative comparison

In general, reference MOMO spectra (based on bold parameters in table 4.1) are rather dark and even simulations with additional white scatterers ($b = 10 \text{ m}^{-1}$) only slightly brightens the reflectance. Simulations for phytoplankton in deeper layers are even darker (cf. section 2.2.3). However, the simulated phytoplankton peak is located in a series of measurements shown in fig. 4.10a for Indonesian waters (InW) and fig. 4.10b for North Sea (NoS) and fits the magnitude of some measurements. Figures 4.10c and 4.10d show MOMO BOA reference reflectance (coloured) and *in situ* measurement reflectance (grey) with a correlation greater than 0.95, which apply to simulations with low to medium a_{440} up to 1.5 m^{-1} . “Brightening” simulation spectra with an increase of white scatterers, the number of matching measurement spectra due to correlation increases but still refer only to the lowest a_{440} simulations.

According to Fischer and Kronfeld (1990), applying *FLH* with a baseline constrained at 645 nm and 670 nm and signal wavelength at 685 nm, the MOMO BOA radiance peak height ranges from $10^{-4} \text{ W m}^{-2} \text{ sr nm}$ to $2.8 \cdot 10^{-3} \text{ W m}^{-2} \text{ sr nm}$ for a_{440} of 0.1 m^{-1} to 10.1 m^{-1} . Fischer and Kronfeld (1990) reported an *FLH* up to $1.2 \cdot 10^{-3} \text{ W m}^{-2} \text{ sr nm}$ for 100 mg m^{-3} . Gilerson et al. (2007) retrieved similar results with a function relating *chl-a* to fluorescence and HydroLight simulations for coastal waters. Gitelson (1992) reported redshifts of the peak that strongly vary in the relation to *chl-a*. The redshift ranges from 684 nm to 715 nm for *chl-a* up to 100 mg m^{-3} which fits MOMO redshift excellently (see figs. 4.5g to 4.5i). Gilerson et al. (2007) and Schalles (2006) reported similar results.

It is difficult to split pure fluorescence from reflectance measurements which is interactively produced by a combination of phytoplankton absorption and scattering and the process of fluorescence as outlined in previous sections. Simulating reflectance and fluor-

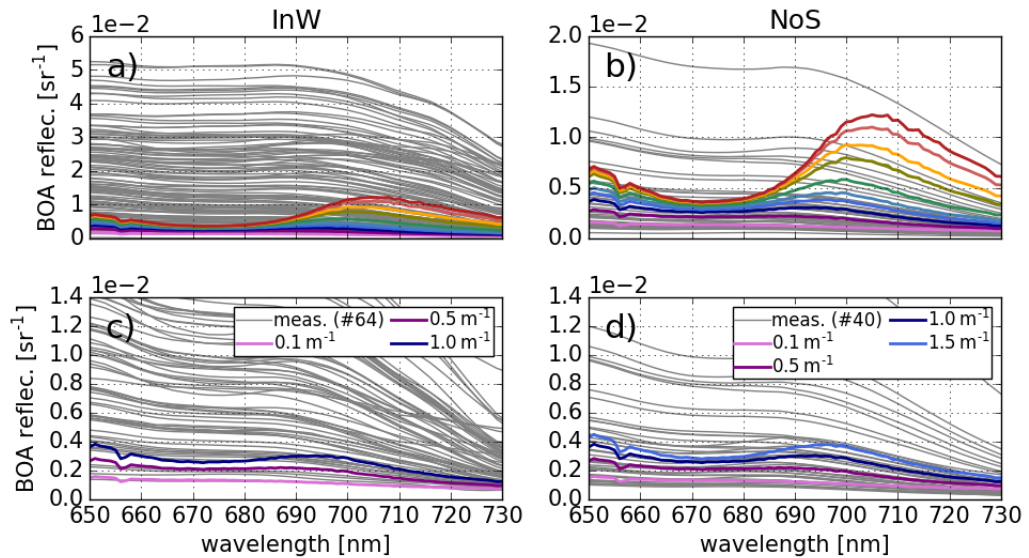


Figure 4.10: Validation of the MOMO phytoplankton peak comparing in situ measurements at Indonesian waters (InW) in a) and c) and at the North Sea (NoS) in b) and d) in grey. The coloured lines are simulations for different phytoplankton amounts. The panels c) and d) show measurements and simulations that exhibit correlation coefficients greater than 0.95 which applies to simulations for low to medium a440.

escence with MOMO, the “pure” fluorescence signal is easily retrieved from eq. (4.2). Wang et al. (2017) presented fluorescence signals retrieved from a polarization measurement technique and obtained signals near 683 nm in units of radiance ($\text{W m}^{-2} \text{sr nm}$). Their fluorescence measurement ranged from around $10^{-5} \text{W m}^{-2} \text{sr nm}$ to $10^{-4} \text{W m}^{-2} \text{sr nm}$ for *chl-a* from 7mg m^{-3} to 225mg m^{-3} displayed in fig. 2.8b of chapter 2. MOMO reflectance fluorescence magnitude displayed in figs. 4.3d and 4.5d to 4.5f and MOMO fluorescence in radiance units (not shown) range in the same magnitude from $5 \cdot 10^{-5} \text{sr}^{-1}$ to $5 \cdot 10^{-4} \text{sr}^{-1}$ and $5 \cdot 10^{-5} \text{W m}^{-2} \text{sr nm}$ to $5 \cdot 10^{-4} \text{W m}^{-2} \text{sr nm}$.

In conclusion, MOMO reveals strong extinction coefficients simulating relatively dark reflectance spectra. The simulated phytoplankton peak near 690 nm is strongly dependent on phytoplankton scattering and exhibits a magnitude as expected from literature. Magnitude and position of the peak related to fluorescence and the fluorescence portion are also in accordance to literature. Applying hyper-spectral *in situ* measurements with extreme phytoplankton amounts would likely match simulations for high algae content.

3 Methodology

3.1 Total Algae Peak

In order to obtain phytoplankton properties, reflectance in the fluorescence domain from 650 nm to 730 nm is used. Reflectance offsets, e.g. by non-algal scattering, can be reduced by using reflectance residuals. Accounting for the local chlorophyll-a absorption maximum, the reflectance minimum near 670 nm $R(\lambda_1)$ at λ_1 within 665 nm to 680 nm is selected (see eq. (4.5)). The phytoplankton peak's magnitude, shape, and location is considered by integrating residual reflectance within the integration limits λ_1 and λ_2 . The lower integration limit λ_1 hardly spectrally shifts for increasing chlorophyll-a concentration and λ_2 is defined by the equality of $R(\lambda_1)$ equals $R(\lambda_2)$ (eq. (4.6)). In eq. (4.7), the integrated reflectance area is defined as TAP (shaded area in fig. 4.11).

$$(4.5) \quad \lambda_1 = \operatorname{argmin} \{R(\lambda)\} \quad \text{with } \lambda = [665, 680] \text{ nm}$$

$$(4.6) \quad \lambda_2 = \operatorname{argmin} \{\operatorname{abs}[R(\lambda) - R(\lambda_1)]\} \quad \text{with } \lambda \geq 680 \text{ nm}$$

$$(4.7) \quad TAP = \int_{\lambda_1}^{\lambda_2} [R(\lambda) - R(\lambda_1)] d\lambda$$

Baseline slopes of baseline retrievals such as *FLH* highly depend on the peak's shape and the surrounding spectrum leading to high variability in the difference between signal wavelength and baseline. The TAP baseline, indicated with LW in fig. 4.11, is computed without slope (eqs. (4.5) and (4.6)) and is only dependent on one free parameter λ_1 and the baseline's spectral length highly varies. Thus, TAP accounts for changing spectral shape and size of the peak for various phytoplankton amounts. However, TAP is not solely correlated to fluorescence but also to phytoplankton scattering and chlorophyll-a absorption as outlined in section 1.2.

Additionally, using interpolation on given simulated wavelengths or sensor bands, i) the accuracy of λ_2 and also TAP is increased, and ii) the number of sensor channels becomes less important.

3.2 *TAPIR* functions

As outlined in section 1.2, the phytoplankton peak in the fluorescence domain is produced by phytoplankton scattering and fluorescence and reduced by chlorophyll-a absorption and water absorption. Therefore, the spectrally integrated peak TAP contains information about those properties which are related to phytoplankton amount. Additionally,

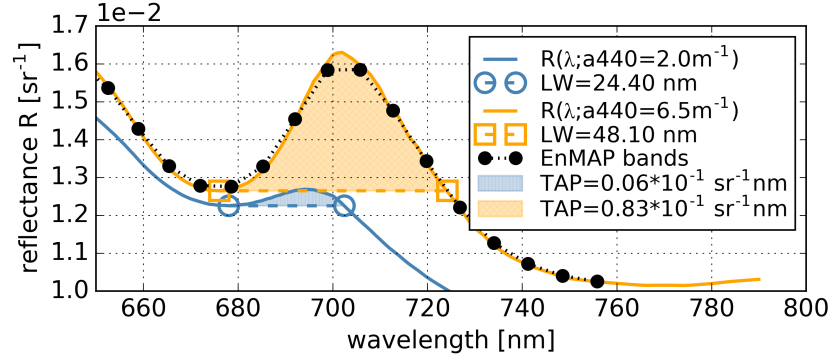


Figure 4.11: TAP for two simulated TOA reflectance spectra. The spectral width of the baselines highly differs but λ_1 hardly deviates from 678 nm.

the chlorophyll-a absorption at 670 nm directly influences the peak and is also related to fluorescence and phytoplankton magnitude which has been introduced in section 1.3. Thus, combining both variables, TAP and $a670$, a retrieval is developed to obtain phytoplankton properties from TOA reflectance measurements in the fluorescence domain:

$$(4.8) \quad TAPIR : \quad f(TAP, a670) = c_0(TAP) * a670^{c_1(TAP)} = TAP$$

The coefficients $c_{1,2}$ are dependent on sensor or model (e.g. MOMO simulations or EnMAP) retrieved reflectance peak areas ($TAPs$). Using TOA MOMO simulations from section 2.1, retrieved $TAPs$ are linked with corresponding $a670$ and reference results are shown as solid lines in fig. 4.12. Variations of TAP due to varied parameters p (table 4.1) are illustrated with dashed lines. Symbols correspond to model input $a440$. According to eq. (4.8), a power function expresses reference $TAPs$ of TOA reflectance $R = L_u/E_d$ with corresponding $a670$.

$$(4.9) \quad TAPIR_{ref}^{TOA} : \quad TAP(a670) = 0.0100 * a670^{1.6619} := f_{ref}(a670).$$

The reference $TAPIR$ function f_{ref} increases linearly for increasing $a670$ up to $0.2 \text{ sr}^{-1} \text{ nm}$ in fig. 4.12 and for low $a670$ it is non-linear or zero. Further $TAPIR$ functions and their uncertainties are described in section 4.3. Although, following sections use $TAPIR$ for TOA applications, the concept can also be applied to air-borne or *in situ* measurements.

4 Algorithm sensitivity and uncertainty

4.1 Sensitivity analysis

In order to estimate the sensitivity of *TAPIR*, fig. 4.13 shows deviations of f_{ref} with variation of parameters. Jacobians $J_p = J_{ij}(p)$ are calculated for *TAPIR* functions f_i with varied parameters p_j with eq. (4.10).

$$(4.10) \quad J_{ij} = \frac{\partial f_i(a670; p_j)}{\partial p_j} \approx \frac{f_{\text{ref}}(a670; p_{j,\text{ref}}) - f_i(a670; p_{j,\text{var}})}{p_{j,\text{ref}} - p_{j,\text{var}}}$$

Δp for parameter a_{ph} is computed with maximum absorption at 670 nm from normalized absorption spectra (fig. 4.2a). Demonstrating the impact of reduced bands, a measurement location, and standard atmospheres, $\Delta p = 1$ applies for EnMAP, BOA, and *atm*. Jacobians are non-zero for $i = j$ and absolute Jacobians generally increase with increasing phytoplankton amount. *TAPIR* is more sensitive to all of the considered parameters for higher $a670$. The sensitivity analysis is grouped in four parts accounting for

- i) water conditions,
- ii) atmosphere conditions,
- iii) phytoplankton parameterization, and
- iv) external conditions.

i) In this study, water conditions vary with considered parameters $cdom$, white scatterer b , surface temperature T and salinity s (figs. 4.12a to 4.12d). In contrast to the blue-green ratio proxy estimating $chl-a$, the spectral range of fluorescence is nearly invariant to $cdom$ absorption (cf. section 2.3.3) and, therefore, negligible dependence on *TAPs* is expected. In-water parameters have minor impact on *TAPIR* due to Jacobians less than two orders of magnitude compared to reference *TAPs* (figs. 4.13a to 4.13d). *TAPs* are hardly sensitive to $cdom$ with Jacobians less than three orders of magnitude. However, the impact of $cdom$ is less than the influence of scatterer b even for high $cdom$ absorption at 440 nm of 3 m^{-1} . “White” scatterers (e.g. sediments) brightens the total visible reflectance spectrum and, therefore, slightly enlarge the peak due to higher available fluorescence excitation and increased total scattering. An influence of salinity and surface temperature can be neglected. Thus, *TAPIR* is applicable for all kind of waters including case-1 and case-2, coastal and inland waters, and regions with high or low sea surface temperature.

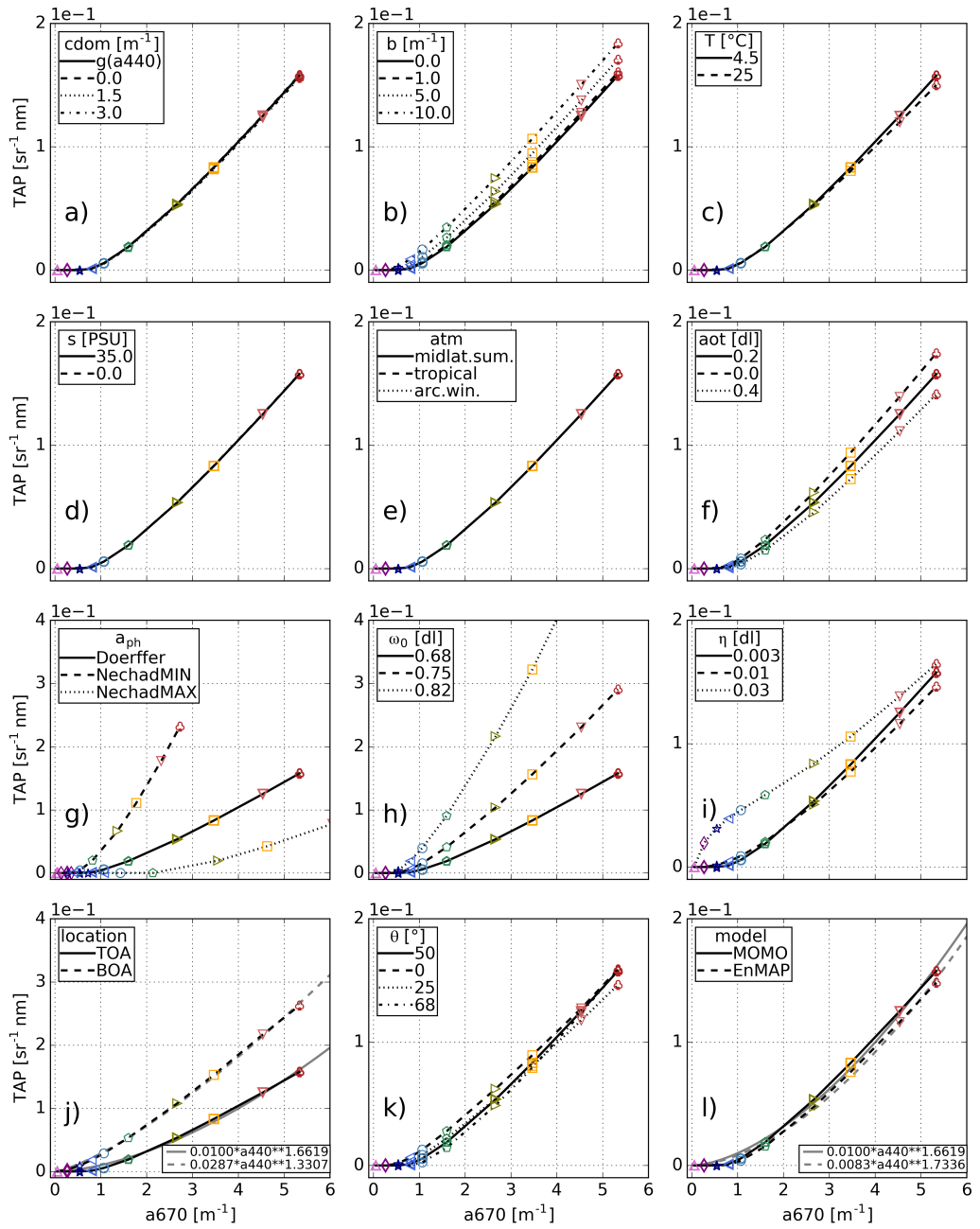


Figure 4.12: Retrieved TAPs over a_{670} and their variants due to adjusted simulation parameters (table 4.1). Solid lines show TAPIR functions computed from eq. (4.13) linking TAPs from reference simulations to a_{670} .

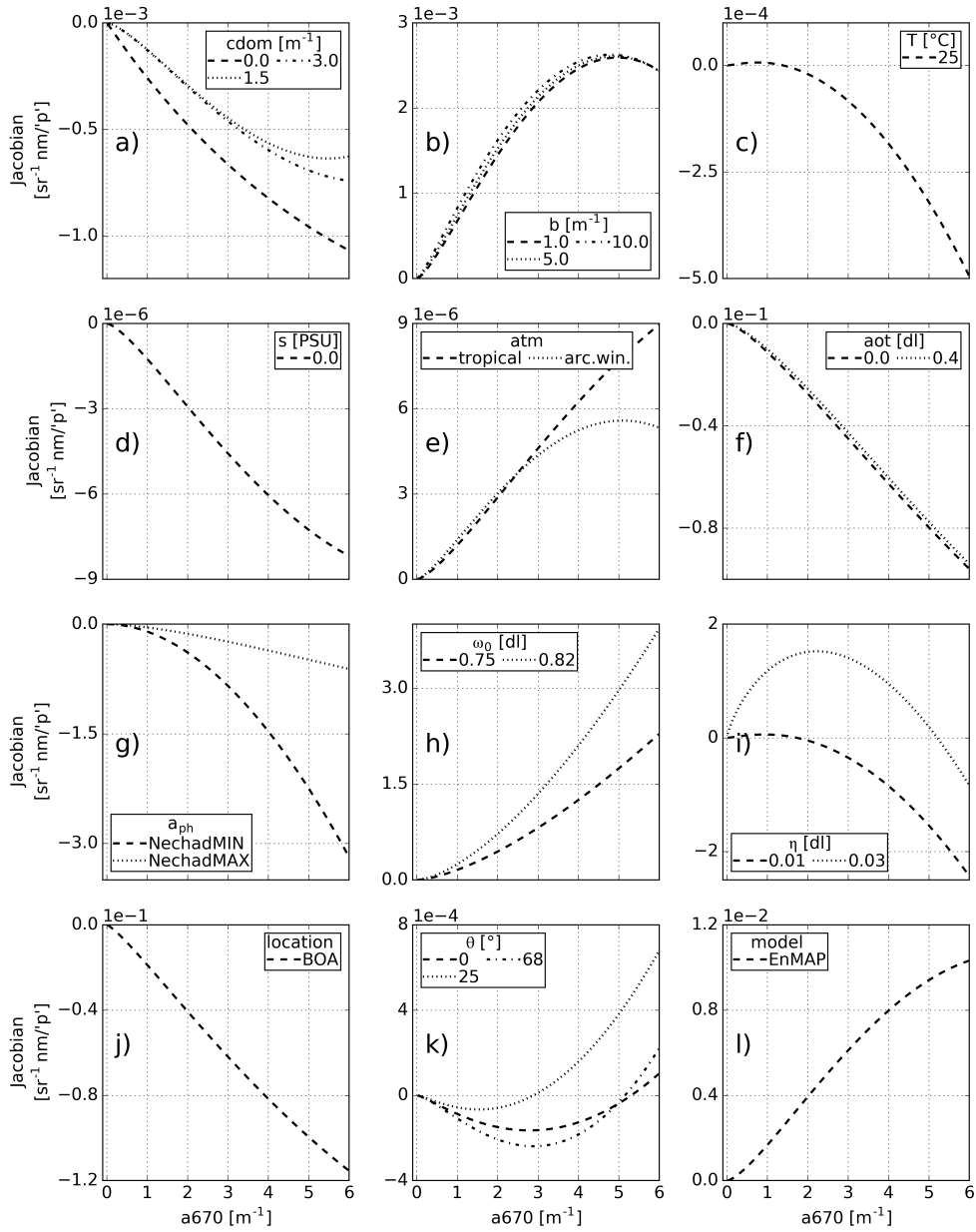


Figure 4.13: Jacobians of reference TAPIR function f_{ref} (eqs. (4.9) and (4.10)) calculated from simulations with reference parameters emphasized in table 4.1. Note different ordinate scales and magnitudes representing sensitivity.

ii) Figures 4.12e and 4.12f display the impact of varying standard atmosphere conditions atm and aerosol optical thickness aot . A change in atmospheric vertical temperature and pressure distribution results in low sensitivity on atmosphere structure with Jacobians below 10^{-5} (fig. 4.13e). In fig. 4.13f, increasing aot diminishes $TAPs$ linearly with increasing $a670$ due to less available light for the fluorescence process and absorption of the upwelling signal in the atmosphere. The sensitivity on aot ranges in reference $TAPIR$ function magnitudes and, therefore, aot must be considered in the retrieval.

iii) MOMO parameterizes phytoplankton using a given normalized phytoplankton absorption spectrum scaled with spectral extinction coefficients and corresponding single scattering albedo (see section 2). Figure 4.2 illustrates variations of chlorophyll-a absorption spectra $a_{ph}(\lambda)$ normalized at 440 nm and corresponding single scattering albedo ω_0 for constant values of 0.68, 0.75 and 0.82 at 440 nm. In this study, varying ω_0 solely changes the ratio of phytoplankton scattering and absorption. The current absorption coefficient remains equal whereas phytoplankton scattering coefficient increases or decreases, respectively. Thus, increasing ω_0 induces increased extinction. $TAPIR$ is strongly sensitive to the underlying absorption spectrum (figs. 4.2a, 4.12g and 4.13g). The lower the absorption spectrum beyond 550 nm the faster rises the $TAPIR$ function slope with increasing $a440$ due to increased scattering (fig. 4.2b). An increase of phytoplankton scattering due to either reduced absorption spectrum or increased single scattering albedo (e.g. NechadMIN and $\omega_0=0.75$, respectively), can double retrieved $TAPs$ for high $a670$ (figs. 4.12g and 4.12h). Strong phytoplankton scattering ($\omega_0=0.82$) increases $TAPs$ by more than factor 3 (figs. 4.12h and 4.13h). Accounting for fluorescence efficiency η , figs. 4.12j and 4.13j reveal strong impact on retrieved $TAPs$ mainly depends on competitive impact of effective fluorescence peak shifting towards shorter wavelength for increasing η and increasing redshift for increasing chlorophyll-a concentrations $a670$. Therefore, the major $TAPIR$ sensitivity originates from phytoplankton IOPs and bio-physical condition.

iv) Measurement location (TOA or bottom of the atmosphere (BOA)), sun zenith angle (θ), and number of available sensor bands are external conditions which can be considered previously to the definition of $TAPIR$ functions. Functions for BOA and TOA in fig. 4.12j highly differ due to Rayleigh scattering and atmospheric interaction. A changing θ slightly influences the $TAPIR$ function slope (fig. 4.12k) but due to small Jacobians in fig. 4.13k the impact of θ can be assumed to play a minor role. For EnMAP applications, 1 nm-resolved MOMO simulations are convolved to 15 EnMAP bands within 650 nm to 750 nm (fig. 4.11). Reduction to lower band resolution reduces $TAPs$ with increasing $a670$ because MOMO reflectance area is not entirely reproduced (figs. 4.11 and 4.12l). However, the sensitivity on reduced band number for EnMAP specifications

ranges below two orders of magnitude of reference *TAPs*. Uncertainties concerning location, radiometric resolution (EnMAP), or sun zenith angle can be avoided by developing separate *TAPIR* functions.

In conclusion, *TAPIR* is mainly sensitive to *a670* and phytoplankton optical properties (single scattering albedo, underlying absorption spectrum, and efficiency), which suggests the opportunity of distinguishing different phytoplankton species. Application of various phytoplankton type dependent absorption spectra may result in variants in *TAPIR* due to slightly shifted absorption maxima and intensities. *Aot* influence cannot be neglected due similar magnitudes of the *TAPIR* function and corresponding Jacobians.

4.2 Uncertainty assessment

TAPIR supports the estimation of phytoplankton property proxy *a670*. Thus, the reference TOA *TAPIR* function from eq. (4.8) is inverted to f^{-1} and an uncertainty propagation for *a670* is conducted. Assuming uncorrelated variables, eq. (4.11) computes uncertainty σ_a . The deviation of f^{-1} depends on $i = 3$ variables x : Fitting coefficients c_0 and c_1 and *TAP* per *a670*.

$$(4.11) \quad \sigma_a^2 = \sum \left(\frac{\partial f^{-1}(x_i)}{\partial x_i} \sigma_{x_i} \right)^2$$

Equation (4.11) determines $\partial_x f^{-1}(x)$ analytically. Fitting simulated TOA *TAPs* to input *a670* in section 4.1, coefficients c_0 and c_1 are empirically retrieved and simultaneously standard deviations σ_{c_0} and σ_{c_1} are obtained and listed in table 4.2.

Uncertainty σ_a additionally depends on accuracy of *TAP* computation with eq. (4.7). *TAP* deviates with varied parameters from table 4.1 and the selection of integration limits λ_1 and λ_2 . Parameters θ , number of measurement bands (e.g. EnMAP), and measurement location (e.g. surface (BOA)) are excluded because they can be considered previously to *TAPIR* function development. *TAP* uncertainty σ_{TAP} for j parameters p is computed with eq. (4.12) .

$$(4.12) \quad \sigma_{TAP}^2 = \sum \left(\frac{\partial TAP(p_j)}{\partial p_j} \sigma_{p_j} \right)^2 \approx \sum \left(\frac{\Delta TAP(p_j)}{\Delta p_j} \sigma_{p_j} \right)^2$$

Summands of eq. (4.12) $\partial_{p_j} TAP$ are numerically estimated. Therefore, the difference between $TAP(p_{j,ref})$ and $TAP(p_{j,var})$ is calculated to retrieve the $\Delta TAP(p_j)$. The values of reference and variants of parameters, p_{ref} and p_{var} , are listed in table 4.3. Reference value for *cdom* is dependent on *a440* with $g(a440)$ (see eq. (2.22) on pp. 39 and 87).

Table 4.2: List of variables x and their σ_x used in uncertainty calculation in eq. (4.11). Exemplarily, the table presents summands of eq. (4.11) $[(\text{m}^{-1})^2]$ for medium (\circ) and high (\square) a_{670} of 1.07 m^{-1} and 3.47 m^{-1} (corresponding to 2.0 m^{-1} and 6.5 m^{-1} a_{440} in MOMO). σ_{TAP} depends on a_{670} . The variables c_0 and c_1 exhibit the units $[\text{sr}^{-1} \text{ nm m}]$ and $[d]$, respectively.

x	σ_x	$[\partial_x f^{-1}(x(\circ))\sigma_x]^2$	$[\partial_x f^{-1}(x(\square))\sigma_x]^2$
c_0	$1.150 \cdot 10^{-3}$	$7.424 \cdot 10^{-2}$	$2.408 \cdot 10^{-1}$
c_1	$7.499 \cdot 10^{-2}$	$3.267 \cdot 10^{-3}$	$1.948 \cdot 10^{-1}$
TAP	$5.765 \cdot 10^{-3}$	$3.325 \cdot 10^{-1}$	—
TAP	$3.799 \cdot 10^{-2}$	—	1.006

Table 4.3: List of parameters p used in the uncertainty estimation in eq. (4.12). The deviation's denominator Δp is computed with p_{var} and p_{ref} and use a reasonable conservative σ_p from literature (column "ref.") or assume it. Table 4.1 lists their units. Exemplarily, the table presents summands of eq. (4.12) $[(\text{sr}^{-1} \text{ nm})^2]$ per parameter for medium (\circ) and high (\square) a_{670} of 1.07 m^{-1} and 3.47 m^{-1} (corresponding to 2.0 m^{-1} and 6.5 m^{-1} a_{440} in MOMO). σ_{atm} is set to 1 because parameter atm contains vertical atmospheric profiles. Values of p_{ref} and p_{var} for parameter a_{ph} are 670 nm coefficients of normalized absorption spectra "Doerfer" and "NechadMIN". Parameters λ_1 and λ_2 depend on selected reflectance spectra and vary with a_{670} . The deviation is estimated by small variations of $\pm 1 \text{ nm}$ and assume σ_λ of 1 nm.

p	p_{ref}	p_{var}	σ_p	ref.	$\sigma_{\text{TAP}}^2(\circ)$	$\sigma_{\text{TAP}}^2(\square)$
c_{dom}	$g(a_{440})$	0.000	0.050	[4.3a]	$1.879 \cdot 10^{-10}$	$1.376 \cdot 10^{-9}$
b	0.000	1.000	0.150	[4.3b]	$1.198 \cdot 10^{-8}$	$1.174 \cdot 10^{-7}$
T	4.500	25.000	1.500	[4.3c]	$6.209 \cdot 10^{-11}$	$3.558 \cdot 10^{-8}$
s	35.000	0.000	0.002	[4.3d]	$7.360 \cdot 10^{-18}$	$1.119 \cdot 10^{-16}$
atm	midlat	arcwin	1.000	—	$1.703 \cdot 10^{-12}$	$2.904 \cdot 10^{-11}$
aot	0.200	0.000	0.070	[4.3e]	$7.353 \cdot 10^{-7}$	$1.393 \cdot 10^{-5}$
a_{ph}	0.533	0.273	0.020	[4.3f]	$5.320 \cdot 10^{-6}$	$4.985 \cdot 10^{-4}$
ω_0	0.680	0.750	0.050	—	$2.705 \cdot 10^{-5}$	$9.225 \cdot 10^{-4}$
η	0.003	0.010	0.005	—	$8.132 \cdot 10^{-8}$	$7.815 \cdot 10^{-6}$
λ_1	$\lambda_1(a_{440})$	$\lambda_1 \pm 1 \text{ nm}$	1.000	—	$3.522 \cdot 10^{-8}$	$4.493 \cdot 10^{-7}$
λ_2	$\lambda_2(a_{440})$	$\lambda_2 \pm 1 \text{ nm}$	1.000	—	$1.237 \cdot 10^{-9}$	$9.267 \cdot 10^{-9}$

^{4.3a} Lefering et al. (2017), ^{4.3b} Binding et al. (2005), ^{4.3c} Kennedy (2014), ^{4.3d} Le Menn (2011), ^{4.3e} Sayer et al. (2013), ^{4.3f} McKee et al. (2013),

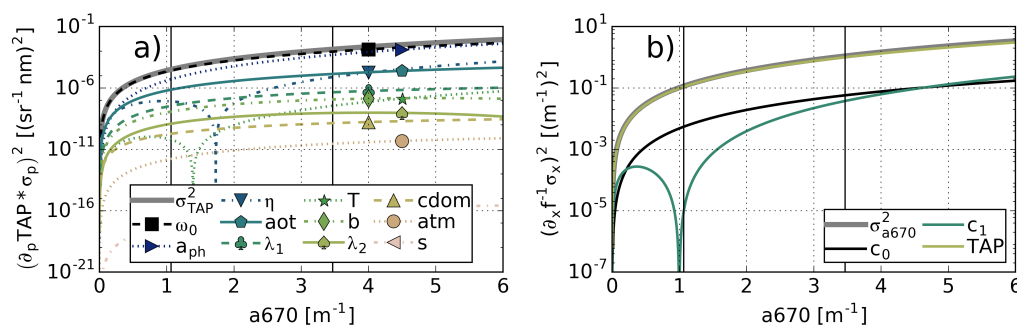


Figure 4.14: Summands of eq. (4.12) (coloured lines with markers indicate parameter) and σ_{TAP}^2 (grey line) in panel a). Panel b) shows summands of eq. (4.11) (coloured) and final σ_a^2 (grey). Squared uncertainties relate to values listed in tables 4.2 and 4.3.

a_{ph} we extract the 670 nm absorption coefficient from the normalized spectra “Doerffer” and “NechadMIN” (fig. 4.2a). The deviation Δp_j is the difference between parameter $p_{j,ref}$ and its variation $p_{j,var}$. Δp_{atm} is set to 1 because parameter atm contains vertical profiles. Parameter dependent uncertainties σ_x are conservatively chosen from literature or assumed with reasonable values (see table 4.3).

Figure 4.14a illustrates σ_{TAP}^2 summands (black lines) from eq. (4.12) which exponentially increase with increasing 670. Final σ_{TAP}^2 (thick grey line) mainly consist of uncertainties due to ω_0 . The “spikes” near 2.0 m^{-1} appear due to logarithmic presentation and local minimum close to zero, which shifts or disappears using alternative $p_{j,var}$. Analogous, fig. 4.14b shows σ_a^2 summands (black lines) from eq. (4.11) and final squared uncertainty for a_{670} (grey) which mainly consists of TAP uncertainty. Therefore, a_{670} accuracy primarily depends on phytoplankton parameterization.

Generally, σ_a^2 increases exponentially with increasing a_{670} and ranges from approximately 10^{-4} m^{-2} to 10^1 m^{-2} . a_{670} and σ_a range in the same magnitude and exemplary σ_a of 0.34 m^{-1} and 1.05 m^{-1} for a_{670} of 1.07 m^{-1} and 3.47 m^{-1} is retrieved. Absorption coefficients a_{670} greater than 0.50 m^{-1} exhibit relative uncertainties from 30 % to 35 % and less than 50 % for the entire a_{670} range from 0.02 m^{-1} to 6.00 m^{-1} .

4.3 Supplemental TAPIR functions

Functions and their uncertainties are provided for hyper-spectral sensors EnMAP, HICO on board International Space Station (ISS) and TROPOMI mounted on Sentinel-5 (S5). Additionally, a BOA function corresponding to reference simulations from table 4.1 for

the surface is shown. Afterwards, the technique is slightly extended to apply *TAPIR* to multi-spectral sensor OLCI.

$$(4.13) \quad TAPIR_{BOA} : \quad TAP(a670) = 0.0287 * a670^{1.3307} := f_{BOA}(a670)$$

$$(4.14) \quad TAPIR_{EnMAP}^{TOA} : \quad TAP(a670) = 0.0083 * a670^{1.7336} := f_{EnMAP}(a670)$$

$$(4.15) \quad TAPIR_{HICO}^{TOA} : \quad TAP(a670) = 0.0080 * a670^{1.7599} := f_{HICO}(a670)$$

$$(4.16) \quad TAPIR_{TROPOMI}^{TOA} : \quad TAP(a670) = 0.0099 * a670^{1.6642} := f_{TROPOMI}(a670).$$

The functions of TROPOMI, EnMAP and HICO are rather similar to $TAPIR_{ref}$ due to a sufficient capture of MOMO simulations with provided instrument bands (fig. 4.15a). Retrieved $a670$ uncertainty σ_a only differs slightly from $\sigma_a(MOMO)$ (fig. 4.15b) with absolute difference maxima of 0.015 m^{-1} , 0.032 m^{-1} and 0.001 m^{-1} for HICO, EnMAP, and TROPOMI, respectively. As expected, TROPOMI reveals the lowest deviation from MOMO due to high band resolution. Absolute uncertainties σ_a of all sensors for $a670$ of 1.07 nm^{-1} and 3.47 nm^{-1} are listed in table 4.4. The relative uncertainty ranges within 30 % to 35 % for all of the considered hyper-spectral sensors for $a670$ greater than 0.5 m^{-1} . For BOA applications, $a670$ uncertainty ranges from 20 % to 25 %.

Actually, *TAPIR* is designed for hyper-spectral sensors due to necessary peak capturing with sufficient measurement bands. However, pre-processing multi-spectral measurements, *TAPIR* can be used for OLCI. Multi-spectral OLCI provides only 5 bands in the red VIS/NIR (orange in fig. 4.15a and coloured dashed lines in fig. 4.16a). Compared to MOMO simulations (grey), a fitted polynomial of degree 3 (“ $OLCI_{poly}$ ”; coloured solid lines in fig. 4.16a) does not reproduce the “original” spectral shape. However, using only the relative shape of the polynomial peak, *TAPs* of $OLCI_{poly}$ and MOMO are linearly related for parameter variations from table 4.1 which is illustrated in fig. 4.16b. The Root Mean Square Error (RMSE) is rather small with $0.01 \text{ sr}^{-1} \text{ nm}$.

Using a polynomial, *TAPIR* can be applied to OLCI because a function substitutes spectrally poor resolved measurement bands. $TAP(OLCI_{poly})$ does not represent actual phytoplankton properties but can be re-calculated to $TAP(OLCI)$ using the relation

Table 4.4: *Uncertainty of supplemental sensors for $a670$ of 1.07 nm^{-1} and 3.47 nm^{-1} . All quantities in $[\text{m}^{-1}]$*

$a670$	MOMO	TROPOMI	EnMAP	HICO	OLCI
1.07	0.341	0.341	0.337	0.355	0.379
3.47	1.052	1.052	1.057	1.064	1.100

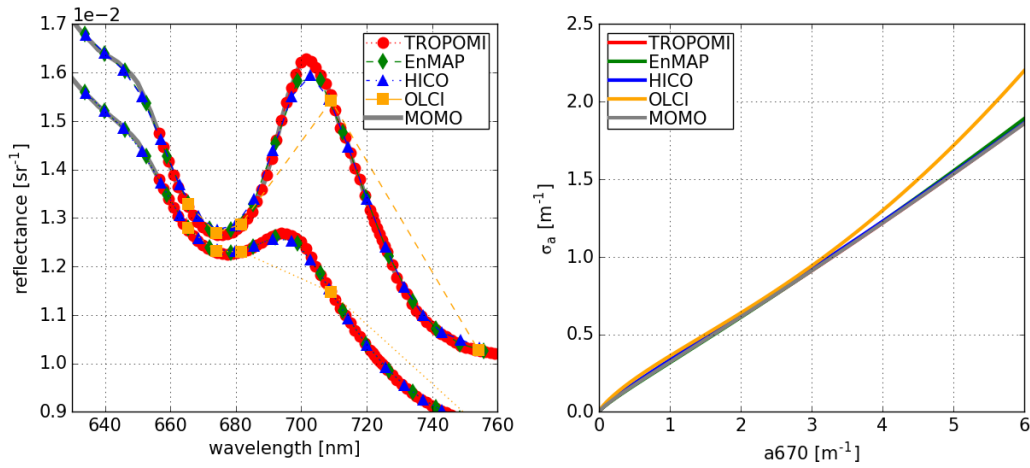


Figure 4.15: Spectral band arrangement of HICO, EnMAP, and TROPOMI which all capture the MOMO simulation rather well in panel a) for a_{440} of 2.0 nm^{-1} and 6.5 nm^{-1} , and the difference of the uncertainty σ_a compared to the one of MOMO in panel b). OLCI (orange) only provides few bands and cannot represent the hyper-spectral MOMO reflectance. However, using a polynomial, TAPIR can be applied to OLCI with reasonable uncertainty (refer to text and fig. 4.16).

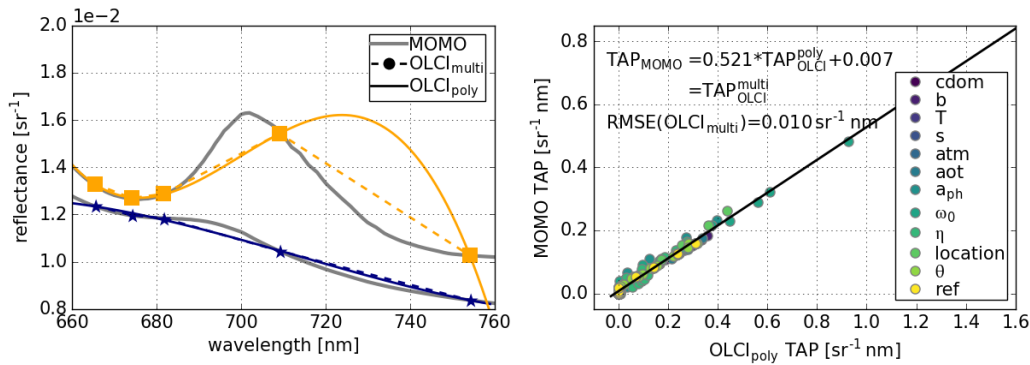


Figure 4.16: OLCI bands (dashed lines) and fitted plenum of third degree (solid) compared to MOMO reflectance simulations (grey). Although, polynomial curves based on the OLCI bands do not capture the “truth”, their TAPs are linearly related to the TAPs of MOMO.

between $TAP(OLCI_{poly})$ and $TAP(MOMO)$:

$$(4.17) \quad TAP(OLCI) := 0.5208 * TAP(OLCI_{poly}) + 0.0068$$

Fitting uncertainties are 0.0044 for c_0 and $0.0008 \text{ sr}^{-1} \text{ nm}$ for c_1 . Using recalculated TAP s of OLCI a $TAPIR$ function can be found:

$$(4.18) \quad TAPIR_{OLCI}^{TOA} : \quad TAP(a670) = 0.0071 * a670^{1.9084} := f_{OLCI}(a670)$$

OLCI uncertainties are slightly larger than retrieved σ_a for MOMO, EnMAP, HICO, and TROPOMI listed in table 4.4. Relative uncertainties of about 30 % and 35 % are promising and could be improved with phytoplankton specific parameterization in the model because phytoplankton properties majorly contribute to uncertainty. Additionally, polynomial fitting permits application of multi-spectral sensors such as OLCI, MERIS, and MODIS. The polynomial approach may also be applied to hyper-spectral sensors for consistency reasons but this may introduce additional uncertainties.

5 Initial algorithm validation efforts

This section presents early efforts for a qualitative algorithm validation and discusses possible sources of uncertainties and inaccuracies. *TAPIR* likely promises valuable results for higher *chl-a* in optically complex waters with additional OACs.

Hyper-spectral data from satellites are rare up to date. EnMAP's launch is scheduled for 2019 (Guanter et al., 2015) and first measurements from TROPOMI will be available in April 2018 (R. Lindstrot, pers. communication, 2018-02-14). In order to retrieve first preliminary insight in the performance of *TAPIR* and under the assumption that the radiative transfer model MOMO simulated TOA and BOA reflectance consistently, *TAPIR* BOA function f_{BOA} (eq. (4.13)) is applied to *in situ* data. Two measurement data sets merged from Nechad et al. (2015) already have been introduced in section 2. Due to unavailable simultaneously measured chlorophyll-a absorption and reflectance, concentration has been converted to *a670* using the BOM at 670 nm from Bricaud et al. (1995, p. 13 326; cf. eq. (2.21) in chapter 2):

$$(4.19) \quad a_{ph}(670 \text{ nm}) = 0.0189 * chl-a^{(1-0.149)} = a670$$

Retrieved *a670* range within 0.015 m^{-1} to 0.50 m^{-1} for NoS and InW. According to section 4, *a670* is expected to have relatively high uncertainties in this value regime. Nevertheless, *TAPs* are calculated for 92 InW and 48 NoS reflectance spectra and correlated to computed *a670* (fig. 4.17a). *Chl-a* and additionally provided measurements of total suspended matter (*TSM*) range within 0.8 mg m^{-3} to 47 mg m^{-3} and 0 g m^{-3} to 200 g m^{-3} , respectively.

There are 24 of 92 and 20 of 48 zero *TAPs* of InW (grey squares) and NoS (black triangles), respectively, due to an unapparent peak in reflectance spectra. Zero *TAPs* occur for *TSM* and *chl-a* measurements within 0 g m^{-3} to 50 g m^{-3} and 0.8 mg m^{-3} to 10 mg m^{-3} , respectively. A combination of low *chl-a* ($<10 \text{ mg m}^{-3}$) and the occurrence of non-phytoplankton *TSM* may result in an unapparent peak. However, there are measurements of similar conditions with an apparent peak and non-zero *TAP*.

Applying *OC4* (O'Reilly et al., 2000) in fig. 4.17b, retrieved *OC4 chl-a* match up with measured *chl-a* for less than 10 mg m^{-3} which borders the upper algorithm definition limit. *OC4 chl-a* remains stable near 10 mg m^{-3} for measured *chl-a* greater than 10 mg m^{-3} .

In fig. 4.17c, InW and NoS *TAPs* are inverted with $f_{\text{BOA}}^{-1} = a670$ to retrieve *a670* which is converted to chlorophyll-a concentration with the inverse of eq. (4.19). *Chl-a* retrieved

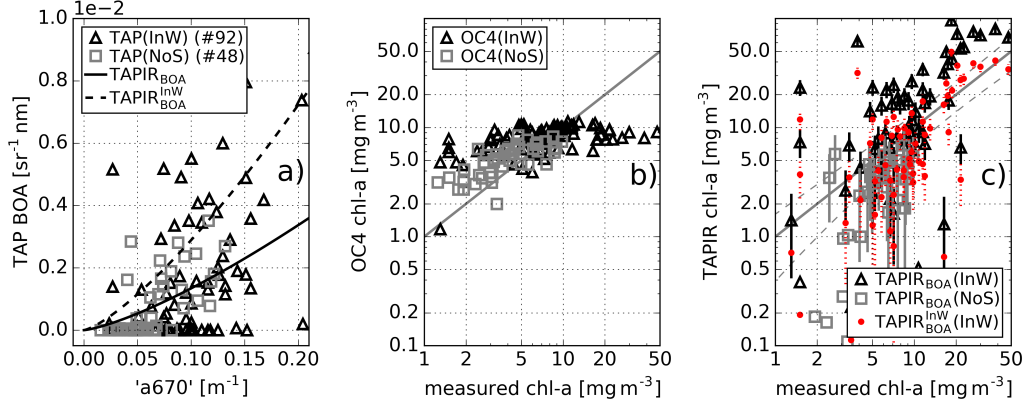


Figure 4.17: TAPs of surface measurements at North Sea (NoS) and Indonesian waters (InW) collected from Nechad et al. (2015) and functions $TAPIR_{BOA}$ and $TAPIR_{BOA}^{InW}$ (eqs. (4.13) and (4.20)) in a). Panels b) and c) show performance of OC4 and TAPIR retrievals on logarithmic scale. Vertical bars in panel c) represent calculated TAPIR chl-a uncertainties for BOA applications. Red circle markers with thin dashed error bars display chl-a(InW) estimated from empirical $TAPIR_{BOA}^{InW}$ function (dashed line in panel a) and eq. (4.20)).

from $TAPIR$ (triangles and squares with error bars in fig. 4.17c) is blurrier distributed than $OC4$ $chl-a$ for $chl-a$ measurements below 10 mg m^{-3} but still exhibits a good estimation. For larger $chl-a$, $TAPIR$ overestimates $chl-a$ with current $TAPIR_{BOA}$ from eq. (4.13) but in contrast to $OC4$, $TAPIR$ is able to reproduce higher $chl-a$ according to the 1:1 line. The maximum $a670$ for this data set is less than 0.5 m^{-1} and section 4.2 shows higher uncertainties for absorption coefficients below 0.5 m^{-1} . However, $TAPIR$ reproduces sufficient $chl-a$ estimations for the North Sea (grey squares in fig. 4.17c).

15 $TAP(InW)$ are remarkably raised compared to $TAPs$ expected from the $TAPIR_{BOA}$ function (black solid line, cf. eq. (4.13)) which eventually leads to higher $a670$ calculated from the inverse from $TAPIR$ (fig. 4.17c). A raised portion of non-phytoplankton $TSM > 70 \text{ g m}^{-3}$, a tight packaging of phytoplankton chloroplasts, and cell walls itself can cause an increased scattering (cf. sections 4.1 and 4.2) which may increase the peak magnitude. Therefore, an empirical $TAPIR$ function (eq. (4.20)) based on $TAPs$ in Indonesian Waters (dashed black line in fig. 4.17a) is developed. The slope of the function is raised compared to the BOA function.

$$(4.20) \quad TAPIR_{BOA}^{InW} : \quad TAP(a670) = 0.061 * a670^{1.324}$$

Applying the empirical $TAPIR_{BOA}^{InW}$ function from eq. (4.20), retrieved $TAPIR$ $chl-a$ (red bullets with dashed error bars) in fig. 4.17c more closely approach the 1:1 line for measured $chl-a$ greater than 10 mg m^{-3} . The deviation from measured $chl-a$ may occur due to

- i) phytoplankton parameterization,
- ii) unavailable $a670$ measurements,
- iii) chosen bio-optical model to convert $a670$ to $chl-a$,
- iv) $a670$ value regime, and
- v) $chl-a$ measurements.

i) The $TAPIR$ function in eq. (4.13) is developed with reference parameters for the surface. Applying different phytoplankton parameterization (e.g. $a_{ph} = \text{NechadMIN}$) considering increased scattering, may improve $chl-a$ accuracy with $TAPIR$. Increasing coefficients of $TAPIR_{BOA}$ function slightly, which is demonstrated with eq. (4.20), in order to “simulate” increased scattering according to fig. 4.12, $chl-a$ estimations for InW approach the 1:1 line.

ii) In order to assign retrieved $TAPs$ to $a670$ in fig. 4.17a, it was necessary to convert measured $chl-a$ to $a670$ applying a bio-optical model which likely adds additional uncertainties. Therefore, there is an intrinsic dependency between measured $chl-a$ and $TAPIR_{BOA}^{InW}$ (red bullets).

iii) Using the bio-optical model from Bricaud et al. (1995), retrieved $a670$ are converted to $chl-a$ in fig. 4.17c. Possibly, alternative BOMs perform differently for Indonesian and North Sea waters and calculated $chl-a$ rather match measurements.

iv) As outlined in previous sections, low $a670$ as in this section becomes inaccurate with high uncertainties due to very small $TAPs$ and quite small and sometimes negligible reflectance peaks in the fluorescence domain.

v) Finally, $chl-a$ is measured rather differently and at various depths. According to Nechad et al. (2015), available $chl-a$ measurements are averaged for upper 10 m in the provided dataset. There is no information given about number and depth of measured $chl-a$ samples and, therefore, $chl-a$ values may correspond to measurements below 3 m which cannot be detected with $TAPIR$ due to the maximum penetration depth (cf. section 2.2.3).

6 Discussion

In an algae cell, the processes photosynthesis, dissipation, and fluorescence antagonistically consume energy of absorbed photons. Nevertheless, fluorescence can also occur in deceased phytoplankton but the aquatic community mainly focuses on living cells. Thus, measuring fluorescence, chlorophyll-a amount and living activity could be estimated (Maxwell and Johnson, 2000). Estimation and interpretation of fluorescence remain still complex because an increase in fluorescence occurs either due to more *chl-a* or reduction of one or both of the other processes. Among others, the fluorescence process depends on algae type, physiology, health, and environmental conditions. The study focuses on increase of fluorescence due to increase of *chl-a* and *a670*, respectively.

MOMO simulations reveal that the peak near 690 nm does not solely occur due to fluorescence but is mainly induced by phytoplankton scattering which has been mentioned exemplary by Gilerson et al. (2008). In contrast to *FLH* retrievals often claiming results of solely fluorescence (e.g Fischer and Kronfeld, 1990, Gilerson et al., 2007), investigating the reflectance peak within the fluorescence domain from 650 nm to 730 nm, both fluorescence and algae scattering is obtained. Chlorophyll-a absorption influences and scales both properties.

MOMO sufficiently reproduces the process of fluorescence and reflectance magnitude matches literature with respect to the spectral interval from 650 nm to 730 nm (Fischer and Kronfeld, 1990, Wang et al., 2017). However, the model validation only operates for simulations of low phytoplankton absorption coefficients which correspond to lower chlorophyll-a concentration. The validation of reflectance in a specific spectral range is complex due to IOPs and reflectance dependencies on environmental conditions and phytoplankton physiology which have to be considered in simulations accordingly to the measurements. Rather dark simulated reflectance spectra are suggested with high total absorption. It might be necessary to collect data in highly eutrophic waters to compare reflectance measurements and phytoplankton properties with simulations of high algae content. Although Wang et al. (2017) showed laboratory estimations of fluorescence with a polarization technique, the pure fluorescence signal is hardly to discriminate from reflectance measurements. The efficiency is still a high uncertainty factor with an assumed range between 0.003 to 0.01 (Gilerson et al., 2007, Schalles, 2006) and its estimation is based on further assumptions such as relative reflectance portion reflectance, spectral distribution, chlorophyll-a concentration, and phytoplankton species (Gordon, 1979, Gower, 2016, Babin et al., 2003).

On the one hand, fluorescence depends on phytoplankton condition and properties and on the other hand on available fluorescence excitation from the ambient light field and fluorescence efficiency. According to Maxwell and Johnson (2000), fluorescence efficiency magnitude is depending on two additional processes consuming energy of absorbed photons: Heat dissipation and photosynthesis which both are not directly obtained from remote sensing measurements. In order to obtain absolute fluorescence portion or relative fraction of the reflectance measurement additional information such as absolute relation between reflectance magnitude (cleared from additional influence such as sediment scattering) to phytoplankton depth is required. MOMO simulations reveal high dependency on the vertical location of phytoplankton. The presence of aquatic and atmospheric constituents change the amount of light available for absorption which directly changes available excitation amount for fluorescence. Assuming ideal conditions (clear atmosphere, little water constituents), fluorescence can be smaller than expected due to a low efficiency factor – maybe due to the physiological condition of algae (Maxwell and Johnson, 2000) – or phytoplankton not located beneath the surface.

Quantifying fluorescence and also phytoplankton scattering with *TAP*, the selection of the lower integration limit λ_1 depends on available signal bands near 670 nm. λ_1 constrains integration and can influence the final *TAP* due to the definition of the “reflectance constant” $R(\lambda_1)$, which reduces total reflectance, and upper integration limit λ_2 . The impact of λ_1 has to be considered but, usually, most of the sensors (e.g. EnMAP) have lower radiometric resolution than MOMO which limits the choice of λ_1 to 1 or 2 possible bands. Therefore, developing sensor specific *TAPIR* functions from simulations relativizes the relation between *TAP* and *a440* among each other. Of course, *TAPIR* requires a minimum number of bands for a proper integration whereas EnMAP specifications promise sufficient results. The minimum number has to be investigated for a pre-defined acceptance uncertainty. However, Lu et al. (2016) reported a band distribution in about 5 nm intervals is sufficient for water colour observations. Accounting for sensors with fewer bands than EnMAP (e.g. Hyperion or OLCI with 10 and 5 bands within 660 nm to 750 nm, respectively), the peak can be estimated with a fitting function. Unfortunately, absorption properties of phytoplankton and water highly influence the peak’s shape which complicates the application of a unique function (e.g. Gauß). However, applying a polynomial of degree 3 depending on individual measurements of OLCI, the shape of the peak is not reproduced but the integral of the peak sufficiently represents the relation between absorption and peak area. Therefore, retrieved uncertainties of sensors EnMAP, HICO, TROPOMI, and even multi-spectral OLCI only slightly differ from MOMO *a670* uncertainties.

Uncertainties retrieved in this study are about 30 % to 35 % of phytoplankton absorp-

tion a_{670} . They are dependent on a_{670} itself and mainly phytoplankton IOPs. Considering alternative parameter values and parameter uncertainties σ_p , they likely change. The assumption of σ_p particularly influences final a_{670} uncertainty σ_a . As outlined beforehand, both reflectance and optical properties depend on phytoplankton species. Chlorophyll-a absorption coefficients can be used to obtain chlorophyll-a concentration (see chapter 2 section 2.3.5) but they are dependent on species and often environmental conditions. Alternative assumed absorption spectra led to different *TAPIR* functions which might be used for phytoplankton species discrimination.

Nevertheless, *TAPIR* provides advantages by “catching” the total effective reflectance peak with its variable magnitude, location, and shape. In contrast to *FLH*, *TAPIR* functions exhibit a monotonically increasing slope with increasing a_{670} obviating ambiguous a_{670} for higher chlorophyll-a concentrations and assimilates to natural behaviour of the effective peak by avoiding constant measurement bands. Unfortunately, the impact of a_{ot} ranges in similar magnitudes of *TAPIR* TOA functions and may not be neglected. Nevertheless, future studies may reveal a constant linear relation (fig. 4.13f) which can support a simple correction of *TAPIR* results. A_{ot} is less important for BOA applications.

7 Conclusions

This study introduces Total Algae Peak Integration Retrieval (*TAPIR*) which links phytoplankton induced reflectance peak in the fluorescence domain 650-730nm to chlorophyll-a absorption at 670 nm (a_{670}). Firstly, the peak located near 683 nm induced by chlorophyll-a fluorescence and phytoplankton scattering is quantified with an integration (*TAP*). Secondly, a *TAPIR* function is developed for top of the atmosphere (TOA) simulated data depending on a_{670} . Afterwards, function's inverse provides the possibility to retrieve a_{670} from reflectance data. Therefore, *TAPIR* and its functions support relation to phytoplankton absorption, scattering, fluorescence, and concentration. The algorithm development is based on RTM simulations with MOMO. MOMO properly reproduces the process of fluorescence and is valid for low absorption coefficients. Sensitivity studies on various atmospheric and aquatic parameters reveal a major dependence on phytoplankton parameterization (IOPs and fluorescence efficiency factor), some aerosol influence, and little impact on water constituents. *TAPIR* applies to all kind of waters relating to optical complexity, geographical location, measurement location, and water constituents. The uncertainty of a_{670} from TOA signals is approximately 30 % to 35 % (e.g. $(1.07 \pm 0.34) \text{ m}^{-1}$ and $(3.47 \pm 1.05) \text{ m}^{-1}$). The simulations for EnMAP specific conditions are promising for an accurate fluorescence and *chl-a* retrieval and studies can benefit from a high spatial resolution (30 m). Uncertainties for hyper-spectral sensors such as HICO, TROPOMI, and EnMAP are similar to MOMO a_{670} uncertainties. Applying a polynomial of degree 3, *TAPIR* can be applied on multi-spectral sensors such as OLCI which opens a wide generality and opportunity of the algorithm.

In order to retrieve phytoplankton properties (absorption coefficient, scattering coefficient, portion of fluorescence, efficiency factor, phytoplankton amount), *TAPIR* provides a first step towards advanced retrievals. Due to the dependency on more than one property future algorithms could include redshift/blueshift, absolute amplitude of the maximum reflectance peak and possibly NIR measurement which might be raised due to high phytoplankton scattering. Providing specific *TAPIR* functions for several external conditions (number of bands, θ , TOA/BOA), we can use these globally in inland and coastal waters and open oceans due to insensitivity on salinity, temperature, and pressure. The impact of strongly absorbing gases in the visible could have been underestimated. Therefore, water vapour, ozone, and oxygen should be considered sensitively in future studies and simulations.

Sediments and *cdom* hardly influence *TAPIR* and it is applicable to optically complex

waters. *TAPIR* mainly depends on phytoplankton IOPs producing the highest uncertainties and largest sensitivities. Further investigations of phytoplankton type specific measurements accounting for chlorophyll-a absorption spectra, scattering spectra, phase function, and efficiency factor support phytoplankton parameterization in optical models. This might be an opportunity for retrievals based on *TAPIR* to obtain phytoplankton types or fluorescence exclusively. Additionally, Roesler et al. (1989) proposed an approach for *cdom* absorption retrieval near 440 nm based on phytoplankton absorption and total absorption. The solitude optical approach of *TAPIR* could contribute a_{670} from reflectance spectra for phytoplankton. Reflectance is highly reduced by at least half of the magnitude for already slightly deeper layered phytoplankton of 1 m. According to the maximum penetration depth of red light of 3 m (Gordon and McCluney, 1975) and assuming only phytoplankton containing waters, there might be potential to discriminate the location of phytoplankton.

Abstract

The algorithms for snow and ice classification from chapter 3 and Total Algae Peak Integration Retrieval (*TAPIR*) from chapter 4 are applied on two scenes of Lake Erie (USA/Canada) measured with Ocean and Land Colour Imager (OLCI) and Sea and Land Surface Temperature Radiometer (SLSTR) on-board Sentinel-3 (S3). Lake Erie has been chosen because it can be observed with passive remote sensing instruments the entire year due to its location in the mid-latitudes in contrast to Greenland. The first scene shows an extreme algae bloom and the second one a partly snow and ice covered Lake Erie. The application of *TAPIR* reveals reliable results for high *chl-a* (algae bloom scene) but for lower concentrations the algorithm cannot detect the required phytoplankton peak if there is any (lake ice scene). In comparison to meteorological data, the snow and ice classification provides highly comprehensible results. More than 80 % of the pixels are valid for classification and 50 % are assigned to classes. The characterization reveals a negligible portion of *wet* pixels that exclude the assumed required habitat for ice algae which are confirmed by a range of chlorophyll-a algorithms without retrieving any phytoplankton content.

1 Observing Lake Erie

Lake Erie is the southernmost of the five Great Lakes located near the border of Canada and the United States (fig. 5.1). In contrast to Greenland, Lake Erie can be observed with remote sensing the entire year due to its location between 41°N and 43°N. The northern-west Lake St Clair contributes the major inflow. Lake Erie majorly outflows in the northern east located Lake Ontario connected by the famous Niagara Falls. Lake Erie is relatively shallow with an average depth of about 19 m and reaches only about 7 m deep (Lake Erie LaMP, 2008) in the western basin. The inland sea is an important fresh water supply for adjacent cities and agricultural economy and provides natural habitat for many animal and vegetation species such as salmon, zebra mussels, and algae.

The climate at the lake is typical humid continental with temperatures around the freezing point in winter and warm summers with temperatures up to around 25 °C with average precipitation around 75 mm to 100 mm per month. In winter, arctic dry air masses warms over the Great Lakes and collects water vapour which freezes in the upper troposphere and falls as snow (Lake Erie LaMP, 2008). The so-called Lake Effect causes heavy snow falls (“Snow Belt”) when cold air masses meet the lakes which are warmer than surrounding land (Fuller and Shear, 1995). In autumn and winter, Lake Erie is partly covered with sea ice that can become up to 0.6 m thick^{5a}. A frozen Lake Erie reduces the possibility of the Lake Effect due to a smaller temperature gradient between air masses and lake surface. In summer, in combination with water temperatures that can reach more than 25 °C (Rowe et al., 2016) and a huge nutrient inflow by rivers loaded with agricultural sediments, Lake Erie suffers from extreme harmful algae blooms (HABs) every year (Fuller and Shear, 1995, Vincent et al., 2004, Heisler et al., 2008, Stumpf et al., 2012, Moore et al., 2014, Rowe et al., 2016). Extreme eutrophication harms animals and environment due to toxic degradation products of algae and oxygen depletion.

In the following, Lake Erie is analysed with the retrievals for snow/ice and phytoplankton from chapter 3 and chapter 4 applying sensors OLCI and SLSTR from Sentinel-3A. According to chapter 4 section 4.3, *TAPIR* can be applied to multi-spectral instruments such as OLCI. For *TAPIR*, OLCI L1B top of the atmosphere (TOA) radiance and solar flux measurements from the channels 8 to 12 are used to compute TOA reflect-

^{5a}GLCFS ICE Products, <https://www.glerl.noaa.gov/res/glcfs/glcfs-ice.php?lake=e&type=N&hr=00>, accessed 2018-03-02

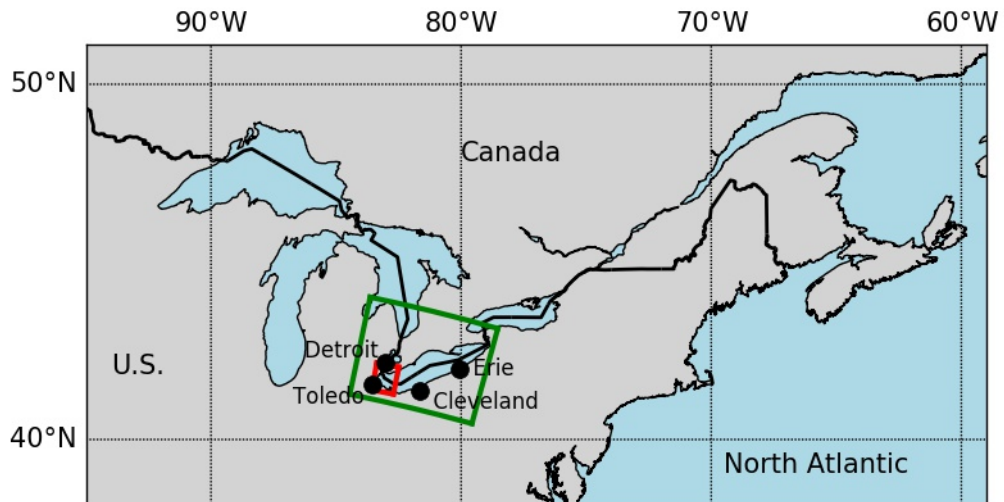


Figure 5.1: Location of Lake Erie at the American-Canadian border. Green and red tiles show location of S3 OLCI/SLSTR scenes in 2017-09-05 with an extreme algae bloom and in 2018-02-12 with a partly frozen lake, respectively.

ance. OLCI and SLSTR heritage of Medium Resolution Imaging Spectrometer (MERIS) and Advanced Along-Track Spectral Radiometer (AATSR) and can be used for cryospheric characterization. Investigating snow and ice cover, SLSTR brightness temperature measurements in nadir and oblique view for central wavelengths 11 μm and 12 μm are applied according to AATSR settings from chapter 3.

A clear-sky scene from 2017-09-15 at the western basin of Lake Erie is chosen (red frame in fig. 5.1) presenting an extreme HAB (“Algae bloom” in section 2.1). At 2018-02-12, OLCI and SLSTR captured a completely clear-sky scene of frozen Lake Erie (“Lake ice” in section 2.2) and partly snow-covered land (green frame in fig. 5.1). *TAPIR* is applied to both scenes which have been masked with OLCI’s L1B mask for fresh water avoiding invalid results over land masses. For the cryospheric characterization, the “Lake ice” scene has been masked for non-cryospheric pixels with techniques described in chapter 3 section 2.4.

2 Case studies

2.1 Algae bloom

Figure 5.2a shows an OLCI RGB image for 2017-09-15 which already reveals an extreme bloom. Chlorophyll-a concentration measurements provided by the Great Lakes Research Laboratory^{5b} confirm the first guess with extreme surface concentrations of more than 500 mg m^{-3} and more than 100 mg m^{-3} in less than 1 m depth for the Western basin at 2017-09-18. Extreme values correspond to a “green soup” shown in fig. 2.5c in chapter 2 and due to high surface concentrations. Lower phytoplankton layers exhibit lower concentrations (but still extreme) because they are cut off the necessary light.

Therefore, extreme a_{670} of more than 20 m^{-1} retrieved from *TAPIR* with OLCI measurements may be reliable qualitatively (fig. 5.2b). The bloom has a mean a_{670} of $(7.92 \pm 4.73) \text{ m}^{-1}$ with minimum and maximum values of 0.28 m^{-1} and 26.11 m^{-1} . Zero values are excluded from the statistics. The spatial extend of the bloom is perfectly matched and low phytoplankton concentrations (“blue” water in the RGB) could not be assessed (dark grey area). Values below 0.4 m^{-1} are hardly covered by *TAPIR* method due to *TAPIR* functions exhibiting extreme low values close to zero for low absorption coefficients and quickly increasing slope for higher a_{670} (see chapter 4 section 4.1).

Applying commonly used *chl-a* algorithms, Fluorescence Line Height (*FLH*) and Maximum Chlorophyll Index (*MCI*), differences are retrieved in figs. 5.3a and 5.3b due to different signal bands at 681.25 nm and 708 nm, respectively. *FLH* becomes strongly negative and *MCI* positive because the observed phytoplankton peak shifted towards longer wavelength due to the strong absorption feature near 670 nm for high concentrations. In figs. 5.3c and 5.3d, *BG* and Ocean Colour quartic algorithm for MERIS (*OC4E*) represent the spatial extend of the bloom but highly underestimate extreme *chl-a* as expected due to limitation of the methodology to case-1 waters which contain solely phytoplankton. Additionally, for high chlorophyll-a concentrations, *BG* is expected to be lower than 1 due to higher reflectance in green than in blue bands. There is also non-algal content like sediments present in lake Erie perturbing *MCI* (Stumpf et al., 2012) likely influencing results from baseline retrievals and *BG*.

However, combining Cyanobacterial Index (*CI*) which is the negative of *FLH* (Wynne et al., 2008) in units of reflectance with a bio-optical model for Lake Erie after Stumpf

^{5b}database of measurement sites at the western basin of Lake Erie: https://www.glerl.noaa.gov/res/HABs_and_Hypoxia/WLEMicrocystin.html, accessed 2018-02-22

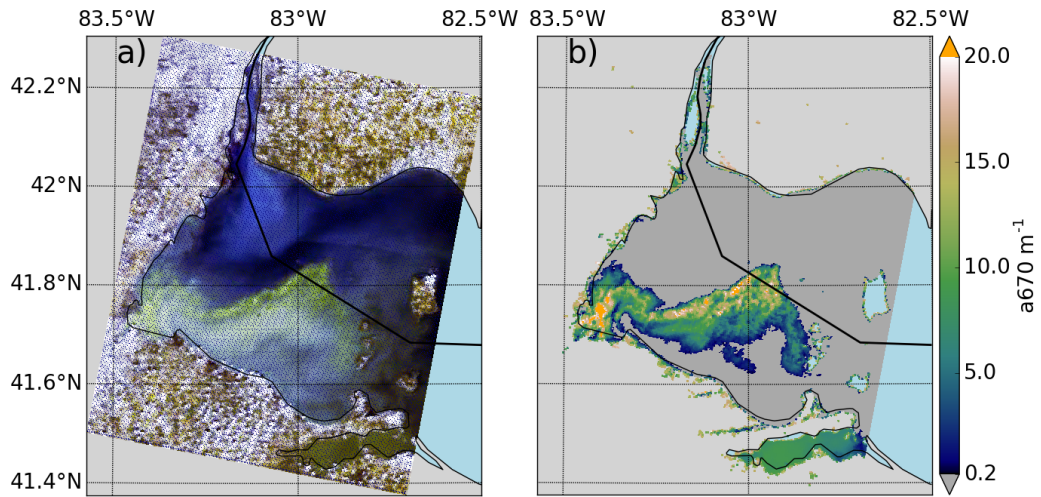


Figure 5.2: Lake Erie, known for growing extensive HABs, shows an algae bloom in the Western part in 2017-09-15 (panel a). Applying TAPIR for OLCI, the bloom can be easily identified by extreme absorption coefficients.

et al. (2012), more appropriate *chl-a* quantities are retrieved in fig. 5.3e.

$$(5.1) \quad chl-a = 12570 * CI + 10 = -12570 * FLH + 10$$

According to Stumpf et al. (2012), CI of 10^{-3} sr^{-1} refers to $10^{11} \text{ cells m}^{-3}$ which amounts to 23 mg m^{-3} in Lake Erie (Rowe et al., 2016). Therefore, in Lake Erie at 2017-09-15, maximum CI values of $8.5 \cdot 10^{-3} \text{ sr}^{-1}$ chlorophyll-a concentration yield about $23 \text{ mg m}^{-3} * 8.5 \approx 200 \text{ mg m}^{-3}$. The model from Stumpf et al. (2012) retrieves concentrations of $(28.3 \pm 15.2) \text{ mg m}^{-3}$ with minimum and maximum values of 10.0 mg m^{-3} and 120.0 mg m^{-3} for the current scene considering pixels with valid TAPIR $a670$. Qualitatively, $chl-a(CI)$ is still too low compared to in situ measurements mentioned above.

The scatter plot in fig. 5.3f compares $a670$ and CI $chl-a$ and seems to reveal two regimes. The upper “line” exhibits to have a larger peak area, which equals higher $a670$, where FLH retrieves similar results and, therefore, similar CI chlorophyll-a concentrations. This likely might be a first hint towards advantages using TAPIR integration method due to improved estimation of the reflectance peak.

However, finding an appropriate bio-optical model (BOM) for Lake Erie based on chlorophyll-a absorption coefficients at 670 nm, TAPIR may be a fast and possibly more accurate method retrieving $chl-a$ in addition to the existing Harmful Algae Tracker based

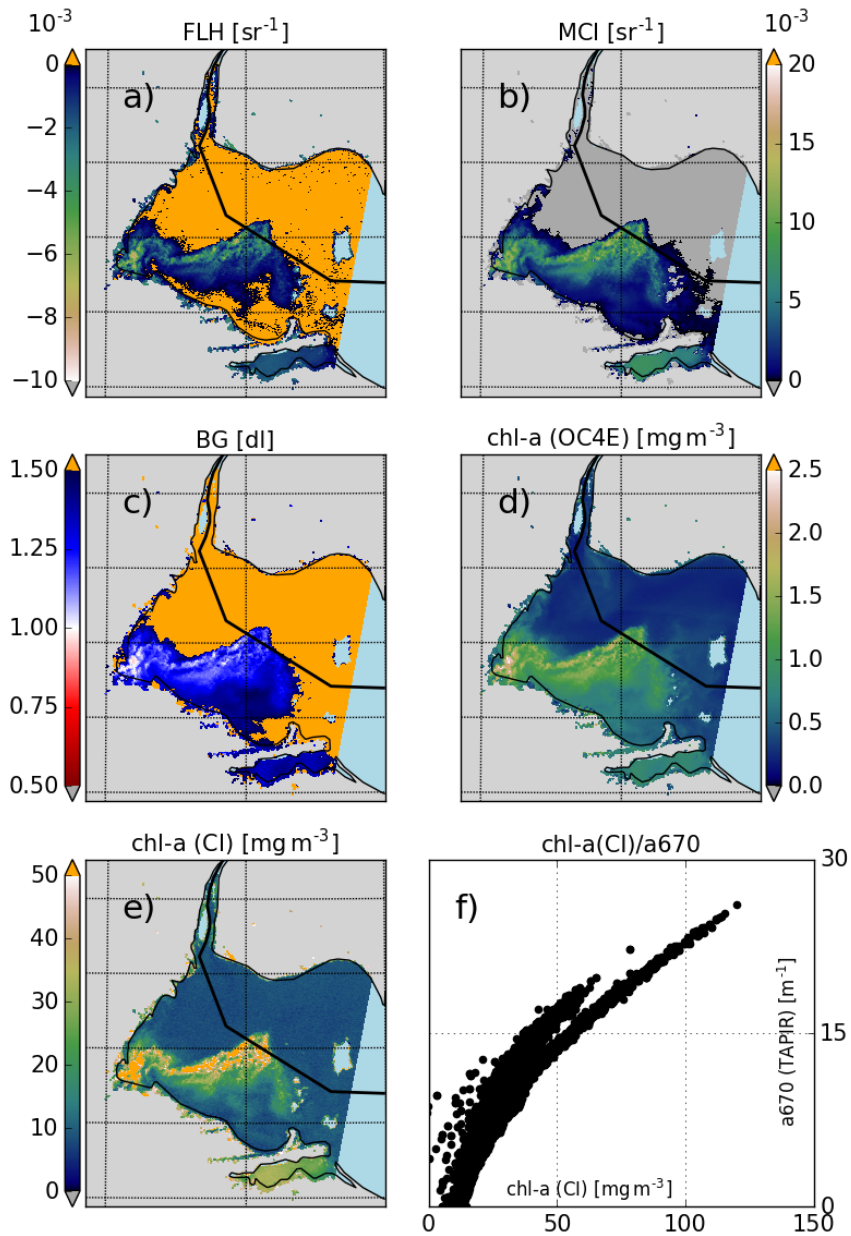


Figure 5.3: Chlorophyll-a retrievals applied to Lake Erie from the scene at 2017-09-15: a) FLH, b) MCI, c) BG, d) OC4E based on BG, and e) CI based on FLH. Panel f) shows the correlation between concentrations retrieved from CI and absorption coefficient retrieved from TAPIR, respectively.

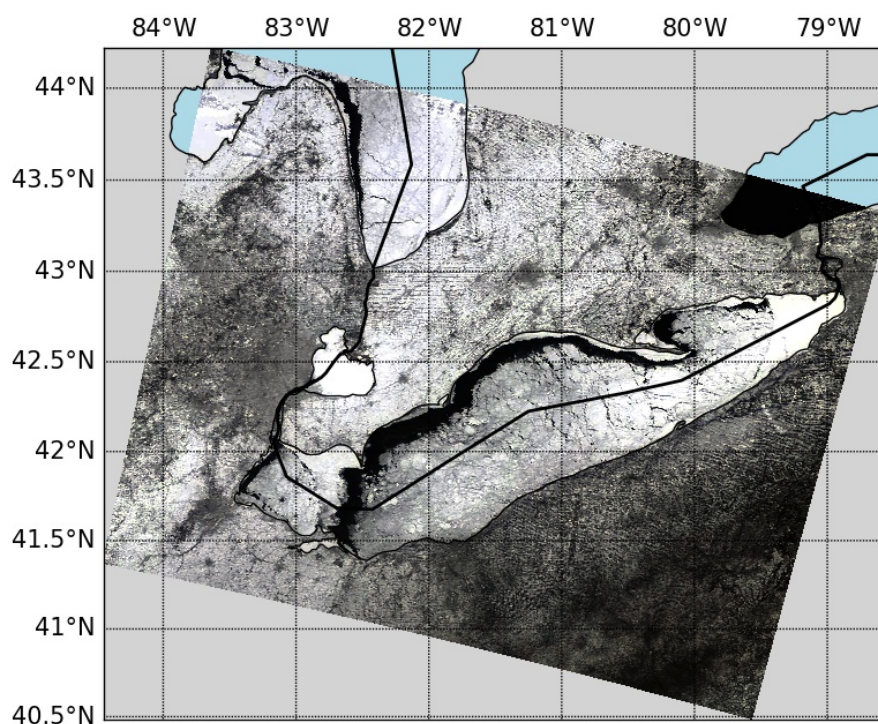


Figure 5.4: OLCI RGB image from 2018-02-12 of a partly frozen and snow covered Lake Erie.

on *CI* to be accessed via https://www.glerl.noaa.gov/res/HABs_and_Hypoxia/habTracker.html.

2.2 Lake ice

TAPIR is also applied to the second scene from 2018-02-12 where Lake Erie is partly ice covered displayed in fig. 5.4. Unfortunately, shown in fig. 5.5, *TAPIR* does not retrieve any a_{670} values except for 0 m^{-1} resulting from an unrecognized or unapparent phytoplankton peak near 690 nm. However, even *FLH* and *MCI* algorithms do not show any response for chlorophyll-*a*. In figs. 5.5a and 5.5b, *FLH* and *MCI* show slightly positive and negative values, respectively, over ice and results close to zero for water pixels. Small negative *MCI* and positive *FLH* indicate low to very low *chl-a* if a peak near 680 nm is apparent that is not redshifted.

In figs. 5.5c and 5.5d, *BG* and *chl-a* from *OC4E*, which are designed for low *chl-a*,

suggest no *chl-a* above ice. Results from *OC4E* around 2 mg m^{-3} (orange) occur due to polynomial calculation with a logarithmic *BG* in eq. (2.19) close to zero (white and light blue in fig. 5.5c). Above water surfaces, slightly positive *BG* (orange) and low *chl-a* up to 1 mg m^{-3} is retrieved from *OC4E*. However, the results are rather similar to very high *chl-a* in fig. 5.3d and *OC4E* is limited to case-1 waters with negligible additional constituents and possible adjacency effects such as sea ice. Analogously, *CI* retrieves *chl-a* around 10 mg m^{-3} due to the offset of 10 mg m^{-3} in eq. (5.1) and *FLHs* around 0 sr^{-1} . The algorithm is designed for medium to high *chl-a* and is therefore not valid for low *chl-a* as shown in fig. 5.5e which occur due to the slightly positive values of the *FLH* above ice. *TAPIR* retrieves no *a670* for water and absorption coefficients up to around 8 m^{-1} above the ice surface (fig. 5.5f). A qualitative comparison between Red-Green-Blue (RGB) and *a670* reveals higher *TAPIR* results for brighter surfaces in the VIS which suggest an influence of high reflectivity. At darker snow and ice areas, *TAPIR* retrieves lower *a670* around 1 m^{-1} to 2 m^{-1} . In conclusion, either there is no phytoplankton near or on the lake ice or none of the *chl-a* algorithms is able to detect the algae due to adjacency effects or an extremely low concentration (see this-chapter in section 3).

Characterization of snow and ice reveals large areas of *fine* and *medium* grained snow and *suncrust* on land and Lake Erie is partly covered from *suncrust* and *coarse* grained snow in fig. 5.6. Spare white areas occur due to the water-land-mask and there are almost no *wet* or *ice* pixels apparent. Lake St Clair and Lake Hurton in the northern west show shows medium grained snow and a comparison to the RGB indeed suggest a snow cover due to the homogeneous bright surface (see this-chapter section 3).

The snow and ice characterization algorithm retrieved about 80 % *valid* and 50 % classified pixels of all un-masked pixels (fig. 5.7a). Portions of *fine*, *medium*, *coarse*, and unclassified pixels range within 10 % to 20 %. Figure 5.7b reveals most of *invalid* pixels occur due to 1 or 2 retrieved emissivities per pixel (11 % and 8 %, respectively) which exceed the classification scheme (cf. fig. 3.5 in chapter 3 section 3.5). Forward view emissivities are mainly responsible for invalidity due to emissivities larger than the upper limit of class *fine* or above the physical value of 1 (red and blue checked in fig. 5.8).

However, the total number of *invalid* pixels is rather low and mostly occurs at regions exhibiting more complex topography (e.g. the northern west of the scene) where the angular dependency may mismatch. There are less than 1 % pixels labelled *wet* because temperatures are below freezing point for the entire scene. This may support the hypothesis that there is no liquid water on ice and snow areas of Lake Erie apparent and phytoplankton cannot grow in a completely frozen habitat.

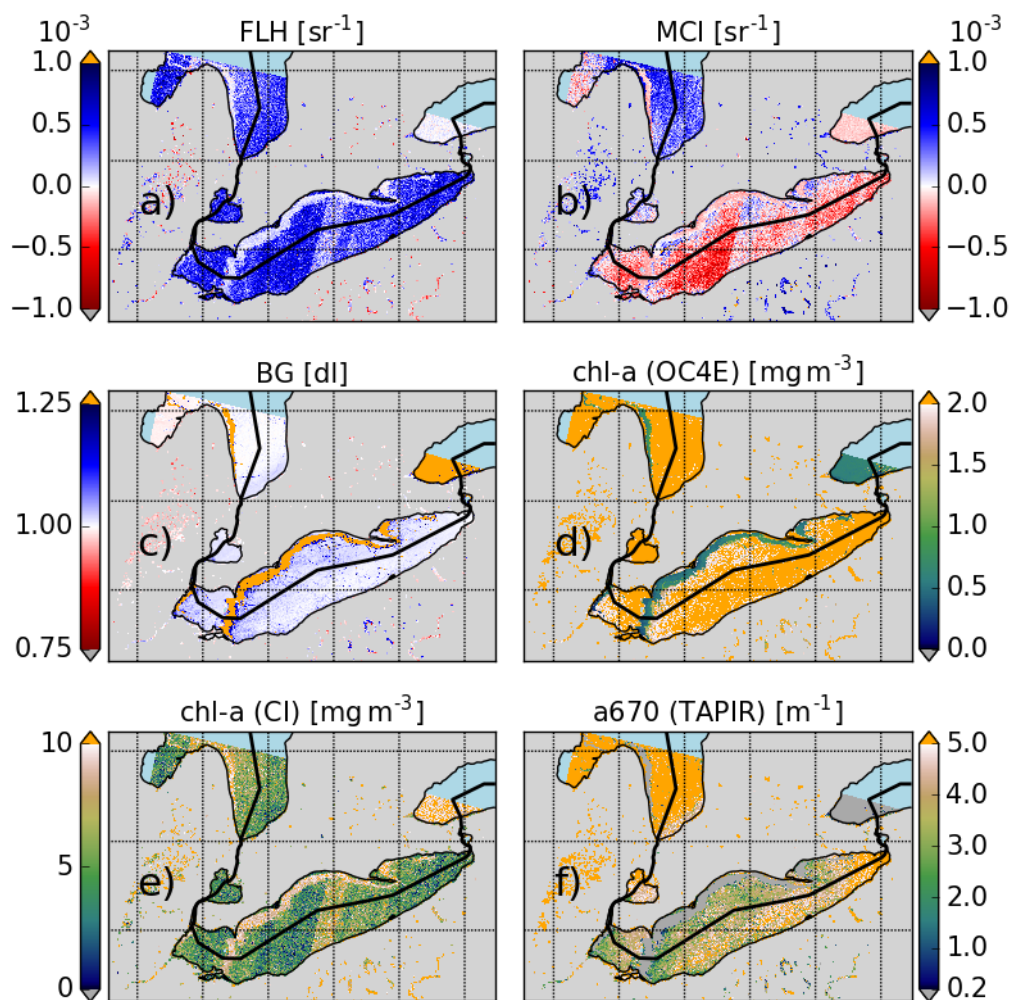


Figure 5.5: Analogously to fig. 5.3 for panels a)-e) for the OLCI scene from 2018-02-12. Panel f) shows the results from TAPIR. The high values (orange) in panels d) and e) result from particular calculation technique with offsets and constants for input values of zero (cf. panels c) and a), respectively).

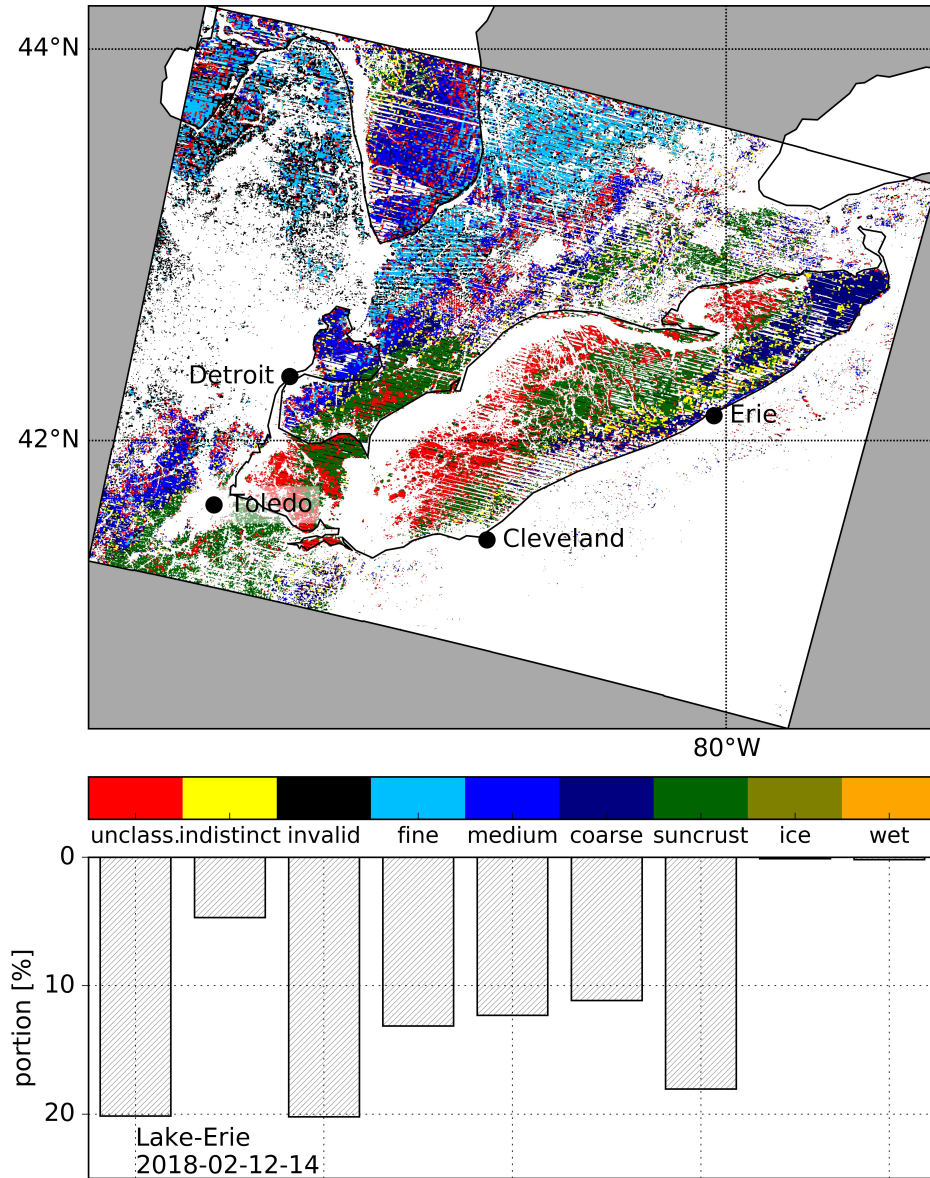


Figure 5.6: Map of classified snow and ice pixels at Lake Erie from 2018-02-12. The histogram provides portion of each class and invalid, indistinct, and unclassified but valid pixels. Colours in the map correspond to histogram labels. White areas in the map occur due to the water-land mask applied to the scene beforehand and collocation interpolation between OLCI and SLSTR.

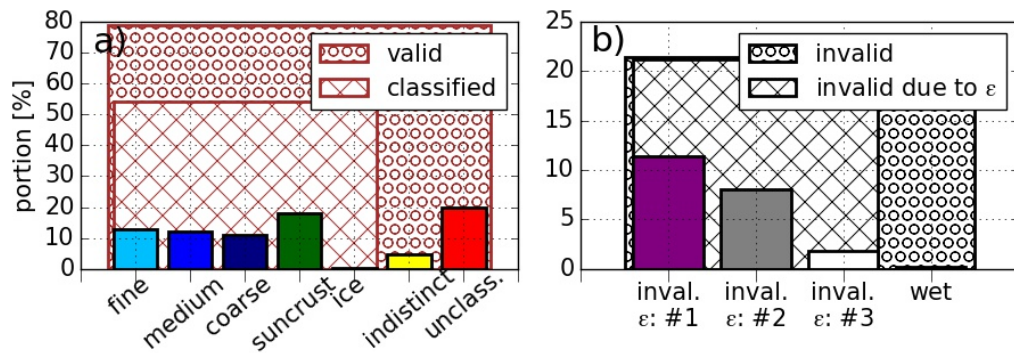


Figure 5.7: Histograms of classified and invalid pixels for the lake ice scene at Lake Erie from 2018-02-12. Panel a) shows about 80 % valid pixels of all available (un-masked) pixels with about 50 % pixels assigned to classes. Panel b) illustrates the portion on invalid pixels due to the number of ϵ per pixel mismatching the classification scheme. There is a negligible portion of wet pixels of less than 1 %.

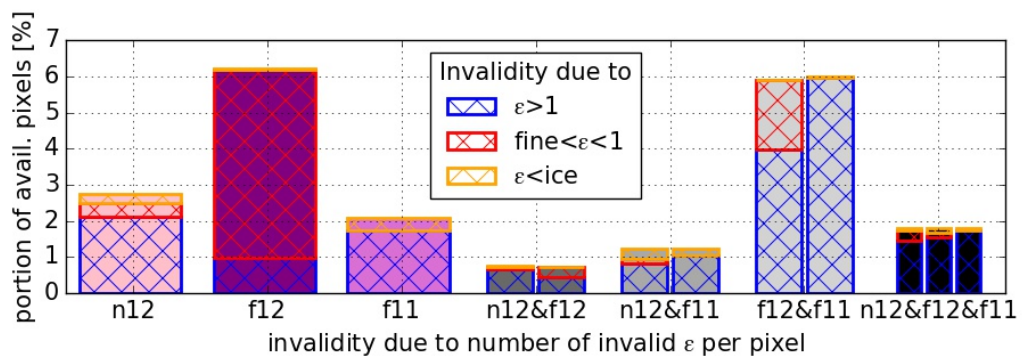


Figure 5.8: A pixel becomes invalid if at least one out of the three retrieved emissivities per pixel exceed the classification scheme (cf. fig. 3.5). For Lake Erie scene from 2018-02-12, most of invalid pixels occur due to emissivities in forward view (f12 in purple and f12&f11 in light grey) exceeding the upper classification range (red and blue checked).

3 Discussion and conclusions

Lake Erie at the American/Canadian border is an ideal testing site for remote sensing retrievals of snow/ice and *chl-a*. The lake provides a frozen surface in winter and extreme algae blooms in summer. Additionally, it can be observed the entire year with passive remote sensing instruments due to its location in the mid-latitudes.

Applying *TAPIR* to an OLCI scene from 2017-09-15 at the western basin of Lake Erie, large and extreme phytoplankton absorption coefficients at 670 nm of more than 20 m^{-1} are retrieved. The results correspond to *chl-a* retrieved from a BOM, which is particularly designed for Lake Erie, which is based on negative *FLH*, qualitative comparison with an OLCI RGB image, and in situ *chl-a* measurements. The lowest value retrieved with *TAPIR* is about 0.3 m^{-1} mainly induced by *TAPIR* function slope approaching zero for low a_{670} . Therefore, low phytoplankton content may not be detected from *TAPIR*. The application of *TAPIR* to the second scene, which includes a partly snow and ice covered Lake Erie, from 2018-02-12 affirms the assumption that *TAPIR* cannot retrieve low *chl-a*. However, none of the applied phytoplankton identification algorithms (*FLH*, *MCI*, *CI*, *OC4E*, *TAPIR*) retrieve reliable phytoplankton concentration or absorption coefficients for the Lake Erie scene. Non-detection either occurs due to un-apparent reflectance peak or negligible phytoplankton concentrations or used algorithms are not able to detect *chl-a*.

The identification algorithm of snow and ice areas of the second scene reveals a negligible number of *wet* pixels where a thin liquid water layer could provide required habitat for phytoplankton. This leads to the assumption that no phytoplankton is apparent in this scene. Possibly, phytoplankton migrated to deeper waters layers or below the lake ice to exploit the slightly warmer temperature in contrast to surface layers.

In total, more than 80 % of the pixels, which are available for snow and ice classification, are *valid* and 50 % are assigned to classes. The characterization classifies areas of *fine* and *medium* grained snow and *sun crust* above land surfaces and *sun crust* and *coarse* snow above Lake Erie. According to meteorological measurements in fig. 5.9 at Detroit, Toledo, Cleveland, and Erie (see maps in figs. 5.1 and 5.6), measured temperature and snow depth time series for 5th February to 15th February 2018 match the retrieved classification.

In Detroit, temperatures range below -5°C and at the 9th February heavy snow fall happened (increase of snow depth of 15 cm) which explains homogeneous white area at Lake St Clair and Lake Hurton in the north western part of the scene. The

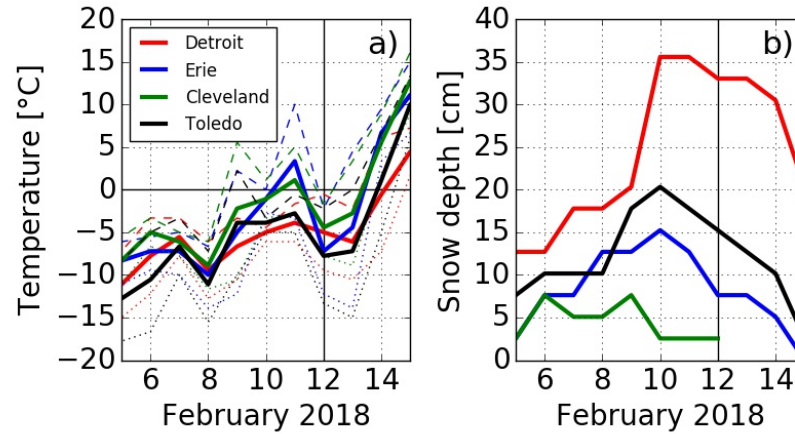


Figure 5.9: Meteorological conditions around Lake Erie in February 2018 with data from the National Weather Service Forecast Office operated by the National Oceanic and Atmospheric Administration (NOAA) accessible via <http://w2.weather.gov/climate/>.

snow depth remains stable and decreases from 10th to 12th of February in fig. 5.9. Similar conditions occurred for Toledo at the western coast of Lake Erie. Therefore, the observed snow cover with SLSTR at 12th of February is already a few days old. The classification scheme characterizes pixels in the western and north western part of the scene with *medium* and *suncrust* which matches snow of an age of a few days. In the northern part around Lake Huron, *fine* snow is retrieved which may be caused by newly fallen snow. Unfortunately, the national weather archive from Canada (http://climate.weather.gc.ca/index_e.html, accessed 2018-03-01) issues missing data for the snow depth for the entire February 2018 for most of the stations between Lake Erie and Lake Huron.

The cities Cleveland and Erie are located at the southern coast of Lake Erie where temperatures increased above the freezing point until the 11th of February and then rapidly fell to less than -5°C on the 12th. There has been a snow fall event at the 9th and 10th of February which contributed a few centimetres of snow. However, temperatures above the freezing point on the 11th may induced a melting of the surface snow which froze again on the 12th. The eastern part of the classified SLSTR scene from the 12th shows *suncrust* and *coarse* grained snow which can be related to an older and re-frozen snow cover due to the meteorological circumstances.

In conclusion, the quantitative comparison of the cryospheric classification with met-

eteorological data suggest proper and valid characterization of the snow and ice covered surface. In order to avoid missing data due to topography and collocation, the classification algorithm could be refined for angular dependency.

The application of *TAPIR* suggests good results for high *chl-a* but it does not support the retrieval for low concentrations from remote sensing instruments. Possibly, a proper atmospheric correction for water vapour and oxygen (O2B band) may improve results because simulated bottom of the atmosphere (BOA) reflectances exhibit a more apparent peak for lower concentrations. Additionally, snow and ice surfaces are relatively bright in the visible spectrum (VIS) which may influence signals near 690 nm and lead to false overestimation of integrated phytoplankton area. Thus, *TAPIR* may not be applicable to detect phytoplankton on snow and ice surfaces assuming bright surfaces and low algae concentration.

An application to the Greenland ice sheet may be complicated because ice algae are assumed to exhibit specific pigmentation and absorption features (Yallop et al., 2012) which have to be considered. However, *TAP* calculation is rather fast and simple and, therefore, *TAPIR* might be a good tracker for extreme events such as HABs.

Abstract

This last chapter recapitulates previous chapters and gives a concluding summary and a brief outlook.

Oceans, inland and coastal waters, ice sheets of Greenland and Antarctica, sea ice, and glaciers are known to play an important role in global radiation and energy budget and, therefore, for climate and climate variability. Snow and ice albedo significantly contribute to reflection of shortwave radiation and waters and phytoplankton are important participants in the global carbon cycle. Therefore, algae on ice, e.g. on the Greenland ice sheet or lake ice, is current research objective and remote sensing retrievals exploiting wavelength and object (snow/ice and phytoplankton) specific properties as introduced in this dissertation are supposed to contribute to future applications and investigations.

The classification of snow and ice are based on conversion of thermal infra-red (TIR) brightness temperatures of different viewing angles to surface emissivity. Emissivity provides the advantage to be highly specific to object, wavelength, and viewing geometry. The TIR domain around $11\ \mu\text{m}$ to $12\ \mu\text{m}$ is solely influenced by water vapour and radiation originates from atmospheric and surface emission. Three retrieved emissivities per pixel are sorted in a classification scheme based on measurements of Hori et al. (2006). A *valid* pixel can either be classified with *fine*, *medium*, *coarse* grained snow, *suncrust*, or *ice*, *indistinct* within classes, or unclassified due to mismatching of at least one of the emissivities in the scheme. *Invalid* pixels occur due to emissivity values exceeding classification intervals which might be caused by complex topography or high reflection on sea ice. *Wet* pixels are classified for physical temperatures above the freezing point. The algorithm is successfully applied to AATSR scenes in Greenland, Antarctica, and North America in 2007 and 2008 and to a SLSTR scene of Lake Erie in 2018. Major obstacles are complex topographic surfaces which influence the actual viewing angle and, therefore, might introduce uncertainties, misclassification and *invalid* pixels. The analysis of *invalid* pixels confirmed that mostly forward view emissivities exceed the classification range or do not match with nadir view emissivity which might be resulting from nadir/forward view collocation. Highly reflective areas are often unclassified although the three pixel emissivities are in range. The effect occurs often at edges of sea and lake ice and might correspond to melting snow and ice.

Ice algae live in a wet habitat, which is supposed to be detected with the cryospheric characterization, and may be quantified with Total Algae Peak Integration Retrieval (*TAPIR*) exploiting the reflectance peak in the red visible/near infra-red (NIR) domain from 650 nm to 730 nm. The peak originates from effects of optical phytoplankton properties (absorption, scattering, fluorescence) and additional water constituents play a minor or negligible role. Chlorophyll-a fluorescence, chlorophyll-a absorption and phytoplankton scattering are highly specific on algae species and amount. Using Matrix Operator Model (MOMD) simulations, the influence of these properties are investigated and *TAPIR*

is developed. The peak's size mainly results from phytoplankton scattering and fluorescence and absorption is responsible for shape and location of the reflectance maximum. *TAPIR* links the spectral integrated phytoplankton reflectance peak to the chlorophyll-a absorption coefficient at 670 nm (a_{670}) which inherits information about chlorophyll-a absorption, phytoplankton scattering, chlorophyll-a fluorescence, and depth. The algorithm is highly sensitive to phytoplankton properties and aerosol-optical thickness for top of the atmosphere (TOA) applications and the uncertainty in retrieving a_{670} ranges within 30 % to 35 %. The application to insitu measurements from North Sea and Indonesian waters and two OLCI scenes of Lake Erie reveal that *TAPIR* can detect medium to high concentrations of algae.

Lake Erie at the Canadian/American border exhibits extreme algae blooms during summer and partly freezes in winter. Both introduced retrievals showed sufficient results analysing OLCI and SLSTR scenes. In order to obtain ice algae in optically complex environments, such as coastal waters or melt ponds in Greenland, which can be found with the cryospheric algorithm, *TAPIR* might only be applied to scenes with medium to high algae content.

The two retrievals for snow and ice classification and phytoplankton characterizations are based on TIR emissivity and phytoplankton inherent optical properties (IOPs) in the VIS. In the future, the cryospheric algorithm would benefit from a continuous classification scheme based on simultaneous measurements of ice crystals and their emissivity. This would refine the classification scheme and omit classification gaps or overlaps and the scheme possibly could be extended with alternative and additional classes. TIR sensors providing different or more measurement bands within 8 μm to 14 μm or different viewing angles are suggested to improve the classification. Instead of using two TIR bands in two viewing modes as provided by SLSTR and AATSR, the algorithm could be tested using multiple measurement bands in the TIR in nadir view (e.g. MODIS bands 31-36). In this thesis, Radiative Transfer for TIROS Operational Vertical Sounder (RTTOV) was used to generate a forward model for surface emissivities from TOA brightness temperatures. Using alternative models such as full-range Matrix-Operator Model FR-MOMO (Doppler et al., 2014) and advanced optimization methods such as optimal estimation are supposed to confirm and refine results. Qualitatively and quantitatively, the snow and ice classification require to be validated with in situ measurements and remote sensing products from micro-wave measurement, for instance.

Analogously to the cryospheric algorithm, *TAPIR* requires to be compared to in situ measurements of chlorophyll-a concentration and absorption. In April 2018, TROPOMI measurements will be available which is a promising candidate for *TAPIR* applications which can be extended with EnMAP measurements launching in 2019. Measurements

from Sentinel-3 series carrying OLCI could extensively tested on applicability of *TAPIR* which opens the field to multi-spectral sensors. Exploiting shape, location, and magnitude of the reflectance peak in the fluorescence domain and the linkage to IOPs near 670 nm provides possible discrimination powers of phytoplankton species and amount. The reflectance peak is dependent on magnitude of absorption, scattering, and fluorescence of phytoplankton and therefore specific coefficients can be tested to discriminate between phytoplankton species with *TAPIR*. Additionally, it might be beneficial to use hyper-spectral reflectance in the fluorescence domain to discriminate absorption and scattering of phytoplankton near 670 and possibly obtain the fraction of fluorescence. Therefore, magnitude and redshift/location of the reflectance peak could play a role. After obtaining an absorption coefficient for phytoplankton in the red visible spectrum, an algorithm could be developed to discriminate *cdom* and phytoplankton absorption or amount in the blue based on the relation of maximum absorption of phytoplankton near 440 nm and 670 nm.

In order to investigate ice algae, it would be beneficial to apply a specific ice algae parameterization to obtain results as accurate as possible. It is also supposed to be required to analyse the ambient light field in melt ponds and highly reflective environments such as snow and ice which might have an impact on the measured reflectance phytoplankton peak.

Bibliography

- Aas, E., Refractive index of phytoplankton derived from its metabolite composition, *Journal of Plankton Research*, 18(12) (1996):2223–2249, ISSN 0142-7873. URL <http://dx.doi.org/10.1093/plankt/18.12.2223>.
- Ahn, Y.-H., Shanmugam, P., Derivation and analysis of the fluorescence algorithms to estimate phytoplankton pigment concentrations in optically complex coastal waters, *Journal of Optics A: Pure and Applied Optics*, 9(4) (2007):352–362, ISSN 1464-4258. URL <http://dx.doi.org/10.1088/1464-4258/9/4/008>.
- Anesio, A. M., Lutz, S., Christmas, N. A. M., Benning, L. G., The microbiome of glaciers and ice sheets, *npj Biofilms and Microbiomes*, 3(1) (2017):10, ISSN 2055-5008. URL <http://dx.doi.org/10.1038/s41522-017-0019-0>.
- Aoki, T., Hori, M., Motoyoshi, H., Tanikawa, T., Hachikubo, A., Sugiura, K., Yasunari, T. J., Storvold, R., Eide, H. a., Stamnes, K., Li, W., Nieke, J., Nakajima, Y., Takahashi, F., ADEOS-II/GLI snow/ice products — Part II: Validation results using GLI and MODIS data, *Remote Sensing of Environment*, 111(2-3) (2007):274–290, ISSN 00344257. URL <http://dx.doi.org/10.1016/j.rse.2007.02.035>.
- Babin, M., Stramski, D., Ferrari, G. M., Claustre, H., Bricaud, A., Obolensky, G., Hoepffner, N., Variations in the light absorption coefficients of phytoplankton, nonalgal particles, and dissolved organic matter in coastal waters around Europe, *Journal of Geophysical Research*, 108(C7) (2003):3211, ISSN 0148-0227. URL <http://dx.doi.org/10.1029/2001JC000882>.
- Bani Shahabadi, M., Huang, Y., Garand, L., Heilliette, S., Yang, P., Validation of a weather forecast model at radiance level against satellite observations allowing quantification of temperature, humidity, and cloud-related biases, *Journal of Advances in Modeling Earth Systems*, 8(3) (2016):1453–1467, ISSN 19422466. URL <http://dx.doi.org/10.1002/2016MS000751>.
- Behrenfeld, M. J., Westberry, T. K., Boss, E. S., O'Malley, R. T., Siegel, D. A., Wiggert, J. D., Franz, B. A., McClain, C. R., Feldman, G. C., Doney, S. C., Moore, J. K., Dall'Olmo, G., Milligan, A. J., Lima, I., Mahowald, N., Satellite-detected fluorescence reveals global physiology of ocean phytoplankton, *Biogeosciences*, 6(5) (2009):779–794, ISSN 1726-4189. URL <http://dx.doi.org/10.5194/bg-6-779-2009>.
- Bennartz, R., Shupe, M. D., Turner, D. D., Walden, V. P., Steffen, K., Cox, C. J., Kulie, M. S., Miller, N. B., Pettersen, C., July 2012 Greenland melt extent enhanced by low-level liquid clouds, *Nature*, 496(7443) (2013):83–86, ISSN 0028-0836. URL <http://dx.doi.org/10.1038/nature12002>.
- Benning, L. G., Anesio, A. M., Lutz, S., Tranter, M., Biological impact on Greenland's albedo, *Nature Geoscience*, 7(10) (2014):691–691, ISSN 1752-0894. URL <http://dx.doi.org/10.1038/ngeo2260>.

Bibliography

- Binding, C., Bowers, D., Mitchelson-Jacob, E., Estimating suspended sediment concentrations from ocean colour measurements in moderately turbid waters; the impact of variable particle scattering properties, *Remote Sensing of Environment*, 94(3) (2005):373–383, ISSN 00344257. URL <http://dx.doi.org/10.1016/j.rse.2004.11.002>.
- Blondeau-Patissier, D., Gower, J. F. R., Dekker, A. G., Phinn, S. R., Brando, V. E., A review of ocean color remote sensing methods and statistical techniques for the detection, mapping and analysis of phytoplankton blooms in coastal and open oceans, *Progress in Oceanography*, 123 (2014):123–144, ISSN 00796611. URL <http://dx.doi.org/10.1016/j.pocean.2013.12.008>.
- Bohren, C. F., Clothiaux, E. E., *Fundamentals of Atmospheric Radiation*, Wiley-VCH Verlag GmbH, Weinheim, Germany (2006), ISBN 9783527618620. URL <http://dx.doi.org/10.1002/9783527618620>.
- Bokhorst, S., Pedersen, S. H., Brucker, L., Anisimov, O., Bjerke, J. W., Brown, R. D., Ehrich, D., Essery, R. L. H., Heilig, A., Ingvander, S., Johansson, C., Johansson, M., Jónsdóttir, I. S., Inga, N., Luojus, K., Macelloni, G., Mariash, H., McLennan, D., Rosqvist, G. N., Sato, A., Savela, H., Schneebeli, M., Sokolov, A., Sokratov, S. A., Terzago, S., Vikhamar-Schuler, D., Williamson, S., Qiu, Y., Callaghan, T. V., Changing Arctic snow cover: A review of recent developments and assessment of future needs for observations, modelling, and impacts, *Ambio*, 45(5) (2016):516–537, ISSN 0044-7447. URL <http://dx.doi.org/10.1007/s13280-016-0770-0>.
- Box, J. E., Fettweis, X., Stroeve, J. C., Tedesco, M., Hall, D. K., Steffen, K., Greenland ice sheet albedo feedback: thermodynamics and atmospheric drivers, *The Cryosphere*, 6(4) (2012):821–839, ISSN 1994-0424. URL <http://dx.doi.org/10.5194/tc-6-821-2012>.
- Brewin, R. J., Hardman-Mountford, N. J., Lavender, S. J., Raitsos, D. E., Hirata, T., Uitz, J., Devred, E., Bricaud, A., Ciotti, A., Gentili, B., An intercomparison of bio-optical techniques for detecting dominant phytoplankton size class from satellite remote sensing, *Remote Sensing of Environment*, 115(2) (2011):325–339, ISSN 00344257. URL <http://dx.doi.org/10.1016/j.rse.2010.09.004>.
- Brewin, R. J., Raitsos, D. E., Dall'Olmo, G., Zarokanellos, N., Jackson, T., Racault, M.-F., Boss, E. S., Sathyendranath, S., Jones, B. H., Hoteit, I., Regional ocean-colour chlorophyll algorithms for the Red Sea, *Remote Sensing of Environment*, 165 (2015):64–85, ISSN 00344257. URL <http://dx.doi.org/10.1016/j.rse.2015.04.024>.
- Bricaud, A., Babin, M., Morel, A., Claustre, H., Variability in the chlorophyll-specific absorption coefficients of natural phytoplankton: Analysis and parameterization, *Journal of Geophysical Research*, 100(C7) (1995):13321–13332. URL <http://dx.doi.org/10.1029/95JC00463>.
- Bricaud, A., Ciotti, A. M., Gentili, B., Spatial-temporal variations in phytoplankton size and colored detrital matter absorption at global and regional scales, as derived from twelve years of SeaWiFS data (1998–2009), *Global Biogeochemical Cycles*, 26(1) (2012), ISSN 08866236. URL <http://dx.doi.org/10.1029/2010GB003952>.
- Bricaud, A., Morel, A., Babin, M., Allali, K., Claustre, H., Variations of light absorption by suspended particles with chlorophyll a concentration in oceanic (case 1) waters: Analysis and implications for bio-optical models, *Journal of Geophysical Research: Oceans*, 103(C13) (1998):31033–31044, ISSN 01480227. URL <http://dx.doi.org/10.1029/98JC02712>.
- Bricaud, A., Morel, A., Prieur, L., Absorption by dissolved organic matter of the sea (yellow substance) in the UV and visible domains, *Limnology and Oceanography*, 26(1) (1981):43–53, ISSN 0024-3590. URL <http://dx.doi.org/10.4319/lo.1981.26.1.0043>.
- Brucker, L., Picard, G., Fily, M., Snow grain-size profiles deduced from microwave snow emissivities in Antarctica, *Journal of Glaciology*, 56(197) (2010):514–526, ISSN 0022-1430. URL <http://dx.doi.org/10.1017/S0022143010000514>.

- org/10.3189/002214310792447806.
- Buckingham, C. E., Cornillon, P. C., Schloesser, F., Obenour, K. M., Global observations of quasi-zonal bands in microwave sea surface temperature, *Journal of Geophysical Research: Oceans*, 119(8) (2014):4840–4866, ISSN 21699275. URL <http://dx.doi.org/10.1002/2014JC010088>.
- Butterbach-Bahl, K., Wolf, B., Warming from freezing soils, *Nature Geoscience*, 10(4) (2017):248–249, ISSN 1752-0894. URL <http://dx.doi.org/10.1038/ngeo2915>.
- Cardaci, M., ENVISAT-1 Products Specifications Volume 7: AATSR Products Specifications (IDEAS-SER-IPF-SPE-0288) (2013). URL <https://earth.esa.int/documents/10174/437508/Vo1-07-Aats-4C.pdf>.
- Carr, M.-E., Friedrichs, M. A., Schmeltz, M., Noguchi Aita, M., Antoine, D., Arrigo, K. R., Asanuma, I., Aumont, O., Barber, R., Behrenfeld, M., Bidigare, R., Buitenhuis, E. T., Campbell, J., Ciotti, A., Dierssen, H., Dowell, M., Dunne, J., Esaias, W., Gentili, B., Gregg, W., Groom, S., Hoepffner, N., Ishizaka, J., Kameda, T., Le Quéré, C., Lohrenz, S., Marra, J., Mélin, F., Moore, K., Morel, A., Reddy, T. E., Ryan, J., Scardi, M., Smyth, T., Turpie, K., Tilstone, G., Waters, K., Yamanaka, Y., A comparison of global estimates of marine primary production from ocean color, *Deep Sea Research Part II: Topical Studies in Oceanography*, 53(5-7) (2006):741–770, ISSN 0967-0645. URL <http://dx.doi.org/10.1016/J.DSR2.2006.01.028>.
- Chandrasekhar, S., *Radiative Transfer*, Dover Publications, Inc., New York (1960), ISBN 0486605906. URL <http://store.doverpublications.com/0486605906.html>.
- Chang, A., Foster, J., Hall, D., Rango, A., Hartline, B., Snow water equivalent estimation by microwave radiometry, *Cold Regions Science and Technology*, 5(3) (1982):259–267, ISSN 0165232X. URL [http://dx.doi.org/10.1016/0165-232X\(82\)90019-2](http://dx.doi.org/10.1016/0165-232X(82)90019-2).
- Chapman, R. L., Algae: the world's most important “plants”—an introduction, *Mitigation and Adaptation Strategies for Global Change*, 18(1) (2013):5–12. URL <http://dx.doi.org/10.1007/s11027-010-9255-9>.
- Chen, J., He, X., Zhou, B., Pan, D., Deriving colored dissolved organic matter absorption coefficient from ocean color with a neural quasi-analytical algorithm, *Journal of Geophysical Research: Oceans*, 122(11) (2017):8543–8556, ISSN 21699275. URL <http://dx.doi.org/10.1002/2017JC013115>.
- Chylek, P., Robinson, S., Dubey, M. K., King, M. D., Fu, Q., Clodius, W. B., Comparison of near-infrared and thermal infrared cloud phase detections, *Journal of Geophysical Research Atmospheres*, 111(20) (2006):1–8, ISSN 01480227. URL <http://dx.doi.org/10.1029/2006JD007140>.
- Ciais, P., Sabine, C., Bala, G., Bopp, L., Brovkin, V., Canadell, J., Chhabra, A., DeFries, R., Galloway, J., Heimann, M., Jones, C., Quéré, C. L., Myneni, R., Piao, S., Thornton, P., Carbon and Other Biogeochemical Cycles, in *Climate Change 2013: The Physical Science Basis. Contribution of Working Group I to the Fifth Assessment Report of the Intergovernmental Panel on Climate Change*, edited by T. Stocker, D. Qin, G.-K. Plattner, M. Tignor, S. Allen, J. Boschung, A. Nauels, Y. Xia, V. Bex, P. Midgley, chap. 6, Cambridge University Press, Cambridge, United Kingdom and New York, NY, USA (2013). URL <http://www.ipcc.ch/report/ar5/wg1/>.
- Claustre, H., Morel, A., Babin, M., Cailliau, C., Marie, D., Marty, J.-C., Tailliez, D., Vaultot, D., Variability in particle attenuation and chlorophyll fluorescence in the tropical Pacific: Scales, patterns, and biogeochemical implications, *Journal of Geophysical Research: Oceans*, 104(C2) (1999):3401–3422, ISSN 01480227. URL <http://dx.doi.org/10.1029/98JC01334>.
- Clifford, D., Global estimates of snow water equivalent from passive microwave instruments: history, challenges and future developments, *International Journal of Remote Sensing*, 31(14) (2010):3707–3726, ISSN 0143-1161. URL <http://dx.doi.org/10.1080/01431161.2010.483482>.

Bibliography

- Cook, J., Edwards, A., Takeuchi, N., Irvine-Fynn, T., Cryoconite, *Progress in Physical Geography*, 40(1) (2016):66–111, ISSN 0309-1333. URL <http://dx.doi.org/10.1177/0309133315616574>.
- Cox, C., Munk, W., Measurement of the Roughness of the Sea Surface from Photographs of the Sun's Glitter, *Journal of the Optical Society of America*, 44(11) (1954):838, ISSN 0030-3941. URL <http://dx.doi.org/10.1364/JOSA.44.000838>.
- , Slopes of the sea surface deduced from photographs of sun glitter, *UC San Diego: Scripps Institution of Oceanography Library*, 6(9) (1956):401–488. URL <https://escholarship.org/uc/item/1p202179>.
- Dall'Olmo, G., Brewin, R. J. W., Nencioli, F., Organelli, E., Lefering, I., McKee, D., Röttgers, R., Mitchell, C., Boss, E., Bricaud, A., Tilstone, G., Determination of the absorption coefficient of chromophoric dissolved organic matter from underway spectrophotometry, *Optics Express*, 25(24) (2017):A1079, ISSN 1094-4087. URL <http://dx.doi.org/10.1364/OE.25.0A1079>.
- Dee, D., Fasullo, J., Shea, D., Walsh, J., The Climate Data Guide: Atmospheric Reanalysis: Overview & Comparison Tables. (2016). URL <https://climatedataguide.ucar.edu/climate-data/atmospheric-reanalysis-overview-comparison-tables>.
- Doerffer, R., Fischer, J., Concentrations of chlorophyll, suspended matter, and gelbstoff in case II waters derived from satellite coastal zone color scanner data with inverse modeling methods, *Journal of Geophysical Research*, 99(C4) (1994):7457, ISSN 0148-0227. URL <http://dx.doi.org/10.1029/93JC02523>.
- Doerffer, R., Schiller, H., The MERIS Case 2 water algorithm, *International Journal of Remote Sensing*, 28(3-4) (2007):517–535, ISSN 0143-1161. URL <http://dx.doi.org/10.1080/01431160600821127>.
- Doppler, L., Preusker, R., Bennartz, R., Fischer, J., k-bin and k-IR: k-distribution methods without correlation approximation for non-fixed instrument response function and extension to the thermal infrared—Applications to satellite remote sensing, *Journal of Quantitative Spectroscopy and Radiative Transfer*, 133 (2014):382–395, ISSN 00224073. URL <http://dx.doi.org/10.1016/j.jqsrt.2013.09.001>.
- Dozier, J., Marks, D., Snow mapping and classification from landsat thematic mapper data, *Annals of Glaciology*, 9 (1987):97–103. URL <ftp://ftp.nwrc.ars.usda.gov/publications/1988/Marks-SnowVolumeComparisonsforAtmosphericDepositionMonitoring.pdf>.
- Dozier, J., Schneider, S. R., McGinnis, D. F., Effect of grain size and snowpack water equivalence on visible and near-infrared satellite observations of snow, *Water Resources Research*, 17(4) (1981):1213–1221, ISSN 00431397. URL <http://dx.doi.org/10.1029/WR017i004p01213>.
- Dozier, J., Warren, S. G., Effect of viewing angle on the infrared brightness temperature of snow, *Water Resources Research*, 18(5) (1982):1424–1434, ISSN 00431397. URL <http://dx.doi.org/10.1029/WR018i005p01424>.
- Enriquez-Alonso, A., Sanchez-Lorenzo, A., Calbó, J., González, J.-A., Norris, J. R., Cloud cover climatologies in the Mediterranean obtained from satellites, surface observations, reanalyses, and CMIP5 simulations: validation and future scenarios, *Climate Dynamics*, 47(1-2) (2016):249–269, ISSN 0930-7575. URL <http://dx.doi.org/10.1007/s00382-015-2834-4>.
- ESA, MERIS Product Handbook, *Tech. Rep. 2*, ESA (2006). URL https://earth.esa.int/pub/ESA_DOC/ENVISAT/MERIS/meris.ProductHandbook.2_1.pdf.
- , AATSR Product Handbook, *Tech. rep.*, ESA (2007). URL https://earth.esa.int/pub/ESA_DOC/ENVISAT/AATSR/aatsr.ProductHandbook.2_2.pdf.
- , Sentinel-3 User Handbook, *Tech. Rep. 1* (2017). URL <https://sentinel.esa.int/web/>

- sentinel/user-guides/sentinel-3-olci/document-library.
- EUMETSAT, MSG Level 1.5 Image Data Format Description, *Tech. Rep. 105-v8*, Darmstadt (2017). URL <https://www.eumetsat.int/website/home/Data/TechnicalDocuments/index.html>.
- Eyre, J., A fast radiative transfer model for satellite sounding systems, *ECMWF Technical Memorandum*, 176 (1991):1–28. URL <https://www.ecmwf.int/en/elibrary/9329-fast-radiative-transfer-model-satellite-sounding-systems>.
- Fell, F., Fischer, J., Numerical simulation of the light field in the atmosphere–ocean system using the matrix-operator method, *Journal of Quantitative Spectroscopy and Radiative Transfer*, 69(3) (2001):351–388, ISSN 00224073. URL [http://dx.doi.org/10.1016/S0022-4073\(00\)00089-3](http://dx.doi.org/10.1016/S0022-4073(00)00089-3).
- Fellman, J. B., Hood, E., Spencer, R. G. M., Fluorescence spectroscopy opens new windows into dissolved organic matter dynamics in freshwater ecosystems: A review, *Limnology and Oceanography*, 55(6) (2010):2452–2462, ISSN 00243590. URL <http://dx.doi.org/10.4319/lo.2010.55.6.2452>.
- Field, C. B., Primary Production of the Biosphere: Integrating Terrestrial and Oceanic Components, *Science*, 281(5374) (1998):237–240, ISSN 1095-9203. URL <http://dx.doi.org/10.1126/science.281.5374.237>.
- Fily, M., Comparison of in situ and Landsat Thematic Mapper derived snow grain characteristics in the alps, *Remote Sensing of Environment*, 59(3) (1997):452–460, ISSN 00344257. URL [http://dx.doi.org/10.1016/S0034-4257\(96\)00113-7](http://dx.doi.org/10.1016/S0034-4257(96)00113-7).
- Fischer, J., Grassl, H., Radiative transfer in an atmosphere–ocean system: an azimuthally dependent matrix-operator approach, *Applied Optics*, 23(7) (1984):1032, ISSN 0003-6935. URL <http://dx.doi.org/10.1364/AO.23.001032>.
- Fischer, J., Kronfeld, U., Sun-stimulated chlorophyll fluorescence 1: Influence of oceanic properties, *International Journal of Remote Sensing*, 11(12) (1990):2125–2147, ISSN 0143-1161. URL <http://dx.doi.org/10.1080/01431169008955166>.
- Foster, J. L., Sun, C., Walker, J. P., Kelly, R., Chang, A., Dong, J., Powell, H., Quantifying the uncertainty in passive microwave snow water equivalent observations, *Remote Sensing of Environment*, 94(2) (2005):187–203, ISSN 00344257. URL <http://dx.doi.org/10.1016/j.rse.2004.09.012>.
- Fournier, G. R., Forand, J. L., Analytic phase function for ocean water, vol. 2258, International Society for Optics and Photonics (1994), pp. 194–201. URL <http://dx.doi.org/10.1117/12.190063>.
- Fournier, G. R., Jonasz, M., Computer-based underwater imaging analysis, vol. 3761, International Society for Optics and Photonics (1999), pp. 62–70. URL <http://dx.doi.org/10.1117/12.366488>.
- Fuller, K., Shear, H. (eds.), *The Great Lakes: An environmental atlas and resource book*, 3 ed., Great Lakes National Program Office, U.S. Environmental Protection Agency, Chicago, Illinois (1995), ISBN 0662234413. URL <https://nepis.epa.gov/Exe/ZyPDF.cgi/P1004ICU.PDF?Dockey=P1004ICU.PDF>.
- Gentemann, C., Meissner, T., Wentz, F., Accuracy of Satellite Sea Surface Temperatures at 7 and 11 GHz, *IEEE Transactions on Geoscience and Remote Sensing*, 48(3) (2010):1009–1018, ISSN 0196-2892. URL <http://dx.doi.org/10.1109/TGRS.2009.2030322>.
- Gilerson, a., Zhou, J., Hlaing, S., Ioannou, I., Gross, B., Moshary, F., Ahmed, S., Fluorescence component in the reflectance spectra from coastal waters. II. Performance of retrieval algorithms., *Optics express*, 16(4) (2008):2446–2460, ISSN 1094-4087. URL <http://dx.doi.org/10.1364/OE.16.002446>.
- Gilerson, A., Zhou, J., Hlaing, S., Ioannou, I., Schalles, J., Gross, B., Moshary, F., Ahmed, S., Fluorescence component in the reflectance spectra from coastal waters. Dependence on water composition, *Optics Express*, 15(24) (2007):15702, ISSN 1094-4087. URL <http://dx.doi.org/10.1364/OE.15>.

Bibliography

- 015702.
- Gitelson, A., The peak near 700 nm on radiance spectra of algae and water: relationships of its magnitude and position with chlorophyll concentration, *International Journal of Remote Sensing*, 13(17) (1992):3367–3373, ISSN 0143-1161. URL <http://dx.doi.org/10.1080/01431169208904125>.
- Gordon, H. R., Diffuse reflectance of the ocean: the theory of its augmentation by chlorophyll a fluorescence at 685 nm, *Applied Optics*, 18(8) (1979):1161, ISSN 0003-6935. URL <http://dx.doi.org/10.1364/AO.18.001161>.
- Gordon, H. R., Brown, O. B., Evans, R. H., Brown, J. W., Smith, R. C., Baker, K. S., Clark, D. K., A semianalytic radiance model of ocean color, *Journal of Geophysical Research*, 93(D9) (1988):10909, ISSN 0148-0227. URL <http://dx.doi.org/10.1029/JD093iD09p10909>.
- Gordon, H. R., McCluney, W. R., Estimation of the Depth of Sunlight Penetration in the Sea for Remote Sensing, *Applied Optics*, 14(2) (1975):413, ISSN 0003-6935. URL <http://dx.doi.org/10.1364/AO.14.000413>.
- Gower, J., On the use of satellite-measured chlorophyll fluorescence for monitoring coastal waters, *International Journal of Remote Sensing*, 37(9) (2016):2077–2086, ISSN 0143-1161. URL <http://dx.doi.org/10.1080/01431161.2015.1111542>.
- Gower, J. F. R., Doerffer, R., Borstad, G. a., Interpretation of the 685nm peak in water-leaving radiance spectra in terms of fluorescence, absorption and scattering, and its observation by MERIS, *International Journal of Remote Sensing*, 20(9) (1999):1771–1786, ISSN 0143-1161. URL <http://dx.doi.org/10.1080/014311699212470>.
- Gower, J., King, S., Borstad, G., Brown, L., Use of the 709 nm band of meris to detect intense plankton blooms and other conditions in coastal waters, *European Space Agency, (Special Publication) ESA SP*, 26(572) (2005):365–368, ISSN 03796566. URL <http://dx.doi.org/10.1080/01431160500075857>.
- Guanter, L., Kaufmann, H., Segl, K., Foerster, S., Rogass, C., Chabrillat, S., Kuester, T., Hollstein, A., Rossner, G., Chlebek, C., Straif, C., Fischer, S., Schrader, S., Storch, T., Heiden, U., Mueller, A., Bachmann, M., Mühle, H., Müller, R., Habermeyer, M., Ohndorf, A., Hill, J., Buddenbaum, H., Hostert, P., van der Linden, S., Leitão, P., Rabe, A., Doerffer, R., Krasemann, H., Xi, H., Mauser, W., Hank, T., Locherer, M., Rast, M., Staenz, K., Sang, B., The EnMAP Spaceborne Imaging Spectroscopy Mission for Earth Observation, *Remote Sensing*, 7(7) (2015):8830–8857, ISSN 2072-4292. URL <http://dx.doi.org/10.3390/rs70708830>.
- Hawcroft, M., Dacre, H., Forbes, R., Hodges, K., Shaffrey, L., Stein, T., Using satellite and reanalysis data to evaluate the representation of latent heating in extratropical cyclones in a climate model, *Climate Dynamics*, 48(7-8) (2017):2255–2278, ISSN 0930-7575. URL <http://dx.doi.org/10.1007/s00382-016-3204-6>.
- Heisler, J., Glibert, P., Burkholder, J., Anderson, D., Cochlan, W., Dennison, W., Dortch, Q., Gobler, C., Heil, C., Humphries, E., Lewitus, A., Magnien, R., Marshall, H., Sellner, K., Stockwell, D., Stoecker, D., Suddleson, M., Eutrophication and harmful algal blooms: A scientific consensus, *Harmful Algae*, 8(1) (2008):3–13, ISSN 15689883. URL <http://dx.doi.org/10.1016/j.hal.2008.08.006>.
- Hestir, E. L., Brando, V. E., Bresciani, M., Giardino, C., Matta, E., Villa, P., Dekker, A. G., Measuring freshwater aquatic ecosystems: The need for a hyperspectral global mapping satellite mission, *Remote Sensing of Environment*, 167 (2015):181–195, ISSN 00344257. URL <http://dx.doi.org/10.1016/j.rse.2015.05.023>.
- Hocking, J., Rayer, P., Rundle, D., Saunders, R., Matricardi, M., Geer, A., Brunel, P., Vidot, J., RTTOV v11 Users Guide (2013). URL http://nwpsaf.eu/oldsite/deliverables/rtm/docs_rttov11/users_guide_11_v1.4.pdf.

- Hollstein, A., Fischer, J., Radiative transfer solutions for coupled atmosphere ocean systems using the matrix operator technique, *Journal of Quantitative Spectroscopy and Radiative Transfer*, 113(7) (2012):536–548, ISSN 00224073. URL <http://dx.doi.org/10.1016/j.jqsrt.2012.01.010>.
- Hollstein, A., Fischer, J., Carbajal Henken, C., Preusker, R., Bayesian cloud detection for MERIS, AATSR, and their combination, *Atmospheric Measurement Techniques*, 8(4) (2015):1757–1771, ISSN 1867-8548. URL <http://dx.doi.org/10.5194/amt-8-1757-2015>.
- Hori, M., Aoki, T., Stamnes, K., Li, W., ADEOS-II/GLI snow/ice products — Part III: Retrieved results, *Remote Sensing of Environment*, 111(2-3) (2007):291–336, ISSN 00344257. URL <http://dx.doi.org/10.1016/j.rse.2007.01.025>.
- Hori, M., Aoki, T., Tanikawa, T., Hachikubo, A., Sugiura, K., Kuchiki, K., Niwano, M., Modeling angular-dependent spectral emissivity of snow and ice in the thermal infrared atmospheric window, *Applied Optics*, 52(30) (2013):7243, ISSN 0003-6935. URL <http://dx.doi.org/10.1364/AO.52.007243>.
- Hori, M., Aoki, T., Tanikawa, T., Motoyoshi, H., Hachikubo, A., Sugiura, K., Yasunari, T. J., Eide, H., Storvold, R., Nakajima, Y., Takahashi, F., In-situ measured spectral directional emissivity of snow and ice in the 8–14 μm atmospheric window, *Remote Sensing of Environment*, 100(4) (2006):486–502, ISSN 00344257. URL <http://dx.doi.org/10.1016/j.rse.2005.11.001>.
- Hu, C., Feng, L., Modified MODIS fluorescence line height data product to improve image interpretation for red tide monitoring in the eastern Gulf of Mexico, *Journal of Applied Remote Sensing*, 11(1) (2016):012003, ISSN 1931-3195. URL <http://dx.doi.org/10.1117/1.JRS.11.012003>.
- Huot, Y., Brown, C. a., Cullen, J. J., Retrieval of phytoplankton biomass from simultaneous inversion of reflectance, the diffuse attenuation coefficient, and Sun-induced fluorescence in coastal waters, *Journal of Geophysical Research*, 112(C6) (2007):C06013, ISSN 0148-0227. URL <http://dx.doi.org/10.1029/2006JC003794>.
- IPCC, *Climate Change 2013 - The Physical Science Basis*, Cambridge University Press, Cambridge (2013), ISBN 9781107415324. URL <http://dx.doi.org/10.1017/CB09781107415324>.
- Istomina, L. G., von Hoyningen-Huene, W., Kokhanovsky, a. a., Burrows, J. P., The detection of cloud-free snow-covered areas using AATSR measurements, *Atmospheric Measurement Techniques*, 3(4) (2010):1005–1017, ISSN 1867-8548. URL <http://dx.doi.org/10.5194/amt-3-1005-2010>.
- Jerlov, N. G., Influence of Suspended and Dissolved Matter on the Transparency of Sea Water, *Tellus*, 5(1) (1953):59–65, ISSN 00402826. URL <http://dx.doi.org/10.1111/j.2153-3490.1953.tb01036.x>.
- Jones, G. S., Kennedy, J. J., Sensitivity of Attribution of Anthropogenic Near-Surface Warming to Observational Uncertainty, *Journal of Climate*, 30(12) (2017):4677–4691, ISSN 0894-8755. URL <http://dx.doi.org/10.1175/JCLI-D-16-0628.1>.
- Kalle, K., Nährstoff-Untersuchungen als hydrographisches Hilfsmittel zur Unterscheidung von Wasserkörpern., *Annl. Hydrogr. Berl.*, 65 (1937):1–18.
- , Fluoreszenz und Gelbstoff im Bottnischen und Finnischen Meerbusen, *Deutsche Hydrographische Zeitschrift*, 2 (1949):117–124.
- , What do we know about the “Gelbstoff”?, in *Symp. on radiant energy in the sea, UGGI monograph*, 10, Helsinki (1961), pp. 59–62.
- Keck, T., *Klassifizierung von Schnee und Eis anhand fernerkundeter Emissivität*, Master’s thesis, Freie Universität Berlin (2014). URL http://userpage.fu-berlin.de/geoiss/ress/Master/MSc-Keck_Therese-2014.pdf.
- Keck, T., Preusker, R., Fischer, J., Remote Sensing of Environment Retrieving snow and ice charac-

Bibliography

- teristics by remotely sensed emissivity using the multi-view brightness temperature within 8 μm to 14 μm , *Remote Sensing of Environment*, 201(September) (2017):181–195, ISSN 0034-4257. URL <http://dx.doi.org/10.1016/j.rse.2017.09.006>.
- , Estimating Chlorophyll-a Absorption with the Total Algae Peak Integration Retrieval TAPIR Considering Chlorophyll-a Fluorescence from Hyperspectral Top of the Atmosphere Signals in Optically Complex Waters (2018). URL <http://dx.doi.org/10.20944/PREPRINTS201802.0097.V1>.
- Kennedy, J. J., A review of uncertainty in in situ measurements and data sets of sea surface temperature, *Reviews of Geophysics*, 52(1) (2014):1–32, ISSN 87551209. URL <http://dx.doi.org/10.1002/2013RG000434>.
- Krause, G. H., Weis, E., Chlorophyll Fluorescence and Photosynthesis: The Basics, *Annual Review of Plant Physiology and Plant Molecular Biology*, 42(1) (1991):313–349, ISSN 1040-2519. URL <http://dx.doi.org/10.1146/annurev.pp.42.060191.001525>.
- Krüger, O., Kokhanovsky, A., Brockmann, C., Fischer, J., Pouliainen, J., Preusker, R., Rozanov, V., STSE - SnowRadiance Final Report (2011).
- Kumar, P., Kishtawal, C. M., Pal, P. K., Impact of satellite rainfall assimilation on Weather Research and Forecasting model predictions over the Indian region, *Journal of Geophysical Research: Atmospheres*, 119(5) (2014):2017–2031, ISSN 2169897X. URL <http://dx.doi.org/10.1002/2013JD020005>.
- Lake Erie LaMP, Lake Erie Binational Nutrient Management Strategy: Protecting Lake Erie by Managing Phosphorus. Prepared by the Lake Erie LaMP Work Group Nutrient Management Task Group, *Tech. rep.*, U.S. Department of Energy Office of Science (2008). URL https://www.epa.gov/sites/production/files/2015-09/documents/binational_nutrient_management.pdf.
- Le, C., Li, Y., Zha, Y., Sun, D., Specific absorption coefficient and the phytoplankton package effect in Lake Taihu, China, *Hydrobiologia*, 619(1) (2009a):27–37, ISSN 0018-8158. URL <http://dx.doi.org/10.1007/s10750-008-9579-6>.
- Le, C., Li, Y., Zha, Y., Sun, D., Huang, C., Lu, H., A four-band semi-analytical model for estimating chlorophyll a in highly turbid lakes: The case of Taihu Lake, China, *Remote Sensing of Environment*, 113(6) (2009b):1175–1182, ISSN 00344257. URL <http://dx.doi.org/10.1016/j.rse.2009.02.005>.
- Le Menn, M., About uncertainties in practical salinity calculations, *Ocean Science*, 7(5) (2011):651–659, ISSN 1812-0792. URL <http://dx.doi.org/10.5194/os-7-651-2011>.
- Lefering, I., Röttgers, R., Utschig, C., McKee, D., Uncertainty budgets for liquid waveguide CDOM absorption measurements, *Applied Optics*, 56(22) (2017):6357, ISSN 1559-128X. URL <http://dx.doi.org/10.1364/AO.56.006357>.
- León, P., Walsham, P., Bresnan, E., Hartman, S. E., Hughes, S., Mackenzie, K., Webster, L., Seasonal variability of the carbonate system and coccolithophore *Emiliana huxleyi* at a Scottish Coastal Observatory monitoring site, *Estuarine, Coastal and Shelf Science* (2018), ISSN 02727714. URL <http://dx.doi.org/10.1016/j.ecss.2018.01.011>.
- Letelier, R., An analysis of chlorophyll fluorescence algorithms for the moderate resolution imaging spectrometer (MODIS), *Remote Sensing of Environment*, 58(2) (1996):215–223, ISSN 00344257. URL [http://dx.doi.org/10.1016/S0034-4257\(96\)00073-9](http://dx.doi.org/10.1016/S0034-4257(96)00073-9).
- Li, X., Yang, X., Zheng, W., Zhang, J. A., Pietrafesa, L. J., Pichel, W. G., Synergistic Use of Satellite Observations and Numerical Weather Model to Study Atmospheric Occluded Fronts, *IEEE Transactions on Geoscience and Remote Sensing*, 53(9) (2015):5269–5279, ISSN 0196-2892. URL <http://dx.doi.org/10.1109/TGRS.2015.2420312>.
- Lindstrot, R., Preusker, R., Diedrich, H., Doppler, L., Bennartz, R., Fischer, J., 1D-Var retrieval of day-

- time total columnar water vapour from MERIS measurements, *Atmospheric Measurement Techniques*, 5(3) (2012):631–646, ISSN 1867-8548. URL <http://dx.doi.org/10.5194/amt-5-631-2012>.
- Lindstrot, R., Stengel, M., Schröder, M., Fischer, J., Preusker, R., Schneider, N., Steenbergen, T., Bojkov, B. R., A global climatology of total columnar water vapour from SSM/I and MERIS, *Earth System Science Data*, 6(1) (2014):221–233, ISSN 1866-3516. URL <http://dx.doi.org/10.5194/essd-6-221-2014>.
- Liu, X., Zhang, Y., Yin, Y., Wang, M., Qin, B., Wind and submerged aquatic vegetation influence bio-optical properties in large shallow Lake Taihu, China, *Journal of Geophysical Research: Biogeosciences*, 118(2) (2013):713–727, ISSN 21698961. URL <http://dx.doi.org/10.1002/jgrg.20054>.
- Loisel, H., Mériaux, X., Berthon, J.-F., Poteau, A., Investigation of the optical backscattering to scattering ratio of marine particles in relation to their biogeochemical composition in the eastern English Channel and southern North Sea, *Limnology and Oceanography*, 52(2) (2007):739–752, ISSN 00243590. URL <http://dx.doi.org/10.4319/lo.2007.52.2.0739>.
- Loisel, H., Stramski, D., Mitchell, B. G., Fell, F., Fournier-Sicre, V., Lemasle, B., Babin, M., Comparison of the ocean inherent optical properties obtained from measurements and inverse modeling., *Applied Optics*, 40(15) (2001):2384–97, ISSN 1559-128X. 98/98JC-02712, URL <http://dx.doi.org/10.1364/AO.40.002384>.
- Lu, Y., Li, L., Hu, C., Li, L., Zhang, M., Sun, S., Lv, C., Sunlight induced chlorophyll fluorescence in the near-infrared spectral region in natural waters: Interpretation of the narrow reflectance peak around 761 nm, *Journal of Geophysical Research: Oceans*, 121(7) (2016):5017–5029, ISSN 21699275. URL <http://dx.doi.org/10.1002/2016JC011797>.
- Lutz, S., Anesio, A. M., Raiswell, R., Edwards, A., Newton, R. J., Gill, F., Benning, L. G., The biogeography of red snow microbiomes and their role in melting arctic glaciers, *Nature Communications*, 7 (2016):11968, ISSN 2041-1723. URL <http://dx.doi.org/10.1038/ncomms11968>.
- Lyapustin, A., Tedesco, M., Wang, Y., Aoki, T., Hori, M., Kokhanovsky, A., Retrieval of snow grain size over Greenland from MODIS, *Remote Sensing of Environment*, 113(9) (2009):1976–1987, ISSN 00344257. URL <http://dx.doi.org/10.1016/j.rse.2009.05.008>.
- Maritorena, S., Morel, A., Gentili, B., Determination of the fluorescence quantum yield by oceanic phytoplankton in their natural habitat, *Applied Optics*, 39(36) (2000):6725, ISSN 0003-6935. URL <http://dx.doi.org/10.1364/AO.39.006725>.
- Marks, H., Heygster, G., Istomina, L., Cloud filtering with MERIS and AATSR for melt pond detection on Arctic sea ice, in *2016 IEEE International Geoscience and Remote Sensing Symposium (IGARSS)*, IEEE (2016), ISBN 978-1-5090-3332-4, pp. 7671–7674. URL <http://dx.doi.org/10.1109/IGARSS.2016.7731000>.
- Mascarenhas, V. J., Keck, T., Ocean optics and ocean color remote sensing, in *YOUMARES 8 proceedings*, Springer-Verlag, submitted for publication (2018).
- Matricardi, M., An assessment of the accuracy of the RTTOV fast radiative transfer model using IASI data, *Atmospheric Chemistry and Physics Discussions*, 9(2) (2009):9491–9535, ISSN 1680-7375. URL <http://dx.doi.org/10.5194/acpd-9-9491-2009>.
- Matthews, M. W., Bernard, S., Robertson, L., An algorithm for detecting trophic status (chlorophyll-a), cyanobacterial-dominance, surface scums and floating vegetation in inland and coastal waters, *Remote Sensing of Environment*, 124 (2012):637–652, ISSN 00344257. URL <http://dx.doi.org/10.1016/j.rse.2012.05.032>.
- Matthews, M. W., Odermatt, D., Improved algorithm for routine monitoring of cyanobacteria and eutrophication in inland and near-coastal waters, *Remote Sensing of Environment*, 156 (2015):374–

Bibliography

- 382, ISSN 00344257. URL <http://dx.doi.org/10.1016/j.rse.2014.10.010>.
- Maxwell, K., Johnson, G. N., Chlorophyll fluorescence—a practical guide, *Journal of Experimental Botany*, 51(345) (2000):659–668, ISSN 1460-2431. URL <http://dx.doi.org/10.1093/jexbot/51.345.659>.
- McClatchey, R. A., Fenn, R. W., Selby, J. E. A., Volz, F. E., Garing, J. S., Optical Properties of the atmosphere, *Tech. rep.* (1972). URL <http://www.dtic.mil/dtic/tr/fulltext/u2/753075.pdf>.
- McKee, D., Piskozub, J., Röttgers, R., Reynolds, R. A., Evaluation and Improvement of an Iterative Scattering Correction Scheme for in situ Absorption and Attenuation Measurements, *Journal of Atmospheric and Oceanic Technology*, 30(7) (2013):1527–1541, ISSN 0739-0572. URL <http://dx.doi.org/10.1175/JTECH-D-12-00150.1>.
- McKee, D., Röttgers, R., Neukermans, G., Calzado, V. S., Trees, C., Ampolo-Rella, M., Neil, C., Cunningham, A., Impact of measurement uncertainties on determination of chlorophyll-specific absorption coefficient for marine phytoplankton, *Journal of Geophysical Research: Oceans*, 119(12) (2014):9013–9025, ISSN 21699275. URL <http://dx.doi.org/10.1002/2014JC009909>.
- Meland, B., Kleiber, P. D., Grassian, V. H., Young, M. A., Correlated IR spectroscopy and visible light scattering measurements of mineral dust aerosol, *Journal of Geophysical Research*, 115(D20) (2010):D20208, ISSN 0148-0227. URL <http://dx.doi.org/10.1029/2010JD014389>.
- Merico, A., Tyrrell, T., Cokacar, T., Is there any relationship between phytoplankton seasonal dynamics and the carbonate system?, *Journal of Marine Systems*, 59(1-2) (2006):120–142, ISSN 09247963. URL <http://dx.doi.org/10.1016/j.jmarsys.2005.11.004>.
- Meroni, M., Rossini, M., Guanter, L., Alonso, L., Rascher, U., Colombo, R., Moreno, J., Remote sensing of solar-induced chlorophyll fluorescence: Review of methods and applications, *Remote Sensing of Environment*, 113(10) (2009):2037–2051, ISSN 00344257. URL <http://dx.doi.org/10.1016/j.rse.2009.05.003>.
- Mitchell, B. G., Algorithms for determining the absorption coefficient for aquatic particulates using the quantitative filter technique, in *Ocean Optics X*, vol. 1302, International Society for Optics and Photonics (1990), ISBN 9788578110796, ISSN 1098-6596, pp. 137–148. 1011.1669, URL <http://dx.doi.org/10.1117/12.21440>.
- Mobley, C. D., Estimation of the remote-sensing reflectance from above-surface measurements., *Applied optics*, 38(36) (1999):7442–7455, ISSN 0003-6935. URL <http://dx.doi.org/10.1364/AO.38.007442>.
- Mobley, C. D., Sundman, L. K., Boss, E., Phase function effects on oceanic light fields, *Applied Optics*, 41(6) (2002):1035, ISSN 0003-6935. URL <http://dx.doi.org/10.1364/AO.41.001035>.
- Moore, T. S., Dowell, M. D., Bradt, S., Ruiz Verdu, A., An optical water type framework for selecting and blending retrievals from bio-optical algorithms in lakes and coastal waters, *Remote Sensing of Environment*, 143 (2014):97–111, ISSN 00344257. URL <http://dx.doi.org/10.1016/j.rse.2013.11.021>.
- Moreira, D., Pires, J. C., Atmospheric CO₂ capture by algae: Negative carbon dioxide emission path, *Bioresource Technology*, 215 (2016):371–379, ISSN 0960-8524. URL <http://dx.doi.org/10.1016/J.BIORTECH.2016.03.060>.
- Morel, A., Optical modeling of the upper ocean in relation to its biogenous matter content (case I waters), *Journal of Geophysical Research*, 93(C9) (1988):10749, ISSN 0148-0227. URL <http://dx.doi.org/10.1029/JC093iC09p10749>.
- , Bio-optical Models, in *Encyclopedia of Ocean Sciences*, Elsevier (2001), pp. 317–326. URL <http://dx.doi.org/10.1006/rwos.2001.0407>.

- Morel, A., Prieur, L., Analysis of variations in ocean color, *Limnology and Oceanography*, 22(4) (1977):709–722, ISSN 00243590. URL <http://dx.doi.org/10.4319/lo.1977.22.4.0709>.
- Myhre, G., Shindell, D., Bréon, F.-M., Collins, W., Fuglestedt, J., Huang, J., Koch, D., Lamarque, J.-F., Lee, D., Mendoza, B., Nakajima, T., Robock, A., Stephens, G., Takemura, T., Zhang, H., Anthropogenic and natural radiative forcing, in *Climate Change 2013: The Physical Science Basis. Contribution of Working Group I to the Fifth Assessment Report of the Intergovernmental Panel on Climate Change*, edited by T. Stocker, D. Qin, G.-K. Plattner, M. Tignor, S. Allen, J. Boschung, A. Nauels, Y. Xia, V. Bex, P. Midgley, Cambridge University Press, Cambridge, United Kingdom and New York, NY, USA (2013). URL <http://www.ipcc.ch/report/ar5/wg1/>.
- Nechad, B., Ruddick, K., Schroeder, T., Oubelkheir, K., Blondeau-Patissier, D., Cherukuru, N., Brando, V., Dekker, A., Clementson, L., Banks, A. C., Maritorena, S., Werdell, P. J., Sá, C., Brotas, V., Caballero de Frutos, I., Ahn, Y.-H., Salama, S., Tilstone, G., Martinez-Vicente, V., Foley, D., McKibben, M., Nahorniak, J., Peterson, T., Siliò-Calzada, A., Röttgers, R., Lee, Z., Peters, M., Brockmann, C., CoastColour Round Robin data sets: a database to evaluate the performance of algorithms for the retrieval of water quality parameters in coastal waters, *Earth System Science Data*, 7(2) (2015):319–348, ISSN 1866-3516. URL <http://dx.doi.org/10.5194/essd-7-319-2015>.
- Neff, W., Compo, G. P., Martin Ralph, F., Shupe, M. D., Continental heat anomalies and the extreme melting of the Greenland ice surface in 2012 and 1889, *Journal of Geophysical Research: Atmospheres*, 119(11) (2014):6520–6536, ISSN 2169897X. URL <http://dx.doi.org/10.1002/2014JD021470>.
- Neville, R. a., Gower, J. F. R., Passive remote sensing of phytoplankton via chlorophyll α fluorescence, *Journal of Geophysical Research*, 82(24) (1977):3487–3493, ISSN 01480227. URL <http://dx.doi.org/10.1029/JC082i024p03487>.
- Nolin, A. W., Dozier, J., Estimating snow grain size using AVIRIS data, *Remote Sensing of Environment*, 44(2-3) (1993):231–238, ISSN 00344257. URL [http://dx.doi.org/10.1016/0034-4257\(93\)90018-S](http://dx.doi.org/10.1016/0034-4257(93)90018-S).
- Nordenskiöld, A. E., V.—Account of an Expedition to Greenland in the Year 1870, *Geological Magazine*, 9(98) (1872):355, ISSN 0016-7568. URL <http://dx.doi.org/10.1017/S0016756800465325>.
- Odén, S., Die Huminsäuren. Chemische, physikalische und bodenkundliche Forschungen, *Kolloid-chemische Beihefte*, 11(3-9) (1919):76–260. URL <https://link.springer.com/content/pdf/10.1007/BF02557436.pdf>.
- O'Reilly, J. E., Maritorena, S., Siegel, D., O'Brien, M. O., Toole, D., Mitchell, B. G., Kahru, M., Chavez, F., Strutton, P. G., Cota, G. F., Hooker, S. B., McClain, C., Carder, K., Muller-Karger, F., Harding, L., Magnuson, A., Phinney, D., Moore, G., Aiken, J., Arrigo, K. R., Letelier, R. M., Culver, M., *Ocean color chlorophyll a algorithms for SeaWiFS, OC2, and OC4: Version 4*, vol. 11, chap. 2, Goddard Space Flight Center, Greenbelt, Md. (2000), pp. 9–23. URL https://oceancolor.gsfc.nasa.gov/SeaWiFS/TECH_REPORTS/PLVo111.pdf.
- Otto, L., Investigations on optical properties and water-masses of the Southern North Sea, *Netherlands Journal of Sea Research*, 3(4) (1967):532–551, ISSN 00777579. URL [http://dx.doi.org/10.1016/0077-7579\(67\)90002-6](http://dx.doi.org/10.1016/0077-7579(67)90002-6).
- Painter, T. H., Dozier, J., Roberts, D. A., Davis, R. E., Green, R. O., Retrieval of subpixel snow-covered area and grain size from imaging spectrometer data, *Remote Sensing of Environment*, 85(1) (2003):64–77, ISSN 00344257. URL [http://dx.doi.org/10.1016/S0034-4257\(02\)00187-6](http://dx.doi.org/10.1016/S0034-4257(02)00187-6).
- Palmer, S., Odermatt, D., Hunter, P., Brockmann, C., Présing, M., Balzter, H., Tóth, V., Satellite remote sensing of phytoplankton phenology in Lake Balaton using 10years of MERIS observations, *Remote Sensing of Environment*, 158 (2015):441–452, ISSN 00344257. URL <http://dx.doi.org/>

Bibliography

- 10.1016/j.rse.2014.11.021.
- Pedrós, R., Moya, I., Goulas, Y., Jacquemoud, S., Chlorophyll fluorescence emission spectrum inside a leaf, *Photochemical & Photobiological Sciences*, 7(4) (2008):498, ISSN 1474-905X. URL <http://dx.doi.org/10.1039/b719506k>.
- Pepe, M., Brivio, P. a., Rampini, a., Nodari, F. R., Boschetti, M., Snow cover monitoring in Alpine regions using ENVISAT optical data, *International Journal of Remote Sensing*, 26(21) (2005):4661–4667, ISSN 0143-1161. URL <http://dx.doi.org/10.1080/01431160500206635>.
- Petty, G. W., *A First Course in Atmospheric Science*, 2. Edition, Sundog Publishing, Madison, Wisconsin (2006), ISBN 0972903313.
- Petzold, T. J., Volume Scattering Functions For Selected Ocean Waters, *Tech. rep.*, Naval Air Development Center, Warminster, Pennsylvania (1972).
- Plass, G. N., Kattawar, G. W., Radiative Transfer in an Atmosphere–Ocean System, *Applied Optics*, 8(2) (1969):455, ISSN 0003-6935. URL <http://dx.doi.org/10.1364/AO.8.000455>.
- Pope, R. M., Fry, E. S., Absorption spectrum (380–700 nm) of pure water II Integrating cavity measurements, *Applied Optics*, 36(33) (1997):8710, ISSN 0003-6935. URL <http://dx.doi.org/10.1364/AO.36.008710>.
- Porcar-Castell, A., Tyystjärvi, E., Atherton, J., Van Der Tol, C., Flexas, J., Pfündel, E. E., Moreno, J., Frankenberg, C., Berry, J. a., Linking chlorophyll a fluorescence to photosynthesis for remote sensing applications: Mechanisms and challenges, *Journal of Experimental Botany*, 65(15) (2014):4065–4095, ISSN 14602431. URL <http://dx.doi.org/10.1093/jxb/eru191>.
- Reinart, A., Paavel, B., Pierson, D., Niklas, S., Inherent and apparent properties of Lake Peipsi, Estonia, *Boreal Environment Research*, 9 (2004):429–445. URL https://www.researchgate.net/profile/Birgot_Paavel/publication/229045387_Inherent_and_apparent_optical_properties_of_Lake_Peipsi_Estonia/links/0fcfd503c634ea3066000000.pdf.
- Rhein, M., Rintoul, S., Aoki, S., Campos, E., Chambers, D., Feely, R., Gulev, S., Johnson, G., Josey, S., Kostianoy, A., Mauritzen, C., Roemmich, D., Talley, L., Wang, F., Observations: Ocean, in *Climate Change 2013: The Physical Science Basis. Contribution of Working Group I to the Fifth Assessment Report of the Intergovernmental Panel on Climate Change*, edited by T. Stocker, D. Qin, G.-K. Plattner, M. Tignor, S. Allen, J. Boschung, A. Nauels, Y. Xia, V. Bex, P. Midgley, chap. 3, Cambridge University Press, Cambridge, United Kingdom and New York, NY, USA (2013). URL <http://www.ipcc.ch/report/ar5/wg1/>.
- Roesler, C. S., Perry, M. J., In situ phytoplankton absorption, fluorescence emission, and particulate backscattering spectra determined from reflectance, *Journal of Geophysical Research*, 100(C7) (1995):13279, ISSN 0148-0227. URL <http://dx.doi.org/10.1029/95JC00455>.
- Roesler, C. S., Perry, M. J., Carder, K. L., Modeling in situ phytoplankton absorption from total absorption spectra in productive inland marine waters, *Limnology and Oceanography*, 34(8) (1989):1510–1523, ISSN 00243590. URL <http://dx.doi.org/10.4319/lo.1989.34.8.1510>.
- Rowe, M. D., Anderson, E. J., Wynne, T. T., Stumpf, R. P., Fanslow, D. L., Kijanka, K., Vanderploeg, H. A., Strickler, J. R., Davis, T. W., Vertical distribution of buoyant *Microcystis* blooms in a Lagrangian particle tracking model for short-term forecasts in Lake Erie, *Journal of Geophysical Research: Oceans*, 121(7) (2016):5296–5314, ISSN 21699275. URL <http://dx.doi.org/10.1002/2016JC011720>.
- Ryu, J.-H., Han, H.-J., Cho, S., Park, Y.-J., Ahn, Y.-H., Overview of geostationary ocean color imager (GOCI) and GOCI data processing system (GDPS), *Ocean Science Journal*, 47(3) (2012):223–233, ISSN 1738-5261. URL <http://dx.doi.org/10.1007/s12601-012-0024-4>.

- Salisbury, J. W., D'Aria, D. M., Wald, A., Measurements of thermal infrared spectral reflectance of frost, snow, and ice, *Journal of Geophysical Research: Solid Earth*, 99(B12) (1994):24235–24240, ISSN 01480227. URL <http://dx.doi.org/10.1029/94JB00579>.
- Santer, B. D., Solomon, S., Pallotta, G., Mears, C., Po-Chedley, S., Fu, Q., Wentz, F., Zou, C.-Z., Painter, J., Cvijanovic, I., Bonfils, C., Comparing Tropospheric Warming in Climate Models and Satellite Data, *Journal of Climate*, 30(1) (2017):373–392, ISSN 0894-8755. URL <http://dx.doi.org/10.1175/JCLI-D-16-0333.1>.
- Sayer, A. M., Hsu, N. C., Bettenhausen, C., Jeong, M.-J., Validation and uncertainty estimates for MODIS Collection 6 “Deep Blue” aerosol data, *Journal of Geophysical Research: Atmospheres*, 118(14) (2013):7864–7872, ISSN 2169897X. URL <http://dx.doi.org/10.1002/jgrd.50600>.
- Scambos, T., Haran, T., Fahnestock, M., Painter, T., Bohlander, J., MODIS-based Mosaic of Antarctica (MOA) data sets: Continent-wide surface morphology and snow grain size, *Remote Sensing of Environment*, 111(2-3) (2007):242–257, ISSN 00344257. URL <http://dx.doi.org/10.1016/j.rse.2006.12.020>.
- Schaeffer, B., Loftin, K., Stumpf, R., Werdell, P., Agencies Collaborate, Develop a Cyanobacteria Assessment Network, *Eos*, 96 (2015), ISSN 2324-9250. URL <http://dx.doi.org/10.1029/2015E0038809>.
- Schalles, J. F., Optical remote sensing techniques to estimate phytoplankton chlorophyll a concentrations in coastal, in *Remote sensing of aquatic coastal ecosystem processes*, edited by L. L. Richardson, E. F. LeDrew, chap. 3, Springer Science & Business Media (2006), ISBN 1402039670, pp. 27–79. URL http://dx.doi.org/10.1007/1-4020-3968-9_3.
- Schmetz, J., Pili, P., Tjemkes, S., Just, D., Kerkmann, J., Rota, S., Ratier, A., An Introduction to Meteosat Second Generation (MSG), *Bulletin of the American Meteorological Society*, 83(7) (2002):977–992, ISSN 0003-0007. URL [http://dx.doi.org/10.1175/1520-0477\(2002\)083<0977:AITMSG>2.3.CO;2](http://dx.doi.org/10.1175/1520-0477(2002)083<0977:AITMSG>2.3.CO;2).
- Seiz, G., Foppa, N., Meier, M., Paul, F., The Role of Satellite Data Within GCOS Switzerland, *Remote Sensing*, 3(12) (2011):767–780, ISSN 2072-4292. URL <http://dx.doi.org/10.3390/rs3040767>.
- Snyder, W. C., Wan, Z., Zhang, Y., Feng, Y.-Z., Classification-based emissivity for land surface temperature measurement from space, *International Journal of Remote Sensing*, 19(14) (1998):2753–2774, ISSN 0143-1161. URL <http://dx.doi.org/10.1080/014311698214497>.
- Stamnes, K., Li, W., Eide, H., Aoki, T., Hori, M., Storvold, R., ADEOS-II/GLI snow/ice products — Part I: Scientific basis, *Remote Sensing of Environment*, 111(2-3) (2007):258–273, ISSN 00344257. URL <http://dx.doi.org/10.1016/j.rse.2007.03.023>.
- Stamnes, K., Tsay, S.-C., Wiscombe, W., Jayaweera, K., Numerically stable algorithm for discrete-ordinate-method radiative transfer in multiple scattering and emitting layered media, *Applied Optics*, 27(12) (1988):2502, ISSN 0003-6935. URL <http://dx.doi.org/10.1364/AO.27.002502>.
- Stengel, M., Stapelberg, S., Sus, O., Schlundt, C., Poulsen, C., Thomas, G., Christensen, M., Carbajal Henken, C., Preusker, R., Fischer, J., Devasthale, A., Willén, U., Karlsson, K.-G., McGarragh, G. R., Proud, S., Povey, A. C., Grainger, R. G., Meirink, J. F., Feofilov, A., Bennartz, R., Bojanowski, J. S., Hollmann, R., Cloud property datasets retrieved from AVHRR, MODIS, AATSR and MERIS in the framework of the Cloud_cci project, *Earth System Science Data*, 9(2) (2017):881–904, ISSN 1866-3516. URL <http://dx.doi.org/10.5194/essd-9-881-2017>.
- Stibal, M., Box, J. E., Cameron, K. A., Langen, P. L., Yallop, M. L., Mottram, R. H., Khan, A. L., Molotch, N. P., Christmas, N. A. M., Cali Quaglia, F., Remias, D., Smeets, C. J. P. P., van den Broeke, M. R., Ryan, J. C., Hubbard, A., Tranter, M., van As, D., Ahlstrøm, A. P., Algae Drive Enhanced Darkening of Bare Ice on the Greenland Ice Sheet, *Geophysical Research Letters*, 44(22)

Bibliography

- (2017):11,463–11,471, ISSN 00948276. URL <http://dx.doi.org/10.1002/2017GL075958>.
- Stroeve, J., Nolin, A., Steffen, K., Comparison of AVHRR-derived and in situ surface albedo over the greenland ice sheet, *Remote Sensing of Environment*, 62(3) (1997):262–276, ISSN 00344257. URL [http://dx.doi.org/10.1016/S0034-4257\(97\)00107-7](http://dx.doi.org/10.1016/S0034-4257(97)00107-7).
- Stumpf, R. P., Wynne, T. T., Baker, D. B., Fahnenstiel, G. L., Interannual Variability of Cyanobacterial Blooms in Lake Erie, *PLoS ONE*, 7(8) (2012):1–11, ISSN 1932-6203. URL <http://dx.doi.org/10.1371/journal.pone.0042444>.
- Tagliabue, A., Bopp, L., Gehlen, M., The response of marine carbon and nutrient cycles to ocean acidification: Large uncertainties related to phytoplankton physiological assumptions, *Global Biogeochemical Cycles*, 25(3) (2011):1–3, ISSN 08866236. URL <http://dx.doi.org/10.1029/2010GB003929>.
- Takeuchi, N., Kohshima, S., Segawa, T., Effect of cryoconite and snow algal communities on surface albedo on maritime glaciers in south alaska, *Bulletin of Glaciological Research*, 20 (2003):21–27. URL https://www.researchgate.net/publication/267631131_Effect_of_cryoconite_and_snow_algal_communities_on_surface_albedo_on_maritime_glaciers_in_south_Alaska.
- Tanikawa, T., Aoki, T., Nishio, F., Remote sensing of snow grain-size and impurities from Airborne Multispectral Scanner data using a snow bidirectional reflectance distribution function model, *Annals of Glaciology*, 34(1) (2002):74–80, ISSN 02603055. URL <http://dx.doi.org/10.3189/172756402781817437>.
- Tedesco, M., Fettweis, X., van den Broeke, M. R., van de Wal, R. S. W., Smeets, C. J. P. P., van de Berg, W. J., Serreze, M. C., Box, J. E., The role of albedo and accumulation in the 2010 melting record in Greenland, *Environmental Research Letters*, 6(1) (2011):1–6, ISSN 1748-9326. URL <http://dx.doi.org/10.1088/1748-9326/6/1/014005>.
- Tedstone, A. J., Bamber, J. L., Cook, J. M., Williamson, C. J., Fettweis, X., Hodson, A. J., Tranter, M., Dark ice dynamics of the south-west Greenland Ice Sheet, *The Cryosphere*, 11(6) (2017):2491–2506, ISSN 1994-0424. URL <http://dx.doi.org/10.5194/tc-11-2491-2017>.
- Thies, B., Bendix, J., Satellite based remote sensing of weather and climate: recent achievements and future perspectives, *Meteorological Applications*, 18(3) (2011):262–295, ISSN 13504827. URL <http://dx.doi.org/10.1002/met.288>.
- Trenberth, K. E., Fasullo, J. T., Kiehl, J., Earth's Global Energy Budget, *Bulletin of the American Meteorological Society*, 90(3) (2009):311–323, ISSN 0003-0007. URL <http://dx.doi.org/10.1175/2008BAMS2634.1>.
- Treut, L., Somerville, R., Cubasch, U., Ding, Y., Mauritzen, C., Mokssit, A., Peterson, T., Prather, M., Qin, D., Manning, M., Chen, Z., Marquis, M., Averyt, K. B., Tignor, M., Kingdom, U., Historical Overview of Climate Change Science, in *Climate Change 2007: The Physical Science Basis. Contribution of Working Group I to the Fourth Assessment Report of the Intergovernmental Panel on Climate Change*, edited by S. Solomon, D. Qin, M. Manning, Z. Chen, M. Marquis, K. Averyt, M. Tignor, H. Miller, chap. 1, Cambridge, United Kingdom and New York, NY, USA (2007), pp. 92–128. URL <https://www.ipcc.ch/pdf/assessment-report/ar4/wg1/ar4-wg1-chapter1.pdf>.
- Uetake, J., Naganuma, T., Hebsgaard, M. B., Kanda, H., Kohshima, S., Communities of algae and cyanobacteria on glaciers in west Greenland, *Polar Science*, 4(1) (2010):71–80, ISSN 18739652. URL <http://dx.doi.org/10.1016/j.polar.2010.03.002>.
- U.S. DOE, Carbon Cycling and Biosequestration. Report from the March 2008 Workshop,, *Tech. rep.*, U.S. Department of Energy Office of Science (2008). URL <http://genomicscience.energy.gov/carboncycle/report/>.
- Valente, A., Sathyendranath, S., Brotas, V., Groom, S., Grant, M., Taberner, M., Antoine, D., Arnone,

- R., Balch, W. M., Barker, K., Barlow, R., Bélanger, S., Berthon, J.-F., Beşiktepe, , Brando, V., Canuti, E., Chavez, F., Claustre, H., Crout, R., Frouin, R., García-Soto, C., Gibb, S. W., Gould, R., Hooker, S., Kahru, M., Klein, H., Kratzer, S., Loisel, H., McKee, D., Mitchell, B. G., Moisan, T., Muller-Karger, F., O’Dowd, L., Ondrusek, M., Poulton, A. J., Repecaud, M., Smyth, T., Sosik, H. M., Twardowski, M., Voss, K., Werdell, J., Wernand, M., Zibordi, G., A compilation of global bio-optical in situ data for ocean-colour satellite applications, *Earth System Science Data*, 8(1) (2016):235–252, ISSN 1866-3516. URL <http://dx.doi.org/10.5194/essd-8-235-2016>.
- Vaughan, D., Comiso, J., Allison, I., Carrasco, J., Kaser, G., Kwok, R., Mote, P., Murray, T., Paul, F., Ren, J., Rignot, E., Solomina, O., Steffen, K., Zhang, T., Observations: Cryosphere, in *Climate Change 2013: The Physical Science Basis. Contribution of Working Group I to the Fifth Assessment Report of the Intergovernmental Panel on Climate Change*, edited by T. Stocker, D. Qin, G.-K. Plattner, M. Tignor, S. Allen, J. Boschung, A. Nauels, Y. Xia, V. Bex, P. Midgley, chap. 4, Cambridge University Press, Cambridge, United Kingdom and New York, NY, USA (2013). URL <http://www.ipcc.ch/report/ar5/wg1/>.
- Vermote, E., Justice, C., Csizsar, I., Early evaluation of the VIIRS calibration, cloud mask and surface reflectance Earth data records, *Remote Sensing of Environment*, 148 (2014):134–145, ISSN 00344257. URL <http://dx.doi.org/10.1016/j.rse.2014.03.028>.
- Vincent, R. K., Qin, X., McKay, R. L., Miner, J., Czajkowski, K., Savino, J., Bridgeman, T., Phycocyanin detection from LANDSAT TM data for mapping cyanobacterial blooms in Lake Erie, *Remote Sensing of Environment*, 89(3) (2004):381–392, ISSN 0034-4257. URL <http://dx.doi.org/10.1016/J.RSE.2003.10.014>.
- Wan, Z., Zhang, Y., MODIS UCSB Emissivity Library (1999). URL <http://www.icess.ucsb.edu/modis/EMIS/html/em.html>.
- Wang, Y., Huang, X., Liang, H., Sun, Y., Feng, Q., Liang, T., Tracking Snow Variations in the Northern Hemisphere Using Multi-Source Remote Sensing Data (2000–2015), *Remote Sensing*, 10(1) (2018):136, ISSN 2072-4292. URL <http://dx.doi.org/10.3390/rs10010136>.
- Wang, L., Qiu, Z., Pang, H., Liu, Y., Chen, Y., Jiang, L., Chlorophyll fluorescence extraction from water-leaving radiance of algae-containing water through polarization, *Journal of Ocean University of China*, 16(6) (2017):1003–1008, ISSN 1672-5182. URL <http://dx.doi.org/10.1007/s11802-017-3276-x>.
- Wentz, F. J., Satellite Measurements of Sea Surface Temperature Through Clouds, *Science*, 288(5467) (2000):847–850, ISSN 00368075. URL <http://dx.doi.org/10.1126/science.288.5467.847>.
- Williamson, C. J., Anesio, A. M., Cook, J., Tedstone, A., Poniecka, E., Holland, A., Fagan, D., Tranter, M., Yallop, M. L., Ice algal bloom development on the surface of the Greenland Ice Sheet, *FEMS Microbiology Ecology*, 94(3) (2018), ISSN 1574-6941. URL <http://dx.doi.org/10.1093/femsec/fiy025>.
- Wiscombe, W. J., Warren, S. G., A Model for the Spectral Albedo of Snow. I: Pure Snow, *Journal of the Atmospheric Sciences*, 37(12) (1980):2712–2733, ISSN 0022-4928. URL [https://doi.org/10.1175/1520-0469\(1980\)037<2712:AMFTSA>2.0.CO;2](https://doi.org/10.1175/1520-0469(1980)037<2712:AMFTSA>2.0.CO;2).
- Wynne, T. T., Stumpf, R. P., Tomlinson, M. C., Warner, R. A., Tester, P. A., Dyble, J., Fahnenstiel, G. L., Relating spectral shape to cyanobacterial blooms in the Laurentian Great Lakes, *International Journal of Remote Sensing*, 29(12) (2008):3665–3672, ISSN 0143-1161. URL <http://dx.doi.org/10.1080/01431160802007640>.
- Xing, X.-G., Zhao, D.-Z., Liu, Y.-G., Yang, J.-H., Xiu, P., Wang, L., An overview of remote sensing of chlorophyll fluorescence, *Ocean Science Journal*, 42(1) (2007):49–59, ISSN 1738-5261. URL <http://>

Bibliography

- [//dx.doi.org/10.1007/BF03020910](http://dx.doi.org/10.1007/BF03020910).
- Xiong, J., Toller, G., Chiang, V., Sun, J., Esposito, J., Barnes, W., MODIS Level 1B Algorithm Theoretical Basis Document, *Tech. rep.*, National Aeronautics Space and Administration (2013). URL http://mcst.gsfc.nasa.gov/sites/mcst.gsfc/files/file_attachments/MODIS_L1B_ATBD_ver4.pdf.
- Yallop, M. L., Anesio, A. M., Perkins, R. G., Cook, J., Telling, J., Fagan, D., MacFarlane, J., Stibal, M., Barker, G., Bellas, C., Hodson, A., Tranter, M., Wadham, J., Roberts, N. W., Photophysiology and albedo-changing potential of the ice algal community on the surface of the Greenland ice sheet, *ISME Journal*, 6(12) (2012):2302–2313, ISSN 17517362. URL <http://dx.doi.org/10.1038/ismej.2012.107>.
- Yang, J., Gong, P., Fu, R., Zhang, M., Chen, J., Liang, S., Xu, B., Shi, J., Dickinson, R., The role of satellite remote sensing in climate change studies, *Nature Climate Change*, 3(10) (2013):875–883, ISSN 1758-678X. URL <http://dx.doi.org/10.1038/nclimate1908>.
- Zarco-Tejada, P. J., Miller, J. R., Mohammed, G. H., Noland, T. L., Sampson, P. H., Estimation of chlorophyll fluorescence under natural illumination from hyperspectral data, *International Journal of Applied Earth Observation and Geoinformation*, 3(4) (2001):321–327, ISSN 03032434. URL [http://dx.doi.org/10.1016/S0303-2434\(01\)85039-X](http://dx.doi.org/10.1016/S0303-2434(01)85039-X).
- Zheng, G., Stramski, D., DiGiacomo, P. M., A model for partitioning the light absorption coefficient of natural waters into phytoplankton, nonalgal particulate, and colored dissolved organic components: A case study for the Chesapeake Bay, *Journal of Geophysical Research: Oceans*, 120(4) (2015):2601–2621, ISSN 21699275. URL <http://dx.doi.org/10.1002/2014JC010604>.
- Zhou, J., Gilerson, A., Ioannou, I., Hlaing, S., Schalles, J., Gross, B., Moshary, F., Ahmed, S., Retrieving quantum yield of sun-induced chlorophyll fluorescence near surface from hyperspectral in-situ measurement in productive water, *Optics Express*, 16(22) (2008):17468, ISSN 1094-4087. URL <http://dx.doi.org/10.1364/OE.16.017468>.
- Zickfeld, K., Solomon, S., Gilford, D. M., Centuries of thermal sea-level rise due to anthropogenic emissions of short-lived greenhouse gases, *Proceedings of the National Academy of Sciences*, 114(4) (2017):657–662, ISSN 0027-8424. URL <http://dx.doi.org/10.1073/pnas.1612066114>.

List of Tables

2.1	Constants for Planck's Law	26
3.1	Overview of selected AATSR snow and ice scenes	50
3.2	Surface temperature and $TCWV$ of atmospheric vertical standard profiles	56
3.3	Temperature and emissivity residuals statistics of snow and ice pixels	57
3.4	Portions of <i>valid</i> , <i>invalid</i> , classified and <i>indistinct</i> snow and ice pixels	60
4.1	Overview of parameters varied in MOMO simulations	87
4.2	List of variables x and their σ_x used in uncertainty calculation of σ_a	107
4.3	List of parameters p and their σ_p used in the uncertainty estimation of σ_{TAP}	107
4.4	Uncertainty of supplemental sensors	109

List of Figures

1.1	Snow coverage of the northern hemisphere in April and September 2003	3
1.2	Meteosat-10 RGB image of Europe	6
1.3	Radiative energy budget	8
1.4	Radiative forcing	8
1.5	Remotely sensed number of days of snow coverage and melt-onset	10
1.6	Scheme of the carbon cycle in the marine ecosystem	11
1.7	Algae on the western Greenland ice sheet	13
1.8	Reflectance of snow, bare ice, and algae growing on ice	15
2.1	Spectral atmospheric radiation and the major absorbing components	24
2.2	Concept of a blackbody	26
2.3	Planck's Law	27
2.4	Relation of brightness temperature and emissivity	28
2.5	Colours of waters	30
2.6	Water IOPs	30
2.7	Phytoplankton phase function	32
2.8	The process end effects of fluorescence	33
2.9	Spectral absorption of cdom	35
2.10	Bio-optical models for phytoplankton for various oceanic regions	38
2.11	Atmospheric transmission	42
3.1	Map of AATSR scenes	49
3.2	RGB image of North-Greenland	51
3.3	Measured nadir emissivity above snow with various grain sizes	54
3.4	Vertical atmospheric standard profiles of temperature and water vapour	55
3.5	Snow and ice emissivity classification scheme	64
3.6	Nested portions of <i>valid</i> and <i>invalid</i> snow and ice pixels for case 8	67
3.7	Map of <i>valid</i> and <i>invalid</i> pixels for scene 8	68

List of Figures

3.8	Details of <i>invalid</i> pixels for case 8	69
3.9	Portions of classified, <i>unclassified</i> , <i>indistinct</i> , <i>wet</i> , and <i>invalid</i> pixels for all AATSR scenes	70
4.1	Details of simulated BOA reflectance	82
4.2	Phytoplankton absorption and single scattering albedo	88
4.3	MOMO sensitivity to fluorescence	89
4.4	Experimental MOMO simulations analysing implemented fluorescence	91
4.5	Variation of phytoplankton IOPs in MOMO	93
4.6	Excitation and <i>FA</i> dependent on depth	95
4.7	Relative error using 1 m-layers in simulations	96
4.8	Reflectance and fluorescence for lowered phytoplankton	97
4.9	Impact of lowering phytoplankton	97
4.10	MOMO phytoplankton peak compared to measurements	99
4.11	Integration of reflectance peak (TAP)	101
4.12	Retrieved <i>TAPs</i> over <i>a670</i> and their variants	103
4.13	Jacobians of reference <i>TAPIR</i> function	104
4.14	Summands of uncertainty calculation	108
4.15	Spectral arrangement and <i>a670</i> uncertainty of supplemental sensors	110
4.16	Preparing Ocean and Land Colour Imager (OLCI) reflectance for TAPIR	110
4.17	TAPIR validation	113
5.1	Location of Lake Erie	123
5.2	Lake Erie RGB and TAPIR/OLCI for 2017-09-15	125
5.3	Chlorophyll-a retrievals applied to Lake Erie	126
5.4	OLCI RGB image of a partly frozen and snow covered Lake Erie	127
5.5	Chlorophyll-a retrievals applied to a partly snow and ice covered Lake Erie	129
5.6	Map of classified snow and ice pixels at Lake Erie	130
5.7	Histograms of classified and invalid pixels for Lake Erie scene	131
5.8	Portion of invalid pixels of the scene at Lake Erie	131
5.9	Meteorological conditions around Lake Erie in February 2018	133

List of acronyms

AATSR	Advanced Along-Track Spectral Radiometer
ADEOS-2	Advanced Earth Observing Satellite 2
AERONET	Aerosol Robotic Network
AMSR-E	Advanced Microwave Scanning Radiometer - Earth Observing System
<i>aot</i>	aerosol optical thickness
AVHRR	Advanced Very High Resolution Radiometer
AVIRIS	Airborne Visible/Infrared Imaging Spectrometer
<i>BG</i>	blue-green ratio
BOA	bottom of the atmosphere
BOM	bio-optical model
<i>cdom</i>	coloured dissolved organic matter
CFC	Chlorofluorocarbon
<i>CI</i>	Cyanobacterial Index
CO ₂	carbon dioxide
COMS-1	Communication Ocean and Meteorological Satellite 1
DISORT	Discrete Ordinate Radiative Transfer Model
DWD	<i>Deutscher Wetterdienst</i>
ECV	essential climate variables
EnMAP	Environmental Mapping and Analysis Program
ENVISAT	Environmental Satellite
<i>FF</i>	Fournier-Forand phase function
<i>F</i>	fluorescence

List of acronyms

<i>FLH</i>	Fluorescence Line Height
GCOS	Global Climate Observation System
GLI	Global Imager
GOCI	Geostationary Ocean Color Imager
HAB	harmful algae bloom
HICO	Hyperspectral Imager for the Coastal Ocean
HSI	Hyperspectral Imager
IMS	Indian Micro-Satellite
InW	Indonesian waters
IOP	inherent optical property
IPCC	Intergovernmental Panel on Climate Change
ISS	International Space Station
LT	local time
LUT	look-up table
<i>MCI</i>	Maximum Chlorophyll Index
MEMSCAG	Multiple Endmember Snow-Covered Area and Grain size
MERIS	Medium Resolution Imaging Spectrometer
MOA	Mosaic over Antarctica
MODIS	Moderate Resolution Imaging Spectrometer
MOM0	Matrix Operator Model
<i>MPH</i>	Maximum Peak Height
MSG	Meteosat Second Generation
MSG-10	Meteosat Second Generation 10
NDCI	Normalised Difference Cloud Index
NIR	near infra-red
NoS	North Sea
OAC	optically active constituent
<i>OC4</i>	Ocean Colour quartic algorithm
<i>OC4E</i>	Ocean Colour quartic algorithm for MERIS
OLCI	Ocean and Land Colour Imager
PAR	photosynthetical active radiation
RGB	Red-Green-Blue

RMSE	Root Mean Square Error
RTE	radiative transfer equation
RTM	radiative transfer model
RTTOV	Radiative Transfer for TIROS Operational Vertical Sounder
S3	Sentinel-3
S5	Sentinel-5
SEVIRI	Spinning Enhanced Visible and Infrared Imager
SLSTR	Sea and Land Surface Temperature Radiometer
SNAP	Sentinel Application Platform
SWIR	short-wave infra-red
<i>TAP</i>	total algae peak
<i>TAPIR</i>	Total Algae Peak Integration Retrieval
TIR	thermal infra-red
TIROS-N	Television Infrared Observation Satellite Next-generation
TM	Thematic Mapper
TOA	top of the atmosphere
TOMS	Total Ozone Mapping Spectrometer
TROPOMI	Tropospheric Monitoring Instrument
<i>TSM</i>	total suspended matter
UV	ultra-violet
VIS	visible spectrum

List of symbols

<i>A</i>	fluorescence excitation [W m^{-2}]
<i>a</i>	absorption coefficient [m^{-1}]
<i>a440</i>	chlorophyll-a absorption coefficient at 440 nm [m^{-1}]
<i>a670</i>	chlorophyll-a absorption coefficient at 670 nm [m^{-1}]
<i>aot</i>	aerosol optical thickness [dl]
<i>atm</i>	vertical profile model
<i>B</i>	spectral radiance of a body [$\text{W m}^{-2} \mu\text{m}^{-1} \text{sr}^{-1}$]
<i>b</i>	scattering coefficient [m^{-1}]
<i>BG</i>	blue-green ratio [dl]
<i>BT</i>	brightness temperature [K]
<i>BT_{meas}^{TOA}</i>	measured brightness temperature at top of the atmosphere [K]
<i>BT_{sim}^{TOA}</i>	simulated brightness temperature at top of the atmosphere [K]
<i>c</i>	extinction coefficient [m^{-1}]
<i>cdom</i>	coloured dissolved organic matter (yellow substance, gelbstoff) [m^{-1}]
χ	deviation of the brightness temperature with the emissivity [K]
<i>chl-a</i>	chlorophyll-a concentration [mg m^{-3}]
<i>c_s</i>	speed of light in a vacuum $2.998 \cdot 10^8 \text{ m s}^{-1}$
<i>E</i>	irradiance (hemispherically integrated radiance) [$\text{W m}^{-2} \text{nm}^{-1}$]
<i>E_d</i>	downwelling irradiance [$\text{W m}^{-2} \text{nm}^{-1}$]
ε	emissivity [dl]
ε^*	emissivity at 10.85 nm of 0.99 [dl]
<i>F</i>	fluorescence [sr^{-1}]
<i>FF</i>	Fournier-Forand phase function for phytoplankton [sr^{-1}]

List of symbols

G	Gaussian distribution [dl]
h	Planck constant $6.626 \cdot 10^{-24}$ Js
J	RTE source function [$\text{W m}^{-2} \text{sr nm}$]
k_B	Boltzmann constant $1.381 \cdot 10^{-23}$ J K ⁻¹
L	radiance or radiant intensity [$\text{W m}^{-2} \text{nm}^{-1} \text{sr}^{-1}$]
λ	wavelength [nm]; centre wavelength of a sensor's channel [nm]
LST	land surface temperature [K]
L_u	upwelling radiance [$\text{W m}^{-2} \text{nm}^{-1} \text{sr}^{-1}$]
L_w	water-leaving radiance [$\text{W m}^{-2} \text{nm}^{-1} \text{sr}^{-1}$]
ω_0	single scattering albedo [dl]
R	reflectance (ratio of L_u and E_d) [$\text{W m}^{-2} \text{sr}^{-1}$]
R_{RS}	remote sensing reflectance (ratio of L_w and E_d) [$\text{W m}^{-2} \text{sr}^{-1}$]
T	temperature [K]
TAP	total algae peak (integrated) [$\text{sr}^{-1} \text{nm}$]
$TCWV$	total column water vapour [mm]
θ	sun zenith angle [°]
ϑ	viewing zenith angle [°]
T_s	surface temperature [K]
TSM	total suspended matter [mg m^{-3}]

Curriculum Vitae

For reasons of data protection, the curriculum vitae is not included in the online version.

Danksagung

Ich möchte mich sehr herzlich bei Prof. Dr. Jürgen Fischer für die langjährige Zusammenarbeit und die Ermöglichung zur Anfertigung meiner Doktorarbeit sowie deren Betreuung bedanken. Prof. Dr. Luis Guanter, danke ich für die Übernahme des Zweit-Gutachtens und äußerst lehrreiche Vorlesungen während meines Studiums.

René Preusker leistete mir bei vielen geistigen und technischen Problemen wichtige Hilfestellungen und Nicole Docter war die beste vorstellbare Büro-Kollegin. Abseits des Bildschirms habem mir alle ehemaligen und derzeitigen Kollegen am WeW eine wunderbar angenehme Arbeitsatmosphäre mit ausgedehnten Kaffeepausen, Balkon-Ausflügen, Darts-Runden, amüsanten Konferenzfahrten und inspirierende Gespräche geschaffen. Danke Bennet, Lena und Nicole für's Korrekturlesen. Bei meinen Freunden möchte ich mich für Nachsicht in intensiven Phasen und für allgemeine Erheiterung bedanken. Juchhe!

Ein ganz besonderen Dank gebührt meinen Eltern, die mir während meines gesamten Studiums vom ersten Bachelor-Semester bis nun zur Abgabe der Dissertation nicht nur finanziell und mit Rat und Tat zur Seite standen, sondern mir von klein auf einen freien, moralischen und selbstbestimmten und Lebensweg aufzeigten.

